Reduced-order models for blood flow in the large arteries : applications to cardiovascular pathologies

Jeanne Ventre



Sorbonne Université

École doctorale Sciences Mécaniques, Acoustique, Électronique et Robotique

Thèse de doctorat

Spécialité Mécanique des Fluides

Modèles réduits d'écoulement sanguin dans les grandes artères

Applications aux pathologies cardiovasculaires

Reduced-order models for blood flow in the large arteries

Applications to cardiovascular pathologies

Par : **Jeanne Ventre**

Sous la direction de Pierre-Yves Lagrée, Directeur de Recherche
José Maria Fullana, Professeur

à l'Institut Jean le Rond ∂'Alembert, Sorbonne Université, CNRS, UMR 7190.

Soutenue le 6 octobre 2020

Devant le jury composé de :

Valérie Deplano	Directrice de Recherche	Rapporteure
Irène Vignon-Clémentel	Directrice de Recherche	Rapporteure
Abdul Barakat	Directeur de Recherche	Examinateur
Quentin Grimal	Professeur	Examinateur
Franck Nicoud	Professeur	Examinateur
Anne-Virginie Salsac	Directrice de Recherche	Examinatrice
Chloé Audebert	Maître de Conférence	Invitée
Pierre-Yves Lagrée	Directeur de Recherche	Directeur de thèse
José-Maria Fullana	Professeur	Co-directeur de thèse

Abstract

Reduced-order model for blood flow in the large arteries
Applications to cardiovascular pathologies

Understanding and predicting the hemodynamics of cardiovascular pathologies is crucial to improve the management and diagnosis of such diseases. Mathematical blood flow models are a suited alternative to classical approaches such as invasive measurements, data analysis methods, and medical imaging techniques. To be used as predictive tools for patient-specific studies, blood flow models need to be computed in real medical time, typically the diagnosis time. Three-dimensional models that simulate the interaction between the fluid and the mechanics of the arterial wall provide really precise data, however, they require important computational resources. Reduced-order models allow determining the pressure and flow fields with a low computational cost and in regions of the arterial network inaccessible to visualization techniques and invasive measurements. The goal of this thesis is therefore to derive a hierarchy of reduced-order models, from simple to complex, that we apply to study different pathologies.

After detailing the derivation of the models, the resolution methods, and testing the hypotheses, we focus on applying them to several scenarios, suggested by our physician collaborators. Each model is suited for a particular medical situation depending on the scale of the problem. We first investigate vascular stenoses, defined as a narrowing of the lumen of a vessel, that can lead to important modifications of the hemodynamics. This pathology can appear in different locations of the network: in the aorta for instance, as in Aortic Coarctation, a congenital disease found in children. In this case, the measurement of pressure is essential to determine the treatment strategy. We, therefore, use all the reduced-order models to compute the pressure in the stenosis and compare it with invasive data to validate our approach. Stenoses can also appear after the creation of an arteriovenous fistula, a connection between an artery and a vein to speed-up the blood filtration for patients with kidney failure. We use the simplest models to reproduce and predict the distribution of blood in the system and when a venous stenosis develops. When stenoses become too severe, a surgical intervention is necessary. We thus explore the impact of aortic-cross-clamping during stenoses repair surgeries. Clamping consists of momentarily stopping the circulation to prevent blood from flowing in the operation zone. This procedure provokes modifications in the vascular properties that we investigate with reduced-order models. Finally, we study one last pathology pulmonary hypertension in order to evaluate different mechanical properties and classify the pathologies according to these properties.

Keywords: Cardiovascular pathologies, blood flow, reduced-order models, arterial network.

Résumé

Modèles réduits d'écoulement sanguin dans les grandes artères
Applications aux pathologies cardiovasculaires

Comprendre et prédire l'hémodynamique impliquée dans les pathologies cardiovasculaires est essentiel pour améliorer la gestion et le diagnostic de ces maladies. Les modèles d'écoulement sanguins sont une alternative intéressante aux approches classiques comme les examens invasifs et les techniques d'imagerie médicale. Pour être utilisés comme des outils prédictifs pour des simulations patient-spécifique, les modèles doivent avoir un temps de calcul réduit, de l'ordre de celui du diagnostic médical. Les modèles complexes tri-dimensionnels qui considèrent les interactions entre le fluide et la structure du tissue artériel fournissent des données très précises. Néanmoins, ils nécessitent un coût, à la fois numérique et paramétrique, trop important pour être utilisés dans de grands réseaux vasculaires. Les modèles dits réduits permettent, eux, de déterminer les champs de pression et vitesse avec un coût de calcul faible et à des emplacements du réseau artériel inaccessible aux techniques de visualisation ou aux méthodes de mesure classiques. Cette thèse se concentre donc sur ces modèles réduits et nous dérivons une hiérarchie de modèles, du plus simple au plus complexe, que nous appliquons pour étudier différentes pathologies.

Après avoir détaillé la dérivation des modèles, leurs méthodes de résolution et avoir testé les hypothèses, nous nous intéressons à les appliquer dans plusieurs scénarios, proposés par nos collaborateurs médecins. Chaque modèle est adéquat pour une situation médicale particulière, en fonction du degré de complexité et de l'échelle du problème. Tout d'abord, nous étudions la sténose vasculaire, un rétrécissement du diamètre d'un vaisseau, qui entraine des modifications importantes de l'hémodynamique. Cette pathologie peut apparaître à différents endroits du réseau : dans l'aorte comme lors de la Coarctation Aortique, une maladie congénitale trouvée chez l'enfant. Dans ce cas, la mesure de la pression est essentielle pour déterminer la méthode de traitement. Nous utilisons donc tous les modèles à notre disposition pour calculer la pression dans la sténose et comparons avec des mesures invasives pour valider notre approche. Les sténoses peuvent également apparaître après la création d'une fistule artério-veineuse, une connexion entre une artère et une veine du bras pour accélérer la filtration du sang pour les patients avec une insuffisance rénale. Nous utilisons les modèles les plus simples pour reproduire et prédire la distribution du sang dans ce système et lorsqu'une sténose veineuse se développe. Lorsque les sténoses sont trop sévères, une opération chirurgicale est nécessaire. Nous nous intéressons donc à l'impact du clampage aortique lors de chirurgies réparatrices de sténose. Le clampage consiste à couper la circulation momentanément afin d'opérer dans une zone où le sang ne s'écoule pas. Cette procédure provoque des modifications des propriétés vasculaires, que nous étudions avec des modèles réduits. Enfin, nous nous intéressons à une dernière pathologie, l'hypertension pulmonaire afin d'évaluer des propriétés mécaniques du réseau vasculaire pulmonaire et discriminer les differentes pathologies.

Keywords: Pathologies cardiovasculaires, écoulement sanguin, modèles réduits, réseau artériel.

Remerciements

Je ne peux que commencer ces remerciements par Pierre-Yves et José, sans qui rien n'aurait été possible. Depuis 2017, quand je suis venue vous voir pour faire une thèse en biomécanique, vous m'avez accueillie avec bienveillance, et m'avez toujours prodigué les meilleurs conseils. Pendant ma thèse, vous m'avez laissé une grande liberté sur les sujets abordés tout en me donnant les moyens pour réussir, et les opportunités pour élargir le champ des possibles. Vous vous êtes toujours rendus disponibles pour discuter de science mais avez aussi toujours été à l'écoute de mes interrogations sur le plan professionnel. Finalement, merci pour la confiance que vous m'avez accordé tout au long de ces trois années.

Je souhaite remercier Valérie Deplano et Irène Vignon-Clémentel pour avoir accepté de rapporter ma thèse avec minutie et bienveillance. Merci aussi aux autres membres du jury, Abdul Barakat, Quentin Grimal, Chloé Audebert, Franck Nicoud et Anne-Virginie Salsac pour le temps qu'ils m'ont accordé, et leurs remarques et questions qui ont grandement amélioré la qualité de ce manuscrit et m'ont donné des pistes de réflexions très intéressantes. Je suis très reconnaissante que la plupart d'entre vous ait accepté d'assister à ma soutenance en présentiel malgré la situation. Je tiens tout particulièrement à témoigner ma reconnaissance à Anne-Virginie pour son implication dans ma thèse à travers le comité de suivi.

Cette thèse a été le fruit de nombreuses collaborations avec des chercheurs de divers horizons que je tiens à remercier sincèrement. Tout d'abord, merci Teresa, ton enthousiasme et ta curiosité ont rendu nos interactions enrichissantes et passionnantes et comptent parmi les meilleures expériences de ma thèse. Grâce à ta rigueur, nos échanges m'ont permis de grandir scientifiquement. Je n'aurais pas pu rêver mieux comme collaboratrice. Merci également à Juan pour tes brillantes idées qui m'inspirent grandement. Merci également à tous les collaborateurs du projet ECOS-Sud notamment Claudia Capurro qui m'a accueillie chaleureusement à l'occasion de mes deux séjours dans son laboratoire. Je ne peux oublier les membres du Laboratorio de Biomembranas qui ont été d'une extrême gentillesse pendant mes séjours en Argentine. Je remercie vivement Salam Abou Taam et Francesca Raimondi pour nos collaborations fructueuses ainsi que tous les autres médecins avec qui j'ai pu interagir pendant ces trois années. Un grand merci à Mami Matsukawa et ses étudiants Fumiaki Iwase et Hiroto Shimizu pour leur accueil à l'Université Doshisha, pour m'avoir permis de contribuer à leurs expériences et découvrir le Japon. Je remercie sincèrement Arthur Ghigo pour son temps et sa bienveillance au début de ma thèse qui m'a fait me sentir à l'aise au laboratoire et avec mon sujet. Je remercie aussi les stagiaires de passage à ∂'Alembert qui m'ont aidé à déblayer certains aspects de ma thèse : Elisa, Maxime, Atish, Laureline.

J'ai également une pensée particulière pour tous les professeurs que j'ai eu la chance d'avoir en cours durant mes années de licence et master, que j'ai ensuite recroisé à l'institut ou avec qui j'ai pu enseigner. Après 8 ans passés à l'université, je ne peux que les remercier pour leur bienveillance. Je tiens aussi à remercier toute l'équipe administrative de l'Institut pour avoir facilité toutes mes démarches au cours de cette thèse : en particulier Olivier Labbey et Simona Otarasanu qui ont toujours été d'une aide précieuse dès que j'en ai eu le besoin.

Je souhaiterais remercier l'ensemble des doctorants et post-doctorants de l'Institut ∂' Alembert qui m'ont accompagné au cours de ces trois années. Je ne me voyais pas écrire ces remerciements sans mentionner quelques noms qui ont tout particulièrement marqué mon

passage à ∂'Alembert. À commencer par Antoine Lagarde, merci d'avoir été là pendant ces trois ans qui auraient été bien moins agréable sans toi. Je suis vraiment heureuse de t'avoir côtoyé dès le début de ma thèse et de pouvoir te compter aujourd'hui parmi mes amis. Tu es la personne la plus inspirante que je connaisse, autant humainement que scientifiquement. Alexis, ton humour et ta bonne humeur ont fait régner au labo une ambiance agréable et pour ça je te remercie. Cécile, même si on se connaissait avant que tu arrives à ∂'Alembert, je suis vraiment heureuse d'avoir pu ces deux dernières années découvrir la personne incroyable, drôle et douce que tu es. Antoine Monier, grâce à toi, mon frère au Japon, mes collègues en Argentine et mes grand-parents au fin fond de la Loire ont pu écouter ma soutenance alors merci. Mais par dessus tout, merci d'être un ami si bienveillant, ton humour me manquera au quotidien. Mathis merci pour ta gentillesse et pour avoir toujours été une oreille attentive pendant ces 3 ans. Hugo ça a toujours un plaisir de parler de mode, musique ou bouffe avec toi. Anaïs, merci pour ta bienveillance et tes conseils pour la préparation de ma soutenance, ton soutien et le temps que tu m'as consacré.

Un grand merci à mes co-bureaux du 317A et B, qui ont rendu ce bureau un lieu de travail agréable et vivant : Alice, Toufik, Antoine W., Manuel, Franck, Aidan. Et bien sûr les autres doctorants avec qui j'ai toujours pris beaucoup de plaisir à déjeuner ou discuter autour d'une bière : Serena, Quentin, Sagar, Adrien etc. Merci aussi à tous les anciens de ∂'Alembert, en particulier mes anciens co-bureaux Paul et Gauthier, mes partenaires de TP Raphaël et Nicolas, sans oublier Valentin G., Virgile, Arthur L. et bien d'autres qui m'ont permis de m'intégrer facilement à ∂'Alembert et m'y sentir à l'aise.

Enfin je souhaite remercier mes amis, en commençant par le Chinese Gang ; lorsque j'ai commencé ma thèse nous étions 6 et nous ne sommes plus que 5 aujourd'hui. Bruno, te perdre a été l'épreuve la plus difficile de ma vie mais m'a fait prendre conscience de la chance que j'avais d'être entourée d'amis si fidèles. Alors un immense merci à Manon, Martyna, Julien et Thierry, je suis si reconnaissante de vous avoir. Annie, je suis tellement heureuse d'avoir une amie avec qui je partage autant de passions et je suis vraiment ravie de t'avoir dans ma vie. Une pensée pour tous mes copains de Master (Yohan, Charles, Gaetan, Norma et les autres) que j'aurais adoré voir à ma soutenance même si la situation n'a pas pu le permettre. Merci à ma meilleure amie Olivia, qui m'a montré que les années ne pourraient pas nous séparer.

Merci évidemment à mes parents, qui, depuis toujours me soutiennent et m'encouragent dans tous mes choix, de mon entrée à l'université jusqu'à ma sortie aujourd'hui. Merci pour votre confiance et vos conseils que ce soit sur le plan professionnel ou personnel. Je remercie mon frère Louis, qui n'avait jusqu'à maintenant pas la moindre idée de ce sur quoi ma thèse portait et qui pensait que les modèles 1D étaient indé. Merci pour ta gentillesse et ton incroyable générosité. Un immense merci également à mon oncle Laurent pour ses conseils toujours avisés et bienveillants sur ma thèse et mes projets professionnels. Merci à mon grand-père d'avoir assisté lui aussi de loin à ma soutenance. Je pense également très fort à ma grand-mère Mamone qui je l'espère est fière de moi.

Finalement, je tiens à remercier une des personnes les plus importantes de ma vie. Merci à Damien, mon partner in crime, confident et amoureux. Merci de me supporter et de me soutenir dans toutes mes décisions.

Contents

Nomenclature

Dimensionless numbers

Re	Reynolds number
Ma	Mach number
Sh	Shapiro number
α	Womersley number

Fluid properties

ρ	Fluid density
μ	Fluid dynamic viscosity
ν	Fluid kinematic viscosity
τ	Shear stress
$\dot{\gamma}$	Shear rate

Flow variables of the 1D model

A	Cross-section
Q	Flow rate
p	Pressure
U	Velocity
τ_w	Wall Shear Stress
C_f	Friction coefficient
R_t	Reflection coefficient
Z_0	Impedance
c	Wave velocity
λ	Wavelength
ψ	Shape factor
$W_{1,2}$	Riemann invariants

Properties of the 0D models

R_p	Proximal resistance
R_d	Distal resistance
R_{tot}	Total resistance

C	Compliance
I	Inductance
τ	Diastolic time-constant
T_c	Heart period
T_{ej}	Ejection period
V_s	Systolic volume

Geometrical properties

R_0	Reference radius
D_0	Reference diameter
A_0	Reference cross-section
h	Wall thickness
L	Length
R_{st}	Stenosis radius
A_{st}	Stenosis cross-section
β	Degree of constriction of stenosis
L_{st}	Stenosis length

Mechanical properties

$\boldsymbol{\epsilon}$	Strain tensor
$\mathbf{u}$	Displacement field
$\mathbf{F}$	Deformation gradient
$\boldsymbol{\sigma}$	Cauchy stress tensor
Ψ	Strain density function
$\mathbf{P}$	Piola Kirchhoff stress tensor
J	Jacobian of the deformation tensor
E	Young's modulus
ν_w	Poisson coefficient
λ_w	Lamé coefficient
μ_w	Lamé coefficient
K	Elastic coefficient
K_ν	Viscoelastic coefficient

C_ν Linearized viscoelastic coefficient

ϕ Wall viscosity coefficient

Numerical parameters

Δt Time step

Δx Space step in the x-direction

Δy Space step in the y-direction

N_r Number of rings in the Multi-Ring model

N_x Number of cells in the x-direction

Optimization parameters

$\mathcal{J}$ Cost function

$\mathcal{P}$ Set of parameters to estimate

B Hessian matrix

Statistical parameters

δ Mean

σ Standard deviation

N Sample size

ρ Pearson's correlation coefficient

R^2 Correlation coefficient

1 Introduction

1.1 A bit of history

In the fourth century B. C., the Greek philosopher Aristotle identified the heart as the most important, first organ of the body to form and center of vitality in the body. In the second century A. D., Claudius Galenus (Claude Galien in french) reaffirmed some of the known concepts about the heart but contradicted others in matter of detailed anatomy, such as Aristotle's claim that the heart was the origin of the nerves [1].

Galien's theory states that there are three main systems in the body: the brain and nerves, the heart and arteries, and the liver and veins. He was indeed the first to identify the physiological difference between veins and arteries. According to Galien's theory, the venous blood formed in the liver, traveled through the veins and the entire body to deliver nourishment to maintain tissues. Blood would come into contact with air in the lungs and go to the heart. The blood did not return to the liver or the heart but would instead be consumed by the body. Sometimes the liver produced too much blood which led to illness cured at the time by bloodletting to restore the equilibrium by drawing off the excess fluid.

For almost fifteen centuries, the knowledge about physiology and anatomy only relied on Galien's theory. Opinions about these long-existing theories started to be challenged in the thirteenth century by the Egyptian doctor Ibn al-Nafis who described the pulmonary circulation [2]. Despite promising work, it did not echo internationally and thus did not influence Medieval and Renaissance medicine.

At the beginning of the Renaissance, experimental investigations started to develop in particular with Leonardo Da Vinci who first dissected cadavers and began to view the heart based on mechanical principles (Figure 1.1). Around this time, Vesalius became the undisputed master of anatomy with his very influential books "*De Humani Corporis Fabrica Libri Septem*" (On the fabric of the human body in seven books) [3]. He, however, did not refute Galien's assertions on blood circulation.

It is only in the mid-seventeenth century that William Harvey revolutionized the ideas of the cardiovascular system with his book "*Exercitatio Anatomica de Motu Cordis et Sanguinis in Animalibus*" (An Anatomical Exercise on the Motion of the Heart and Blood in Living Beings) [4], considered as the founding of modern physiology. From repeated dissections of human cadavers and animal species, he thoroughly demonstrated that the blood flows through the heart and lungs, from which it is sent to the rest of the organism. He showed that the blood goes to the tissues thanks to their porosity and that it comes back from the extremities to the center of the body in the right atrium to form a closed-loop system. He

also described the heart as a muscular hydraulic pump that ensures the continuity of flow thanks to pulsatility.

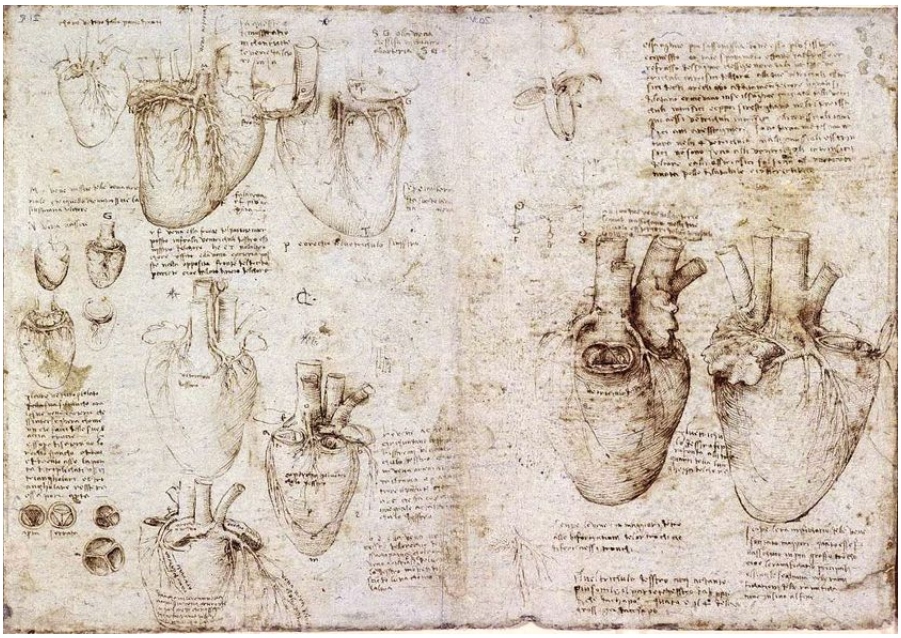

FIGURE 1.1 – Drawing of the heart and coronaries from Leonardo Da Vinci taken from "*Oeuvre anatomique*" (Anatomic work), a book constituted of drawings of different part of the human body. Image found here.

Although medicine had been around for centuries B.C., it is at the end of the nineteenth century that the first surgical acts emerged. In 1896, the doctor Ludwig Rehn successfully closed a heart stab wound by means of a direct suture, which marked the beginning of heart surgery [5]. Three other surgeons became leaders of experimental cardiac surgery before World War I and provided the base for its further clinical application. After that, arose multiple successes in cardiac surgery with operations on the pericardium, pulmonary embolectomy, removal of aneurysms, and many others.

The clinical achievements of the end of the nineteenth century were remarkable however there was still no accurate mean of measuring arterial blood pressure other than by operation [6]. Indeed, the pressure had been known as a crucial indicator as changes in pressure had been linked to the pathogenesis of many Cardiovascular diseases (CVDs). Karl von Vierordt was the first to introduce the sphygmograph in 1854 (Figure 1.2 left), a measurement tool to record the pulse pressure of blood. The French physician Etienne-Jules Marey considerably improved the technique of graphic recording and the accuracy of establishing the blood pressure in patients in 1863 (Figure 1.2 right). In 1896 the Riva-Rocci cuff was introduced. Since then, extensive efforts have been made to improve the assessment of blood pressure non-invasively which remains to this day a pressing issue in cardiovascular medicine.

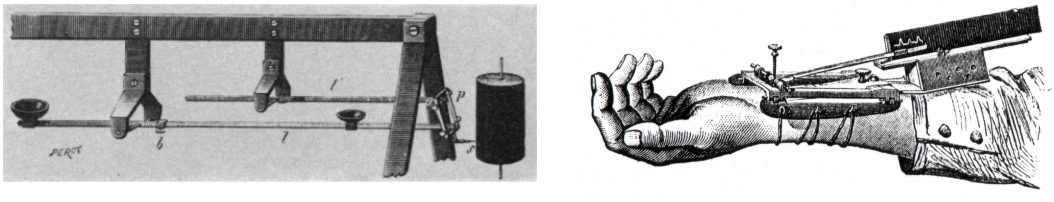

FIGURE 1.2 – Sphygmograph: measurement tool to record the pulse, the principle is to apply a counter pressure to overcome the arterial pressure Left: Karl von Vierordt' sphygmograph. Right: Etienne-Jules Marey's sphygmograph. Images from [6].

The main discoveries discussed here were carried by men however, historically women have occupied important roles in medicine and care-taking. Merit-Ptah was the earliest woman in the history of science in the Early Dynastic Period ($\sim$ 3,000 years B.C.). Agnodice was the first female physician to practice legally in the 4th century B.C. in Greece. Metrodora was also a Greek physician of this period, regarded as the first medical writer. Her book "On the Diseases and Cures of Women" was the oldest medical book written by a woman and covered all areas of medicine related to women, developing various therapies and surgical techniques that were revolutionary in her time.

During the Middle Ages, convents were important places of education for women that provided opportunities for women to contribute to scholarly research. For instance, Hildegard of Bingen was a German abbess in the 11th century and wrote about various scientific subjects such as medicine, botany, and natural history [7, 8] (Figure 1.3 left). She is considered the first German female physician. Among many unfounded belief-based practices, she gave intuitive statements that will prove true later, particularly on human physiology and blood circulation. Another important female figure of the Middle Age was Trota of Salerno (Figure 1.3 right), a physician who collected many of her empirical practices in writing. Part of her work was incorporated into the so-called Trotula compendium of writings on women's medicine and cosmetics.

FIGURE 1.3 – Representation of two important female figures of the Middle Ages in the history of medicine. Left: Hildegard of Bingen (11-12th century), image found here. Right: Trota of Salerno (12-13th century), image found here.

In the following, we summarize some key elements about current knowledge of cardiovascular physiology (Section 1.2) before presenting a brief literature review of the numerical models in the study of blood flows.

1.2 Cardiovascular physiology

The cardiovascular system is a closed-loop circuit composed of three main blocks (Figure 1.5) the heart, which pumps the blood, and distributes it into two networks of vessels, the systemic and the pulmonary, that convey blood to the body and drain it from the body tissues to the heart. In the following, we briefly describe the mechanical function of the cardiac pump (Section 1.2.1), the pulmonary circulation, and the systemic circulation (Section 1.2.2).

1.2.1 The cardiac pump

The heart is a muscular organ composed of two synchronized pumps each divided into two chambers, ventricles and atria. The cavities have the following role: the upper left (LA) and right (RA) atria collect the blood from the veins and lower left (LV) and right (RV) ventricles contract to propel the blood into the systemic and pulmonary veins (Figure 1.4). The right side collects de-oxygenated blood (represented in blue in Figure 1.4) from the systemic veins, the superior and inferior vena cava, and perfuses the lung through the pulmonary arteries. The left side collects oxygenated blood (represented in red in Figure 1.4) from the pulmonary veins and perfuses the rest of the body through the aorta which is the main artery of the systemic circulation.

Each chamber is separated by a valve: the mitral valve between the LV and the LA, the aortic valve between the LV and the aorta, and the corresponding valves in the right heart are the tricuspid valve between the RA and RV and the pulmonary valve between the RV and the root of the main pulmonary artery.

The cardiac cycle is a two-stage pumping process, the systole and the diastole (Figure 1.6), that occur over a period of about 1 s corresponding to 60 Beat Per Minute (BPM). These two stages can be defined in several manners, that are similar, depending if we consider the trigger to be electrical or mechanical. Systole can be defined as the contraction of the heart to pump the blood, diastole as the relaxation of the heart to refill with blood. The four main phases of the ventricular activity can be defined by the state of the inlet and outlet valves. Indeed, the role of the valves is to regulate the blood pressure between the cavities and vessels and prevent backflow.

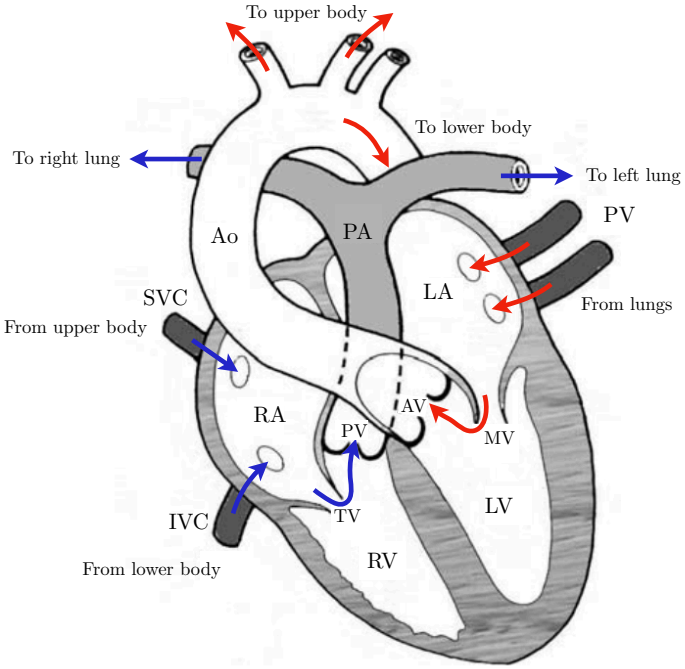

FIGURE 1.4 – Schematic representation of the heart chambers and blood circulation from [9]. Heart chambers: RA: Right Atrium, RV: Right Ventricle, LA: Left Atrium, LV: Left Ventricle. Vessels: Ao: Aorta, PA: Pulmonary Artery, PV: Pulmonary Vein, SVC: Superior Vena Cava, IVC: Inferior Vena Cava. Valves: TV: Tricuspid Valve, PV: Pulmonary Valve, MV: Mitral Valve, AV: Aortic Valve. The red arrows correspond to the flow of oxygenated blood, the blue arrows to the flow of deoxygenated blood.

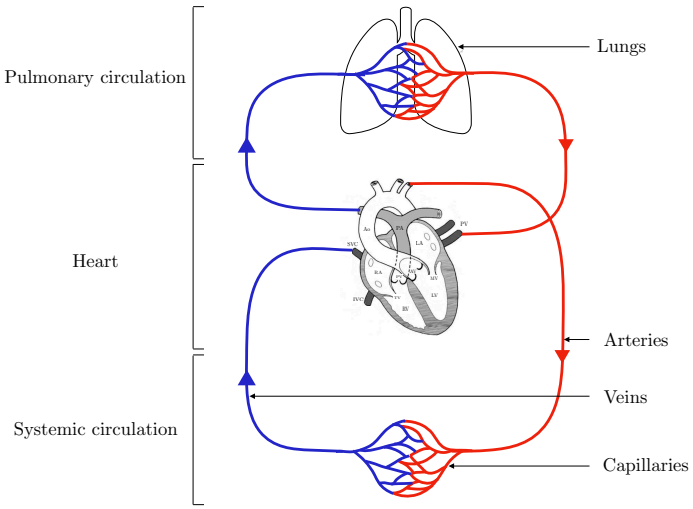

FIGURE 1.5 – Schematic representation of the cardiovascular system including the pulmonary circulation, the heart (image from [9]), and the systemic circulation. The blood circulation in the heart is detailed in Figure 1.4. Blue corresponds to the veins and red corresponds to the arteries.

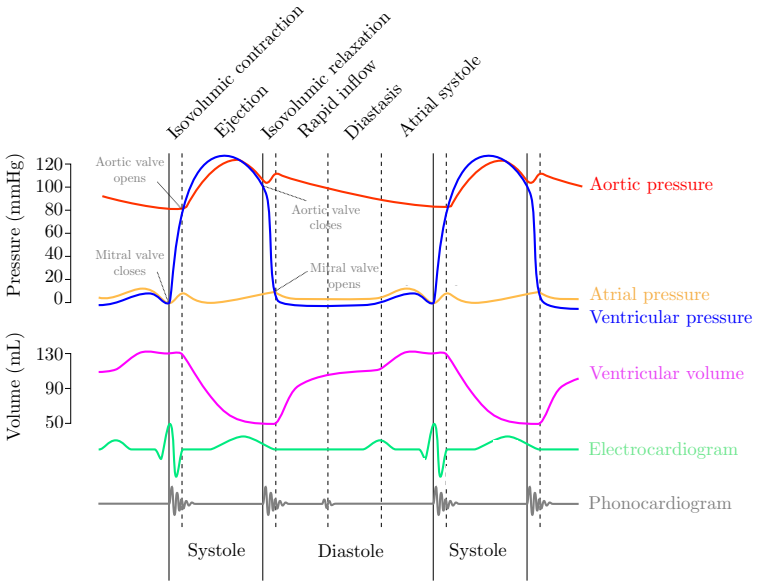

FIGURE 1.6 – Cardiac cycle events. Diagram found here.

1.2.2 The systemic and pulmonary circulations

Both blood circuits, systemic and pulmonary, are composed of three types of vessels: arteries, capillaries, and veins (Table 1.1). The role of the pulmonary circuit is to oxygenate the blood leaving the right heart and return oxygenated blood in the left heart whereas the systemic circuit delivers the oxygen and nutrients to the tissues and removes carbon dioxide (Figure 1.5). Despite similar topologies, the pulmonary circulation is a low pressure and low resistance system unlike the systemic circulation (Figure 1.7).

The arteries can be discriminated in three categories according to their size: the large arteries, the small arteries, and the arterioles. The large arteries are also called elastic arteries because the wall has a large number of collagen and elastin filaments (Figure 2.1). The main large artery, the aorta, is connected to the left ventricle. When the heart ejects blood, the elastic arteries dilate and regulate the pressure in the network, *i.e.* the variations of pressure in the arteries are much smaller than the variations in the heart. These arteries then divide into smaller arteries and arterioles who themselves divide into millions of smaller capillaries constituting the capillary bed. This microcirculation, present in all organs, muscles, and tissues, carries the exchange of oxygen and nutrients. The small capillaries then merge into venules and connect progressively into veins to deliver the deoxygenated blood to the heart at low-pressure. The pressure at this level drops to almost zero. Compared to arteries, veins have some different features: first, there are valves in some veins to keep the flow uni-directional, second the venous wall is very collapsible due to the low pressure difference, and third, the wall is thinner, and the elasticity much smaller. One of the main differences between arteries and veins is the pressure inside the vessels as well as the pulsatility, that almost does not exist in the veins unlike in the arteries (Figure 1.7). The flow of blood in the veins is partly governed by physical activity. In terms of mechanics, the large arteries and veins are differentiated from other vessels by their size and the predominance of inertial effects over viscous effects in the flow of blood in them, characterized by relatively large values of the Reynolds number ($Re \approx 1000$, see Table 2.3). In the capillaries, the viscous effects dominate and the

TABLE 1.1 – Characteristic values of diameter, occurence, and mean pressure of the human systemic vessels adapted from [9].

Vessel	Diameter (mm)	Number of vessels	Mean pressure (kPa)
Aorta	25	1	12.5
Large arteries	1-10	50	12
Small arteries	0.5-1	10^3	12
Arteriole	0.01-0.5	10^4	7
Capillary	0.006-0.01	10^6	3
Venule	0.01-0.5	10^4	1.5
Vein	0.5-15	10^3	1
Vena cava	30	2	0.5

flow can be governed by the Poiseuille equation.

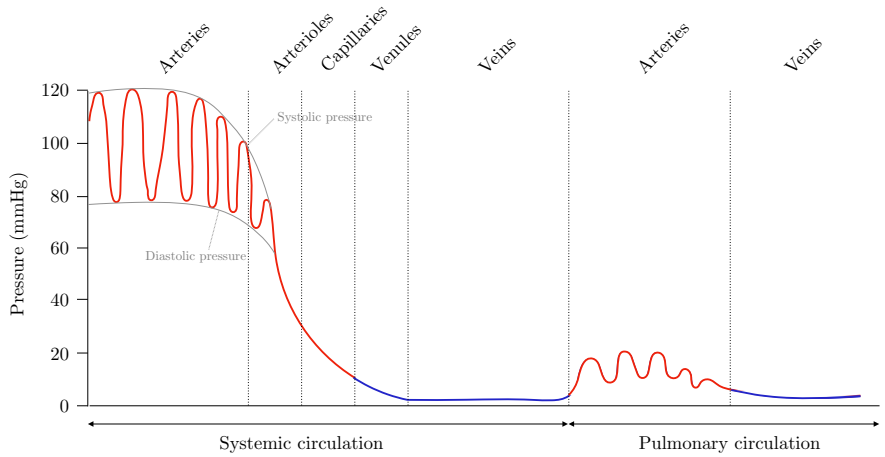

FIGURE 1.7 – Systemic and pulmonary blood pressure and pulsatility depending on the vessels. Blue corresponds to the veins and red corresponds to the arteries. Diagram inspired by the textbook Anatomy & Physiology, OpenStax College.

The flow in the cardiovascular system is driven by the stages of the cardiac cycle [10] (Figure 1.6). During systole, blood is ejected which causes a dilation of the elastic arterial wall, during diastole, the vessel wall relaxes. This dilation-relaxation process propagates a pressure wave at a finite, but large, velocity along the arteries. These waves give rise to reflections whenever there is a discontinuity in the geometrical or elastic properties of the arteries. Bifurcations and high resistance regions create reflections that propagate back towards the heart. These backward waves are themselves reflected by the bifurcations giving rise to a very complex pattern of reflected and re-reflected waves that determine the complex local pressure and velocity waveforms in the arteries [11].

Because most CVDs originate from arteries, we choose to restrict our study to the arterial circulation of the cardiovascular system. Closed-loop models, including heart and veins, have been studied in the literature [12–14]. In this thesis, we mainly study the arterial systemic circulation (Chapter 6, 7, 8) considering the challenges proposed by our clinician collaborators, however, we also investigate the pulmonary circulation in Chapter 9.

In this section, we summarized only the main elements of the cardiovascular system but it is much more complex and involves interactions with biology and chemistry. More detail can be found in textbooks such as [9, 10, 15–17].

1.3 Motivation

Over the last decades, clinicians have made tremendous improvements in the understanding of physiology and the management of CVDs. However, they remain to this day the number 1 cause of death globally, taking an estimated 17.9 million lives each year, according to the World Health Organization. CVDs are responsible for more than half of the mortality in developed countries. In France, they are the first cause of death for women and take about 140,000 lives each year (54% of women) against for instance $\sim$ 30,000 for the Covid-19 (54% of men) according to Santé publique France.

These cardiovascular pathologies include, among others, heart failure, stroke, atherosclerosis, and aneurysm which can appear in various locations of the system and have lethal consequences. They are usually slowly progressing diseases that can remain asymptomatic until their last stages which makes them even more dangerous. People with CVDs or who are at high cardiovascular risk (due to the presence of one or more risk factors such as hypertension, diabetes, or already established disease) need early detection and management.

Clinicians have developed a wide variety of treatment strategies to prevent the progression of diseases. The principal diagnosis tools for CVDs are catheterization, an invasive pressure measurement technique and imaging such as Magnetic Resonance Imaging (MRI), Echocardiography, or Computed Tomography (CT) that are non-invasive tools [17]. However, the development of CVDs is a complex multiphysics and multiscale process involving a combination of biological, chemical, and mechanical factors. All of these factors cannot be apprehended all together using only non-invasive measurements and topological considerations. Indeed, the invasive measurements must nowadays be carefully justified for medical care purposes as they often present risks and side-effects. Therefore and thanks to advances in computer sciences, clinicians have considered relevant the idea of mathematical models to represent the hemodynamics at different vascular scales to complement other forms of measurements. There is now a widespread recognition that mathematical models can provide an additional understanding of the mechanisms involved in CVDs.

One way of obtaining information on the cardiovascular system is by studying the pressure and flow waveforms. Pulse waves of pressure and flow rate in the arterial system can be correctly captured by reduced-order models of blood flow. By analyzing and modeling flow waveforms, we can deduce important vascular features even in regions of the network inaccessible to visualization techniques or given easily-obtained routine hemodynamic information. These models are attractive because of the good compromise between modeling complexity and computational resources.

1.4 Mathematical models

Understanding and predicting the wave dynamics in the network of vessels is crucial in hemodynamics and mathematical models are of great clinical relevance. The mathematical modeling of the various functions of the cardiovascular system is an incredibly challenging problem because of the difference in space and time scale of the mechanisms involved. It is then useful to identify a hierarchy of models, each suited for a different type of investigation or different parts of the system.

In the following, we present a brief literature review on the different blood flow models, experimental and numerical, inspired by [9, 15, 18]. We however only focus on mechanical approaches which mean that we discard the biologic exchanges, the chemical interactions, and all other phenomena that are not mechanical.

1.4.1 In vitro models

Etienne-Jules Marey contributed to the understanding of the pulse wave propagation with his sphygmograph (Figure 1.2 right) that allowed him to accurately measure and analyze the waves. To complement these measured data, he developed *in vitro* models of the heart (Figure 1.8 left) and the arterial circulation (Figure 1.8 right) to provide new insights on the mechanical principles of the cardiovascular system.

Since then, *in vitro* circulation models have been used to reproduce *in vivo* conditions as in [19] in which the authors built a 1:1 scale model of the heart and the 28 main arteries. In [20], the authors also built a 9-artery network to study the propagation and reflection of the pulse waves and the effects of viscosity and viscoelasticity[1]. A similar approach is carried in [21, 22] in a 37-artery network, and the results are compared to numerical blood flow models. Numerous experimental studies focused on modeling the detailed flow field in areas sensitive to arterial diseases such as arterial bifurcations [20, 23–25].

These *in vitro* models allow reproducing data in unavailable locations of the arterial network and are particularly useful to validate numerical blood flow models that we present in the following.

1.4.2 Three-dimensional Navier-Stokes models

Any numerical model of blood flow in the arteries is based on Fluid-Structure Interaction (FSI) methods where the fluid dynamics and flexible wall movement equations are coupled. In these models, blood flow is governed by the three-dimensional (3D) incompressible Navier-Stokes equations. In this approach, the wall deformation usually obeys a visco-elastic law relating strain et stress even though the arterial wall mechanics is far more complex [26]. The system coupling the fluid and solid equations has been solved with many different FSI resolution methods [27–30].

1. during a stay at Doshisha University in Japan, we studied how to build these models.

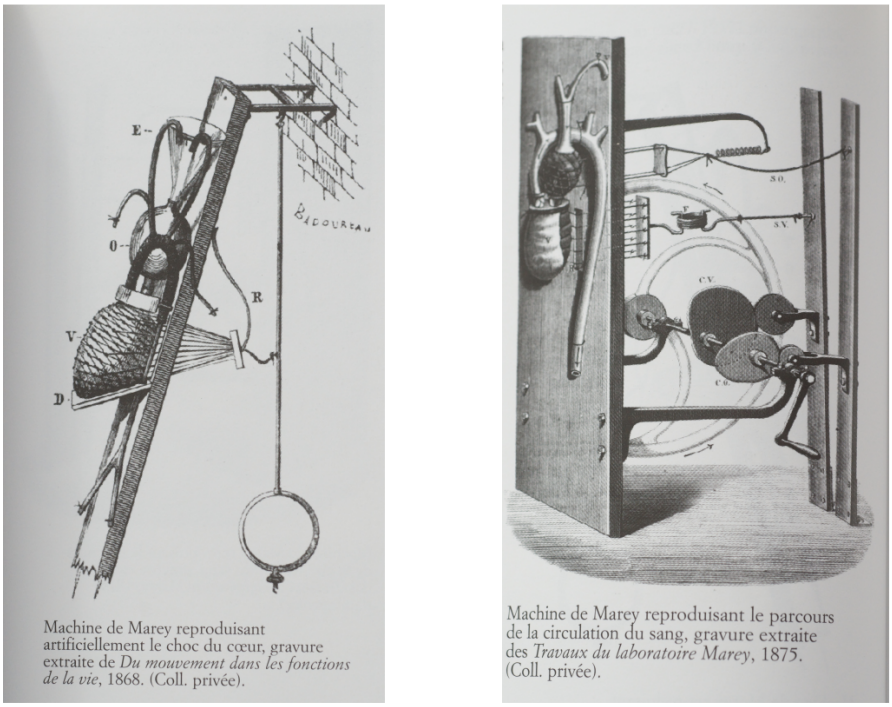

FIGURE 1.8 – Two experimental machines of the cardiovascular system built by Etienne-Jules Marey from [31]. Left: machine modeling the heart contraction from "*Du mouvement dans les fonctions de la vie*". Right: machine modeling the blood flow in the systemic circulation from "*Travaux du laboratoire Marey*".

Some studies also introduce turbulence models in the 3D Navier-Stokes equations, for instance k-ϵ or LES models, to correctly capture the flow in the heart [32], in particular after the aortic valve, and in the ascending aorta [33] and because it may appear in a variety of pathophysiological effects [34] such as stenoses [35] or aneurysms [36].

The 3D approach enables a complete description of all relevant scales but is usually restricted to small regions of the systemic circulatory system [37, 38] for instance bifurcations, aneurysms, or stenoses. Based on medical imaging, a 3D FSI patient-specific simulation of the large arteries of the whole body was performed [39]. While this simulation provides many details of the flow field in a patient-specific geometry, it is very expensive to compute. Moreover, it requires a large number of parameters, which cannot necessarily be measured but highly influences the results of the simulation.

Despite the work proposed in [39], 3D blood flow models remain difficult to apply in an extended network of vessels. The computational and modeling costs of the 3D approach are high, making it inadequate for real-time medical applications. Multiscale approaches have developed and consist of coupling a 3D model to simpler reduced-order models that describe the pulse wave propagation in the rest of the vascular tree. These reduced-order models, such as zero-dimensional (0D) and one-dimensional (1D) models, are cost-effective alternatives to 3D FSI models.

1.4.3 Two-dimensional models

Two-dimensional (2D) models are not the most common when it comes to modeling blood flow. In the case of arteries, we can consider the vessel as an axisymmetric tube and solve the 2D axisymmetric Navier-Stokes equations as in [40].

1.4.4 Simplified two-dimensional models

The long-wavelength hypothesis is appropriate in the case of arteries and allows simplifying the 2D equations. This assumption leads to the Reduced Navier-Stokes Prandtl (RNSP) equations which are a rich dynamic system of equations able to describe many asymptotic flow regimes in rigid tubes [41–43]. This model has mostly been computed in steady conditions in stenoses [41, 44].

Recently, some interest has been drawn to simplified 2D models with the development of a new approach based on the multi-layer model for the shallow water equations [45]. This model, called the Multi-Ring model, introduced by Ghigo in 2017 [46], solves the RNSP equations in an artery divided in rings. It has only been used in few studies to compute the pressure drop in a stenosis [47, 48], *i.e.* a constriction of the lumen of an artery, with more accuracy than the classical 1D model.

1.4.5 One-dimensional models

The 1D equations are the next level of simplifications and are obtained by averaging the long-wavelength Navier-Stokes equations over the cross-section of the artery. In the integration process, only the radial dependency is lost, therefore, they account for pulse wave propagation and reflection in the arterial network which are important phenomena for understanding cardiovascular hemodynamics [15].

Euler introduced the 1D equations for the conservation of mass and the continuity of momentum in 1775 in his essay "*Principia pro motu sanguinis per arterias determinando*" (On the flow of blood in the arteries) [49] with the intent of describing blood flow in the human arteries. He was however unable to solve the equations and thus did not recognize the wave characteristics of the system. Riemann did not directly work on arterial mechanics or waves in elastic tubes, but he made an important contribution to the subject when he published the method of characteristics and a general solution for hyperbolic systems of partial differential equations in 1860. Since then, the advances in computer science allowed solving the equations numerically and efficiently using a wide variety of numerical methods [50–54].

We find in the literature variations of the 1D model, detailed in [55], in particular on: 1) the incorporation of a Left Ventricle (LV) model studying the ventricular-vascular coupling effects, 2) the completeness of the systemic arterial tree (9-artery to 107-artery networks) including the venous circulation, 3) a detailed description of the cerebral, coronary, and pulmonary arteries, 4) the inclusion of the wall hyperelastic or viscoelastic properties, 5) the approximation of the Wall Shear Stress (WSS), 6) the boundary conditions. Indeed, to obtain physiological waveforms from the 1D model, the boundary conditions have to be realistic to reproduce the influence of the capillary bed [56–58], the heart mechanics [54, 59] and venous circulation [14] must be taken into account, and the flow in the bifurcations must be accurate [60, 61].

The 1D models have been extensively applied to the main systemic arteries [22,55,62–67] (Figure 1.9a), the entire cardiovascular system [14,54], the cerebral arteries [68–70], the pulmonary circulation [71]. The 1D model has been used in many different medical configurations for instance to study the influence of stenoses or aneurysms [48,50,53], to model or predict surgical outcome [67,72], in humans [11], and animals [73]. In time, the goal is to integrate the numerical prediction of the 1D model in routine clinical practice to provide information on pressure and flow waveforms and vascular features that cannot be obtained otherwise.

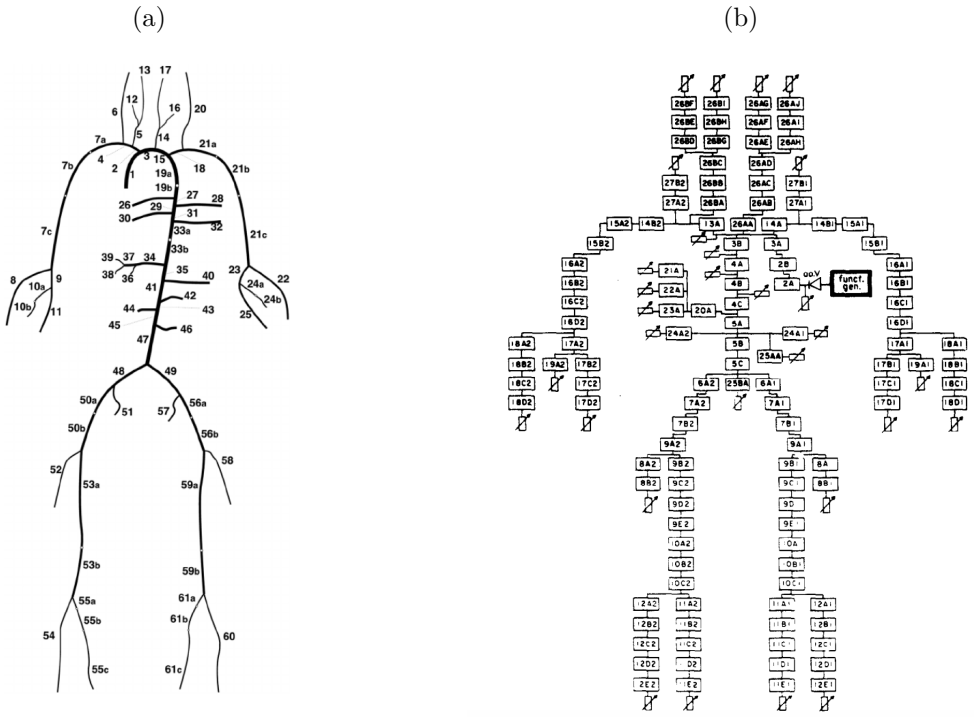

FIGURE 1.9 – (a) A one-dimensional (1D) representation of the arterial systemic circulation from [52]. Frequently, the outlet of the 1D arteries is a 0D Windkessel model. (b) A zero-dimensional (0D) representation of the arterial systemic circulation from [74] as an electrical circuit analogy. Each block represents an artery and is modeled by a 0D Winkdessel model.

1.4.6 Zero-dimensional models

The 0D models, also called lumped parameter models, are the simplest approach to describe blood flow. They are derived by averaging the blood flow equations over all spatial dimensions and can be interpreted as an electrical analogy where voltage is assimilated to pressure and current to flow rate. In this integration process, the axial and radial dependencies are lost hence the 0D models can only describe the relationship between the inlet and outlet pressure and flow rate. In this electrical analogy, the models are composed of resistors, capacitors, and inductors each modeling the resistive, compliant, and inertial effects.

The first and universal model is the Windkessel model [75], introduced by Frank [76] in his paper of 1899 "*Die Grundform des Arteriellen Pulses*" (The basis of arterial pulses). He considered the arteries as a single compliant compartment and used the conservation of mass to analyze their change of volume during diastole. The Windkessel model theory is particu-

larly successful to describe the pressure variations during diastole but fails to reproduce the systolic pressure. The other drawback of the Windkessel model and 0D models in general, is that, conversely to 1D models, they discard the wave propagation and reflections which play an important role during systole and are crucial to understanding hemodynamics. They however provide valuable information for medical diagnosis at low computational and modeling cost [67, 77].

To overcome the limitations, 0D models of one artery, similar to the Windkessel were introduced and connected together to form an electrical analogy of the systemic arterial network (Figure 1.9b) [74, 78, 79] composed of resistors, capacitors, and inductors. This model was able to reproduce the behavior observed in an *in vivo* system.

The 0D models have also been applied [80, 81] to describe the flow of blood in the heart [14, 59, 65, 82] and other organs [12], and to create models of the cerebral arterial network [69]. The most important use of the 0D models is to characterize the microcirculation at the outlet of 3D FSI models [29, 83] and 1D network models [22, 58, 72].

1.5 Aims and outline of the thesis

Considerable efforts have been made on developing high-performance and efficient resolution algorithms for all reduced-order models presented below such that now, they can be computed within minutes, a relevant order of magnitude for medical diagnosis. The models have also been extensively tested and validated against analytic, linear, and asymptotic solutions, *in vitro* and *in vivo* measurements.

Generally, all the models have their advantages and drawbacks. The Multi-Ring and the steady RNSP models are good compromises between complexity, computational resources, and precision. The 1D model is indisputably successful when it comes to predicting pressure and flow waveforms. The 0D models are relevant to identify global and constant vascular features or as boundary conditions models. Each model is suited for particular medical scenarios depending on the clinical issue and the scale of the results we are seeking. The goal of this thesis is thus to use the appropriate reduced-order models to provide a diagnosis, predictive or decision-making tool for clinicians in different medical scenarios.

One of the remaining challenges when using mathematical models of the cardiovascular system regardless of the scale is their dependence on a wide range of parameters whether they are model or physiological parameters. The goal of carrying patient-specific computations cannot be attained without this patient-specific information. Therefore, in this thesis, we focus on using efficient techniques of parameter estimation to identify properties of the cardiovascular system and thus make patient-specific diagnosis or prediction.

The following manuscript is divided into two parts. Part I, that includes Chapters 2 to 5, focuses on the modeling, theoretical and methodological aspects used in the second part. Part II deals with the medical applications of the models and methods described in the first part.

- **Chapter 2** deals with the derivation of the blood flow equations to obtain four reduced-order models used in the following chapters. We detail the assumptions on the arterial

wall behavior, on the fluid rheology, flow symmetries, and closure hypotheses to obtain a hierarchy of combined fluid-solid reduced-order models. We derive two laws for the arterial wall: an elastic and a visco-elastic law, and four models for the fluid: the steady RNSP model, the Multi-Ring model, the 1D model, and the 0D model.

- **Chapter 3** presents hyperelastic arterial wall models. Similarly to Chapter 2, we derive three hyperelastic laws to characterize the arterial wall mechanics from the literature. We then propose to combine them to the 1D model of Chapter 2 and compare the wave propagation in an artery with the classic elastic model of Chapter 2.

- **Chapter 4** focuses on the methods used in this thesis. As the models are non-linear and do not have analytic solutions, we solve them numerically using appropriate resolution schemes that we detail in this chapter. We also present optimization methods: we review the methods of the literature and detail the ones used in the medical applications of Part II to estimate the model parameters.

- **Chapter 5** consists of testing the model hypotheses against analytic solutions and experimental data. First, we compare the models to analytic solutions from the literature: the entry effect and the Womersley solution. Second, we carry experimental measurements in artificial arteries to validate the Multi-Ring and 1D models in two configurations: a network of nine artificial arteries and an artery with a stenosis, *i.e.* a narrowing of the cross-section.

- **Chapter 6** describes how we use the reduced-order models to assess non-invasively the pressure drop across a stenosis using 4D Flow MRI. We present the measurement techniques that are: the invasive catheterization to validate the models, and the 4D Flow MRI to obtain the geometrical and flow properties of the stenosis. We model an idealized stenosis using the steady RNSP, the Multi-Ring, the 1D, and the 0D model and compare the model against the invasive data.

- **Chapter 7** presents a 0D network model of the arm to study the impact of the creation of an Arterio-Venous Fistula (AVF) which is a connection between an artery and a vein performed to purify the blood in case of renal insufficiency. The procedure can lead to the formation of stenoses and thus we investigate the evolution of the AVF using the 0D network model and the 1D model.

- **Chapter 8** presents a comparison between experimental data and reduced models to study the impact of aortic cross-clamping during surgery on the vascular mechanics. We study and compare the 1D model, the 0D Windkessel model, and arterial waveform analysis to identify the changes in the vascular parameters during this procedure.

- **Chapter 9** describes the study of pulmonary hypertension. We present the invasive Swan-Ganz catheter and the non-invasive measurements in different locations of the pulmonary network. We review and develop a pulmonary valve model that we combine with the 1D model. Similarly to Chapter 8, we also use the 0D Windkessel model to

evaluate the resistance, compliance and diastolic time-constant in patients with pulmonary hypertension.

- **Chapter 10** summarizes the main result of the thesis and discusses the short and long-term perspectives of the present work.

The manuscript also includes supplementary material in the Appendices that include:

- **Appendix A** describes the Kálmán filter algorithm which can be used a parameter estimation strategy that we test on the damped harmonic oscillator equation.

- **Appendix B** presents supplementary results of the experimental measurements carried in the artificial arteries presented in Chapter 5.

- **Appendix C** gives additional information about the statistical analysis and the full parameter estimation results of each patient for the study of aortic cross-clamping of Chapter 8.

Part I

Modeling and theory

Understanding and predicting the hemodynamics and mechanisms involved in cardiovascular pathologies is of great clinical relevance. Mathematical blood flow models constitute a suited alternative to invasive measurements, data analysis methods, and medical imaging techniques. To be used as predictive tools for patient-specific studies, blood flow models need to be computed in real medical time, typically the diagnosis time. A series of assumptions on the flow symmetries, the rheological properties of blood or the arterial wall and the geometry of the arteries allow deriving reduced-order models that can be solved numerically in a few minutes. Currently, the classical arterial wall models do not account for the non-linear behavior of the arterial wall and thus requires a novel hyperelastic approach. The main drawback of the mathematical models in general is their dependence on a large number of parameters, weather they are physical or modeling parameters, that usually cannot be assessed through routine clinical monitoring or procedures, hence the interest of optimization methods to estimate patient-specific parameters. As stated above, all these blood flow models are based on a series of hypotheses and numerical approximations, validation against analytic solutions and experimental measurements is necessary.

2 Blood Flow Models

Mathematical blood flow modeling is now considered as a relevant alternative to invasive measurements to study cardiovascular pathologies. Reduced-order models allow computing the flow in real medical time but the underlying hypotheses must be carefully justified. We start by detailing the assumptions on the arterial wall behavior and geometry to obtain two wall models, first an elastic and second a viscoelastic model. We then discuss the hypotheses on the fluid rheology, flow symmetries, and closure hypotheses to obtain step by step the 2D axisymmetric Navier-Stokes equations, the RNSP model, the Multi-Ring model, the 1D model, and finally the 0D model. We also present the order of magnitudes of all the variables involved in blood flow in the centimeter, gram, second (CGS) unit system. None of these models are original however, the derivation step by step in this way is uncommon.

Keywords: Navier-Stokes Equations, Reduced Navier-Stokes Prandtl model, Multi-Ring model, one-dimensional model, zero-dimensional model, arterial wall.

Contents

2.1 Introduction

In Chapter 1, we reviewed the different existing models for studying blood flows in the arteries and presented the main limits of the complex models. The purpose of the present chapter is to derive synthetically the reduced-order models used in this work from the conservation laws of mechanics.

From continuum mechanics and geometrical assumptions, we describe a simplified arterial wall model in Section 2.2. In Section 2.3, we assume a few weak hypotheses on the behavior of blood flow in the large arteries to obtain four reduced-order models of different levels of complexity. The analysis is led with a purely mechanical approach thus we discard the thermal, chemical, and biological phenomena.

We also present the orders of magnitude of the variables of interest. We use the centimeter, gram, second (CGS) unit system, frequently used to describe the cardiovascular system: the characteristic length scale of the large artery is about $1 - 20$ cm, the time scale is the heartbeat, typically 60 Beat Per Minute (BPM), corresponding to 1 s per beat and finally the blood density is about 1 g/cm^3. The choice of CGS units is in fact a hidden adimensionalization because space and time are of the order of one of these units.

2.2 Derivation of the linear solid equations

We follow [84] to derive a simplified model of the arterial wall. We start by detailing the hypotheses on the geometry and mechanical behavior of the wall in Section 2.2.1. In Section 2.2.2, we derive an elastic model of the arterial wall mechanics. And later in Section 2.2.3, we add a viscoelastic component to the previous law to obtain a Kelvin-Voigt viscoelastic model of the arterial wall.

2.2.1 Simplifying hypotheses for arterial walls

Material hypotheses

The arterial wall is composed of three layers. The inner layer is called the intima, composed of endothelial cells, the medium layer, the media, is composed of smooth muscle cells and fibers and the outer layer of collagen fibers each separated by elastic membranes, as represented in Figure 2.1.

We choose to describe the arterial wall as a homogeneous, isotropic, and isothermal material. The arterial wall does not actually respond to any of these criteria, however these assumptions are necessary for the study of reduced-order models.

Axisymmetric cylinder

We model the artery as a thin, long axisymmetric cylinder of length L and reference radius R_0 as represented in Figure 2.2. This is a crude approximation considering the structure of blood vessels and the presence of external tissues.

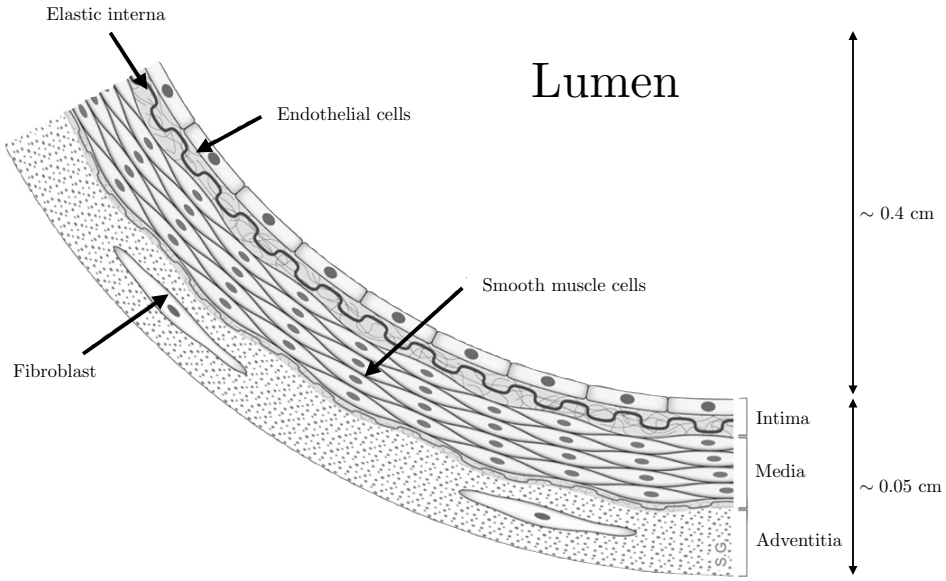

FIGURE 2.1 – Drawing of the three layers of the arterial wall. Image found here.

Thin wall

The thickness of the arterial wall is of the order of 0.05 cm, approximately 10 times smaller than the typical radius of large arteries. We therefore assume that the arterial wall is thin, *i.e.* $\frac{h}{R_0} \ll 1$.

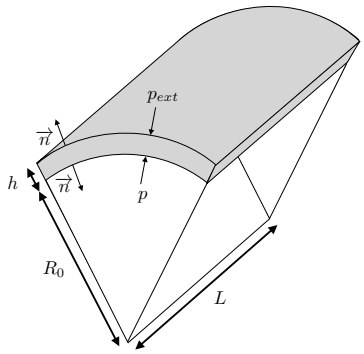

FIGURE 2.2 – Schematic representation of a part of the thin arterial wall of length L, radius R_0, and thickness h. p_{ext} and p represent respectively the external and internal pressure applied to the wall.

Small displacement

We consider that the wall displacement is small, which is a weak hypothesis in physiological conditions, and thus assume that the strain tensor $\boldsymbol{\epsilon}$ writes as

$$\boldsymbol{\epsilon} = \frac{1}{2}\left(\nabla \mathbf{u} + \nabla \mathbf{u}^T\right), \tag{2.1}$$

with $\mathbf{u}$ the wall displacement (not to be confused with the velocity that we refer to as $\mathbf{V} = (u_r, u_\theta, u_x)$). As the displacement in the axial direction is very small compared to the length of the artery, we consider that the axial strain is negligible *i.e.* $\epsilon_{xx} = 0$.

In the following, we first investigate the purely elastic case and then add a viscoelastic component.

2.2.2 Purely elastic arterial wall

Considering the artery as a linear elastic material (Figure 2.3a), the Cauchy stress tensor $\boldsymbol{\sigma}$ and the strain tensor $\boldsymbol{\epsilon}$ are related through Hooke's law

$$\boldsymbol{\sigma} = \lambda_w \mathrm{tr}(\boldsymbol{\epsilon})\mathbb{I} + 2\mu_w \boldsymbol{\epsilon}, \tag{2.2}$$

where λ_w and μ_w are the Lamé coefficients of the wall. The strain stress relation (2.2) can also be written as

$$\boldsymbol{\epsilon} = -\frac{\nu_w}{E}\mathrm{tr}(\boldsymbol{\sigma})\mathbb{I} + \frac{1+\nu_w}{E}\boldsymbol{\sigma} \tag{2.3}$$

where E is Young's modulus and ν_w the Poisson coefficient. Assuming a quasi-static equilibrium, we obtain the following momentum equation

$$\mathrm{div}(\boldsymbol{\sigma}) = 0. \tag{2.4}$$

We also assume that the pressure is the only significant component of the stress applied to the internal and external sides of the artery consequently we add the two following boundary conditions

$$\begin{cases} \boldsymbol{\sigma}\cdot\boldsymbol{n} = -p\boldsymbol{n} & \text{in} \quad r = R \qquad (2.5a) \\ \boldsymbol{\sigma}\cdot\boldsymbol{n} = -p_{ext}\boldsymbol{n} & \text{in} \quad r = R+h, \qquad (2.5b) \end{cases}$$

where p and p_{ext} are respectively the internal and external pressures (Figure 2.2). Combining Hooke's law (2.2) with the momentum equation (2.4) and the previous hypotheses, we obtain

$$(\lambda_w + 2\mu_w)\boldsymbol{\nabla}(\mathrm{div}(\mathbf{u})) - \mu_w \mathrm{rot}(\mathrm{rot}(\mathbf{u})) = 0. \tag{2.6}$$

The classical approach to solve Equation (2.6) which respects symmetries is to choose a kinematically admissible displacement field of the following form

$$\mathbf{u} = r f(r)\boldsymbol{e_r} + g(x)\boldsymbol{e_x}, \tag{2.7}$$

which allows obtaining the expression of the Cauchy stress tensor $\boldsymbol{\sigma}$. Using the thin wall assumption, the following Taylor expansion

$$\begin{cases} r = R_0\left(1 + \dfrac{h}{R_0}\bar{r}\right) & \text{with} \quad \bar{r} = \mathcal{O}(1) \qquad (2.8a) \\ R = R_0\left(1 + \dfrac{h}{R_0}\bar{R}\right) & \text{with} \quad \bar{R} = \mathcal{O}(1) \qquad (2.8b) \end{cases}$$

and keeping the $\mathcal{O}(1)$ terms, we can derive these relations into

$$\begin{cases} \sigma_{rr} = p\left((\bar{r} - \bar{R} - 1) - \dfrac{p_{ext}}{p}(\bar{r} - \bar{R})\right) & \text{(2.9a)} \\ \sigma_{\theta\theta} = \dfrac{pR_0}{h}\left(1 - \dfrac{p_{ext}}{p}\right) & \text{(2.9b)} \end{cases}$$

which indicates that $\sigma_{rr} \ll \sigma_{\theta\theta}$ since $h \ll R_0$. We use Hooke's law (2.2) to link $\boldsymbol{\sigma}$ and $\boldsymbol{\epsilon}$ which gives

$$\begin{cases} \epsilon_{\theta\theta} = \dfrac{1}{E}(\sigma_{\theta\theta} - \nu_w \sigma_{xx}), & \text{(2.10a)} \\ \epsilon_{xx} = 0 = \dfrac{1}{E}(\sigma_{xx} - \nu_w \sigma_{\theta\theta}). & \text{(2.10b)} \end{cases}$$

and finally leads to

$$\sigma_{\theta\theta} = \frac{E}{1 - \nu_w^2}\epsilon_{\theta\theta}, \tag{2.11}$$

which is a linear relation between stress and deformation through the Young's modulus E.

Combining Equations (2.9b) and (2.11), we obtain

$$\frac{R_0}{h}(p - p_{ext}) = \frac{E}{1 - \nu_w^2}\epsilon_{\theta\theta}. \tag{2.12}$$

We note that $\epsilon_{\theta\theta} = \dfrac{u_r}{r}$, which in $r = R$ gives $\epsilon_{\theta\theta} = \dfrac{R - R_0}{R}$, and leads to the well-known elastic relation

$$p - p_{ext} = \frac{E}{1 - \nu_w^2}\frac{h}{R_0^2}(R - R_0), \tag{2.13}$$

which is usually written as a function of the cross-section A and the reference cross-section A_0

$$p - p_{ext} = K\left(\sqrt{A} - \sqrt{A_0}\right), \tag{2.14}$$

with K the parameter characterizing the rigidity of the arterial wall

$$K = \frac{E}{1 - \nu_w^2}\frac{\sqrt{\pi}h}{A_0}. \tag{2.15}$$

In Equation (2.14), the reference cross-section A_0 can depend on the x-position and thus

$$p(x,t) - p_{ext} = K(x)\left(\sqrt{A(x,t)} - \sqrt{A_0(x)}\right), \tag{2.16}$$

where the parameter K can thus also depend on the x-position. We often assume that $p_{ext} = 0$ for simplicity.

Equation (2.16) describes the arterial wall as an elastic spring as represented in Figure 2.3a. However, this elastic approach cannot reproduce the mechanical behavior of such a complex material as the arterial wall [73]. Therefore, in the following section, we present a more realistic model of the arterial wall by adding a time-dependence response of the wall.

2.2.3 Viscoelastic arterial wall

As the arterial wall displays both an elastic and a viscous behavior [85, 86], we take into account the wall viscosity. We include the viscoelastic behavior of the arterial wall adding a linear Kelvin-Voigt model [16, 22, 86] defined by an elastic spring assembled in parallel with a dashpot, as represented in Figure 2.3b. Equation (2.12) becomes

$$(1-\nu_w^2)\frac{R_0}{h}(p-p_{ext}) = E\epsilon_{\theta\theta} + \phi\dot{\epsilon}_{\theta\theta}, \tag{2.17}$$

with ϕ the viscoelastic coefficient. The difference between the internal and external pressure is now also balanced by the time-derivative of the deformation $\dot{\epsilon}_{\theta\theta}$. This model [22] allows deriving a new state law linking the pressure and the cross-section as

$$p - p_{ext} = K\left(\sqrt{A} - \sqrt{A_0}\right) + K_\nu \frac{\partial A}{\partial t}, \tag{2.18}$$

with K_ν the following viscoelastic coefficient

$$K_\nu = \frac{\phi}{1-\nu_w^2}\frac{\sqrt{\pi}h}{2\sqrt{A_0}}\frac{1}{A}. \tag{2.19}$$

Note that, unlike the elastic coefficient K from Equation (2.15), the coefficient K_ν is non-linear as it also depends on the cross-section A.

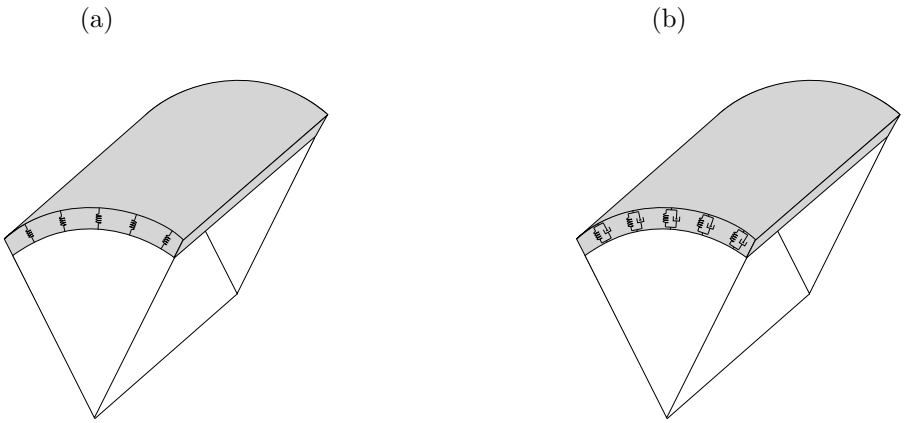

FIGURE 2.3 – Schematic representation of the arterial wall model. (a) Elastic model with an elastic spring proportional to E, (b) Kelvin Voigt viscoelastic model composed of an elastic spring proportional to E and a dashpot proportional to ϕ.

This kind of model was used in multiple studies, for instance [13, 51, 63, 67], as the level of complexity is still manageable compared to the elastic model of Equation (2.16) and gives more physiological predictions when comparing against experimental data [73]. In this chapter, we derived the relations with a linear approximation, we will see in Chapter 3 how to rigorously introduce non-linear terms.

Here, we demonstrated with a mechanical approach how to derive the relation (2.18) by the linear approximation, however the coefficients K and K_ν are *ad hoc* and do not have real

TABLE 2.1 – Orders of magnitude of the "solid" variables defined Section 2.2. E: Young's modulus in g·cm^{-1}·s^{-2}, ν_w: Poisson coefficient, R_0: artery radius in cm, h: arterial wall thickness in cm, K: elastic coefficient defined in Equation (2.15) in g·cm^{-2}·s^{-2}, K_ν: viscoelastic coefficient defined in Equation (2.19) in g·cm^{-3}·s^{-1}.

E	ν_w	R_0	h	K	K_ν
0.4 - 1.6 $\cdot 10^7$	0.5	0.5	0.1	$1 \cdot 10^6$	$2 \cdot 10^4$

physiological meaning. In fact, the vessels are surrounded by tissues that also interact with the arteries and contribute to the values of these coefficients.

The orders of magnitude of the parameters introduced in this section are reported in Table 2.1.

Now we investigate the models for the flow inside the artery.

2.3 Derivation of the fluid equations

We present here four reduced-order models for blood flow modeling that will be used in the next chapters: the steady Reduced Navier-Stokes Prandtl (RNSP) model, the unsteady RNSP named the Multi-Ring model, the one-dimensional (1D) model, and the zero-dimensional (0D) model. All these models derive from the Navier-Stokes equations with some typical hypotheses for the large arteries that we describe in Section 2.3.1. From these assumptions, in Section 2.3.2, we simplify the fluid equations into a two-dimensional (2D) model called the RNSP model. In Section 2.3.3, we average the RNSP model to obtain a 2D hybrid model named the Multi-Ring model. In Section 2.3.4, we derive the classical 1D model, and finally in Section 2.3.6, we average the previous one to obtain the simplest 0D model. We introduce here a hierarchy of models from complicated to simple with introduction step by step of the simplifications.

2.3.1 Simplifying hypotheses for blood flows in arteries

Laminar flow

We assume that the flow in the large arteries is laminar. The Reynolds number based on the mean velocity is well below 2000 in the majority of arteries in normal conditions (Table 2.3). However, in the aorta, the peak Reynolds number through the aortic valve can reach 10,000 [87], which is characteristic of a turbulent flow. The k-ϵ turbulence model, which is one of the most common in fluid mechanics, is not relevant in this case, large eddy simulation (LES) models may improve the large peak flow description [32].

Homogeneous Newtonian fluid

Blood is a complex fluid constituted of three types of blood cells (erythrocytes, leukocytes, and platelets) suspended in plasma [88]. Plasma usually behaves like a Newtonian fluid of dynamic viscosity $\mu = 1.2 \cdot 10^{-2}$ g·cm^{-1}·s^{-1}. The erythrocytes, or Red Blood Cell (RBC), occupy about 45% (level of hematocrit = 0.45) of the blood volume and thus dominate the rheological behavior of the blood. The dimension of a RBC is of the order of a few µm. The

leucocytes, also called white blood cells, are far less numerous than the RBCs and thus have a marginal influence on the properties of blood. Finally, platelets are 10 times less frequent than the RBC. Each constituent of the blood contributes to its apparent viscosity in particular the shear rate, the hematocrit, the temperature, and the plasma viscosity [89]. Overall, in the large arteries, the cells are about four orders of magnitude smaller than the average vessel size.

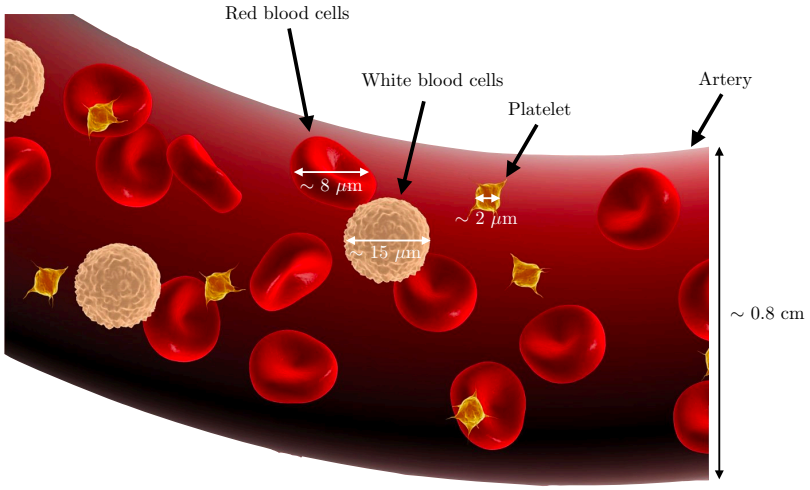

FIGURE 2.4 – Composition of blood and typical dimensions of blood cells. Image found here.

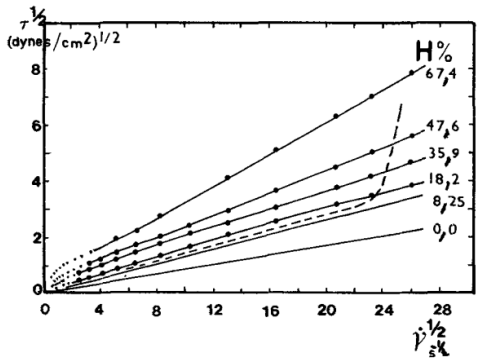

FIGURE 2.5 – Casson diagram from [90] based on experimental measurements of blood at different levels of hematocrit (a normal level of hematocrit in healthy humans is 45%). The diagram represents the shear stress τ as a function of the shear rate $\dot{\gamma}$ (Equation (2.20)).

Because of the blood composition, many studies have investigated blood as a non-Newtonian fluid that exhibits shear-thinning, viscoelastic, and thixotropic behaviors [91]. Experimental measurements show that blood follows the Casson law [10, 90] that links the shear stress τ to the shear rate $\dot{\gamma}$ through

$$\tau^{1/2} = \tau_0^{1/2} + f(\dot{\gamma}^{1/2}) \tag{2.20}$$

as represented in Figure 2.5.

Considering blood as a non-Newtonian fluid is indeed relevant in recirculation areas such as stenosis or aneurysm in which low shear regimes are reached, however in most healthy large arteries, the average shear rate is high enough ($\dot{\gamma} > 10\ \mathrm{s}^{-1}$) to consider blood as a homogeneous and Newtonian fluid with constant viscosity. Indeed, from Figure 2.5, we observe that for $\dot{\gamma} > 10\ \mathrm{s}^{-1}$, the shear stress is linear, the slope is thus the viscosity of blood μ of about $3 - 5{\cdot}10^{-2}\ \mathrm{g{\cdot}cm^{-1}{\cdot}s^{-1}}$.

Incompressible flow

The compressibility of a flow is characterized by the Mach number Ma that measures the ratio between the velocity of the flow and the velocity of sound in the fluid. A flow is incompressible if $Ma < 0.3$. Because the velocity in the arteries rarely exceeds a few meters per second, the velocity of sound in the water ≈ 1500 m/s, the Mach number is small and we can consider that blood flow is incompressible. The motion of blood in arteries with all the previous approximations is thus governed by the three-dimensional (3D) incompressible Navier-Stokes equations

$$\begin{cases} \nabla \cdot \mathbf{V} = 0, & \text{(2.21a)} \\ \rho \left(\dfrac{\partial \mathbf{V}}{\partial t} + (\mathbf{V} \cdot \nabla)\mathbf{V} \right) = -\nabla p + \mu \nabla^2 \mathbf{V}, & \text{(2.21b)} \end{cases}$$

where $\mathbf{V}$ is the fluid velocity vector, p the fluid pressure, ρ the density and μ the dynamic viscosity. Typical values for blood are reported in Table 2.4

Long-wavelength

In the large arteries, the wavelength of the pulse wave is much larger than the characteristic diameter. Indeed, the Moens Korteweg celerity c is of order 10^2 cm/s [92, 93] (Section 2.3.5), the heart period T_c is around 1 s. The axial wavelength of the pulse wave is then $\lambda = cT_c \approx 10^2$ cm, which is much larger than 1 cm, the characteristic diameter of a large artery.

Axisymmetric flow

Following the geometrical simplifications proposed in Section 2.2, we consider that the flow is axisymmetric and thus use the cylindrical coordinate system $\mathbf{V} = (u_r, u_\theta, u_x)$. This assumption leads to $\partial/\partial\theta = 0$ and we can also assume that the tangential velocity u_θ is negligible to simplify Equations (2.21) into

$$\begin{cases} \dfrac{1}{r}\dfrac{\partial r u_r}{\partial r} + \dfrac{\partial u_x}{\partial x} = 0, & \text{(2.22a)} \\ \dfrac{\partial u_r}{\partial t} + u_r \dfrac{\partial u_r}{\partial r} + u_x \dfrac{\partial u_r}{\partial x} = -\dfrac{1}{\rho}\dfrac{\partial p}{\partial r} + \nu \left(\dfrac{1}{r}\dfrac{\partial}{\partial r}\left(r \dfrac{\partial u_r}{\partial r} \right) - \dfrac{u_r}{r^2} + \dfrac{\partial^2 u_r}{\partial x^2} \right), & \text{(2.22b)} \\ \dfrac{\partial u_x}{\partial t} + u_r \dfrac{\partial u_x}{\partial r} + u_x \dfrac{\partial u_x}{\partial x} = -\dfrac{1}{\rho}\dfrac{\partial p}{\partial x} + \nu \left(\dfrac{1}{r}\dfrac{\partial}{\partial r}\left(r \dfrac{\partial u_x}{\partial r} \right) + \dfrac{\partial^2 u_x}{\partial x^2} \right), & \text{(2.22c)} \end{cases}$$

where ν is the kinematic viscosity of blood.

2.3.2 The Reduced-Navier-Stokes Prandtl

We reduce the system of Equations (2.22) by evaluating the importance of each of the terms and introduce the dimensionless variables of Table 2.2.

TABLE 2.2 – Dimensionless variables to adimensionalize Equation (2.22).

$$
\begin{aligned}
t &= T_c \bar{t} \\
r &= R_0 \bar{r} \\
x &= \lambda \bar{x} \quad \text{with } \lambda = cT_c \\
u_r &= U_r \bar{u}_r \\
u_x &= U_x \bar{u}_x \\
p &= p_0 + \Pi \bar{p}
\end{aligned}
$$

We define a small parameter, called the long wave parameter, $\epsilon_\lambda = \dfrac{R_0}{\lambda} \ll 1$ that measures the ratio between the characteristic radius and the wavelength. We adimensionalize the system (2.22) as

$$
\begin{cases}
\left[\dfrac{U_r}{\epsilon_\lambda U_x}\right] \dfrac{1}{\bar{r}} \dfrac{\partial \bar{r} \bar{u}_r}{\partial \bar{r}} + \dfrac{\partial \bar{u}_x}{\partial \bar{x}} = 0, & \text{(2.23a)} \\
\dfrac{\partial \bar{u}_r}{\partial \bar{t}} + \left[\dfrac{U_r}{\epsilon_\lambda c}\right] \bar{u}_r \dfrac{\partial \bar{u}_r}{\partial \bar{r}} + \left[\dfrac{U_x}{c}\right] \bar{u}_x \dfrac{\partial \bar{u}_r}{\partial \bar{x}} = -\left[\dfrac{\Pi}{\rho \epsilon_\lambda U_r c}\right] \dfrac{\partial \bar{p}}{\partial \bar{r}} \\
\qquad + \left[\dfrac{\nu T_c}{R_0^2}\right] \left(\dfrac{1}{\bar{r}} \dfrac{\partial}{\partial \bar{r}} \left(\bar{r} \dfrac{\partial \bar{u}_r}{\partial \bar{r}} \right) - \dfrac{\bar{u}_r}{\bar{r}^2} + \left[\epsilon_\lambda^2\right] \dfrac{\partial^2 \bar{u}_r}{\partial \bar{x}^2} \right), & \text{(2.23b)} \\
\dfrac{\partial \bar{u}_x}{\partial \bar{t}} + \left[\dfrac{U_r}{\epsilon_\lambda c}\right] \bar{u}_r \dfrac{\partial \bar{u}_x}{\partial r} + \left[\dfrac{U_x}{c}\right] \bar{u}_x \dfrac{\partial \bar{u}_x}{\partial \bar{x}} = -\left[\dfrac{\Pi}{\rho U_x c}\right] \dfrac{\partial \bar{p}}{\partial \bar{x}} \\
\qquad + \left[\dfrac{\nu T_c}{R_0^2}\right] \left(\dfrac{1}{\bar{r}} \dfrac{\partial}{\partial \bar{r}} \left(\bar{r} \dfrac{\partial \bar{u}_x}{\partial \bar{r}} \right) + \left[\epsilon_\lambda^2\right] \dfrac{\partial^2 \bar{u}_x}{\partial \bar{x}^2} \right). & \text{(2.23c)}
\end{cases}
$$

According to the principle of least degeneracy [94], we keep the leading order terms in Equations (2.23) and in particular in the mass conservation Equation (2.23a), we keep both terms which gives

$$
U_r = \epsilon_\lambda U_x, \tag{2.24}
$$

and considering the long-wavelength hypothesis $\epsilon_\lambda \ll 1$, we obtain that the radial velocity is much smaller than the axial velocity $U_r \ll U_x$. The principle of least degeneracy [94] also states that the pressure gradient must balance the inertial terms in Equation (2.23c) which leads to $\Pi = \rho U_x c$.

The typical mechanical approach to deal with the type of equations (2.23) is to define dimensionless parameters to compare the importance of each term. Thus we define the Shapiro number Sh

$$
Sh = \frac{U_x}{c}, \tag{2.25}
$$

that characterizes the importance of nonlinear effects. As U_x is generally comprised between 0 and 100 cm/s in the large arteries, the typical range for the Shapiro number is between 0 and

1. It highlights that the non-linear effects are small compared to the pressure and unsteady terms. It can be seen as the equivalent of the Mach number for blood flows.

We also introduce the Womersley number α that describes the competition between unsteady and viscous effects

$$\alpha = R_0\sqrt{\frac{\omega}{\nu}} \tag{2.26}$$

with $\omega = 2\pi/T_c$. With the values reported in Table 2.3, we obtain a Womersley number between 0 and 10 in the large arteries. The values of the Womersley number show that in the aorta the inertial effects dominate compared to the viscous effects unlike in the capillaries where the viscosity controls the flow. So for low values of the Womersley number we observe a quasi-static Poiseuille profile. In average arteries, both effects are important as α has an intermediate value.

The Womersley and Shapiro numbers allow rewriting the Equations (2.23) as

$$\begin{cases} \dfrac{1}{\bar{r}}\dfrac{\partial \bar{r}\bar{u}_r}{\partial \bar{r}} + \dfrac{\partial \bar{u}_x}{\partial \bar{x}} = 0, & \text{(2.27a)} \\ \dfrac{\partial \bar{u}_r}{\partial \bar{t}} + Sh\left(\bar{u}_r\dfrac{\partial \bar{u}_r}{\partial \bar{r}} + \bar{u}_x\dfrac{\partial \bar{u}_r}{\partial \bar{x}}\right) = -\dfrac{1}{\epsilon_\lambda^2}\dfrac{\partial \bar{p}}{\partial \bar{r}} \\ \qquad\qquad + \dfrac{1}{\alpha^2}\left(\dfrac{1}{\bar{r}}\dfrac{\partial}{\partial \bar{r}}\left(\bar{r}\dfrac{\partial \bar{u}_r}{\partial \bar{r}}\right) - \dfrac{\bar{u}_r}{\bar{r}^2} + \left[\epsilon_\lambda^2\right]\dfrac{\partial^2 \bar{u}_r}{\partial \bar{x}^2}\right), & \text{(2.27b)} \\ \dfrac{\partial \bar{u}_x}{\partial \bar{t}} + Sh\left(\bar{u}_r\dfrac{\partial \bar{u}_x}{\partial r} + \bar{u}_x\dfrac{\partial \bar{u}_x}{\partial \bar{x}}\right) = -\dfrac{\partial \bar{p}}{\partial \bar{x}} \\ \qquad\qquad + \dfrac{1}{\alpha^2}\left(\dfrac{1}{\bar{r}}\dfrac{\partial}{\partial \bar{r}}\left(\bar{r}\dfrac{\partial \bar{u}_x}{\partial \bar{r}}\right) + \left[\epsilon_\lambda^2\right]\dfrac{\partial^2 \bar{u}_x}{\partial \bar{x}^2}\right). & \text{(2.27c)} \end{cases}$$

Equations (2.27b) can be simplified by keeping only the $\mathcal{O}(1)$ terms since the small parameter ϵ_λ appears in front of the pressure term. Similarly, we reduce (2.27c) with $\epsilon_\lambda \ll 1$ which finally gives

$$\begin{cases} \dfrac{1}{\bar{r}}\dfrac{\partial \bar{r}\bar{u}_r}{\partial \bar{r}} + \dfrac{\partial \bar{u}_x}{\partial \bar{x}} = 0, & \text{(2.28a)} \\ 0 = -\dfrac{\partial \bar{p}}{\partial \bar{r}}, & \text{(2.28b)} \\ \dfrac{\partial \bar{u}_x}{\partial \bar{t}} + Sh\left(\bar{u}_r\dfrac{\partial \bar{u}_x}{\partial r} + \bar{u}_x\dfrac{\partial \bar{u}_x}{\partial \bar{x}}\right) = -\dfrac{\partial \bar{p}}{\partial \bar{x}} + \dfrac{1}{\alpha^2}\left(\dfrac{1}{\bar{r}}\dfrac{\partial}{\partial r}\left(\bar{r}\dfrac{\partial \bar{u}_x}{\partial \bar{r}}\right)\right). & \text{(2.28c)} \end{cases}$$

The set of Equations (2.28) is called the dimensionless Reduced Navier-Stokes Prandtl equations (RNSP) [41] and was originally derived by Prandtl in [95]. The system can also be found in the literature in the following form with dimensions:

$$\begin{cases} \dfrac{1}{r}\dfrac{\partial r u_r}{\partial r} + \dfrac{\partial u_x}{\partial x} = 0, & \text{(2.29a)} \\ 0 = -\dfrac{1}{\rho}\dfrac{\partial p}{\partial r}, & \text{(2.29b)} \\ \dfrac{\partial u_x}{\partial t} + u_r\dfrac{\partial u_x}{\partial r} + u_x\dfrac{\partial u_x}{\partial x} = -\dfrac{1}{\rho}\dfrac{\partial p}{\partial x} + \nu\left(\dfrac{1}{r}\dfrac{\partial}{\partial r}\left(r\dfrac{\partial u_x}{\partial r}\right)\right). & \text{(2.29c)} \end{cases}$$

TABLE 2.3 – Womersley and Reynolds numbers depending on the location in the arterial network. R_0: radius in cm, α: Womersley number (dimensionless), Re: Reynolds number (dimensionless).

	R_0	α	Re
aorta	1	10	4000
large arteries	0.4	4	1000
small arteries	0.1	1	100
arterioles	0.01	0.1	0.5
capillaries	0.001	0.01	0.03

We add the material interface and axisymmetric boundary conditions

$$\begin{cases} u_r = 0 & \text{in } r = 0, \quad (2.30a) \\ \dfrac{\partial u_x}{\partial r} = 0 & \text{in } r = 0, \quad (2.30b) \\ u_r = \dfrac{\partial R}{\partial t} & \text{in } r = R, \quad (2.30c) \\ u_x = 0 & \text{in } r = R. \quad (2.30d) \end{cases}$$

From the RNSP equations (2.29), we can decline two particular models. The first one consists of removing the unsteady term from the x-momentum Equation (2.29c) supposing a rigid wall similarly to [41], which we refer to as the steady RNSP model. The second consists of coupling Equations (2.29) with an elastic arterial wall, for instance with Equation (2.18), similarly to [46], which we refer to as the Multi-Ring model.

2.3.3 Multi-Ring model

The full reduced model for long wave approximation of the flow is the RNSP model, that we can couple to the elastic wall. The equations for the flow are then the incompressibility Equation (2.29a), the constant pressure across the flow (2.29b), the longitudinal momentum conservation Equation (2.29c) plus the no-slip boundary conditions (2.30c) and (2.30d), and the symmetry at the center boundary conditions (2.30a) and (2.30b). Finally, the Equations for the solid are (2.18). As we will discuss in Section 2.3.4, once integrated over the cross-section, this system gives the 1D model with no extra hypotheses.

But the problem of the numerical resolution of System (2.29)-(2.30) + the arterial wall model (2.18) is not so simple. A first resolution has been proposed by Ling and Atabeck [96] with some approximations, and another one is proposed later in [43]. The recent Multi-Ring model derived in [46] to introduce the elasticity of the arterial wall is a consistent numerical approximation of this system with an interpretation in "rings". The model was inspired by the Multilayer model [45] for the Saint-Venant equations in shallow water flows (see [97] for details and bibliography).

The flow is solved by decomposing the fluid domain into concentric rings. Each ring n is characterized by a width $h_n = R_{n+\frac{1}{2}} - R_{n-\frac{1}{2}}$. The cross-section of each ring A_n and the

average flow rate in the ring Q_n are defined as

$$\begin{cases} A_n = \displaystyle\int_0^{2\pi} \int_{R_{n-\frac{1}{2}}}^{R_{n+\frac{1}{2}}} r \mathrm{d}r\mathrm{d}\theta, & \text{(2.31a)} \\ Q_n = \displaystyle\int_0^{2\pi} \int_{R_{n-\frac{1}{2}}}^{R_{n+\frac{1}{2}}} u_x r \mathrm{d}r\mathrm{d}\theta. & \text{(2.31b)} \end{cases}$$

We can write the Equations (2.29) in terms of the averaged quantities A_n and Q_n on each ring n

$$\begin{cases} \dfrac{\partial A_n}{\partial t} + \dfrac{\partial Q_n}{\partial x} &= G_{n+\frac{1}{2}} - G_{n-\frac{1}{2}}, \\ \dfrac{\partial Q_n}{\partial t} + \dfrac{\partial}{\partial x}\left[\psi_n \dfrac{Q_n^2}{l_n A}\right] + \dfrac{A_n}{\rho}\dfrac{\partial p}{\partial x} &= S_{M,n} + S_{f,n}. \end{cases} \tag{2.32}$$

The parameter ψ_n is the nonlinear shape factor

$$\psi_n = \frac{A_n}{Q_n^2} \int_{R_{n-\frac{1}{2}}}^{R_{n+\frac{1}{2}}} 2\pi r u_x^2 \mathrm{d}r. \tag{2.33}$$

We assume that $\psi_n = 1$ under the hypothesis that the velocity profile is piece-wise constant in each ring n. This assumption is reasonable if the number of rings N_r is sufficiently large. The parameter l_n is the proportion of the total cross-section A occupied by the ring n such that $A_n = l_n A$. The term $G_{n+\frac{1}{2}}$ (respectively $G_{n-\frac{1}{2}}$) in Equation (2.32) represents the radial mass exchange at the interface of $R_{n+\frac{1}{2}}$ (respectively $R_{n-\frac{1}{2}}$)

$$G_{n+\frac{1}{2}} = \frac{\partial}{\partial t}\left(\pi R_{n+\frac{1}{2}}^2\right) + u_{x,n+\frac{1}{2}} \frac{\partial}{\partial x}\left(\pi R_{n+\frac{1}{2}}^2\right) - 2\pi R_{n+\frac{1}{2}} u_{r,n+\frac{1}{2}}. \tag{2.34}$$

The source term $S_{M,n}$ characterizes the momentum associated to the radial mass exchanges in the ring n

$$S_{M,n} = u_{x,n+\frac{1}{2}} G_{n+\frac{1}{2}} - u_{x,n-\frac{1}{2}} G_{n-\frac{1}{2}}. \tag{2.35}$$

Finally the source term $S_{f,n}$ describes the viscous dissipation

$$S_{f,n} = 2\pi\nu \left(r \left.\frac{\partial u_x}{\partial r}\right|_{R_{n+\frac{1}{2}}} - r \left.\frac{\partial u_x}{\partial r}\right|_{R_{n-\frac{1}{2}}} \right). \tag{2.36}$$

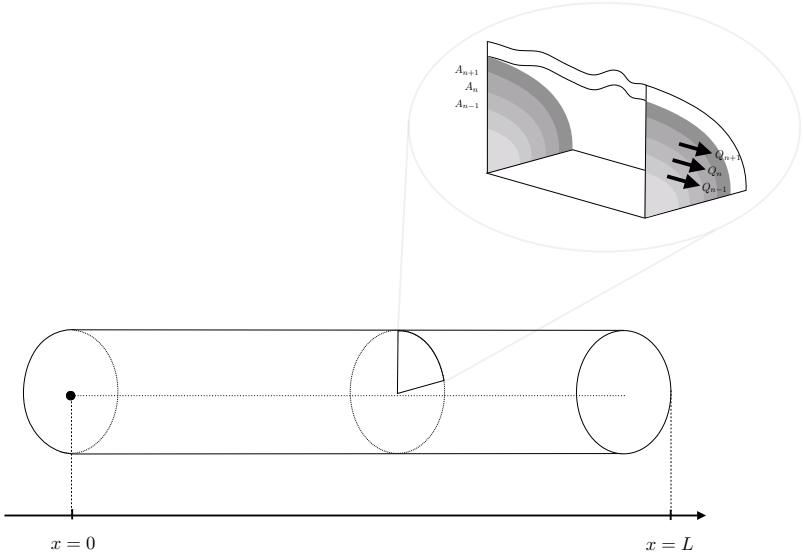

FIGURE 2.6 – Schematic representation of the Multi-Ring model. A_n and Q_n represent respectively the cross-section of ring n and the flow rate in ring n.

The set of Equations (2.32) is expressed in terms of cross-section and flow rate however, we require a third equation to close the system. In Section 2.2, we derived an arterial wall model that links the pressure to the cross-section. By coupling the system of Equation (2.32) with the pressure law (Equation(2.16)) we take into account the elasticity of the arterial wall and write the final closed-form conservative system as

$$\begin{cases} \dfrac{\partial A}{\partial t} + \dfrac{\partial F_A}{\partial x} = 0, & \text{(2.37a)} \\ \dfrac{\partial Q_n}{\partial t} + \dfrac{\partial F_{Q_n}}{\partial x} = S_{M,n} + S_{f,n} + l_n S_T \qquad \text{for} \quad n = 1, ..., N_r, & \text{(2.37b)} \end{cases}$$

with F_A the mass flux and F_Q the momentum flux defined as

$$\begin{cases} F_A = \displaystyle\sum_{i=0}^{N_r} Q_i, & \text{(2.38a)} \\ F_{Q_n} = \psi_n \dfrac{Q_n^2}{l_n A} + l_n \dfrac{K}{3\rho} A^{\frac{3}{2}}, & \text{(2.38b)} \end{cases}$$

and the source term S_T that accounts for the geometrical and mechanical source terms and coming from the fact that the elastic coefficient K and the reference cross-section A_0 both depend on the x-position

$$S_T = \frac{A}{\rho}\left(\frac{\partial}{\partial x}\left(K\sqrt{A_0}\right) - \frac{2}{3}\sqrt{A}\frac{\partial K}{\partial x}\right). \tag{2.39}$$

2.3.4 One-dimensional model

The 1D equations result from averaging the RNSP equations (2.29) over the cross-section of the artery

$$\int_0^{2\pi}\int_0^{R}\begin{pmatrix} \frac{1}{r}\frac{\partial r u_r}{\partial r}+\frac{\partial u_x}{\partial x} &= 0 \\ 0 &= -\frac{1}{\rho}\frac{\partial p}{\partial r}, \\ \frac{\partial u_x}{\partial t}+u_r\frac{\partial u_x}{\partial r}+u_x\frac{\partial u_x}{\partial x} &= -\frac{1}{\rho}\frac{\partial p}{\partial x}+\nu\left(\frac{1}{r}\frac{\partial}{\partial r}\left(r\frac{\partial u_x}{\partial r}\right)\right)\end{pmatrix} r\mathrm{d}r\mathrm{d}\theta. \tag{2.40}$$

This averaging process gives the 1D mass and momentum equations derived in detail in [98]

$$\begin{cases} \dfrac{\partial A}{\partial t}+\dfrac{\partial Q}{\partial x}=0, & \text{(2.41a)} \\ \dfrac{\partial Q}{\partial t}+\dfrac{\partial}{\partial x}\left(\psi\dfrac{Q^2}{A}\right)+\dfrac{A}{\rho}\dfrac{\partial p}{\partial x}=\dfrac{2\pi R_0}{\rho}\tau_w, & \text{(2.41b)} \end{cases}$$

where

$$\begin{cases} A=2\pi\displaystyle\int_0^{R_0} r\mathrm{d}r, & \text{(2.42a)} \\ Q=2\pi\displaystyle\int_0^{R_0} u_x r\mathrm{d}r. & \text{(2.42b)} \end{cases}$$

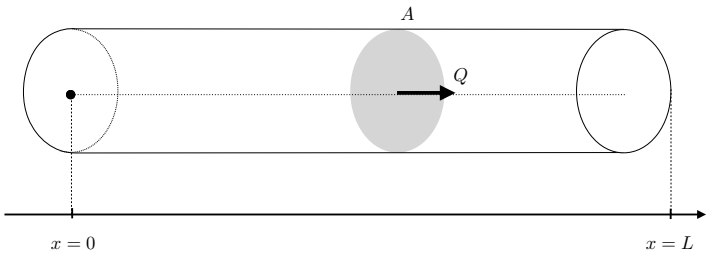

FIGURE 2.7 – Schematic representation of the 1D model. A and Q represent respectively the cross-section and the flow rate.

The coefficient ψ is the nonlinear shape factor similarly to Equation (2.33) with $n = 1$. The Wall Shear Stress (WSS) τ_w in Equation (2.41b) is

$$\tau_w = \mu \left.\frac{\partial u_x}{\partial r}\right|_{r=R_0}. \tag{2.43}$$

In the averaging process, we naturally lose information about the velocity profile and so we need an additional assumption to compute the WSS. A one-dimensional closure hypothesis from [99] suggests that the axial velocity can be of the following form

$$u_x = \Phi\left(\frac{r}{R_0}\right) U, \tag{2.44}$$

where $U = Q/A$ and Φ is the velocity profile shape leading to the following expression of the shape factor

$$\psi = 2\int_0^R \frac{r}{R}\Phi^2 \mathrm{d}r. \tag{2.45}$$

The classical approach consists of assuming a power-law for Φ [99], for instance

$$\Phi = \frac{\xi+2}{\xi}\left(1 - \left(\frac{r}{R_0}\right)^{\xi}\right). \tag{2.46}$$

In [43], more complicated closure hypotheses issued from the Womersley solution are proposed. Equation (2.46) allows calculating the shape factor ψ which gives

$$\psi = 1 + \frac{1}{1+\xi}. \tag{2.47}$$

Combining Equation (2.43) with (2.44), leads to

$$\tau_w = \mu\frac{U}{R_0}(-\xi - 2), \tag{2.48}$$

which allows rewriting the right hand side of Equation (2.41) as

$$\frac{2\pi R_0}{\rho}\mu\frac{U}{R_0}(-\xi-2) = -C_f\frac{Q}{A}. \tag{2.49}$$

where we introduce the friction coefficient

$$C_f = 2\pi\nu(\xi+2). \tag{2.50}$$

The value $\xi = 9$ from [100], corresponding to a flat velocity profile, is commonly used for 1D blood flows [22, 72, 101]. In the case of a Poiseuille velocity profile, $\xi = 2$ as in [48]. The shape factor is comprised between 1 and 4/3 and we thus assume for simplicity that $\psi = 1$, following the literature. By replacing the WSS term by the friction coefficient term in Equations (2.41), the 1D equations can be written as

$$\begin{cases} \dfrac{\partial A}{\partial t} + \dfrac{\partial Q}{\partial x} = 0, & \text{(2.51a)} \\ \dfrac{\partial Q}{\partial t} + \dfrac{\partial}{\partial x}\left(\dfrac{Q^2}{A}\right) + \dfrac{A}{\rho}\dfrac{\partial p}{\partial x} = -C_f\dfrac{Q}{A}. & \text{(2.51b)} \end{cases}$$

Similarly to Equation (2.32), we require a third equation to close and solve this system. By coupling (2.51) with the elastic pressure law (2.14) we can write the 1D system in the following conservative form

$$\begin{cases} \dfrac{\partial A}{\partial t} + \dfrac{\partial Q}{\partial x} = 0, & \text{(2.52a)} \\ \dfrac{\partial Q}{\partial t} + \dfrac{\partial}{\partial x}\left(\dfrac{Q^2}{A} + \dfrac{K}{3\rho}A^{3/2}\right) = -C_f\dfrac{Q}{A}. & \text{(2.52b)} \end{cases}$$

Note that we can also couple Equations (2.51) to (2.16) accounting for the fact that K

and A_0 depend on x, which makes appear a source term as in Equation (2.39). Using the viscoelastic pressure law Equation (2.18), we have a more general form

$$\begin{cases} \dfrac{\partial A}{\partial t} + \dfrac{\partial Q}{\partial x} = 0, & \text{(2.53a)} \\ \dfrac{\partial Q}{\partial t} + \dfrac{\partial}{\partial x}\left(\dfrac{Q^2}{A} + \dfrac{K}{3\rho}A^{3/2}\right) = -C_f\dfrac{Q}{A} + \dfrac{A}{\rho}\dfrac{\partial}{\partial x}\left(K_\nu\dfrac{\partial Q}{\partial x}\right). & \text{(2.53b)} \end{cases}$$

in which we used (2.53a) to substitute $\dfrac{\partial A}{\partial t}$ by $-\dfrac{\partial Q}{\partial x}$.

Unlike the elastic coefficient K, the viscoelastic coefficient K_ν depends on the variable A thus we decide to linearize K_ν around the reference cross-section which finally gives

$$\begin{cases} \dfrac{\partial A}{\partial t} + \dfrac{\partial Q}{\partial x} = 0, & \text{(2.54a)} \\ \dfrac{\partial Q}{\partial t} + \dfrac{\partial}{\partial x}\left(\dfrac{Q^2}{A} + \dfrac{K}{3\rho}A^{3/2}\right) = -C_f\dfrac{Q}{A} + C_\nu\dfrac{\partial^2 Q}{\partial x^2}, & \text{(2.54b)} \end{cases}$$

with

$$C_\nu = \frac{\phi}{\rho(1-\nu_w^2)}\frac{\sqrt{\pi}h}{2\sqrt{A_0}}, \tag{2.55}$$

the linearized viscoelastic coefficient.

Note that the 1D Equations (2.52) can also be interpreted as a particular case of the Multi-Ring model with only one ring, *i.e.* $n = 1$ in Equations (2.37), with the assumption on the velocity profile and the WSS.

In Figures 2.8, we show the difference between the purely elastic model of Equation (2.16) and the viscoelastic model of Equation (2.18) by showing the propagation of a pressure pulse in an artery. We observe in Figure 2.8b that the pulse is attenuated and diffused compared to Figure 2.8a. Indeed, the viscoelastic term in the 1D equations (2.54) can be seen as an analogy with the 1D diffusion equation

$$\frac{\partial Q}{\partial t} = k\frac{\partial^2 Q}{\partial x^2}, \tag{2.56}$$

with k the analog of C_ν in Equation (2.54).

(a) (b)

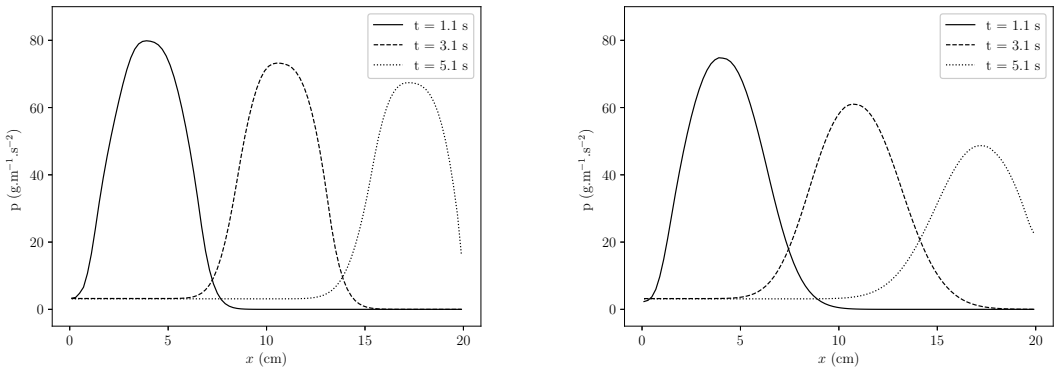

FIGURE 2.8 – Difference between the (a) elastic and (b) viscoelastic effects using the 1D model. (——) is at time $t = 1.1$ s, (- - -) at time $t = 3.1$ s, and (·····) at time $t = 5.1$ s

2.3.5 One-dimensional wave equation

In this section, we demonstrate a very important characteristic of the 1D equations, which is that the system accounts for the propagation of the pulse waves. Indeed, with a linear approximation of the 1D system (2.51), we recover the wave equation, also called the ∂'Alembert equation. If we discard the friction term assuming $C_f \ll 1$ and linearize the system assuming $Q \ll 1$ to remove the non-linear term Q^2/A, the Equations (2.51) become

$$\begin{cases} \dfrac{\partial A}{\partial t} + \dfrac{\partial Q}{\partial x} = 0, & \text{(2.57a)} \\ \dfrac{\partial Q}{\partial t} + \dfrac{A}{\rho}\dfrac{\partial p}{\partial x} = 0. & \text{(2.57b)} \end{cases}$$

We write $\dfrac{\partial p}{\partial x}$ as $\dfrac{\mathrm{d}p}{\mathrm{d}A}\dfrac{\partial A}{\partial x}$ which gives

$$\begin{cases} \dfrac{\partial A}{\partial t} + \dfrac{\partial Q}{\partial x} = 0, & \text{(2.58a)} \\ \dfrac{\partial Q}{\partial t} + c^2\dfrac{\partial A}{\partial x} = 0, & \text{(2.58b)} \end{cases}$$

in which we define the wave velocity c as

$$c = \sqrt{\frac{A}{\rho}\frac{\mathrm{d}p}{\mathrm{d}A}}, \tag{2.59}$$

called the Moens-Korteweg wave velocity [92,93]. We then differentiate Equation (2.58a) with respect to t, Equation (2.58b) with respect to x, combine them and we finally obtain the 1D wave equation

$$\frac{\partial^2 A}{\partial t^2} = c^2\frac{\partial^2 A}{\partial x^2}. \tag{2.60}$$

In the case of the elastic pressure law (2.14), the Moens-Korteweg wave velocity takes the

following form

$$c = \sqrt{\frac{K}{2\rho}\sqrt{A}}. \tag{2.61}$$

2.3.6 Zero-dimensional model

To obtain the 0D equations, we linearize the Equations (2.51) with the elastic pressure law (2.14) around the reference cross-section A_0, similarly to the simplifications of the previous section but keeping the friction term. It gives

$$\begin{cases} \dfrac{\partial A}{\partial p}\dfrac{\partial p}{\partial t} + \dfrac{\partial Q}{\partial x} = 0, & \text{(2.62a)} \\ \dfrac{\rho}{A_0}\dfrac{\partial Q}{\partial t} + \dfrac{\partial p}{\partial x} = -\rho C_f Q. & \text{(2.62b)} \end{cases}$$

We integrate the Equations (2.62) over the length of the artery, *i.e.* between $x = 0$ and $x = L$ which leads to

$$\begin{cases} \dfrac{2\sqrt{A_0}}{K}\dfrac{\mathrm{d}\hat{p}}{\mathrm{d}t} + \dfrac{Q(x=L) - Q(x=0)}{L} = 0, & \text{(2.63a)} \\ \dfrac{\rho}{A_0}\dfrac{\mathrm{d}\hat{Q}}{\mathrm{d}t} + \dfrac{p(x=L) - p(x=0)}{L} = -\rho C_f \hat{Q}, & \text{(2.63b)} \end{cases}$$

where

$$\begin{cases} \hat{p} = \dfrac{1}{L}\displaystyle\int_0^L p\mathrm{d}x, & \text{(2.64a)} \\ \hat{Q} = \dfrac{1}{L}\displaystyle\int_0^L Q\mathrm{d}x, & \text{(2.64b)} \end{cases}$$

following [63], we finally assume that

$$\begin{cases} \hat{p} = p(x=0), & \text{(2.65a)} \\ \hat{Q} = Q(x=L). & \text{(2.65b)} \end{cases}$$

Combining Equations (2.63a) and (2.63b) with the previous assumptions, we obtain the following 0D model

$$\left(1 + R_f C\frac{\mathrm{d}\cdot}{\mathrm{d}t} + CI\frac{\mathrm{d}^2\cdot}{\mathrm{d}t^2}\right) p(x=0) - p(x=L) = \left(R_f + I\frac{\mathrm{d}\cdot}{\mathrm{d}t}\right) Q(x=0), \tag{2.66}$$

with

$$\begin{cases} R_f = \dfrac{\rho L C_f}{A_0^2}, & \text{(2.67a)} \\ C = \dfrac{2L\sqrt{A_0}}{K}, & \text{(2.67b)} \\ I = \dfrac{\rho L}{A_0}, & \text{(2.67c)} \end{cases}$$

where R_f is the viscous resistance, C the vessel compliance, and I the flow inertia. The typical orders of magnitude of these parameters are reported in Table 2.4.

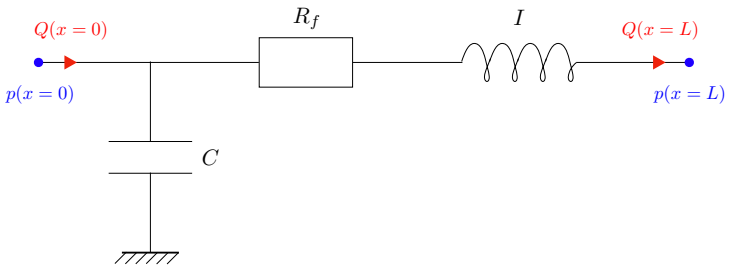

FIGURE 2.9 – Electrical representation of the 0D blood flow model of Equation (2.66). R_f is the viscous resistance (Equation (2.67a)), C the vessel compliance (Equation (2.67b)), I the flow inertia (Equation (2.67c)), p the pressure, and Q the flow rate.

This model can be seen as an electrical analogy and can also be called lumped parameter models. It is the simplest approach to describe blood flow. In this representation, the arterial network can then be interpreted as an electrical circuit constituted of resistors, capacitors, and inductors, as represented in Figure 2.9, where voltage is assimilated to pressure and current to flow rate. Resistors represent frictional forces due to viscosity, capacitors model the compliant effects of arteries, and inductors account for the inertial phenomena.

The 0D models have not only been used for blood flow in the large arteries as in [77] but also to model the blood flow in the heart [14,59,65,82] and other organs [12], to create models of the cerebral arterial network [69], of the entire arterial network [74,79] and to characterize the microcirculation at the outlet of 3D Fluid-Structure Interaction (FSI) models [29,83] and 1D network models [22,55,58,72]. Indeed, the 0D models are unable to account for the wave propagation because of the averaging process and the nonlinear flow effects because of the linearization. They are mostly used as boundary conditions for 3D or 1D models to represent the response of the distal vascular bed. The general form of Equation (2.66) can be simplified into a resistance outflow model by removing all the unsteady terms

$$p(x=0) - p(x=L) = R_f Q(x=0), \tag{2.68}$$

as represented in Figure 2.10 with R_f defined in Equation (2.67a) called the Poiseuille or hydraulic resistance that is often found as

$$R_f = \frac{8\mu L}{\pi R_0^4}. \tag{2.69}$$

This boundary condition model considers the vascular bed as purely resistive and neglects any compliant and inertial effect which is equivalent to assuming that each distal capillary is governed by a Poiseuillan flow in a rigid artery. This outflow boundary condition is equivalent to a reflection boundary condition [63],

$$R_t = \frac{R_f - Z_0}{R_f + Z_0}, \tag{2.70}$$

where R_t is the reflection coefficient comprised between 0 and 1 and Z_0 the impedance of the terminal vessel defined as

TABLE 2.4 – Orders of magnitude of the "fluid" variables defined Section 2.3. ρ: fluid density in g/cm^3, μ: fluid dynamic viscosity in g·cm^{-1}·s^{-1}, R_0: artery radius in cm, L: artery length in cm, λ: wavelength in cm, T_c: heart period in s, c: wave velocity in cm/s, Sh: Shapiro number, α: Womersley number, C_f: friction coefficient in cm^2/s, C_ν: viscoelastic coefficient in cm^2/s, R_f: resistance in g·cm^{-4}·s^{-1}, C: compliance in g^{-1}·cm^4·s^2, I: inertance in g·cm^{-4}.

ρ	μ	R_0	L	λ	T_c	c	Sh	α	C_f	C_ν	R_f	C	I
1	$4{\cdot}10^2$	0.5	10	10^2	1	10^2	0-1	0-25	2	10^4	10^2-10^3	10^{-4}-10^{-3}	10

$$Z_0 = \frac{\rho c}{A_0}. \tag{2.71}$$

with c the Moens-Korteweg wave velocity [92, 93] defined in Equation (2.59).

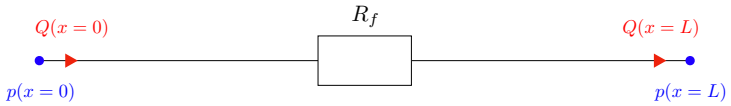

FIGURE 2.10 – Electrical representation of the 0D blood flow model of Equation (2.68). R_f is the viscous resistance (Equation (2.67a) and (2.69)), p the pressure, and Q the flow rate.

This model mainly accounts for the reflection of the incoming pulse waves, one of the most important phenomena when studying hemodynamics [9] and is, therefore, frequently used as an outflow boundary condition of a 1D model [66, 67]. Extensions from this model such as the Windkessel model, described in detail in Section 8.4.1, have been developed and also used as boundary conditions.

2.4 Conclusion

In this chapter, we presented all of the necessary hypotheses to derive two state laws to characterize arterial wall mechanics. We first derived the purely elastic arterial wall law (Equation (2.16)) and then added the viscoelastic component to obtain the second arterial wall law (Equation (2.18)) using the linear approximation. In Chapter 3, we will introduce the non-linear terms rigorously.

In Section 2.3, we developed the main hypotheses in the case of blood flows in the large arteries. From these hypotheses, we derived a hierarchy of models starting from the 3D Navier-Stokes equations. We simplified them into the 2D RNSP Equations (2.29). By averaging these equations on concentric rings and coupling them with the arterial wall law, we obtained the Multi-Ring model. Further simplifications led to the main model of this manuscript which is the 1D model and finally, we presented two examples of 0D models, obtained by averaging the 1D equations over the length of the artery.

The models presented in this chapter are the base of all of the following work, the objective being to use them in different medical scenarios.

3 Hyperelastic arterial wall

The current models of the arterial wall used in the study of blood flow with reduced-order models, described in the previous chapter, only account for the linear elasticity of the wall. However, all investigators of the mechanical behavior of the arterial tissue agree that it does not obey the general linear elasticity theory. Therefore, this chapter focuses on deriving constitutive equations of hyperelastic models from the literature to account for the non-linearity of the wall. We couple these models to the 1D blood flow model derived in Chapter 2 and compare them with the elastic approach.

KEYWORDS: hyperelastic model, arterial wall, one-dimensional model, wave propagation, large deformation.

Contents

3.1 Introduction

The understanding of arterial wall mechanics is a crucial element in the study of hemodynamic models. In particular, in reduced-order models, the interaction between the fluid and the arterial structure is only accounted through a pressure law that characterizes the mechanics of the arterial wall. The choice of this law influences the propagation and reflection of the wave in the arterial network which is one of the most important phenomena in hemodynamics. It is also important to capture the accurate mechanical behavior of the arterial wall as changes in the mechanical properties of the blood vessels are involved in the development and rupture of aneurysms, among other pathologies.

Like most soft tissues, arterial wall mechanics does not follow the linear Hooke's law [102] which means that in most cases the stress-strain relation is non-linear. Unlike the typical elastic models presented in Chapter 2, hyperelastic models account for the large strains. The first hyperelastic models introduced in the literature were the Mooney-Rivlin [103–106] and the Neo-Hookean [107, 108], that are polynomial models. Others have been developed after such as exponential and logarithmic models, in particular the Fung model [26, 102]. Micromechanical-based models are also common to account for different behavior such as the non-linearity due to the microstructure of tissues [109].

As mentioned previously, in the study of reduced-order models, a constitutive pressure law for the wall mechanics is necessary to close and solve the system. In Chapter 2, we introduced two state laws, an elastic and viscoelastic model. We are interested in the constitutive equations used to model the hyperelastic behavior of the arterial wall. In Section 3.2, we summarize the ideas to obtain the hyperelastic constitutive models. In Section 3.3, we derive three of the classical polynomial hyperelastic models, the Neo-Hookean, the Mooney-Rivlin, and the Varga model, assuming a few hypotheses on the symmetries and geometry of the arterial wall, similarly to Section 2.2. Finally, in Section 3.4, we use these hyperelastic arterial wall models in combination with the one-dimensional (1D) blood flow model introduced in Section 2.3.4 and present a comparison with the elastic approach.

3.2 Constitutive modeling

3.2.1 Notations

We summarize the principles of continuum mechanics and point out the notations. When a body deforms from an initial configuration Ω_0 into a deformed configuration Ω_t, a position vector $\mathbf{X}$ in Ω_0 maps into a position vector $\mathbf{x}$ in the deformed configuration Ω_t. The position $\mathbf{X}$ is a Lagrangian, or material, description of the body whereas $\mathbf{x}$ is the Eulerian, or spatial, representation and we can write $\mathbf{x} = \mathbf{x}(\mathbf{X}, t)$. In the Lagrangian description, we denote the displacement field $\mathbf{u}$ as

$$\mathbf{u}(\boldsymbol{X}, t) = \boldsymbol{x}(\boldsymbol{X}, t) - \boldsymbol{X}. \tag{3.1}$$

When moved from Ω_0 to Ω_t, the body is deformed according to the following quantity

$$\mathbf{F}(\boldsymbol{X}, t) = \text{Grad } \boldsymbol{x}(\boldsymbol{X}, t), \tag{3.2}$$

called the deformation gradient. The determinant of the deformation gradient $\mathbf{F}$, called the

Jacobian, is $J(\mathbf{X}, t) = \det \mathbf{F}(\mathbf{X}, t)$, which represents the volume ratio of the change in volume between the reference configuration Ω_0 and the current configuration Ω_t.

We define the right Cauchy-Green tensor $\mathbf{C}$ as

$$\mathbf{C} = \mathbf{F}^T\mathbf{F}, \tag{3.3}$$

and the Cauchy stress tensor $\boldsymbol{\sigma}$ that can be expressed in many forms and in particular

$$\boldsymbol{\sigma} = J^{-1}\mathbf{P}\mathbf{F}^T, \tag{3.4}$$

where $\mathbf{P}$ is the Piola Kirchhoff stress tensor.

3.2.2 General hyperelastic laws

A hyperelastic material postulates the existence of a Helmholtz free-energy function Ψ (also noted W in the literature). If Ψ only depends on the deformation gradient $\mathbf{F}$ then Ψ is called a strain density function. The Piola Kirchhoff stress tensor can thus be written as

$$\mathbf{P} = \frac{\partial \Psi}{\partial \mathbf{F}}. \tag{3.5}$$

Injecting (3.5) in Equation (3.4) leads to the relation between the stress tensor $\boldsymbol{\sigma}$ and the deformation gradient $\mathbf{F}$

$$\boldsymbol{\sigma} = J^{-1}\frac{\partial \Psi}{\partial \mathbf{F}}\mathbf{F}^T, \tag{3.6}$$

called the constitutive equation.

We consider the material as incompressible since biological soft tissues, such as arteries, contain mostly water. The incompressibility constraint is $J = 1$ which leads to the following form of the strain density function

$$\Psi = \Psi(\mathbf{F}) - p(J - 1), \tag{3.7}$$

where the hydro-static pressure p is a Lagrangian multiplier to force the incompressibility. By differentiating Equation (3.7) with respect to the deformation gradient $\mathbf{F}$ and using the fact that $\dfrac{\partial J}{\partial \mathbf{F}} = J\mathbf{F}^{-T}$, we obtain the constitutive relation for the Piola-Kirchhoff stress tensor

$$\mathbf{P} = -p\mathbf{F}^{-T} + \frac{\partial \Psi(\mathbf{F})}{\partial \mathbf{F}}. \tag{3.8}$$

By substituting $\mathbf{P}$ of Equation (3.8) in the Equation (3.4) we obtain the expression of the constitutive equation

$$\boldsymbol{\sigma} = -p\mathbb{I} + \frac{\partial \Psi(\mathbf{F})}{\partial \mathbf{F}}\mathbf{F}^T. \tag{3.9}$$

The strain energy function has to satisfy several constraints detailed in [26, 110] that lead to the equivalent form $\Psi(\mathbf{F}) = \Psi(\mathbf{C})$, with $\mathbf{C}$ the Cauchy-Green tensor. By considering that the material is isotropic, *i.e.* the material property is the same in all directions, the strain energy function can be expressed in terms of the principal isotropic invariants

$$\Psi(\mathbf{C}) = \Psi(I_1, I_2, I_3), \tag{3.10}$$

in which the invariants of $\mathbf{C}$ are

$$\begin{cases} I_1 = tr(\mathbf{C}) = \lambda_1^2 + \lambda_2^2 + \lambda_3^2, & \text{(3.11a)} \\ I_2 = \frac{1}{2}\left((tr\mathbf{C})^2 - tr(\mathbf{C}^2)\right) = \lambda_1^2\lambda_2^2 + \lambda_1^2\lambda_3^2 + \lambda_2^2\lambda_3^2, & \text{(3.11b)} \\ I_3 = \det \mathbf{C} = \lambda_1^2\lambda_2^2\lambda_3^2, & \text{(3.11c)} \end{cases}$$

expressed in terms of the principal stretches λ_1, λ_2 and λ_3 where subscript 1 corresponds to the θ-direction, 2 to the x-direction and 3 to the r-direction. Note that $J = \lambda_1\lambda_2\lambda_3$ the volume ratio is equal to 1 when the material is incompressible. Assuming incompressibility, we can now write $\Psi = \Psi(\lambda_1, \lambda_2, \lambda_3)$, and the Cauchy stress tensor

$$\sigma_i = -p + \lambda_i \frac{\partial \Psi}{\partial \lambda_i}, \tag{3.12}$$

with $i = 1, 2, 3$.

As an example of Ψ, Ogden [111, 112] formulated the strain density function in terms of the principal stretches λ_i, with $i = 1, 2, 3$ as

$$\Psi = \sum_{n=1}^{N} \frac{\mu_n}{\alpha_n} \left(\lambda_1^{\alpha_n} + \lambda_2^{\alpha_n} + \lambda_3^{\alpha_n} - 3\right), \tag{3.13}$$

with the consistency condition

$$2\mu = \sum_{n=1}^{N} \mu_n \alpha_n, \tag{3.14}$$

where μ is the shear modulus from the linear theory and α_n are dimensionless constants determined experimentally. Combining the Ogden formulation of the strain density function Equation (3.13) with Equation (3.12), we can write a general expression of the Cauchy stress tensor as

$$\sigma_i = -p + \sum_{n=1}^{N} \mu_n \lambda_i^{\alpha_n}. \tag{3.15}$$

To compute the pressure, we calculate the force balance between the pressure difference $\Delta p = p - p_{ext}$ and the stress σ_1 as

$$\Delta p = 2\frac{H}{R}\sigma_1, \tag{3.16}$$

with the definitions of the principal stretches

$$\begin{cases} H = \lambda_3 h, & \text{(3.17a)} \\ R = \lambda_1 R_0. & \text{(3.17b)} \end{cases}$$

In the following, we introduce the main assumptions on the symmetries and geometry in the case of arteries. It allows deriving the strain density functions of the Neo-Hookean, Mooney-Rivlin, and Varga models in order to couple it with the 1D model.

3.3 Hyperelastic models in the case of arteries

In the case of the large arteries, we can introduce two additional hypotheses similarly to Section 2.2:

- the radial stress is negligible as the thickness of the arterial wall is small compared to the other directions, *i.e.* $h \ll R_0$ and we have $\sigma_3 = 0$ (denotes $\sigma_{rr} = 0$ in Section 2.2). Introducing this assumption in Equation (3.15), we obtain an expression for the Lagrange multiplier p.

- the axial displacement is small so that we consider that the stretch in the x-direction λ_2 is 1 (*i.e.* $\epsilon_{xx} = 0$ in Section 2.2).

We now apply these assumptions to compute the stress, pressure and wave velocity in the case of the Neo-Hookean, the Mooney-Rivlin and the Varga models.

The previous assumptions allow simplifying Equation (3.16) into

$$\Delta p = 2\frac{h}{R_0}\frac{\sigma_1}{\lambda_1^2}, \tag{3.18}$$

in which we usually assume $p_{ext} = 0$, as in Section 2.2.

3.3.1 Neo-Hookean model

The strain density function of the Neo-Hookean model [107, 108] is expressed in terms of the principal invariant I_1

$$\Psi = \frac{\mu_1}{2}(I_1 - 3), \tag{3.19}$$

and is a particular case of the Ogden model (3.13) with $N = 1$ and $\alpha_1 = 2$

$$\Psi = \frac{\mu_1}{2}(\lambda_1^2 + \lambda_2^2 + \lambda_3^2 - 3). \tag{3.20}$$

where $\mu_1 = \mu$ from the consistency condition of Equation (3.14).

From the assumption $\sigma_3 = 0$, we calculate the Lagrangian multiplier p using Equation (3.12) and the expression of the strain density function for the Neo-Hookean model (3.20) which gives

$$p = \mu_1 \lambda_3^2. \tag{3.21}$$

It allows calculating σ_1

$$\sigma_1 = \mu_1(\lambda_1^2 - (\lambda_1\lambda_2)^{-2}), \tag{3.22}$$

using $\lambda_1\lambda_2\lambda_3 = 1$ to drop off λ_3. Finally, we impose $\lambda_2 = 1$ leading to

$$\sigma_1 = \mu_1(\lambda_1^2 - \lambda_1^{-2}), \tag{3.23}$$

represented in Figure 3.1.

By injecting the expression of σ_1 in Equation (3.18), we obtain the pressure

$$p = 2\frac{h}{R_0}\mu_1(1-\lambda_1^{-4}) \tag{3.24}$$

which can also express as a function of the cross-section $A = \pi R^2$ and $A_0 = \pi R_0^2$

$$p = 2\frac{h}{R_0}\mu_1\left(1-\frac{A_0^2}{A^2}\right), \tag{3.25}$$

represented in Figure 3.2.

We now calculate the Moens-Korteweg wave celerity [92,93] using Equation (2.59) for the Neo-Hookean model

$$c = \sqrt{\frac{2h}{\rho R_0}\mu_1\frac{2A_0^2}{A^2}}, \tag{3.26}$$

that we plot in Figure 3.3.

3.3.2 Mooney-Rivlin model

The strain density function of the Mooney-Rivlin model [103–106] has the following form

$$\Psi = \frac{\mu_1}{2}(I_1-3) + \frac{\mu_2}{2}(I_2-3), \tag{3.27}$$

and can be seen as a special case of Ogden model (3.13) with $N = 2$, $\alpha_1 = 2$, $\alpha_2 = -2$

$$\Psi = \frac{\mu_1}{2}(\lambda_1^2+\lambda_2^2+\lambda_3^2-3) + \frac{\mu_2}{2}(\lambda_1^2+\lambda_2^2+\lambda_3^2-3). \tag{3.28}$$

with $\mu_1 - \mu_2 = \mu$ from the consistency condition of Equation (3.14).

From the assumption $\sigma_3 = 0$, we calculate the Lagrangian multiplier p using Equation (3.12) and the expression of the strain density function for the Mooney-Rivlin model (3.28) which gives

$$p = \mu_1\lambda_3^2 + \mu_2\lambda_3^{-2}. \tag{3.29}$$

It allows calculating σ_1

$$\sigma_1 = -\mu_1(\lambda_1\lambda_2)^{-2} - \mu_2(\lambda_1\lambda_2)^2 + \mu_1\lambda_1^2 + \mu_2\lambda_1^{-2} \tag{3.30}$$

using $\lambda_1\lambda_2\lambda_3 = 1$ to drop off λ_3. Finally, we impose $\lambda_2 = 1$ leading to

$$\sigma_1 = (\mu_1-\mu_2)(\lambda_1^2-\lambda_1^{-2}), \tag{3.31}$$

represented in Figure 3.1.

By injecting the expression of σ_1 in Equation (3.18), we obtain the pressure

$$p = 2\frac{h}{R_0}(\mu_1-\mu_2)(1-\lambda_1^{-4}), \tag{3.32}$$

which can also express as a function of the cross-section $A = \pi R^2$ and $A_0 = \pi R_0^2$

$$p = 2\frac{h}{R_0}(\mu_1 - \mu_2)\left(1 - \frac{A_0^2}{A^2}\right), \tag{3.33}$$

represented in Figure 3.2.

We notice from Equations (3.31) and (3.33) that the Mooney-Rivlin model is the same as the Neo-Hookean model with a different shear modulus, thus the Moens-Korteweg wave celerity of the Mooney-Rivlin model is Equation (3.26) replacing μ_1 by $\mu_1 - \mu_2$.

3.3.3 Varga model

Finally, in the Varga model [113], we set $N = 1$ and $\alpha_1 = 1$ in Equation (3.13) which gives

$$\Psi = \mu_1(\lambda_1 + \lambda_2 + \lambda_3 - 3) \tag{3.34}$$

with $\mu_1 = 2\mu$ from the consistency condition of Equation (3.14).

From the assumption $\sigma_3 = 0$, we calculate the Lagrangian multiplier p using Equation (3.12) and the expression of the strain density function for the Varga model (3.34) which gives

$$p = \mu_1\lambda_3. \tag{3.35}$$

It allows calculating σ_1

$$\sigma_1 = -\mu_1(\lambda_1\lambda_2)^{-1} + \mu_1\lambda_1 \tag{3.36}$$

in which we use $\lambda_1\lambda_2\lambda_3 = 1$ to drop off λ_3. Finally, we impose $\lambda_2 = 1$ leading to

$$\sigma_1 = \mu_1(\lambda_1 - \lambda_1^{-1}), \tag{3.37}$$

represented in Figure 3.1.

By injecting the expression of σ_1 in Equation (3.18), we obtain the pressure

$$p = 2\frac{h}{R_0}\mu_1(\lambda_1^{-1} - \lambda_1^{-3}), \tag{3.38}$$

which can also express as a function of the cross-section $A = \pi R^2$ and $A_0 = \pi R_0^2$

$$p = 2\frac{h}{R_0}\mu_1\left(\frac{\sqrt{A_0}}{\sqrt{A}} - \frac{A_0\sqrt{A_0}}{A\sqrt{A}}\right), \tag{3.39}$$

represented in Figure 3.2.

We now calculate the Moens-Korteweg wave celerity [92,93] using Equation (2.59) for the Varga model

$$c = \sqrt{\frac{2h}{\rho R_0}\mu_1\frac{\sqrt{A_0}}{\sqrt{A}}\left(\frac{3A_0}{A} - \frac{1}{2}\right)}, \tag{3.40}$$

that we plot in Figure 3.3.

Figure 3.1 show the Cauchy stress tensor σ_1 as a function of the principal stretch λ_1. We observe that for all models, the stress increases with the stretch, which is not common for the hyperelastic models, in particular the Neo-Hookean. However, considering the symmetries of the problem (*i.e.* more precisely it is 1D) the hyperelastic relations between stress and stretch are not softening (see Figure 6.3 in [26]).

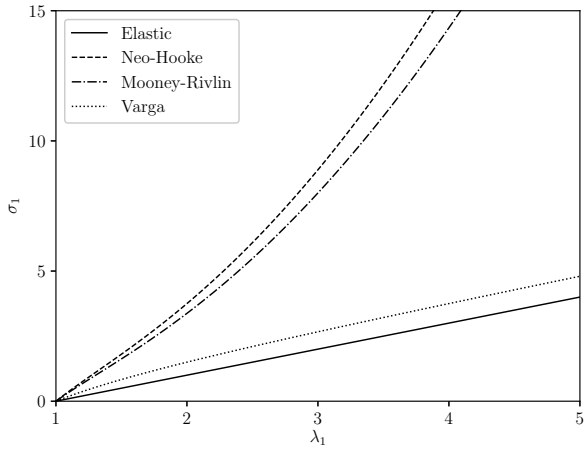

FIGURE 3.1 – Cauchy stress σ_1 as a function of the principal stretch λ_1 for the elastic model (——) of Section 2.2, the Neo-Hookean model (- - -) of Equation (3.23), the Mooney-Rivlin model (-·-·) of Equation (3.31) and the Varga model (·····) of Equation (3.37).

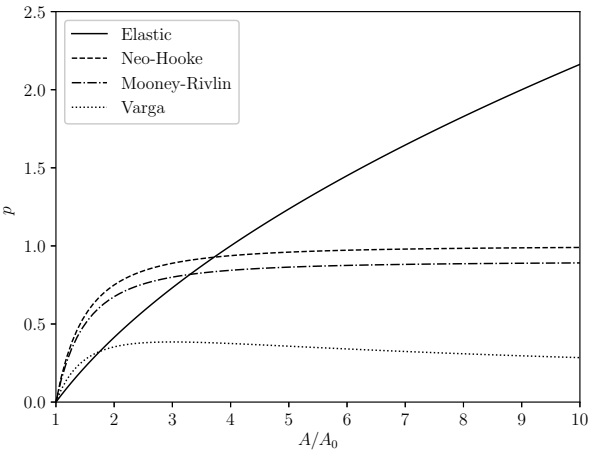

FIGURE 3.2 – Pressure p as a function of the dimensionless cross-section A/A_0 for the elastic model (——) of Section 2.2, the Neo-Hookean model (- - -) of Equation (3.25), the Mooney-Rivlin model (-·-·) of Equation (3.33) and the Varga model (·····) of Equation (3.39).

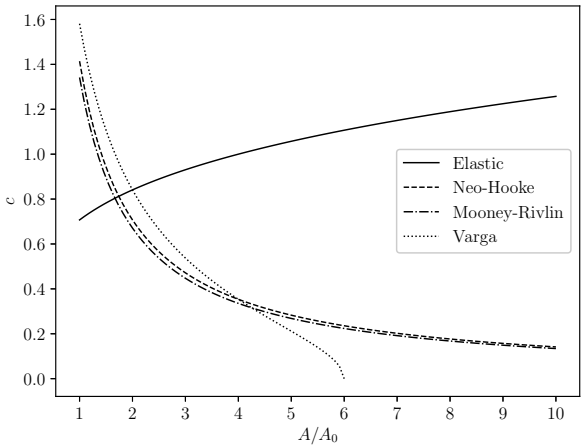

FIGURE 3.3 – Moens Korteweg wave velocity c from Equation (2.59) as a function of the dimensionless cross-section A/A_0 for the elastic model (——) of Section 2.2, the Neo-Hookean model (- - -) of Equation (3.26), the Mooney-Rivlin model (-·-·) and the Varga model (·····) of Equation (3.40).

Figures 3.2 shows the pressure p as a function of the cross-section ratio A/A_0 for the four state laws. We observe that, under large deformation, the pressure inside the artery reaches a plateau and thus does not increase drastically, unlike the elastic model. This means that the hyperelastic models have a "damping" behavior and can prevent shocks.

In Figure 3.3, we note that the dependence of the wave velocity on the cross-section ratio A/A_0 is very different for the elastic and hyperelastic models. Indeed, we observe that for the elastic model, the wave velocity increases with the cross-section whereas, in all three hyperelastic models, the opposite occurs, *i.e.* the wave velocity decreases with the cross-section. We recover in this figure the shock damping phenomenon of the hyperelastic models.

We derived the hyperelastic models with specific assumptions for the arterial wall, now we combine these models to the 1D equations (2.51). We compare them with the elastic approach described in Section 2.2. As the only difference between the Neo-Hookean and Mooney-Rivlin models is the shear modulus, we only study the first one in the following.

3.4 Comparison between the elastic and hyperelastic models

Anticipating Chapter 4 on the resolution methods of the 1D equations, we compute the system (2.51) in combination with the Neo-Hookean and Varga hyperelastic wall models presented in Section 3.3. We solve the model in an artery of length $L = 10$ cm divided into $N_x = 1000$ cells with a time-step $\Delta t = 10^{-5}$ s. We impose the following inlet boundary condition

$$A(x, t = 0) = 1 + A_0 \exp(-8(x - 5)^2)) \tag{3.41}$$

with A_0 the amplitude of the initial condition.

We solve the 1D Equation (2.51) coupled to the pressure laws (2.14), (3.25), and (3.39) for the elastic, Neo-Hookean, and Varga models respectively. We put the system (2.51) + pressure law in the conservative form and compare the influence of the pressure law on the propagation of a pulse in an artery.

The main difference between the elastic and hyperelastic models resides in the large deformations. Under this condition, *i.e.* when the amplitude A_0 of the initial condition is large, a discontinuity or shock appears when computing the elastic model. In Figures 3.4, we show the cross-section A (Figures 3.4a and 3.4b) and the flow rate Q (Figures 3.4c and 3.4d) depending on the value of A_0. We observe that the shock appears when A_0 is large and that both the Neo-Hookean and the Varga model smooth the shock, as expected by hyperelastic models.

(a) $A_0 = 10^{-3}$ (b) $A_0 = 1$

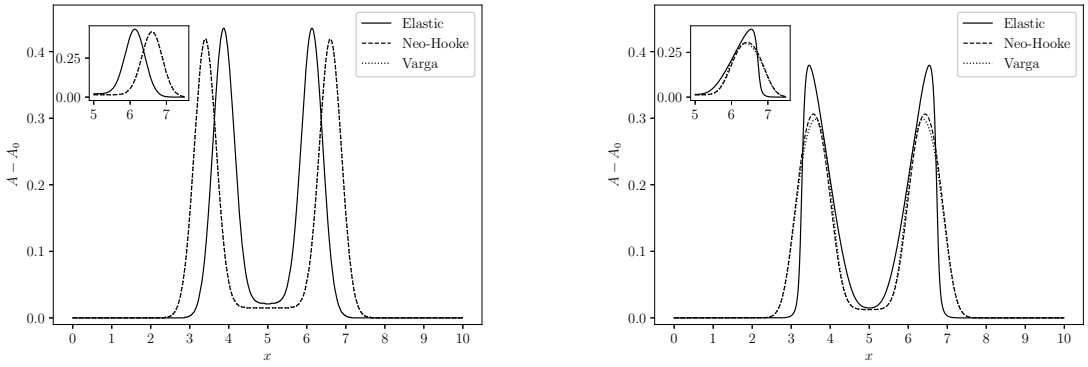

(c) $A_0 = 10^{-3}$ (d) $A_0 = 1$

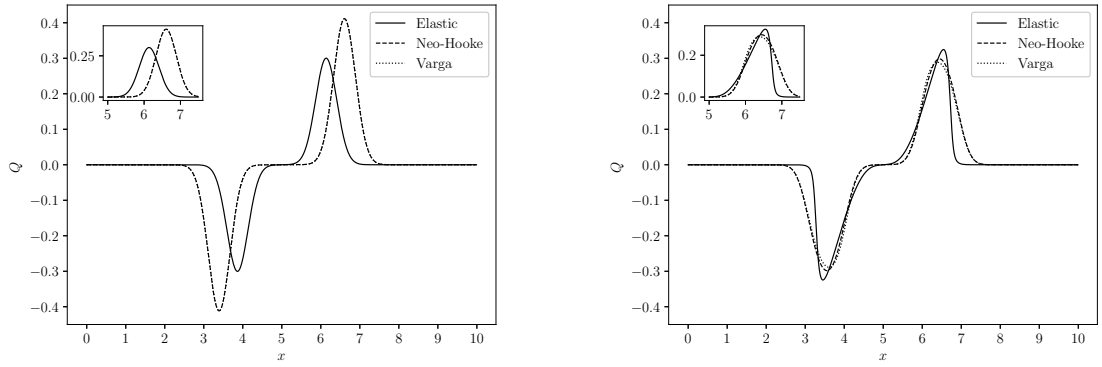

FIGURE 3.4 – Cross-section A and flow rate Q as a function of the x-position with different values of the amplitude A_0 of the initial condition at $t = 1.6$ s. We represent (a) the cross-section A and (b) the flow rate Q with an amplitude of the initial condition $A_0 = 10^{-3}$, (c) the cross-section A and (c) the flow rate Q with an amplitude of the initial condition $A_0 = 1$. (——) corresponds to the elastic model, (- - -) corresponds to the Neo-Hookean model, and (·····) corresponds to the Varga model. N.B: in (a) and (c) the two hyperelastic models are superimposed.

On one hand, we notice that the velocity of the pulse is different between the models with a small amplitude A_0. Indeed, the Moens-Korteweg wave velocity [92,93], defined in Equation

(2.59), is larger for the hyperlastic models than the elastic one as predicted by Figure 3.3. Note that the Neo-Hooke and Varga waves are superimposed in Figures 3.4a and 3.4c, as the wave velocity of both models is of similar magnitude for small deformations (Figure 3.3).

On the other hand, we observe in Figures 3.4b and 3.4d that the pulses of the hyperelastic and elastic models travel at the same velocity with a large amplitude A_0. In Figure 3.3, we observe that when the deformation becomes large ($A/A_0 = 2$), the velocity of the hyperelastic and elastic models is the same, which is why when $A_0 = 1$, we obtain the same velocity for all models. If we further increase A_0, the wave travels faster with the elastic than the hyperelastic models.

We also observe in Figure 3.4 that in all models the attenuation of the pulses is larger when A_0 is large, but we impose the same friction coefficient C_f, and plot the data at the same time step. We note that the amplitude of the pulse is almost the same in the elastic and hyperelastic models for a small amplitude A_0 (Figure 3.4a) which is not the case for a large amplitude (Figure 3.4b). In Figure 3.5, we compare the pulses of the Neo-Hookean and elastic models with friction, *i.e.* $C_f = 0$ in Equation (2.51), and without friction, $C_f \neq 0$ in Equation (2.51). From these figures we deduce that the friction does not differ with a large A_0, it is the non-linearity of the model that attenuates the pulse. Moreover, the hyperelastic models dissipate the pulse faster than the elastic one, which is actually satisfying since the hyperelastic models are expected to smooth the elastic behaviors in large deformations.

(a) $A_0 = 10^{-3}$ (b) $A_0 = 1$

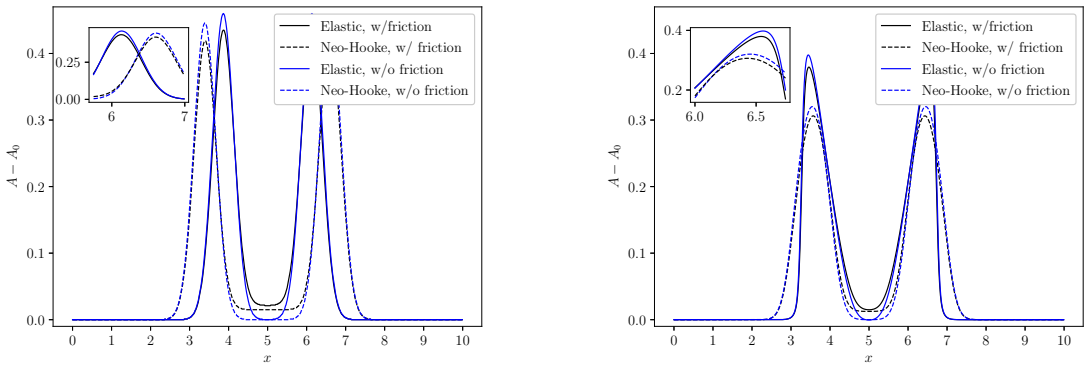

FIGURE 3.5 – Cross-section A as a function of the x-position at $t = 1.6$ s with (a) $A_0 = 10^{-3}$ and (b) $A_0 = 1$ computed with the elastic model (——) and the Neo-Hookean model (- - -) with friction (in black) and without friction (in blue).

To summarize, the amplitude of the initial condition is the only parameter that creates a shock in the elastic models, shock that is smoothed by both the Neo-Hookean and Varga models.

3.5 Conclusion

In this chapter, we derived rigorously three hyperelastic models from the literature (the Neo-Hookean, the Mooney-Rivlin, and the Varga models) to couple to the 1D equations (2.51)

described in Section 2.3.4. We studied the propagation of the wave in an artery with these different models by comparing the elastic approach introduced in Section 2.2 to the hyperelastic models. By varying the parameters of the models, we observed that the amplitude of the inlet boundary condition was the only parameter creating such shock. We also noted that under large deformations, the hyperelastic models, in particular the Neo-Hookean model, smoothed the shocks.

The hyperelastic models provide a more accurate description of the arterial wall. This approach allows considering large deformations of the arterial tissue, that cannot be correctly captured by a linear model. The problem is that we do not have experimental data to validate the hyperelastic approach in conditions where the non-linear elasticity of the arterial wall plays a major role. Indeed, no shocks are usually observed in arteries in normal physiological conditions but shock-like phenomena may arise in veins during walking and running for instance [51]. However, in other biological tissues such as the breast, brain, liver, or kidneys, the hyperelastic models are relevant [109].

For these reasons, we choose to only restrict our study to linear elasticity of the arterial wall, as described in Chapter 2. The validation of these models in a relevant medical scenario however remains a perspective of the present work.

4 Numerical methods

This chapter focuses on the numerical methodologies associated with the reduced-order models presented in Chapter 2. All these models are non-linear and do not have analytic solutions thus the equations have to be solved numerically with appropriate resolution schemes that we briefly introduce here. Despite accurate resolution schemes, predicting patient-specific hemodynamics can only be relevant if the geometric, mechanical, and model properties correspond to the reality. Optimization methods are the solution to estimate patient-specific parameters, thus we review a few of these methods from the literature and introduce the ones we use in Part II.

KEYWORDS: finite volume, finite difference, parameter estimation, gradient-based method.

Contents

4.1 Introduction

In Chapter 2 we presented the four different models that we use in the medical applications of Part II: the two variations of the Reduced Navier-Stokes Prandtl (RNSP) (the steady RNSP and the Multi-Ring), the one-dimensional (1D), and zero-dimensional (0D) models. All these models are non-linear and cannot be solved analytically. We therefore propose appropriate methods to obtain a numerical approximation of the solution of the equations presented in Chapter 2.

Several resolution schemes can be considered for solving flow models. For the full three-dimensional (3D) or the two-dimensional (2D) axisymmetric Navier-Stokes equations, softwares are available for instance FreeFem++ or Sim Vascular that uses finite elements, Basilisk or Ansys Fluent that use finite volumes. We find two types of methods in the literature for the steady RNSP: finite elements [114] or finite differences [41]. As it was inspired by the multilayer model for shallow water equations [45] solved with a finite volume approach in the original article, the Multi-Ring model is usually solved with this same approach [46, 47]. For the 1D model, there is an extensive literature on the numerical schemes, for instance, finite differences [20, 55], finite elements [37, 115, 116], discontinuous Galerkin [54, 117], and finite volume methods [50, 53]. The 0D models, as they only depend on time, are usually solved with finite differences [67, 77].

To summarize, all models can generally be solved with either finite element, finite volume, or finite difference methods. In Section 4.2, we briefly derive the numerical resolution algorithms of the four models that we choose, which are mostly finite difference and volume approaches.

The models of Chapter 2 also depend on parameters varying in a large range of values. They have been estimated in the literature in particular scenarios but do not have a generic value for healthy and pathological conditions. Some parameters can be observed or measured. For instance, the blood flow rate in a compliant artery can be obtained with imaging techniques such as Magnetic Resonance Imaging (MRI), the topology and geometric properties of the arteries can be assessed via Doppler measurements or Magnetic Resonance Angiography (MRA). However, while these measurements are usually limited to a few locations in space, mechanical properties of arteries, such as Young's modulus and wall thickness, are often unknown or were only measured *ex vivo*. In practice, available clinical data are often indirect observations of the hemodynamic measurements of interest. We can also add to the unknowns the model parameters that do not necessarily have a physical meaning but are mandatory for numerical computations such as the boundary conditions, resistance or reflection coefficient for instance. This is where strategies of parameter estimation become necessary: these methods allow assessing relevant model parameters based on measured data to make patient-specific computations. Parameter estimation can also be considered as a diagnostic tool to follow the evolution of a disease in a minimally invasive way [77]. In Section 4.3, we briefly review the literature of optimization techniques and present a few in more detail that will be useful in Part II.

4.2 Numerical methods

In the following, we present the discretization algorithms used to compute first the 2D axisymmetric Navier-Stokes equations used as a target solution in Chapter 5, the steady RNSP

model, the Multi-Ring model, the 1D model, and the 0D model presented in Chapter 2.

4.2.1 Two-dimensional Axisymmetric Navier-Stokes

We solve the 2D axisymmetric Navier-Stokes Equations (2.22) with the software Basilisk that uses a finite volume discretization with a projection method. More detail can be found here.

This model is used in Chapter 5 (Section 5.2.1).

4.2.2 Steady RNSP model

The steady RNSP equations are solved using a finite difference approach, similarly to references [41, 43]. We divide the 2D spatial domain into cells of size $\Delta r \times \Delta x$ with $(u_r, u_x)(r_i = i\Delta r, x_j = j\Delta x)$ for $i \in \{0, ...N_i\}$ and $j \in \{0, ...N_j\}$. The resolution scheme consists of the following steps:

1. we prescribe the pressure term $\left(-\frac{\partial p}{\partial x}\right)^{guess}$ in Equation (2.29c);
2. we calculate the velocity $u^*_{x_{i,j}}$ using the momentum Equation (2.29c) with an implicit discretization. We use a second-order centered finite difference scheme in the r-direction and a first-order uncentered finite difference scheme in the x-direction. We write the system as a tridiagonal system and solve it using Thomas algorithm [118];
3. we calculate the velocity $u^*_{r_{i,j}}$ using the mass conservation Equation (2.29a) with first order uncentered finite difference schemes in r- and x-directions.

The boundary condition (2.30d) is generally not satisfied with these three steps and thus we iterate on the value of the pressure gradient $\left(-\frac{\partial p}{\partial x}\right)^{guess}$ until all boundary conditions (2.30) are respected and then go to the next step $(i+1, j+1)$. To find the optimal pressure gradient, we compute Newton's algorithm 1, described in detail in Section 4.3.1.

This model is used in Chapter 5 and Chapter 6.

4.2.3 Multi-Ring model

The Multi-Ring model is solved by a finite volume approach [46, 47]. We rewrite the system of Equations (2.37) in the general vectorial form

$$\frac{\partial \boldsymbol{U}}{\partial t} + \frac{\partial \boldsymbol{F}(\boldsymbol{U})}{\partial x} = \boldsymbol{S_M}(\boldsymbol{U}) + \boldsymbol{S_f}(\boldsymbol{U}) + \boldsymbol{S_T}(\boldsymbol{U}), \tag{4.1}$$

with

$$\boldsymbol{U} = \begin{bmatrix} A \\ Q_1 \\ \vdots \\ Q_{N_r} \end{bmatrix}, \quad \boldsymbol{F} = \begin{bmatrix} F_A \\ F_{Q_1} \\ \vdots \\ F_{Q_{N_r}} \end{bmatrix}, \tag{4.2}$$

defined in Equation (2.38)[1] and the source terms defined in Section 2.3.3 .

1. the flux $\boldsymbol{F}$ should not be confused with the deformation gradient $\mathbf{F}$ defined in Chapter 3.

We divide the time domain with a constant time step Δt, and define the time $t^n = n \times \Delta t$ for $n \in \{0, ...N_T\}$. The spatial domain is discretized in N_x cells with a constant space step $\Delta x = x_{i+\frac{1}{2}} - x_{i-\frac{1}{2}}$ for $i \in \{1, ...N_x\}$, as represented in Figure 4.1. The radial direction is discretized in N_r rings.

We solve the problem by splitting the Equations (4.1) into two subproblems detailed in the following.

Convective subproblem

The convective subproblem that only accounts for the transport, the mass exchange and the mechanical, and geometrical source terms is discretized as

$$\frac{\boldsymbol{U}^* - \boldsymbol{U}^n}{\Delta t} + \frac{\partial \boldsymbol{F}(\boldsymbol{U}^n)}{\partial x} = \boldsymbol{S_M}(\boldsymbol{U}^n) + \boldsymbol{S_T}(\boldsymbol{U}^n). \tag{4.3}$$

We integrate in space and time the Equation (4.3) and obtain the following explicit finite volume scheme

$$\boldsymbol{U_i^*} = \boldsymbol{U_i^n} - \frac{\Delta t}{\Delta x}\left(\boldsymbol{F^n_{i+\frac{1}{2}}} - \boldsymbol{F^n_{i-\frac{1}{2}}}\right) + \Delta t\left(\boldsymbol{S^n_{M,i}} + \boldsymbol{S^n_{T,i}}\right), \tag{4.4}$$

with

$$\boldsymbol{U_i^n} = \frac{1}{\Delta x}\int_{C_i} \boldsymbol{U^n} \mathrm{d}x, \tag{4.5}$$

and

$$\boldsymbol{F^n_{i+\frac{1}{2}}} = \frac{1}{\Delta t}\int_{t^n}^{t^*} \boldsymbol{F_{x_{i+\frac{1}{2}}}} \mathrm{d}t. \tag{4.6}$$

We compute the flux $\boldsymbol{F}$ with a kinetic approach as in [46] and in [45] for the similar multilayer shallow-water model.

Friction subproblem

The friction subproblem deals with the viscous source term of Equation (4.1)

$$\frac{\boldsymbol{U}^{n+1} - \boldsymbol{U}^*}{\Delta t} = \boldsymbol{S_f}(\boldsymbol{U}^{n+1}). \tag{4.7}$$

We use an implicit finite difference scheme to ensure the stability of the solution. Similarly to the steady RNSP model, we rewrite the viscous subproblem as a tridiagonal system that we solve using the Thomas algorithm [118].

We combine the two subproblems to go from t^n to t^{n+1} as

$$\boldsymbol{U}^n \xrightarrow{(4.3)} \boldsymbol{U}^* \xrightarrow{(4.7)} \boldsymbol{U}^{n+1}. \tag{4.8}$$

Boundary conditions

We define inlet and outlet ghost cells C_{in} and C_{out} in which we impose the boundary conditions, as represented in Figure 4.1. Following the methodology proposed in [119] for the

similar shallow water equations and in [56] for the 1D blood flow equations, we impose only one boundary condition, A_{in}^n or Q_{in}^n in the inlet ghost cell C_{in} and one boundary condition, A_{out}^n or Q_{out}^n in the outlet ghost cell C_{out}. To determine the remaining component of $\boldsymbol{U}_{in}^n$, respectively $\boldsymbol{U}_{out}^n$, we use the incoming W_2 and outgoing W_1 Riemann invariants

$$\begin{cases} W_1 = \dfrac{Q}{A} - 4c, & \text{(4.9a)} \\ W_2 = \dfrac{Q}{A} + 4c, & \text{(4.9b)} \end{cases}$$

where c is the wave velocity defined in Equation (2.59).

The vectors $\boldsymbol{U}_{in}^n$ and $\boldsymbol{U}_{out}^n$ are solved using a Newton's algorithm 1 in a limited number of iterations ($N_{itmax} \sim 5$), described in more detail in Section 4.3.1.

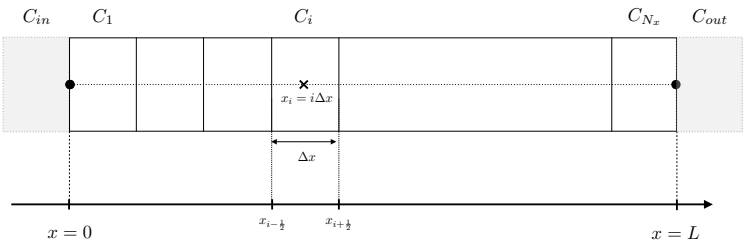

FIGURE 4.1 – Schematic representation of the longitudinal discretization with a finite volume approach for the Multi-Ring and 1D models.

Initial conditions

In most computations, we impose the following initial conditions

$$\begin{cases} Q_n(x, t = 0) = 0, & \text{for } \; n = 1, ..., N_r, \quad \text{(4.10a)} \\ A(x, t = 0) = A_0. & \text{(4.10b)} \end{cases}$$

This model is used in Chapter 5, Chapter 6, and Appendix B.

4.2.4 One-dimensional model

We also choose a finite volume approach [50] to solve the 1D model (2.54). Similarly to the Multi-Ring model, we can rewrite the system in its conservative vectorial form

$$\frac{\partial \boldsymbol{U}}{\partial t} + \frac{\partial \boldsymbol{F}(\boldsymbol{U})}{\partial x} = \boldsymbol{S_f}(\boldsymbol{U}) + \boldsymbol{S_\nu}(\boldsymbol{U}) \quad \text{(4.11)}$$

with

$$\boldsymbol{U} = \begin{bmatrix} A \\ Q \end{bmatrix}, \quad \boldsymbol{F} = \begin{bmatrix} F_A \\ F_Q \end{bmatrix} \quad \text{(4.12)}$$

where the fluxes are defined in Equation (2.38) in the case of the Multi-Ring model

$$\begin{cases} F_A = Q \\ F_Q = \dfrac{Q^2}{A} + \dfrac{K}{3\rho} A^{\frac{3}{2}} \end{cases} \tag{4.13}$$

and the source terms are

$$\boldsymbol{S_f} = \begin{bmatrix} 0 \\ -C_f \dfrac{Q}{A} \end{bmatrix}, \quad \boldsymbol{S_\nu} = \begin{bmatrix} 0 \\ C_\nu \dfrac{\partial^2 Q}{\partial x^2} \end{bmatrix}. \tag{4.14}$$

We use the same discretization as in the Multi-Ring model for the time and spatial domains, represented in Figure 4.1.

We note that, by neglecting the viscous and viscoelastic effects, *i.e.* the source terms $\boldsymbol{S_f}$ and $\boldsymbol{S_\nu}$, the Equation (4.11) is hyperbolic. Indeed the system has two real distinct eigenvalues $\lambda_{1,2} = \dfrac{Q}{A} \pm c$. On the contrary, the viscoelastic source term has a parabolic structure. Thus we decompose the system (4.11) into three subproblems as follows.

Hyperbolic subproblem

We first consider the homogeneous part of Equation (4.11) which is the hyperbolic subproblem that only accounts for the transport as

$$\frac{\partial \boldsymbol{U}}{\partial t} + \frac{\partial \boldsymbol{F}}{\partial x} = 0 \tag{4.15}$$

To solve Equation (4.15), we use the same method as the Multi-Ring model for the convective subproblem (4.3). We compute the flux using a kinetic approach [50, 120, 121] with a second-order monotonic upwind scheme for conservation law (MUSCL) reconstruction [53] and a second-order Adam-Bashforth (AB2) time integration scheme. We impose the boundary conditions when solving this subproblem and give more detail in the following.

Parabolic subproblem

The parabolic subproblem describes the viscoelastic effects as

$$\frac{\partial \boldsymbol{U}}{\partial t} = \boldsymbol{S_\nu}. \tag{4.16}$$

Following [51], we choose a semi-implicit unconditionally stable second-order Cranck-Nicholson finite difference scheme to solve Equation (4.16).

Friction subproblem

Finally, the friction subproblem that accounts for the friction source term is

$$\frac{\partial \boldsymbol{U}}{\partial t} = \boldsymbol{S_f}. \tag{4.17}$$

As the friction subproblem does not involve spatial discretization, we simply use the same second-order Adam-Bashforth as the one used for the hyperbolic problem.

Following [51, 122], to update the solution from t^n to t^{n+1}, we combine the three splitted solutions from the previous problems as

$$\begin{cases} A_i^n \xrightarrow{(4.15)} A_i^{n+1} \\ Q_i^n \xrightarrow{(4.15)} Q_i^* \xrightarrow{(4.16)} Q_i^{**} \xrightarrow{(4.17)} Q_i^{n+1} \end{cases} \tag{4.18}$$

Boundary conditions

Boundary conditions are treated similarly to the Multi-Ring model with the Riemann invariants (4.9) and must be imposed when solving the hyperbolic system (4.15).

Initial conditions

We impose the same initial conditions (4.10) with $n = 1$ as the Multi-Ring model.

Junctions

Unlike the Multi-Ring model code, the 1D model can solve the flow in a network of arteries. The network is a combination of junctions between N_p parent and N_d daughter arteries. In a junction, the flow is highly 3D [123] but can still be represented by 1D junction models. We find two types of models of junction in the literature: the point junction and the control-volume junction. The first consists of assuming that a junction is a single point [124] where the general conservation laws apply, *i.e.* continuity of mass and pressure. Some models like [61] also consider a pressure loss in the junction, which we do not consider as they only have secondary effects on the pulse wave propagation [22]. The junction equations are the following

$$\begin{cases} \displaystyle\sum_{p=1}^{N_p} Q_p - \sum_{d=1}^{N_d} Q_d = 0, & \text{(4.19a)} \\ p_p = p_d + \Delta p_{loss} & \text{(4.19b)} \end{cases}$$

for $(p, d) \in \{1, ...N_p\} \times \{1, ...N_d\}$, with $\Delta p_{loss} = 0$ and the total pressure is

$$p = \frac{1}{2}\rho \left(\frac{Q}{A}\right)^2 + K\left(\sqrt{A} - \sqrt{A_0}\right). \tag{4.20}$$

We solve the junction equations similarly to the boundary conditions imposing the incoming in the daughter and outgoing Riemann invariants in the parent arteries as in Equation (4.9)

$$\begin{cases} W_2(\boldsymbol{U}_{out}^n)_p = W_2(\boldsymbol{U}_{N_x}^n)_p, & \text{(4.21a)} \\ W_1(\boldsymbol{U}_{in}^n)_d = W_1(\boldsymbol{U}_1^n)_d. & \text{(4.21b)} \end{cases}$$

The second type of junction model [60] consists of defining a junction volume parametrized by a length, a cross-section, and a wall rigidity. In the control volume junction model, we impose the 1D mass conservation integrated over the length of the junction and add Neumann boundary conditions on the flow rate of the parent and daughter arteries to impose no spatial variation of the flow rate in the volume.

We consider the first type of junction model as it is more common in the literature. Nevertheless, the volume junction approach has many advantages, in particular it provides more physical results.

This model is used in Chapter 3, Chapter 5, Chapter 6, Chapter 7, Chapter 8, and Chapter 9.

4.2.5 Zero-dimensional model

The 0D models are simply described by first or second-order ordinary differential equations in time and thus only require a time discretization Δt and $t^n = n \times \Delta t$ for $n \in \{0, ...N_T\}$. The most common and efficient method to solve this type of model is to use a finite differences approach. For instance, we can discretize Equation (2.66) with an explicit Euler scheme as follows

$$p_0^n + R_f C \frac{p_0^{n+1} - p_0^n}{\Delta t} + CI \frac{p_0^{n+1} - 2p_0^n + p_0^{n-1}}{\Delta t^2} - p_L^n = R_f Q_0^n + I \frac{Q_0^{n+1} - Q_0^n}{\Delta t}, \tag{4.22}$$

where $p_0^n = p(x = 0, t = t^n)$, $p_L^n = p(x = L, t = t^n)$, and $Q_0^n = Q(x = 0, t = t^n)$. Equation (4.22) can be solved in p or in Q depending on the unknown.

This model or a similar 0D model are used in Chapter 6, Chapter 7, Chapter 8, and Chapter 9.

All of the models described in this Section depend on a certain number of parameters that are often difficult to assess experimentally. To make patient-specific computations, it is thus necessary to estimate the values of these parameters. In the following section, we introduce a panel of optimization methods to estimate the model parameters.

4.3 Optimization methods

In order to enhance the experimental data acquired from routine monitoring studies, we often choose optimization strategies based on experimental measurements to identify model parameters that are otherwise difficult to obtain [67, 125–127]. It is necessary and very common if one wants to make patient-specific predictions in a minimally invasive way [77].

Optimization techniques consist of finding a combination of parameter values that gives the minimum of an objective cost function while satisfying constraints if existing. In general, optimization problems have several optima, *i.e.* local minima, which increases the difficulty of finding the global one (Figure 4.2. The algorithms are usually classified as either local methods such as gradient-based algorithms described in Section 4.3.1 or global methods such as stochastic algorithms described in Section 4.3.2.

For the following, we define $\mathcal{J}$ the cost function to minimize and $\mathcal{P}$ the set of parameters that minimizes this function.

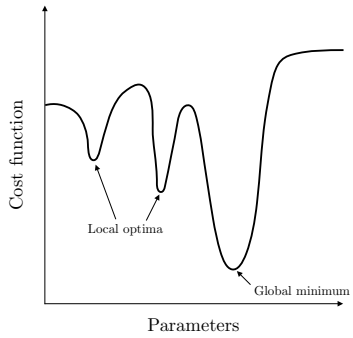

FIGURE 4.2 – Schematic representation of a cost function and its local and global optima.

4.3.1 Local optimization methods

Lots of local optimization algorithms are gradient-based since they were proved to be very efficient in terms of the number of iterations to reach the optimum. These techniques are also designed to solve problems with a large number of variables. However, the major drawback to these methods is that they can only find a local optimum depending on the initial guess of parameters.

Gradient-based optimization methods consist of finding the zero of the gradient of the cost function $\mathcal{J}$ to minimize. The typical algorithms are two-steps processes: the first step is to calculate the gradient to find the search direction which leads to the second step where we move in the search direction until the convergence criterion is reached. In most optimization problems, the gradient cannot be calculated analytically and requires the use of finite differences. It typically provides an approximation with an accuracy depending on the step size. A smaller step size is a better approximation which can be very costly. One of the most classical gradient-based method is Newton's method presented in the following.

Newton's method

Newton's method is a classical gradient-based optimization algorithm for non-linear unconstrained problems, derived from Taylor's expansion. This method requires the calculation of the Hessian matrix B that contains the second-order derivatives of the cost function $\mathcal{J}$. The steps are described in Algorithm 1.

initialization $\mathcal{P}_0$, B_0 ;
while $(\mathcal{P}_{k+1} - \mathcal{P}_k < \epsilon)$ *or* $(k \leq N_{itmax})$ **do**
  $\mathcal{P}_{k+1} = \mathcal{P}_k - B_k^{-1} \nabla \mathcal{J}(\mathcal{P}_k)$;
  $k \leftarrow k + 1$;
end

Algorithm 1: Newton's algorithm.

The method has a quadratic rate of convergence which makes this algorithm very powerful, however the cost to calculate the Hessian matrix B_k at each step is very high which makes this technique highly unusable in most cases. Despite the difficulty to assess the Hes-

sian matrix, Newton's method is deterministic and can thus have a slow rate of convergence or does not converge at all in case of a poor initial estimate.

This method is used every time we solve the steady RNSP, Multi-Ring, and 1D models.

BFGS method

The BFGS method, from the initials of the original authors Broyden [128], Fletcher [129], Goldfarb [130], Shanno [131] is also a gradient-based method for non-linear unconstrained problems. Compared to Newton's descent, it has the major advantage of having low computer memory requirements. The BFGS method is designed to avoid constructing the Hessian matrix B and uses instead an approximation of the inverse of the second derivative of the function to minimize $\mathcal{J}$ by analyzing the gradient. This approximation allows using quasi-Newton's method to find the minimum in the parameter space. The steps are described in Algorithm 2.

initialization $\mathcal{P}_0$, $B_0 = \mathbb{I}$;
while $\dfrac{(\mathcal{J}(\mathcal{P}_k) - \mathcal{J}(\mathcal{P}_{k+1}))}{\max\left(|\mathcal{J}(\mathcal{P}_k)|, |\mathcal{J}(\mathcal{P}_{k+1})|, 1\right)} \leq \epsilon$ **do**
  find $\mathbf{p_k}$ solving $B_k \mathbf{p_k} = -\nabla\mathcal{J}(\mathcal{P}_k)$ where $\mathbf{p_k}$ is the direction of the descent ;
  find the optimal time step α_k by a line search to loosely minimize $\mathcal{J}(\mathcal{P}_k + \alpha_k \mathbf{p_k})$;
  update the solution $\mathcal{P}_{k+1} = \mathcal{P}_k + \alpha_k \mathbf{p_k} = \mathcal{P}_k + \mathbf{s_k}$;
  calculate $\mathbf{y_k} = \nabla\mathcal{J}(\mathcal{P}_{k+1}) - \nabla\mathcal{J}(\mathcal{P}_k)$;
  update the Hessian matrix $B_{k+1} = B_k + \dfrac{\mathbf{y_k}\mathbf{y_k}^T}{\mathbf{y_k}^T\mathbf{s_k}} - \dfrac{B_k\mathbf{s_k}\mathbf{s_k}^T B_k}{\mathbf{s_k}^T B_k \mathbf{s_k}}$. ;
  $k \leftarrow k + 1$;
end

Algorithm 2: BFGS algorithm.

Starting from the identity matrix to initialize the Hessian matrix is the same as running Newton's descent on the first step. The algorithm will further refine the approximation of the Hessian at the next step without having to calculate it analytically.

The L-BFGS-B algorithm, that we mostly used in Part II, is an extension of the BFGS method using a limited amount of computer memory and that allows bound constraints.

As mentioned previously, the disadvantage of the local optimization method is when we deal with the existence of several local minima (Figure 4.2). Global optimization provides a solution to this problem.

4.3.2 Global optimization methods

The methods presented in Section 4.3.1 are deterministic which means that the solution depends on the initial guess $\mathcal{P}_0$. Thus if the initial guess is not relatively close to the optimum, the algorithm could not converge to the general solution. Global optimization methods, that can also be deterministic, ensure that the optimal values are global. They are usually classified into three categories: the deterministic methods such as the Branch and Bound, the

stochastic methods such as Monte-Carlo, and the heuristics and meta-heuristics methods such as the simulated annealing.

We start by introducing the general ideas behind stochastic or random-based methods and then describe in more detail the Basin-Hopping method that is used in the medical application Part II.

Random-based methods

The stochastic global optimization methods usually rely on repeated random sampling which allows solving problems that are a priori deterministic. No information on the derivatives of the cost function being optimized is required, which provides memory for searching over the whole parameter space.

This category of methods involves a four-step process [132]: first, evaluating the objective function $\mathcal{J}$ on a random set of points, second keeping the points that pass the randomized evaluation criteria, third tightening the evaluation criteria, and finally repeating until the convergence criteria are met.

Basin Hopping

The Basin Hopping algorithm [133, 134] is a very effective stochastic algorithm that looks for the global minimum of the cost function $\mathcal{J}$ by creating a random perturbation of the parameters $\mathcal{P}$ at each optimization step. It is particularly useful when the function has many minima separated by large barriers. It is a three-phase method: the first phase consists of perturbing the set of parameters depending on the value of cost function, second running a local minimization using a chosen method (in our case, the L-BFGS-B method), and finally accepting or rejecting the new set of parameters by calculating the cost function value. Usually, the acceptance test is the Metropolis criterion of standard Monte Carlo algorithms [135]. Overall, it provides the optimal values of the model parameters $\mathcal{P}$, in a prescribed parameter space, as the global optima of the cost-function $\mathcal{J}$.

This method, in combination with the L-BFGS-B method, is used in Chapter 6, Chapter 8, and Chapter 9.

4.3.3 Other methods

Considering the importance of parameter estimation in medical studies, many other methods have been developed for that purpose, that we choose not to detail here, for instance, retropropagation [43], adjoint-based methods [136, 137], quasi-Newton methods [138] or the Fletcher-Reeves method [139], also known as the conjugate gradient method.

Filtering approaches such as Kálmán filters are often used for data assimilation to estimate parameters from incomplete or noisy data sets. It is a common strategy in the study of blood flows and has been applied to 0D models [140, 141], 1D models [126, 127, 142], 3D Fluid-Structure Interaction (FSI) models [143, 144] on synthetic or patient data. Most studies that use Kálmán filters look for the elastic properties of the arterial vessels [126, 144] or the values of terminal boundary condition coefficients [56, 125]. We give more detail about this method and run a test on the damped harmonic oscillator equation in Appendix A.

4.4 Conclusion

In this chapter, we detailed the numerical resolution schemes used to solve the four reduced-order models proposed in Chapter 2. Coming from a fluid mechanics background, we mostly use finite difference and finite volume methods however, benchmark studies showed that all methods give the same results when convergence is satisfied [51, 52].

We discussed the interest of optimization methods to estimate model and hemodynamical parameters and thus make patient-specific modeling. We reviewed several optimization methods of the literature and detailed Newton's method for numerical resolution purposes and the combination of the global stochastic algorithm Basin-Hopping with the limited memory gradient-based L-BFGS-B method.

5 Tests of the model hypotheses

Despite accurate numerical resolution schemes, the predictions of the reduced-order models of Chapter 2 need to be tested against appropriate known solutions. This chapter focuses on testing the hypotheses of the steady RNSP, the Multi-Ring, and the 1D models in different scenarios. We compare the models against analytic solutions from the literature and from a computation of the 2D axisymmetric Navier-Stokes equations in steady and unsteady conditions. We also propose experiments to validate the 1D and Multi-Ring models in laboratory conditions. The first experiment consists of building a network of artificial arteries. The second consists of placing a stenosis, *i.e.* a narrowing of the cross-section, in an artificial artery. In both experiments, we study the pulse wave propagation and reflections measured with either a pressure sensor or a PIV set-up.

Keywords: entry effect, Womersley solution, experiments in artificial arteries.

The experimental work was carried during a 3-weeks research internship as part of a collaboration between the Institut Jean le Rond d'Alembert of Sorbonne Université in Paris (France) and the Laboratory of Ultrasonic Electronics of Doshisha University in Kyoto (Japan).

Contents

5.1 Introduction

In Chapter 2, we introduced four reduced-order models to compute blood flow in arteries. The main drawback of this reduced modeling approach is that the more reduced the model, the more information it loses. Therefore it is necessary to do model verifications against analytic solutions or experimental data to evaluate the validity of the models and the underlying hypotheses.

Many studies have tested the hypotheses of the one-dimensional (1D) model by comparing it with asymptotic solution [41, 43, 44], experimental models [20], *ex vivo* [73] or *in vitro* measurements [21,22,57], *in silico* three-dimensional (3D) models [145] and real invasive data [13,55,67,71,72,146,147]. As it is a recent development, only two studies have dedicated to the validation of the Multi-Ring model against analytic solutions [46] and 3D computations [47].

In this chapter, we carry a model comparison against analytic solutions and experiments in artificial arteries. We start in Section 5.2 by testing the hypotheses of the Multi-Ring model by comparing its numerical predictions to analytic solution. First, we study the entry effect which is the development of the boundary layer in a straight rigid tube. We compare the steady Reduced Navier-Stokes Prandtl (RNSP) and the Multi-Ring model to the analytic solution and to a computation of the two-dimensional (2D) axisymmetric Navier-Stokes equations. Second, we present the Womersley solution [42] in a straight elastic tube and we compute the Multi-Ring model to test it in unsteady conditions. In Section 5.3, we compare the 1D and Multi-Ring models with experiments in artificial arteries made from silicon tubes. We study in Section 5.3.3 an arterial network composed of an assembly of these silicon tubes. The second experiment described in Section 5.3.4 consists of pressure and Particle Image Velocimetry (PIV) measurements in a stenosed silicon tube.

5.2 Analytic cases

We propose two classical configurations, numerical and theoretical to test the hypotheses of the steady RNSP and Multi-Ring models presented in Chapter 2 when possible. The first test case is the development of the boundary layer of a flow entering a straight rigid channel where the reduced models (steady RNSP model, Multi-Ring model, and Poiseuille solution) are compared to a complete 2D axisymmetric simulation of the Navier-Stokes equations (2.22). The second is the Womersley solution which is an analytic solution of the RNSP equations in unsteady flows, using the Multi-Ring model.

5.2.1 The entry effect

The first comparison case is the entry effect, represented in Figure 5.1. We investigate the flow entering a straight rigid channel of radius R_0 and length L and we expect that the velocity profile goes from a flat to a fully developed Poiseuille profile. The transition is due to the development of a boundary layer which develops and merges into a Poiseuille profile.

We obtain the Poiseuille equations by simplifying the RNSP Equations (2.29) assuming that the flow is steady, fully developed, and laminar. Using the no-slip boundary condition at the wall $r = R_0$ and the fact that the velocity u_x must be bounded at the center $r = 0$,

we can solve the x-momentum Equation (2.29c) and obtain the following velocity

$$u_x(r) = \frac{1}{4\mu}\frac{\mathrm{d}p}{\mathrm{d}x}(r^2 - R_0^2), \tag{5.1}$$

which we refer to as the Poiseuille velocity profile. We calculate the volumic flow rate by integrating the velocity (5.1) over the cross-section of the tube

$$Q = \int_0^{2\pi}\int_0^{R_0} u_x(r) r \mathrm{d}r\mathrm{d}\theta = -\frac{\pi R_0^4}{8\mu}\frac{\mathrm{d}p}{\mathrm{d}x}. \tag{5.2}$$

Replacing Q by $A_0U_0 = \pi R_0^2 U_0$, where U_0 is the magnitude of the input velocity in Equation (5.2) and integrating, we obtain the pressure $p(x)$ along the tube

$$p(x) = -\frac{8\rho U_0^2}{R_0 Re_R}(x - L), \tag{5.3}$$

where Re_R is the Reynolds number based on the radius defined as

$$Re_R = \frac{\rho U_0 R_0}{\mu}. \tag{5.4}$$

We define the Poiseuille resistance R_f that links the pressure drop $\Delta P = p(x = 0) - p(x = L)$ across a tube to the flow rate Q as

$$R_f = \frac{8\mu L}{\pi R_0^4}. \tag{5.5}$$

Note that this is actually the hydraulic expression of the resistance of the zero-dimensional (0D) outflow model (2.68) presented in Section 2.3.6, defined in Equation (2.69), that links the pressure drop to the flow rate Q.

Finally we can calculate analytically the Wall Shear Stress (WSS) τ_w thanks to Equation (2.43)

$$\tau_w = \frac{4\mu U_0}{R_0}, \tag{5.6}$$

which is Equation (2.48) with $\xi = 2$, the value that corresponds to a Poiseuille velocity profile.

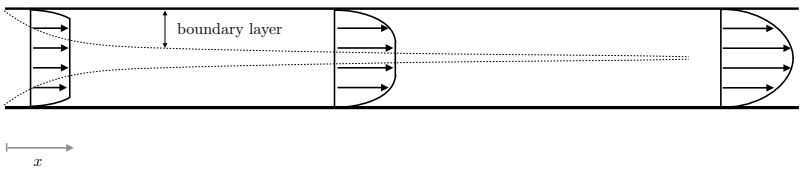

FIGURE 5.1 – Developing and fully developed flows in a channel. The flow is fully developed after the two boundary layers have merged.

We compare the flow velocity and pressure with the steady RNSP, the Multi-Ring, and the Poiseuille solution in a straight rigid tube. We compute the full 2D axisymmetric Navier-

Stokes Equations (2.22) with the software Basilisk presented in Section 4.2.1. We use this exact solution as a target for the other models. The properties of the test case are reported in Table 5.1 and the numerical parameters in Table 5.3.

TABLE 5.1 – Characteristic scales of the entry effect problem. R_0: reference radius in cm, L: artery length in cm, Re_R: Reynolds number defined in Equation (5.4), U_0: input velocity in cm/s, ρ: density in g/cm^3, μ: dynamic viscosity in g·cm^{-1}·s^{-1}, K: elastic coefficient defined in Equation (2.15) in g·cm^{-2}·s^{-2}.

R_0	L	Re_R	U_0	ρ	$\mu = \dfrac{\rho U_0 R_0}{Re_R}$	K
1	25	100	100	1	1	1e7

In Figures 5.2, we plot the dimensionless pressure and velocity at the center-line for the different models. We remark that the numerical results are similar. As expected, we observe in Figure 5.2a that the dimensionless center velocity goes from 1, which is the magnitude of the flat profile, to 2 the maximum of the Poiseuille profile. In Figure 5.2b, we show the dimensionless center pressure loss computed with the different models. The models all fit the 2D axisymmetric Navier-Stokes target computation, and when the boundary layer is fully developed, all models fit the analytic solution for the pressure loss in an rigid tube (Equation (5.3)).

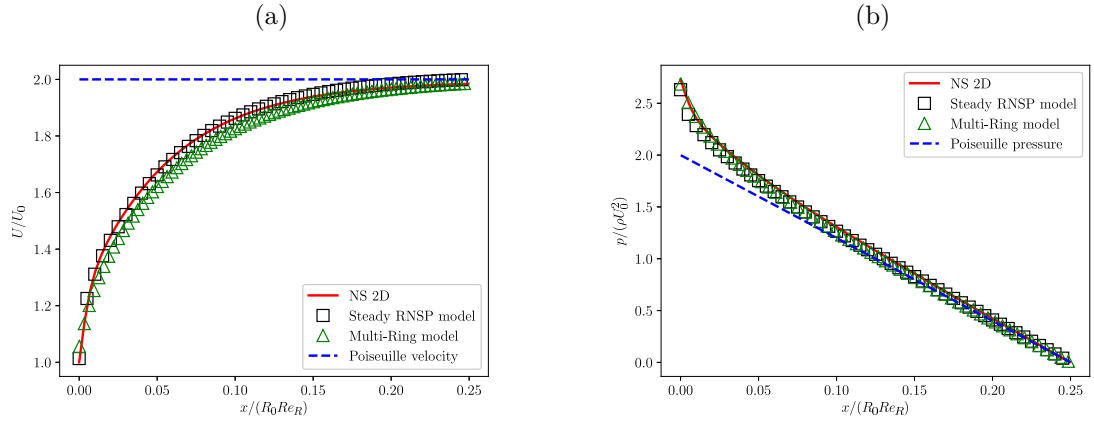

FIGURE 5.2 – Dimensionless (a) velocity and (b) pressure at the center-line as a function of x-position. Comparison of (—) the 2D axisymetric Navier-Stokes solution, (□) the steady RNSP model, (△) the Multi-Ring model, and (- - -) the Poiseuille solution for the entry effect.

In Figures 5.3, we plot the velocity profile at different x-positions in the artery by comparing the 2D axisymmetric Navier-Stokes computation to the steady RNSP model (Figure 5.3a) or the Multi-Ring model (Figure 5.3b). We observe that the models reproduce accurately the development of the velocity profile starting from a flat profile at $x = 0$ cm to the Poiseuille solution at the end of the tube. We observe a slight difference between the Multi-Ring model and the 2D axisymmetric Navier-Stokes in Figure 5.3b due to the axial resolution.

This test case verifies the predictions of the steady RNSP and the Multi-Ring results against the analytic Poiseuille solution and the 2D axisymmetric Navier-Stokes equations in steady conditions. We now test the hypotheses of the Multi-Ring model in an unsteady case.

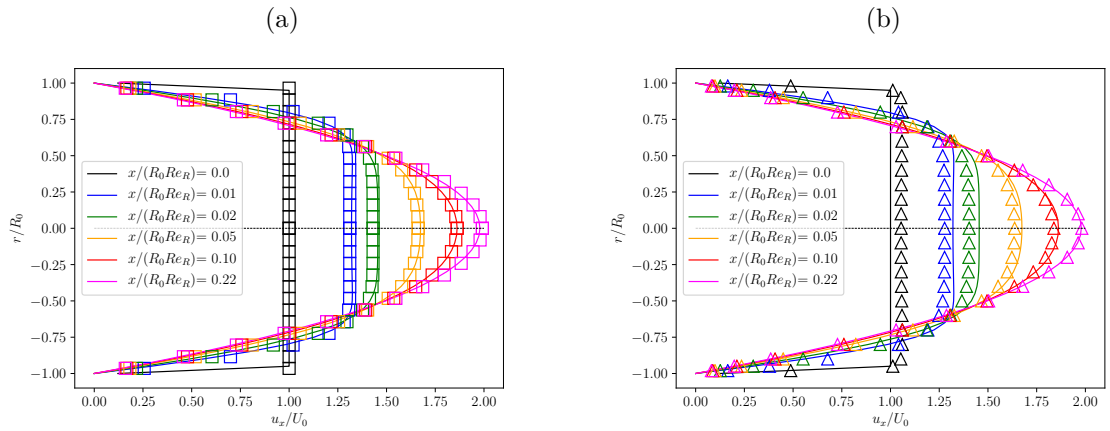

FIGURE 5.3 – Velocity profile comparison between the 2D Navier-Stokes solution (solid line) and (a) the steady RNSP model (□), (b) the Multi-Ring model (△) at $x = 0$ (—), $x = 1$ (—), $x = 2$ (—), $x = 5$ (—), $x = 10$ (—) and $x = 22$ cm (—).

5.2.2 The Womersley problem

The second test case is the analytic solution of the Womersley velocity profile in a straight elastic tube [42] that depends on the Womersley number $\alpha = R_0\sqrt{\omega/\nu}$ defined in Equation (2.26). This is the solution of the unsteady RNSP equations (2.28) where we assume that the flow is linear and periodic. We search for a harmonic solution of the axial velocity u_x and the pressure p as

$$\begin{cases} u_x = \hat{u}_x e^{i(\omega t - kx)}, & \text{(5.7a)} \\ p = p_0 + \hat{p} e^{i(\omega t - kx)}, & \text{(5.7b)} \end{cases}$$

where we set $p_0 = 0$ for simplicity. Injecting these harmonic solution in Equation (2.28c), we recover the classical Womersley equation

$$\frac{\partial^2 \hat{u}_x}{\partial r^2} + \frac{1}{r}\frac{\partial \hat{u}_x}{\partial r} - \frac{i\alpha^2}{R^2}\hat{u}_x = -\frac{i\omega}{\mu c}\hat{p}. \tag{5.8}$$

The solution of Equation (5.8) is (5.7a) with

$$\hat{u}_x = \frac{\hat{p}}{\rho c}\left(1 - \frac{J_0\left(i^{3/2}\alpha\dfrac{r}{R_0}\right)}{J_0\left(i^{3/2}\alpha\right)}\right), \tag{5.9}$$

with $c = \omega/k$ the wave velocity, J_0 the Bessel function, and α the Womersley number. From Equation (5.9), we can compute the flow rate Q and the WSS τ_w

$$\begin{cases} Q = \hat{Q} e^{i(\omega t - kx)} & \text{with } \hat{Q} = \pi R_0^2 \dfrac{\hat{p}}{\rho c}(1 - F_{10}(\alpha)) & \text{(5.10a)} \\ \tau_w = \hat{\tau_w} e^{i(\omega t - kx)}, & \text{with } \hat{\tau_w} = i\dfrac{\nu\alpha^2}{2R_0}\dfrac{\hat{p}}{\rho c}F_{10}(\alpha), & \text{(5.10b)} \end{cases}$$

TABLE 5.2 – Characteristic parameters of the Womersley velocity profile. R_0: initial radius in cm, L: tube length in cm, ρ: density in g/cm^3, μ: dynamic viscosity in g·cm^{-1}·s^{-1}, K: elastic coefficient defined in Equation (2.15) in g·cm^{-2}·s^{-2}, $\hat{R}$: inlet boundary condition in cm, R_t: reflection coefficient, T_c: period in s, t_f: final time of the simulation in s, α: Womersley number.

R_0	L	ρ	μ	K	$\hat{R}$	R_t	T_c	t_f	α
1	200	1	$2\pi\frac{\rho}{T_c}\frac{R_0^2}{\alpha^2}$	10^4	10^{-3}	0	0.5	$12T_c$	{5,20}

TABLE 5.3 – Numerical parameters of the Multi-Ring model for the Womersley velocity profile. N_x: number of cells, N_r: number of rings, dt: time step in s.

N_x	N_r	dt
1600	32	$2{\cdot}10^{-6}$

where $F_{10}(\alpha) = \dfrac{2}{i^{3/2}\alpha}\dfrac{J_1(i^{3/2}\alpha)}{J_0(i^{3/2}\alpha)}$.

To compute the Womersley velocity profile, we impose the following sinusoidal pressure at the inlet

$$p(x=0,t) = \hat{p}\sin\left(2\pi\frac{t}{T_c}\right), \tag{5.11}$$

with the amplitude $\hat{p} = \sqrt{\pi}K\hat{R}$ and a reflection coefficient R_t equal to 0 at the outlet. We compute the Multi-Ring model in a straight elastic tube with the properties reported in Table 5.2 and the numerical parameters in Table 5.3.

In Figures 5.4, we compare the velocity profiles at different times using the Multi-Ring model and the analytic solution (5.7a) for a small Womersley number $\alpha = 5$ (Figure 5.4a) and for a large Womersley number $\alpha = 20$ (Figure 5.4b). We observe that the Multi-Ring model reproduces accurately the analytic solution (5.7a). For $\alpha = 5$, the viscous effects dominate over the unsteady effects, and we thus obtain a slightly deformed oscillating Poiseuille profile. On the other hand, for $\alpha = 20$, the boundary layer is very small as the viscous effects are small. We obtain a flatter velocity profile which tends to look like the slip condition at the wall.

This approach allows calculating the center pressure p, the center velocity $u_x(r=0)$ but also the flow rate Q and the WSS τ_w. We show the comparison of the Multi-Ring model with the analytic solutions in Figures 5.5 for the flow rate Q (Figures 5.5a and 5.5b) and the WSS τ_w (Figure 5.5c and 5.5d) as a function of the dimensionless position along the artery for one specific time. We obtain a very satisfying agreement as the model reproduces the exponential decrease for both Womersley numbers. This second test case allows verifying the hypotheses of the Multi-Ring model under unsteady flow with an elastic arterial wall.

In Section 5.2.1, we compared the steady RNSP and the Multi-Ring model with an analytic case and the reference 2D axisymmetric Navier-Stokes solution in steady conditions with a rigid wall. In this section, we proposed a validation of the Multi-Ring hypotheses in unsteady conditions and of the elastic arterial wall model. In the following section, we test the hypotheses of the 1D model against experiments in artificial arteries.

(a) $\alpha = 5$ (b) $\alpha = 20$

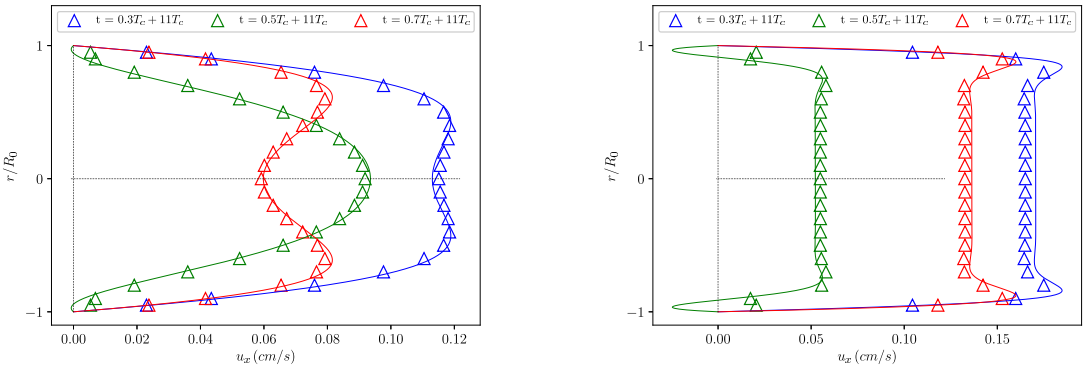

FIGURE 5.4 – Womersley velocity profiles in an elastic tube for (a) $\alpha = 5$ and (b) $\alpha = 20$. Comparison between (△) the Multi-Ring model and (—) the analytic solution (5.7a). —△— is $t = 0.3T_C + 11T_c$, —△— is $t = 0.5T_C + 11T_c$, and —△— is $t = 0.7T_C + 11T_c$.

(a) $\alpha = 5$ (b) $\alpha = 20$

(c) $\alpha = 5$ (d) $\alpha = 20$

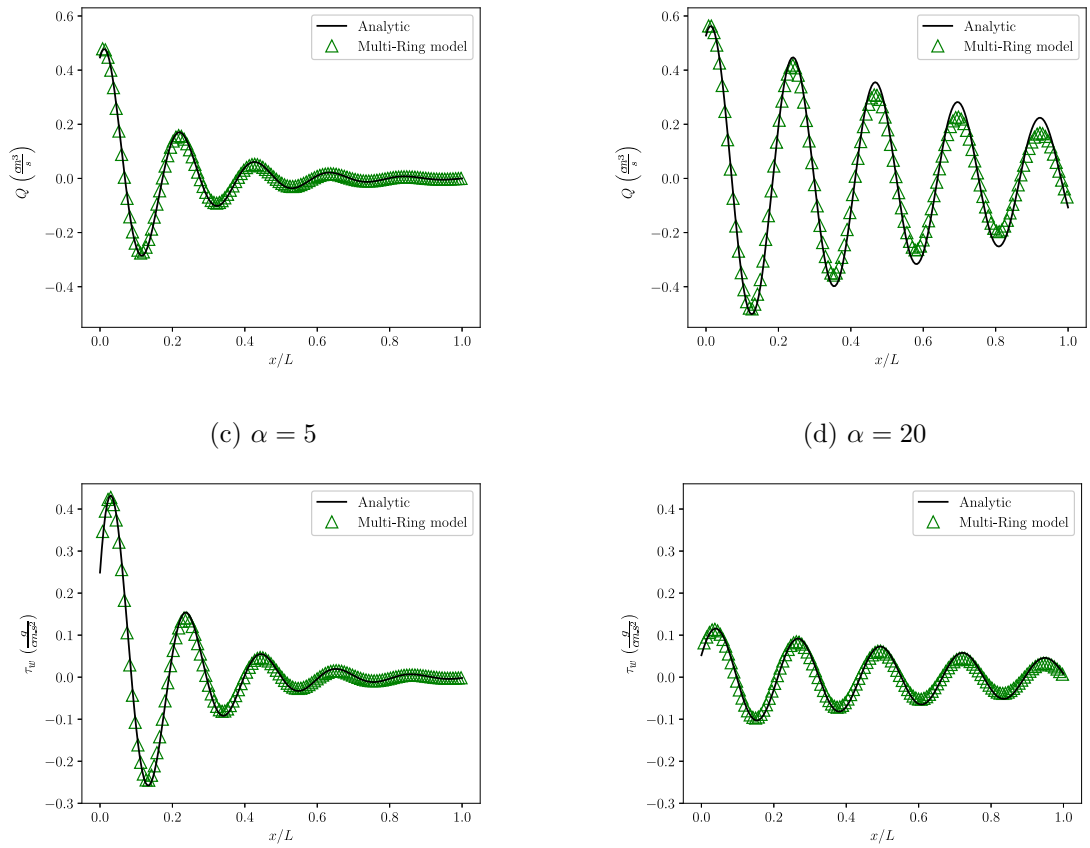

FIGURE 5.5 – Center flow rate Q and WSS τ_w comparison between the Multi-Ring model (△) and the analytic solutions (—) of Equation (5.10) for $\alpha = 5$ (a) and (c) and $\alpha = 20$ (b) and (d) at $t = 0.3T_c + 11T_c$.

5.3 Experiments

The following experimental work was carried during a 3-weeks research internship at the Laboratory of Ultrasonic Electronics of Doshisha University in Kyoto (Japan).

We are now interested in testing the reduced-order models by comparing them with experiments in artificial arteries. The set-up and fabrication of the artificial arteries are described in Section 5.3.1 and 5.3.2. We explore two different experimental set-ups: the first consists of assembling the artificial arteries into a network of 9 tubes (Section 5.3.3). We compute the 1D model and verify that its prediction reproduces the measured pressure wave. The second experiment consists of placing a stenosis, *i.e.* a narrowing of the lumen of the tube, in an artificial artery and compare the velocity measured with PIV with the 1D and Multi-Ring models (Section 5.3.4).

5.3.1 Fabrication of the tubes

We fabricate the tubes using a mixture of two types of silicon gels Momentive Performance TSE3061 and TSE3450. We ensure that the mixture is homogeneous without any air bubble. We pour the mixture between a plastic tube and a stainless rod such that the thickness of the silicone tube is 0.2 cm, as represented in Figure 5.6. We let the mixture solidify overnight. We break the plastic tube and remove the silicon tube from the stainless rod.

To ensure the consistency of the tubes' fabrication, the length of one single tube should not exceed 20 cm. Young's modulus of each tube is supposedly 150 kPa (value provided by the supplier) however we do not perform tensile tests to verify this value.

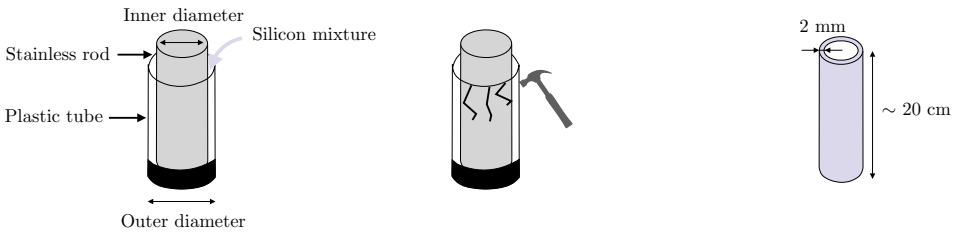

FIGURE 5.6 – Fabrication process of the artificial artery tube models.

5.3.2 Experimental set-up

The experimental set-up consists of a flow pump filled with water plugged into the artificial arteries as shown in Figure 5.7. We use a TOMITA Engineering piston pump as the input of the set-up. The pump imposes a half-sine input flow rate with an amplitude of 100 cm^3/s and an ejection time of 0.3 s. We close the set-up with stainless rods to avoid leaks.

The tubes are pre-filled with water with an inner pressure of approximately 2 kPa. We measure the pressure using a Keyence AP-10S pressure sensor.

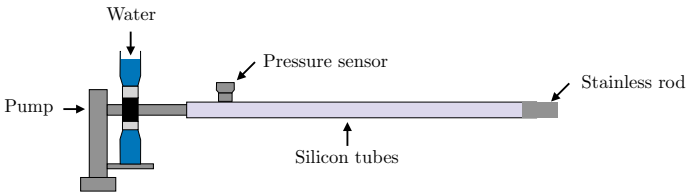

FIGURE 5.7 – Experimental set up to measure the pressure in the artificial arteries.

5.3.3 The clamping experiment

The first experiment, which we refer to as the clamping experiment, consists of assembling the artificial arteries to form an arterial network. We clamp an artery of the network to verify that the model reproduces the reflections that occur after the occlusion of one tube. In the following, we present the experiment, the numerical model, the comparison of the two, and finally the measurement of Young's modulus of the tubes.

Experiment

We connect nines tubes to form a minimal arterial network modeling the nine main arteries of the human systemic circulation, similarly to [20], as represented in Figure 5.8, with the properties reported in Table 5.4. The tubes are assembled into a network by gluing one tube to the next with the silicone mixture. Each terminal tube is occluded with a stainless rod which imposes a total reflection ($R_t = 1$) of the pressure wave. We place the pressure sensor at the position indicated in Figure 5.8. To model an abdominal clamping, we place the clamp at the end of tube 7.

TABLE 5.4 – Geometric properties of the 9-artery network model adjusted from [20, 66, 72]. L: length of each tube in cm, D_0: diameter of each tube in cm, h: arterial wall thickness in cm, R_t: reflection coefficient.

N°	Name	L	D_0	h	R_t
1	Aorta arch A	5	1.8	0.2	—
2	Right subclavian radial artery	75	0.8	0.2	1
3	Aorta arch B	2.2	1.6	0.2	—
4	Left carotid artery	36	0.8	0.2	1
5	Aorta arch C	3.7	1.4	0.2	—
6	Left subclavian radial artery	69	0.8	0.2	1
7	Aorta	35	1.2	0.2	—
8	Right femoral artery	97	1.05	0.2	1
9	Left femoral artery	97	1.05	0.2	1

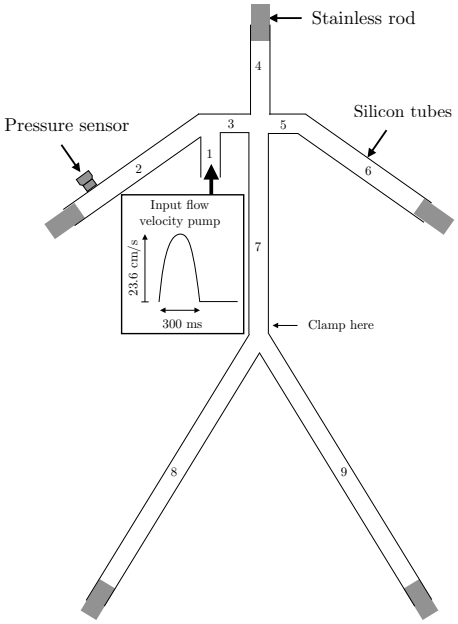

FIGURE 5.8 – 9-artery network made of artificial arteries with a topology adapted from [20, 66, 72]. The pump is placed at the entry of tube 1, the pressure sensor at 60 cm from the beginning of tube 2. The clamp is placed at the end of tube 7.

Numerical model

We use the 1D model described in detail in Section 2.3.4 with the viscoelastic pressure law (2.18) to compare to the experimental pressure measurements. The numerical 1D network has the same properties as the artificial network (Table 5.4). Initially, we assume that Young's modulus E is $1.5{\cdot}10^6$ g·cm^{-1}·s^{-2} (which corresponds to 150 kPa and $C_\nu = 1000$ cm^2/s [20].

The boundary conditions are the following: at the inlet of the network (tube 1), we impose the experimental input signal of the pump. At the end of each terminal tube, we impose reflection coefficients R_t of 1 to model the occlusion by the stainless rods. We model the clamping process by applying a total reflection at the end of tube 7, corresponding to a complete occlusion of the tube. To compare with the experimental measurement, we compute the pressure numerically at the position of the pressure sensor, *i.e.* 60 cm from the beginning of tube 2.

In the following, we refer to the pre-clamp configuration as the case before placing the clamp at the end of tube 7 (the flow occurs in the nine arteries), the post-clamp configuration is after we place the clamp at the end of tube 7 (the flow occurs in only seven arteries).

Comparison between experimental and numerical pressure waves

In Figures 5.9, we compare the pressure measured with the pressure sensor and computed with the 1D model for the pre-clamp (Figure 5.9a) and the post-clamp (Figure 5.9b) configurations. We use the a priori values of Young's modulus $E = 1.5{\cdot}10^6$ g·cm^{-1}·s^{-2} and a viscoelastic coefficient C_ν of 1000 cm^2/s, as in [20]. In these figures, we observe the propaga-

tion, the reflections, and the superposition of all the waves of the pressure pulse sent by the pump. The mean pressure increases from the pre-clamp to the the post-clamp configuration.

When comparing the experimental and numerical pressure waves of Figure 5.9a, the value of the viscoelastic coefficient seems appropriate: the attenuation of the reflection waves follows the experimental data. However, the value of C_ν does not match the post-clamp configuration as shown in Figure 5.9b. We observe that the diffusion of the pulse is too important in the numerical simulation with respect to the data.

In the pre-clamp configuration, the simulated pressure peaks are late compared to the experimental pressure peaks which means that the stiffness should be higher for the waves to propagate faster. However, we observe something different in the post-clamp configuration: the two first pressure pulses are late which supports the fact that the elasticity should be higher for the waves propagating faster. Nonetheless, the third numerical pulse is perfectly synchronized with the experimental one, and from the fourth pulse, the numerical pulse wave is ahead of the experimental one, which suggests a lower elasticity.

We obtain a correlation coefficient R^2 of 0.62 for the pre-clamp configuration and 0.85 for the post-clamp configuration.

(a) Pre-clamp

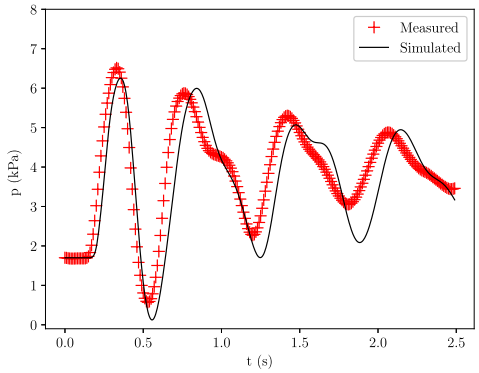

(b) Post-clamp

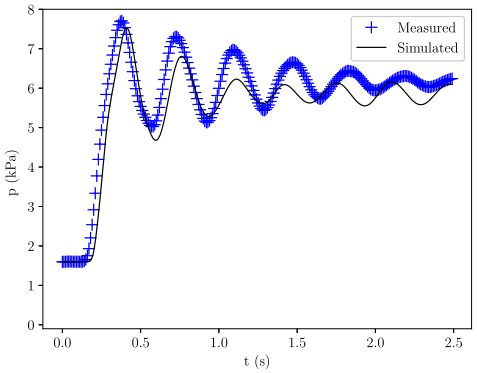

FIGURE 5.9 – Comparison between the 1D model (—) and the experimental measurements for (a) the pre-clamp (+) and (b) the post-clamp configuration (+) using the expected value of Young's modulus of $1.5{\cdot}10^6$ g·cm^{-1}·s^{-2} and a typical value of the viscoelastic coefficient $C_\nu = 1000$ cm^2/s. The correlation coefficient is (a) $R^2 = 0.62$ for the pre-clamp configuration (b) and $R^2 = 0.85$ for the post-clamp configuration.

To get a deeper understanding of the phenomena, we run another simulation increasing Young's modulus from 150 to $1.65{\cdot}10^6$ g·cm^{-1}·s^{-2} and represent the numerical result in Figure 5.10. The agreement between experimental and numerical pressure waves is better for the pre-clamp configuration (Figure 5.10a) when increasing Young's modulus, we obtain a correlation coefficient R^2 of 0.84. For the post-clamp configuration, the two first pressure peaks are now synchronized too, as shown in Figure 5.10b. However, even though the attenuation of the waves is well captured by the 1D model in the pre-clamp configuration, the attenuation is still too high for the post-clamp configuration. We obtain a correlation coefficient R^2 of 0.90.

So far, we can conclude that our 1D wall model is missing an element that could be for instance a non-linear elasticity (Chapter 3). We now try identifying the actual Young's modulus by measuring it experimentally. We prove numerically that the technique fails to identify a single value of the wall elasticity because of the non-linearity of the wall.

(a) Pre-clamp (b) Post-clamp

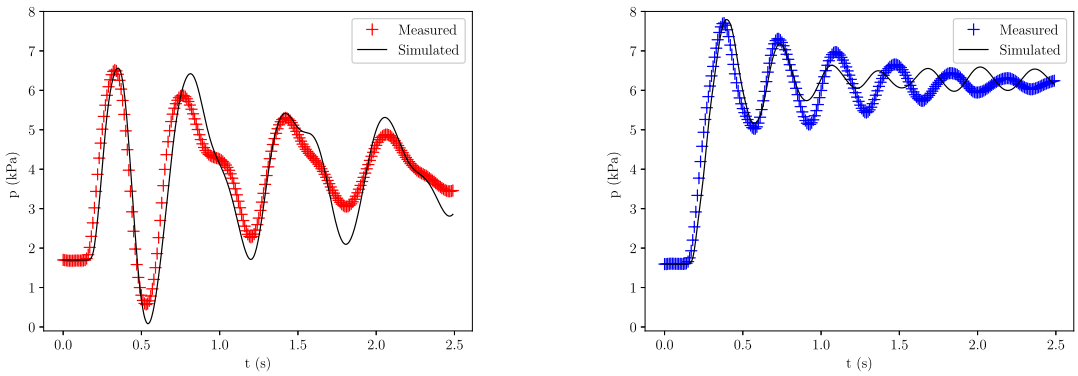

FIGURE 5.10 – Comparison between the 1D model (—) and the experimental measurements for (a) the pre-clamp (+) and (b) the post-clamp (+) configuration using a Young's modulus of $1.65{\cdot}10^6$ g·cm^{-1}·s^{-2} and a typical value of the viscoelastic coefficient $C_\nu = 1000$ cm^2/s. The correlation coefficient is (a) $R^2 = 0.85$ for the pre-clamp configuration (b) and $R^2 = 0.90$ for the post-clamp configuration.

Measurement of Young's modulus

In order to assess the value of Young's modulus, we carry elasticity measurements because tensile test is unavailable as it would require to cut each silicone tube. The method consists of calculating the wave velocity in each tube to obtain Young's modulus value through the Moens Korteweg relation (5.13) [92, 93]. The distance between the two measurement points divided by the time difference allows calculating the wave velocity (5.12) as

$$c = \frac{\Delta L}{\Delta t}, \tag{5.12}$$

with ΔL the distance between the measurement points and Δt the time for the wave to travel from the first to the second measurement point. From Equations (2.15) and (2.59), we obtain the following expression for Young's modulus

$$E = \frac{\rho D_0 c^2 (1 - \nu_w^2)}{h}, \tag{5.13}$$

with ρ the water density, $D_0 = 2R_0$ the tube diameter (Table 5.8), c the wave velocity (5.12), ν_w the Poisson coefficient, and h the tube wall thickness (Table 5.8).

For the experimental measurement of the wave velocity c, we extend the tubes to prevent any reflection to superimpose with the incident wave. We carry these measurements in the arms and legs. We place the pressure sensor at different locations as represented in Figure 5.11 and 5.13 for the measurement of Young's modulus in the arm and leg respectively. The locations of the measurement points are reported in Table 5.5 and 5.9 for the arm and leg

respectively.

For the numerical model, we reproduce this set-up and compute the pressure at the same locations to assess the wave velocity c. We impose an a priori value of Young's modulus E to verify if this technique can identify this value of E. We measure the time difference and wave velocity with three different techniques that correspond to several locations of the first pulse of pressure:

- The first measurement ($\square$) is at the peak of the pressure pulse: we calculate the maximum of the first pressure pulse for each of the three measurement points, the time difference between each pulse and the wave velocity with Equation (5.12).

- The second measurement ($\triangle$) is taking the maximum of the first pressure pulse minus the minimum of the first pressure pulse divided by two.

- The last measurement ($\bigcirc$) of the wave velocity is by adding 20% of the maximum of the first pressure pulse to the minimum of the first pressure pulse.

In the following, we present the experimental results of Young's modulus measurements in the arm and leg and show numerically that this technique fails to identify one value of the elastic coefficient in both the arm and the leg.

Measurement of Young's modulus in the arm

In Table 5.6, we report the five experimental measurements of Young's modulus in the arm. In Tables 5.7 and 5.8, we report the numerical values of Young's modulus obtained with the numerical method for two different values of the viscoelastic coefficient $C_\nu = 500$ and 5000 cm^2/s respectively. In Figures 5.12, we show the pressure wave in the arm at the three measurement points to show how we measure the wave velocity for $C_\nu = 500$ cm^2/s in Figure 5.12a and $C_\nu = 5000$ cm^2/s in Figure 5.12b.

For the arm, the mean experimental value of Young's modulus is $1.174 \pm 0.17 \cdot 10^6$ $\text{g}\cdot\text{cm}^{-1}\cdot\text{s}^{-2}$, corresponding to a 22% difference with respect to the supplier's value of 1.5 $\text{g}\cdot\text{cm}^{-1}\cdot\text{s}^{-2}$. The mean numerical value is $1.62 \pm 0.06 \cdot 10^6$ $\text{g}\cdot\text{cm}^{-1}\cdot\text{s}^{-2}$ for $C_\nu = 500$ cm^2/s (8% difference) and $1.76 \pm 0.15 \cdot 10^6$ $\text{g}\cdot\text{cm}^{-1}\cdot\text{s}^{-2}$ for $C_\nu = 5000$ cm^2/s (17% difference).

We observe that in both experimental and numerical methods, the value of Young's modulus varies a lot from one measurement to another, depending on the location of the measurement point and on the chosen technique. There is indeed a large deviation in Young's modulus measured by the experimental and numerical method, neither the experimental nor the numerical model provides a reliable value.

TABLE 5.5 – Modification of the properties of Table 5.4 and position of the measurements points. The lengths indicated for the measurements points are the distances from the beginning of the tube.

N°	Name	L (cm)	MP1 (cm)	MP2 (cm)	MP3 (cm)
2	Right subclavian radial artery	200	40	60	80

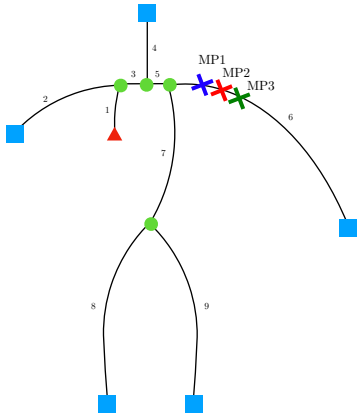

FIGURE 5.11 – Drawing of the 9-artery network for the measurement of the arm elasticity. The crosses represent the points of measurements as reported in Table 5.5.

TABLE 5.6 – Five experimental measurements of Young's modulus in the arm, expressed in 10^6 g·cm^{-1}·s^{-2}.

Measurement n°	1	2	3	4	5
Young's modulus	1.45	1.30	1.09	1.04	0.99

TABLE 5.7 – Young's modulus numerical measurements in the arm in 10^6 g·cm^{-1}·s^{-2} with $C_\nu = 500$ cm^2/s.

	between MP1 and MP2	between MP2 and MP3	between MP1 and MP3
□	1.71	1.71	1.71
△	1.53	1.59	1.56
◯	1.59	1.59	1.59

TABLE 5.8 – Young's modulus numerical measurements in the arm in 10^6 g·cm^{-1}·s^{-2} with $C_\nu = 5000$ cm^2/s .

	between MP1 and MP2	between MP2 and MP3	between MP1 and MP3
□	1.71	1.65	1.67
△	1.58	1.70	1.65
◯	1.92	2.00	1.96

(a) $C_\nu = 500$ cm^2/s (b) $C_\nu = 5000$ cm^2/s

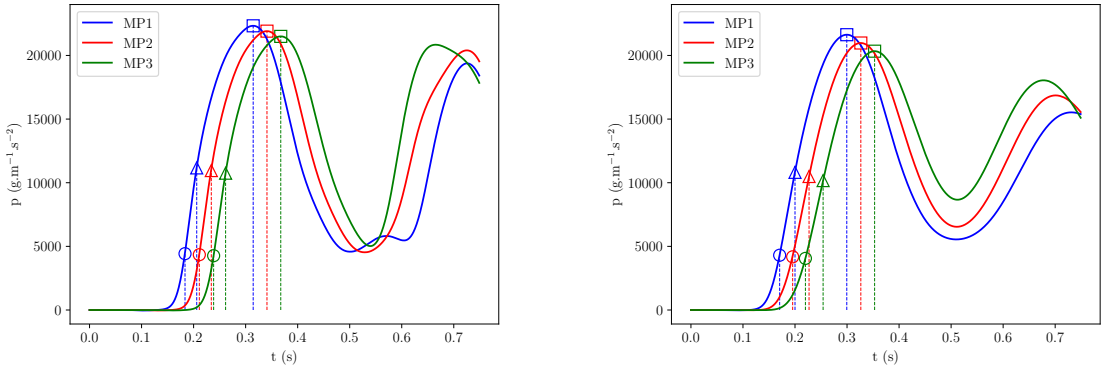

FIGURE 5.12 – Pressure wave in the arm (tube 2) as a function of time from which we measured the wave velocity. (—) is the pressure wave at the measurement point 1 (MP1), (—) is the pressure wave at the measurement point 2 (MP2), and (—) is the pressure wave at the measurement point 3 (MP3). (□), (△), and (◯) correspond respectively to first, second and third measurement method. (a) corresponds to a low viscoelastic coefficient $C_\nu = 500$ cm^2/s , and (b) correspond to a high viscoelastic coefficient $C_\nu = 5000$ cm^2/s.

Measurement of Young's modulus in the leg

In Table 5.10, we report the five experimental measurements of Young's modulus in the leg. In Tables 5.11 and 5.12, we report the numerical values of Young's modulus for two different values of the viscoelastic coefficient $C_\nu = 500$ and 5000 cm^2/s respectively. In Figures 5.14, we show the pressure wave in the arm at the three measurement points to show how we measure the wave velocity for $C_\nu = 500$ cm^2/s in Figure 5.14a and $C_\nu = 5000$ cm^2/s in Figure 5.14b.

For the leg, the mean experimental value of Young's modulus is $1.692 \pm 0.19 \cdot 10^6$ g·cm^{-1}·s^{-2}, corresponding to a 13% difference with respect to the supplier's value of 1.5 g·cm^{-1}·s^{-2}. The mean numerical value is $1.24 \pm 0.05 \cdot 10^6$ g·cm^{-1}·s^{-2} for $C_\nu = 500$ cm^2/s (17% difference) and $1.37 \pm 0.12 \cdot 10^6$ g·cm^{-1}·s^{-2} for $C_\nu = 5000$ cm^2/s (8% difference).

Similarly to the measurements in the arm, we observe that neither the experimental nor numerical method provide one reliable value of Young's modulus.

TABLE 5.9 – Modification of the properties of Table 5.4 and position of the measurements points. The lengths indicated for the measurements points are the distances from the beginning of the tube.

N°	Name	L (cm)	MP1 (cm)	MP2 (cm)	MP3 (cm)
9	Left femoral artery	200	40	60	80

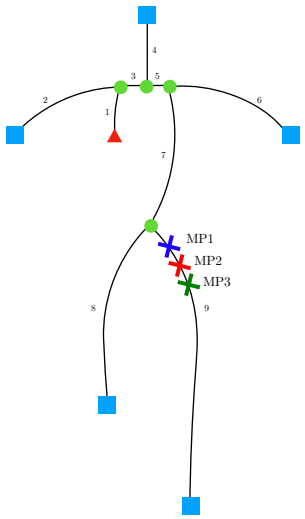

FIGURE 5.13 – Drawing of the 9-artery network for the measurement of the leg elasticity. The crosses represent the points of measurements as reported in Table 5.9.

TABLE 5.10 – Five experimental measurements of Young's modulus in the leg, expressed in 10^6 g·cm^{-1}·s^{-2}.

Measurement n°	1	2	3	4	5
Young's modulus	1.99	1.82	1.66	1.50	1.49

TABLE 5.11 – Young's modulus numerical measurements in the leg in 10^6 g·cm^{-1}·s^{-2} with $C_\nu = 500$ cm^2/s.

	between MP1 and MP2	between MP2 and MP3	between MP1 and MP3
□	1.33	1.29	1.31
△	1.21	1.17	1.19
◯	1.21	1.21	1.21

TABLE 5.12 – Young's modulus numerical measurements in the leg in 10^6 g·cm^{-1}·s^{-2} with $C_\nu = 5000$ cm^2/s.

	between MP1 and MP2	between MP2 and MP3	between MP1 and MP3
□	1.29	1.21	1.24
△	1.33	1.33	1.33
◯	1.53	1.53	1.53

(a) $C_\nu = 500$ cm^2/s (b) $C_\nu = 5000$ cm^2/s

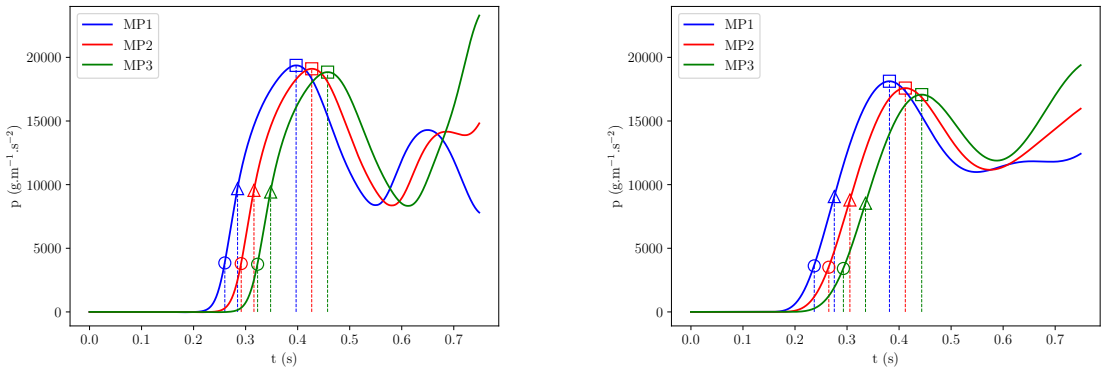

FIGURE 5.14 – Pressure wave in the leg (tube 9) as a function of time from which we measured the wave velocity. (—) is the pressure wave at the measurement point 1 (MP1), (—) is the pressure wave at the measurement point 2 (MP2), and (—) is the pressure wave at the measurement point 3 (MP3). (□), (△), and (◯) correspond respectively to first, second and third measurement method. (a) corresponds to a low viscoelastic coefficient $C_\nu = 500$ cm^2/s, and (b) correspond to a high viscoelastic coefficient $C_\nu = 5000$ cm^2/s.

Discussion

In this section, we showed the comparison between experimental measurements and numerical predictions of the 1D model of the pressure in a 9-artery network. We first noticed that the expected value (*i.e.* the supplier's value) of Young's modulus did not allow fitting the experimental pressure waves. We therefore carried an experiment to measure elasticity but showed that this technique was inappropriate.

Although we could not properly identify a value of Young's modulus, the 1D model gave a good prediction of the pressure wave in the full and clamped network. Indeed, the time delays and amplitudes of the waves were not accurately reproduced but the general morphology and reflections of the model predictions were very similar to the experimental data. The correlation coefficients between the experimental and numerical pressure waves were satisfying ($R^2 > 0.85$).

Regarding the elasticity measurements, we note that the five experimental measurements in the arm were systematically underestimating the expected value of Young's modulus whereas the opposite happened in the leg, *i.e.* Young's modulus was overestimated in the leg measurement compared to its expected value. The numerical method showed the oppo-

site trend: overestimating in the arm measurement, underestimating in the leg measurement. Both experimentally and numerically, we obtained a difference between the supplier value and the estimated value of less than 20% (between 8 and 17%). The exact value of Young's modulus could only be verified with tensile tests on the tubes.

The tubes were fabricated with the same material and a controlled method. It means that the differences between the tubes' elasticities cannot come from the fabrication. The assembly of the tubes to form the network was however not a controlled specific method as it consisted of gluing the tubes with one another. The assembly process does not ensure the reproducibility of the process which is a very important factor in experimental work.

Overall, these arguments highlight three main conclusions. First, the hypotheses of the elasticity measurement technique were not appropriate and thus the technique failed to identify a single value of Young's modulus. Indeed it assumed that the material had a purely elastic behavior but we showed that the viscoelasticity was a necessary component to account for the attenuation of the pressure waves in the network. Second, the fabrication of the tubes was not the cause of the differences in Young's modulus but the assembly of the tubes could create undesirable reflections influencing the pressure wave propagation. Finally, the 1D model reproduced well the morphology and reflections of the pressure wave, the correlation coefficient values were satisfying.

5.3.4 The stenosis experiment

The second experiment to test the numerical models consists of studying the flow in a stenosis, *i.e.* a constriction in the tube. We fabricate a very long tube with a mild narrowing in the middle of the tube. We measure the pressure far from the stenosis and the velocity at three locations around it with a PIV set-up. We compare these experimental data with the numerical results of the 1D and the Multi-Ring models.

Experimental set-up

We fabricate a very long tube of about 500 cm by assembling tubes of 20 cm, following the process described in Section 5.6. The wavelength of the pulse wave is approximately 200 cm/s and thus a long tube prevents reflections from perturbing the incident flow in the stenosis. The stenosis, of length $L_{st} = 4$ cm and of constricted diameter $D_{st} = 0.4$ cm is placed approximately in the middle of the tube as represented in Figure 5.15. The pressure sensor is located 27 cm from the beginning of the tube.

We carry PIV measurements to obtain the velocity at the entry, at the neck, and at the exit of the stenosis. PIV is a flow visualization process that consists of seeding the fluid with particle tracers which are assumed to follow the flow dynamics without perturbing it. We choose nylon particles of 50 μm of diameter and density $\rho = 1.03$ gram/cm^3. The particles are illuminated by a laser sheet of wavelength 532 nm and output 20 mW. The flow is filmed with a high-speed camera at a frequency of 2000 FPS (Figure 5.15).

Results

In Figures 5.16, we show the center-line velocity as a function of time at the entry corresponding to $x = 253$ cm (Figure 5.16a), at the neck $x = 255$ cm (Figure 5.16b), and at the exit (Figure 5.16c) of the stenosis $x = 257$ cm. The first peak in Figures 5.16 represent

the incident wave, imposed by the input pump. The second peak corresponds to the reflected wave at the end of the tube.

We observe in Figure 5.16a that the 1D model and the Multi-Ring model reproduce accurately the first two peaks of the velocity. The third peak is attenuated in the experimental velocity compared to the Multi-Ring and 1D models. In Figures 5.16b and 5.16c, the second velocity peak has a lower amplitude in the experimental data than in the numerical simulations. In Figure 5.16c, the third peak has the same magnitude and shape in both numerical and experimental data.

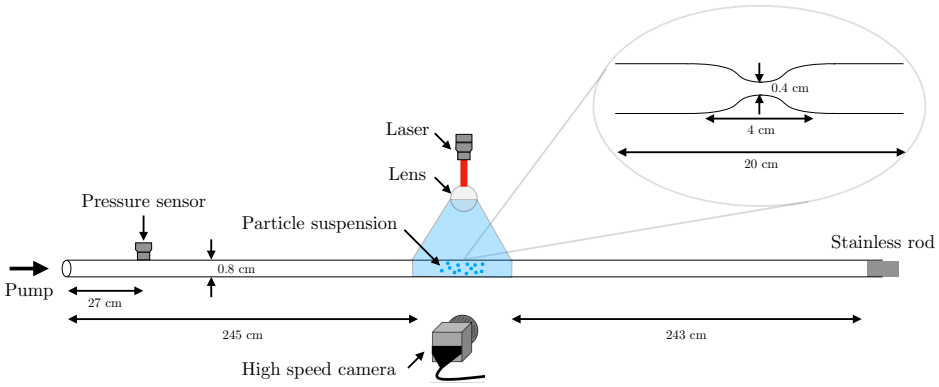

FIGURE 5.15 – Experimental set-up constituted of the artificial artery with the arterial stenosis model, the input flow pump, the pressure sensor and the PIV set-up.

The difference between the measured and simulated data is due to the asymmetry of the measured velocity profile, as can be seen in Figures 5.17. More detail about the velocity profiles measured with PIV and the comparison with the Multi-Ring model can be found in Appendix B.

(a) $x = 253$ cm (b) $x = 255$ cm (c) $x = 257$ cm

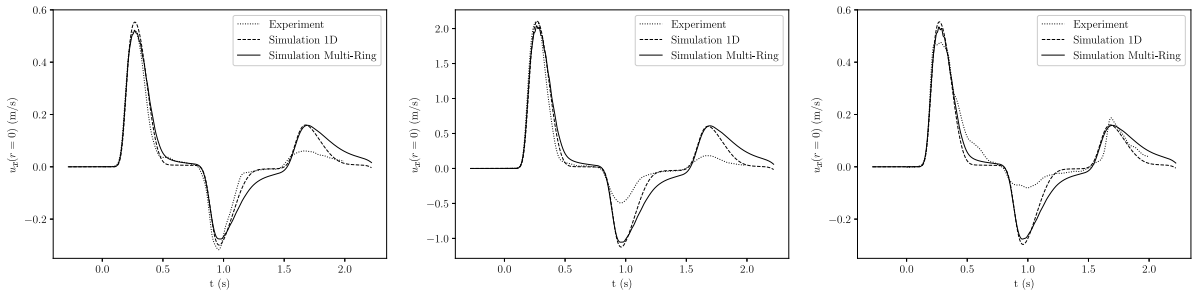

FIGURE 5.16 – Center velocity as a function of time et (a) the entry, (b) the neck, (c) the exit of the stenosis for the experimental PIV measurement (·····), the 1D model (---) and the Multi-Ring (——) model.

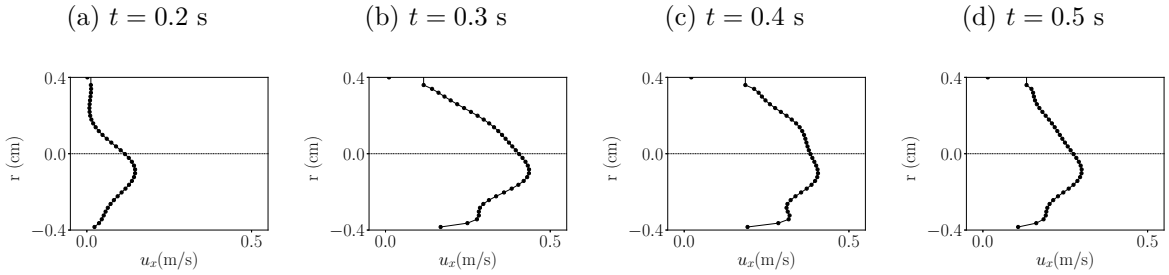

FIGURE 5.17 – Velocity profiles measured with PIV at four different times at the exit of the stenosis $x = 257$ cm.

Discussion

Because the peaks are perfectly synchronized and attenuated compared to the measurement at the entry of the stenosis, we can confirm that the mechanical properties, Young's modulus E and the viscoelastic coefficient C_ν, have the correct values.

The change in water volume depending on the location where it is measured suggests that there may be leaks in the experimental system. However, we obtain a very satisfying agreement between the models and the PIV center-line velocity at the entry of the stenosis which allows validating the models in this experimental case.

Note that the PIV set-up allows assessing the velocity profile at the entry, the neck, and the exit of the stenosis that we show in Appendix B.

5.4 Conclusion

In Section 5.2, we tested the model hypotheses of the steady RNSP and the Multi-Ring models against two analytic solutions, one in steady flow with a rigid wall and one in unsteady flow with an elastic wall. We obtained for both cases a very satisfying agreement between the analytic solutions, the 2D axisymmetric Navier-Stokes solution taken as a target, and the reduced numerical models.

In Section 5.3, we proposed two experiments to test the 1D model and the Multi-Ring model. First, we compared experimental pressure measurements in a network of artificial arteries to the numerical prediction of the 1D model. We showed that the 1D model reproduced the shape of the measured pressure wave but not the exact amplitudes and time delays of the wave reflections. Therefore, we tried estimating experimentally the elastic wall properties by measuring the wave velocity. The wall properties were incorrectly estimated and there was a difference between the supplier's value and the estimated value of 20% or less.

The second experiment consisted of measuring the flow velocity with a PIV set-up and comparing the center-line velocity with the 1D and Multi-Ring models. We obtained a qualitatively good agreement between the measurements and the numerical predictions in terms of magnitude and morphology. This second result highlights the fact that the value of the mechanical properties (viscoelastic coefficient and Young's modulus) were accurate. Nonethe-

less, we found that there was a loss of fluid in the experimental set up which explains why the quantitative agreement between the numerical and experimental models was not so high.

Regarding the two experiments, we can conclude that Young's modulus of the tube might be the expected value of 150 kPa, which could be only be confirmed by tensile tests of each tube. Indeed, it is probably the uncontrolled assembly process that perturbs the entire wave propagation in the network and affects Young's modulus estimation which could explain the lack of agreement in the clamping experiment.

Overall, the comparison with analytic solutions and with two experiments in multiple different conditions suggest that the hypotheses and the numerical resolution of the steady RNSP, the Multi-Ring, and the 1D model are valid.

This first part dealt with the theoretical and modeling aspects of the thesis. We derived two state laws from the linear approximation to characterize the simplified behavior of the arterial wall. We detailed the hypotheses on the flow symmetries, the rheological properties of blood and the arterial wall, and the geometry of the arteries. From these assumptions, we derived several reduced-order models. Then, we improved the description of the arterial wall by rigorously deriving three polynomial hyperelastic model of the arterial wall. Next, we introduced the resolution methods as well as the optimization strategies to estimate the parameters of the models. Finally, we tested the hypotheses of these reduced-order models against analytic solution and experimental data. This part focused on the theoretical and methodological aspects necessary to the second part in which we use all these models and methods to study different cardiovascular pathologies.

Part II

Biomedical applications

Stenosis, defined by a reduction of the lumen of the arteries, is a frequent anomaly in the cardiovascular system and can occur in many different situations. This pathology can appear in different locations of the network: in the aorta for instance, as in Aortic Coarctation, a congenital disease found in children. In this case, the measurement of pressure is essential to determine the treatment strategy. The creation of an Arterio-Venous Fistula (AVF), a necessary procedure in case of kidney insufficiency, can also lead to arterial or venous stenoses. In all cases, stenoses have significant consequences on the flow distribution. When too severe, stenoses can require vascular repair surgeries, for instance in the case of peripheral artery disease. These surgeries usually involve aortic cross-clamping, a procedure performed in over a quarter of million patients yearly, hence the necessity to understand its impact on the vascular mechanics. The reduced modeling approach is also relevant in a variety of other medical scenarios for instance pulmonary hypertension that requires a classification regarding parameters that cannot be directly measured in clinical configurations. All these medical conditions require quick decisions and thus complex modeling cannot provide the relevant information in real-time. The use of reduced-models is therefore considered as a good alternative to bring insights on the underlying mechanisms involved in these pathologies.

6 Pressure drop in stenoses

Stenosis, defined by a partial or full obstruction of the arteries, is a frequent anomaly in the cardiovascular system. The pressure drop across a stenosis indicates the severity of the pathology, however there is currently no non-invasive method to obtain this pressure drop. We therefore resort to reduced-order models to compute the trans-stenotic pressure drop in idealized geometries. In particular, we use he steady RNSP model, the Multi-Ring model, the 1D model, and an algebraic 0D model. To validate these models in this clinical scenario, we obtain invasive trans-stenotic pressure drop and use 4D flow MRI to extract the anatomy and flow velocity during routine medical care with data from Necker Hospital. We compare these models against the invasive measurements and study the influence of the geometry, wall elasticity and flow parameters.

Keywords: reduced-order models, pressure drop, arterial stenoses.

The text in this chapter is greatly inspired by the following published articles

- J. Ventre, F. Raimondi, N. Boddaert, J.M. Fullana, P.Y. Lagrée. Reduced-Order Models for Blood Pressure Drop Across Arterial Stenoses. *Computer Methods, Imaging and Visualization in Biomechanics and Biomedical Engineering. CMBBE 2019. Lecture Notes in Computational Vision and Biomechanics*, vol 36, Springer, Cham, 2020.
- J. Ventre, F. Raimondi, N. Boddaert, J.-M. Fullana, P.-Y. Lagrée. Reduced-order models of blood flow: application to arterial stenoses. *Book Chapter*. publication in 2020

Contents

6.1 Introduction

Aortic CoArctation (CoA) is a congenital heart disease that appears in young children and that accounts for 5 to 8% of all congenital heart diseases [148]. CoA is defined as a partial narrowing of an arterial segment called stenosis and is frequently located either in the area where the ductus arteriosus inserts or in the ascending aorta.

In clinical studies, measurements of the blood pressure drop across a stenosis give significant indications regarding the severity of the pathology. For medical decision making, the patient needs to undergo invasive heart catheterization, as recommended by the American College of Cardiology [149], with its risks and side effects. Clinical guidelines recommend an intervention if the systolic trans-stenotic pressure gradient exceeds 20 mmHg, measured by catheterization as it is the clinical goal standard despite its invasiveness.

In contrast, the European Society of Cardiology advocates the use of alternative non-invasive methods based on imaging techniques to estimate the trans-stenotic pressure drop. In particular, they recommend Doppler echocardiography however this method tends to systematically overestimate the pressure drop. The method is based on the simplified Bernoulli equation $\Delta p = 4V_{max}^2$ [1] [150] which is highly unrealistic in this medical scenario and leaves out many parameters such as the anatomy of the stenosis. Various modifications to the Doppler calculations have attempted to improve its accuracy. Young and Tsai [151, 152] were the first to enrich the Bernoulli principle for arterial constrictions which was then followed by many comparisons with *in vitro* and *in vivo* models [153, 154]. Other studies added for instance the influence of pre-coarctation velocity, the distal diastolic continuation of flow, and the effect of pressure recovery [155, 156]. Doppler remains highly operator-dependent and small errors on the maximal velocity lead to large errors on the trans-stenotic pressure drop as it is a function of the quadratic velocity, which makes the use of this technique unusable for medical diagnosis.

More recently, 4D Magnetic Resonance Imaging (MRI) [157, 158] was proposed as a non-invasive image-based alternative to catheterization and Doppler. It provides anatomic information of the aorta as well as a three-dimensional (3D) time-resolved blood flow velocity mapping. An increasing number of studies have assessed the reliability of 4D flow MRI [159, 160]. The comparison with invasive measurements of the trans-stenotic pressure drop has shown an overall good agreement [161–164]. Although MRI is not operator-dependent, 4D flow measurements present errors particularly due to the low spatial and temporal resolutions (around 5 voxels per diameter). Moreover, its application to clinical routine remains challenging as the current models behind the 4D MRI-based estimation of the trans-stenotic pressure drop requires high computing resources.

Reduced modeling is therefore a relevant option for computing blood flow in stenosed vessels, and deducing pressure data. In this chapter, we propose to use the reduced-order models presented in Chapter 2 to evaluate the trans-stenotic pressure drop in large arteries. To validate the non-invasive trans-stenotic pressure drop computed with the reduced-order

1. this expression is empirical and indeed not homogeneous but is frequently used in clinical studies.

models, we use invasive catheterization data and 4D flow MRI. The objective is to make combined patient-specific / idealized computations. It means that we model the artery as an axisymmetric tube with a degree of constriction, a length of stenosis, and an input velocity extracted from patient-specific data.

The chapter is organized as follows: in Section 6.2, we introduce the data acquisition through the catheterization and 4D flow MRI measurements, the patient population, and a sample size estimation to evaluate the number of necessary patients in the study to validate the models. Then, in Section 6.3, we briefly review the literature on model-based non-invasive measurements of the trans-stenotic pressure drop and recall the models we use in this study. In Section 6.4, we analyze the models in steady conditions by computing the flow in an idealized stenosis to highlight the relevant models, then compare the trans-stenotic pressure drop with the invasive measurements. In Section 6.5, we carry a more theoretical analysis of the trans-stenotic pressure drop by comparing the models in unsteady conditions.

6.2 Data acquisition

In this section, we detail how the catheter measurements and 4D flow MRI are performed, present the patient population, and describe the sample size estimation process.

6.2.1 Measurements

Invasive arterial catheterization is performed at Necker Hospital using calibrated fluid-filled catheters. We measure the peak-to-peak gradient across the stenosis, *i.e.* before and after the stenosis, which is the current clinical reference standard for assessing CoA [149].

4D flow MRI [157] with the 1.5-T system (Signa CV/i; GE Healthcare, Milwaukee, WI, USA, Necker Hospital in Paris) or angiography if the method is available provides the geometric properties of the stenosis and the velocity mapping of the vessel. For one patient the settings are as follows, we obtain 20 time frames over the cardiac cycle, which led to a temporal resolution of 49 ms/frame. The total scan time is 14 min. We set the maximum velocity magnitude to 333 cm/s. The voxel measures $1.96 \times 2.75 \times 1.30$ mm^3.

After the MRI acquisition, the images are uploaded to the software Arterys (from which we extracted Figures 6.1). From the software, we measure the upstream diameter, the minimal diameter, and the length of the constriction. The software also provides the velocity upstream of the stenosis. In Figure 6.1, we show images from the 4D flow MRI sequence at 3 different times. Each figure represents the flow velocity mapping in different orientations.

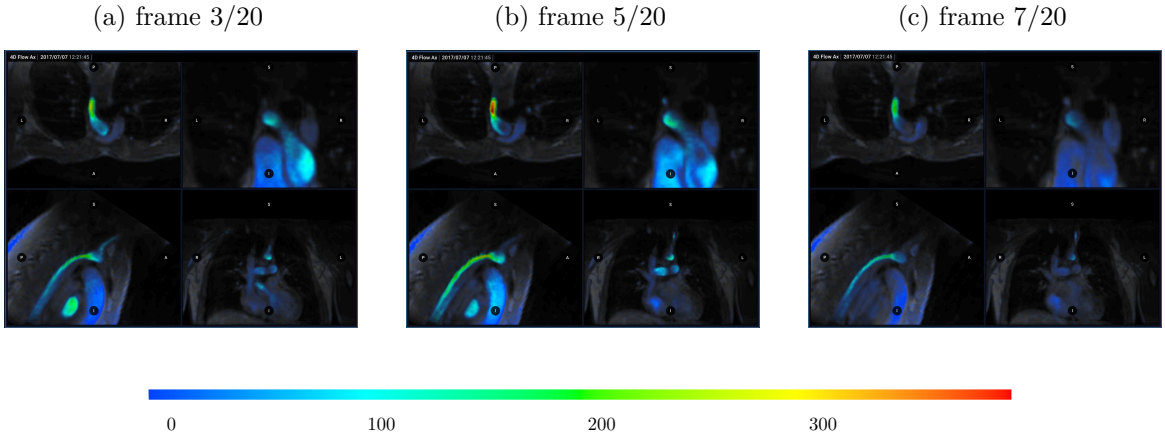

FIGURE 6.1 – Example of a few images of the 4D Flow MRI sequence extracted from the software Arterys for one patient with a stenosis in the ascending aorta. (a) corresponds to the frame 3/20, (b) to the frame 5/20, and (c) to the frame 7/20. The color map indicates the magnitude of the velocity in cm/s.

6.2.2 Patient population

This is a retrospective analysis in which we include patients who underwent both cardiac catheterization and a 4D Flow MRI study. We exclude patients who have (a) a stent that prevents visualizing the geometry of the stenosis unless 3D anatomy can be assessed with a contrast-enhanced CMR angiography, (b) a stenosis at the root of an artery junction (for instance at the junction of the left and right pulmonary arteries).

In the following, we carry a sample size estimation to evaluate the number of patients required in the study to validate the approach.

6.2.3 Sample size estimation

We describe how to choose the sample size, *i.e.* the number of patients required in the study, to validate the models by estimating the 95% Limits of Agreement (LoA). The method we present consists of assessing the agreement between two methods of clinical measurements and is described in [165] in which the authors give a formula for the Confidence Interval (CI) interval for the 95% LoA. The two methods we compare here are the numerical, referred as method A (Section 6.3), and the invasive method, method B (Section 6.2.1), to measure the pressure drop across a vascular stenosis.

To assess the agreement between methods A and B, we define δ the mean difference between the measurements of the two methods A and B as

$$\delta = |\mu(A) - \mu(B)|, \tag{6.1}$$

where $\mu(A)$, respectively $\mu(B)$ is the mean of A, respectively B. The mean difference δ corresponds to the blue solid line in Figure 6.2. The 95% LoA is $\delta \pm 2\sigma$ and corresponds to the red and green solid lines in Figure 6.2, where σ is the Standard Deviation (SD) of the

difference between the measurements of the two methods. The standard error of the mean difference between the measurements of the two methods $sem(\delta)$ is defined as

$$sem(\delta) = \sqrt{\frac{\sigma^2}{N}}, \tag{6.2}$$

which corresponds to the blue dashed lines in Figure 6.2, with N the sample size. Similarly, the standard error of the 95% LoA $sem(\delta \pm 2\sigma)$ is

$$sem(\delta \pm 2\sigma) = \sqrt{\frac{3\sigma^2}{N}}, \tag{6.3}$$

and corresponds to the red and green dotted lines in Figure 6.2.

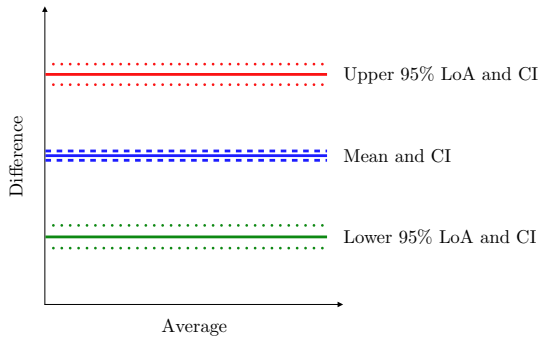

FIGURE 6.2 – Bland Altman plot to assess the agreement between two methods. (——) corresponds to the mean difference between the measurements of the two methods, (- - -) corresponds to the standard error of the mean difference, (——) and (——) correspond respectively to the upper and lower 95% LoA, (·····) and (·····) correspond respectively to the standard error of the the upper and lower 95% LoA.

The classical approach to calculate the sample size consists of using a study from the literature that compares similar methods to assess similar quantities. Therefore, we use [153] that compares a numerical model and invasive measurements of the pressure drop across induced vascular stenoses in dogs. We check with a Shapiro-Wilk normality test that the data follows a normal distribution. We calculate δ and σ from [153] with the classical values $\alpha = 0.05$ and $\beta = 0.2$ [2] and obtain the results reported in Table 6.1.

By inverting Equation (6.2), we can calculate N the number of necessary patients in the study depending on $sem(\delta)$ the standard error of the mean difference between the two methods, reported in Table 6.2. Therefore, if we are accepting a standard error of the mean difference between the two methods of 2 mmHg, we only require three patients to validate our numerical models. It will give us a standard error of the 95% LoA of 3.464 mmHg. We choose this value of the standard error of the mean difference between the two methods as the typical error on the invasive measurements is of the same order of magnitude. Note that a larger

2. α corresponds to the acceptable probability for rejecting the null hypothesis while it is true. β is the opposite; the probability of of accepting the null hypothesis when it's false.

TABLE 6.1 – Calculations from [153]. δ: mean difference between the measurements of the two methods, σ: SD of the difference between the measurements of the two methods, $\delta \pm 2\sigma$: 95% LoA.

δ	σ	$\delta + 2\sigma$	$\delta - 2\sigma$
1.331 mmHg	2.929 mmHg	4.26 mmHg	-1.598 mmHg

TABLE 6.2 – Estimation of the sample size depending on standard error of the mean difference between the measurements of the two methods that we are willing to accept. $sem(\delta)$: the standard error of the mean difference between the measurements of the two methods, N: sample size, $sem(\delta \pm 2\sigma)$: the standard error of the 95% LoA.

$sem(\delta)$	0.5 mmHg	1 mmHg	2 mmHg
N	35	9	3
$sem(\delta \pm 2\sigma)$	0.866 mmHg	1.732 mmHg	3.464 mmHg

sample size (for instance $N = 9$) would lead to a validation of the models with more accuracy.

In the following, we present the numerical models, introduced in Chapter 2, that we compare with the invasive measurements to develop a non-invasive method to measure the trans-stenotic pressure drop.

6.3 Blood flow modeling

There exists a variety of models, experimental [151] and numerical [48], that investigate the flow in constrictions for medical [166] or theoretical purposes [41,44]. Some studies explore the mechanics involved in the development and growth of stenoses. For instance, the Wall Shear Stress (WSS) [167] is known to be affected in aneurysm rupture, development of atherosclerosis, and other pathologies. The influence of pulsatility, turbulence [35] or deformability [27] have also been greatly investigated.

Other studies are more interested in patient-specific computations of the pressure drop across stenoses. Indeed, the improvement of the high-resolution medical imaging field has allowed image-based Computational Fluid Dynamics (CFD) to develop [168]. Extracting the anatomy enables to simulate velocity and pressure fields in patient-specific geometries as in [47, 169]. The 3D models to compute the trans-stenotic pressure drop have been intensively studied in the literature as they enable the highest precision, they however require high computational resources. As our main goal is to provide a time-efficient alternative to catheterization for the assessment of the trans-stenotic pressure drop, we discard the 3D Fluid-Structure Interaction (FSI) models.

Since the 3D approach is inappropriate for medical diagnosis, many investigators have identified the relevant parameters involved in the trans-stenotic pressure drop to reduce the 3D computation to an algebraic formula [47, 48, 166]. These algebraic models are generalizations of Bernoulli's principle, or a balance of mechanical energy, and were each derived in

specific scenarios [152, 154, 170–172]. Similarly, the one-dimensional (1D) model is used in combination with an algebraic model [170, 171] or other approaches [173–175] to account for the trans-stenotic pressure drop.

The most used algebraic model is proposed by Young and Tsai in [152] for the pressure drop assessment in a vascular stenosis

$$\Delta P = \frac{K_v \mu}{D_0} U(t) + K_u \rho L_{st} \frac{\mathrm{d}U(t)}{\mathrm{d}t} + \frac{K_t}{2} \left(\left(\frac{A_0}{A_{st}} \right)^2 - 1 \right) \rho |U(t)| U(t), \tag{6.4}$$

where ΔP is the pressure drop across the length of the stenosis L_{st}, D_0 the diameter, A_0 the reference cross-section, A_{st} the cross-section at the throat of the stenosis, K_v, K_u and K_t are empirical coefficients. The velocity $U(t)$ is the instantaneous input velocity and $|\cdot|$ stands for the absolute value.

The first term captures the Poiseuille viscous loss depending on the coefficient K_v. The second term represents the inertial effect of blood flow in a constriction with an inertial coefficient K_u. The third term accounts for the non-linear effects depending on the coefficient K_t. In the literature [152], the typical values of these coefficients are

$$\begin{cases} K_v = 32 \dfrac{L_a}{D_0} \left(\dfrac{A_0}{A_{st}} \right)^2, & \text{(6.5a)} \\ K_u = 1, & \text{(6.5b)} \\ K_t = 1.52, & \text{(6.5c)} \end{cases}$$

with $L_a = 0.83 L_{st} + 1.64 D_{st}$ a correction of the stenosis length L_{st}, with D_{st} the diameter of the stenosis [154].

Note that the non-linear term $((A_0/A_{st})^2 - 1)$ in [47, 151, 152, 154, 172] and other studies that use this type of algebraic formula is actually $(A_0/A_{st} - 1)^2$. However from the conservation of mass and Bernoulli's equation $p + 1/2 \rho U^2 = cst$, Equation 6.4 seems more straight forward and obvious. We also note that if we discard the second and third terms of the right-hand-side we recover the 0D model of Equation 2.68 that links the pressure drop ΔP to the flow rate $Q = A_0 U(t)$ with

$$R_f = \frac{K_v \mu}{D_0 A_0}. \tag{6.6}$$

In this chapter, we are interested in the following models, introduced in Chapter 2:

- the steady Reduced Navier-Stokes Prandtl (RNSP) model of Equation (2.29),
- the Multi-Ring model of Equation (2.37),
- the 1D model of Equation (2.52),
- the zero-dimensional (0D) or algebraic model of Equation (6.4).

We use these models in steady conditions in Section 6.4 and in unsteady condition in Section 6.5. In each case, we use the appropriate models, for instance, as we solve the RNSP equations (2.29) assuming steadiness, we only use this model for the steady model comparisons of Section 6.4.

For the 1D model, we use the elastic arterial wall model introduced in Section 2.2.2 so we solve the system of Equations (2.52). Indeed, visco-elasticity is an important parameter when studying the pulse wave propagation and reflections. However, we are here interested in a steady quantity that is the trans-stenotic pressure drop so we assume that viscoelasticity does not play a crucial role. We set $\xi = 2$ in Equation (2.50) to compute the friction coefficient of the 1D model.

For the algebraic model of Equation (6.4), we initially use the empirical coefficients (6.5) from [151, 154] in Section 6.4 and then estimate these coefficients in Section 6.5.

In the following, we compute the flow in a rigid wall idealized stenosis in steady conditions to compare the steady RNSP, the Multi-Ring, and the 1D models.

6.4 Comparison of the models: steady case

6.4.1 Geometry of the stenosed artery

The configuration is an idealized stenosed artery of length L, reference radius R_0, stenosis length L_{st} and degree of constriction of the stenosis β, as shown in Figure 6.3. At the inlet of the vessel, we impose a steady input flow, *i.e.* at $x = 0$, $U(t) = U_0$. At the outlet of the vessel, we impose a zero pressure, *i.e.* at $x = L$, $p = 0$. The properties of the configuration are reported in Table 6.3. The shape of the radius of the artery $R(x)$ is

$$R(x) = R_0 \left(1 + \beta \exp\left(-\frac{(x - x_{st})^2}{x_l}\right)\right), \tag{6.7}$$

where x_{st} is the axial position of the throat of the stenosis and x_l is related to the length of the stenosis L_{st}.

The pressure drop ΔP calculated in Section 6.4.3, represented in Figure 6.3 is the difference between the upstream and downstream pressure.

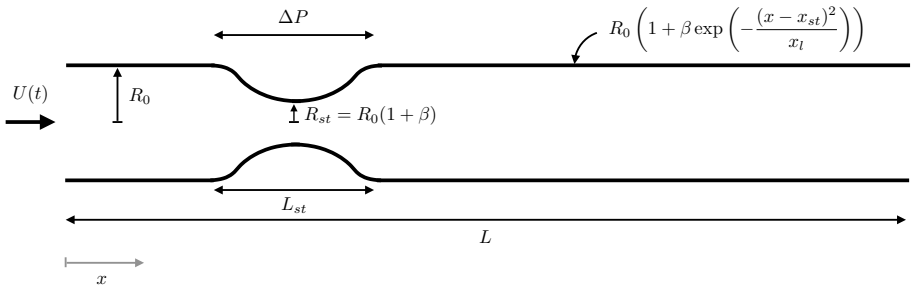

FIGURE 6.3 – Geometry of the idealized rigid stenosed artery of length L, radius R_0, stenosis length L_{st} and stenosis degree β ($\beta < 0$). The shape of the radius of the wall is Equation (6.7), with x_{st} the position of the throat of the stenosis, and x_l related to L_{st}. The pressure drop over the length of the stenosis is ΔP.

TABLE 6.3 – Properties of the idealized rigid stenosed artery. R_0: reference radius in cm, β: degree of constriction of the stenosis, L: artery length in cm, L_{st}: stenosis length in cm, Re_R: Reynolds number based on the radius, U_0: input velocity in cm/s, ρ: fluid density in g/cm^3, μ: dynamic viscosity in g·cm^{-1}·s^{-1}, K: elastic coefficient defined in Equation (2.15) in g·cm^{-2}·s^{-2}.

R_0	β	L	L_{st}	Re_R	U_0	ρ	μ	K
1	-0.4	40	10	100	100	1	$\frac{\rho U_0 R_0}{Re_R}$	10^7

6.4.2 Comparison of the flow field

We compare the steady RNSP, Multi-Ring and 1D models in the rigid stenosed artery against the Poiseuille center pressure (5.3), center velocity (5.1), and WSS (5.6) as shown in Figures 6.4a, 6.4b, and 6.4c respectively.

We observe in Figure 6.4a that the center pressure drop between the beginning and the throat of the stenosis is similar in all models. However, the center pressure downstream of the stenosis is different in the 1D model compared to the steady RNSP and the Multi-Ring. Indeed, the 1D model does not account for the recirculation near the walls and the jet formation in the center of the artery after the stenosis, as can also be seen in Figure 6.4b.

One of the assumptions of the 1D model is the shape of the velocity profile as described in Section 2.3.4. Therefore, the downstream flow is by definition not impacted by the constriction in the 1D model, as opposed to the steady RNSP and Multi-Ring models, that are two-dimensional (2D) models. We observe in Figure 6.4a that the steady RNSP and Multi-Ring models account for the jet and recirculation after the stenosis, which is confirmed by Figure 6.5 in which we show the velocity profiles at different positions along the artery.

Figure 6.4c shows that the WSS computed with the Multi-Ring and steady RNSP models is maximal at the throat of the stenosis, a result that causes a lot of discrepancies in the literature. Indeed, it has been shown that the WSS plays an important role in the development of atherosclerosis [167]. Downstream of the constriction, the WSS becomes negative before going back to the Poiseuille value, which characterizes a backflow near the walls downstream of the stenosis. To compute the friction in the 1D model we assume a Poiseuille profile, *i.e.* $\xi = 2$ in Equation (2.50), so the WSS computed with the 1D model is the Poiseuille WSS (5.6).

We verify the presence of this back-flow by plotting the velocity profile in the stenosis using the Multi-Ring model. The shape of the velocity profile changes when entering the constriction (Figure 6.5d): the magnitude increases and the profile becomes plug-like[3]. The magnitude of the profile is maximal at the throat of the stenosis (Figure 6.5e), *i.e.* at $x = 10$ cm from the entrance. After the throat (Figure 6.5f and 6.5g), we observe the formation of a jet in the center. Far from the stenosis (Figure 6.5h), the velocity profile is no longer affected by the constriction and goes back to the initial entry Poiseuille velocity profile of Figure 6.5a.

3. We recover the plug-like behavior in the PIV measurements in a stenosis carried in Chapter 5, shown in Appendix B (see Figure B.2).

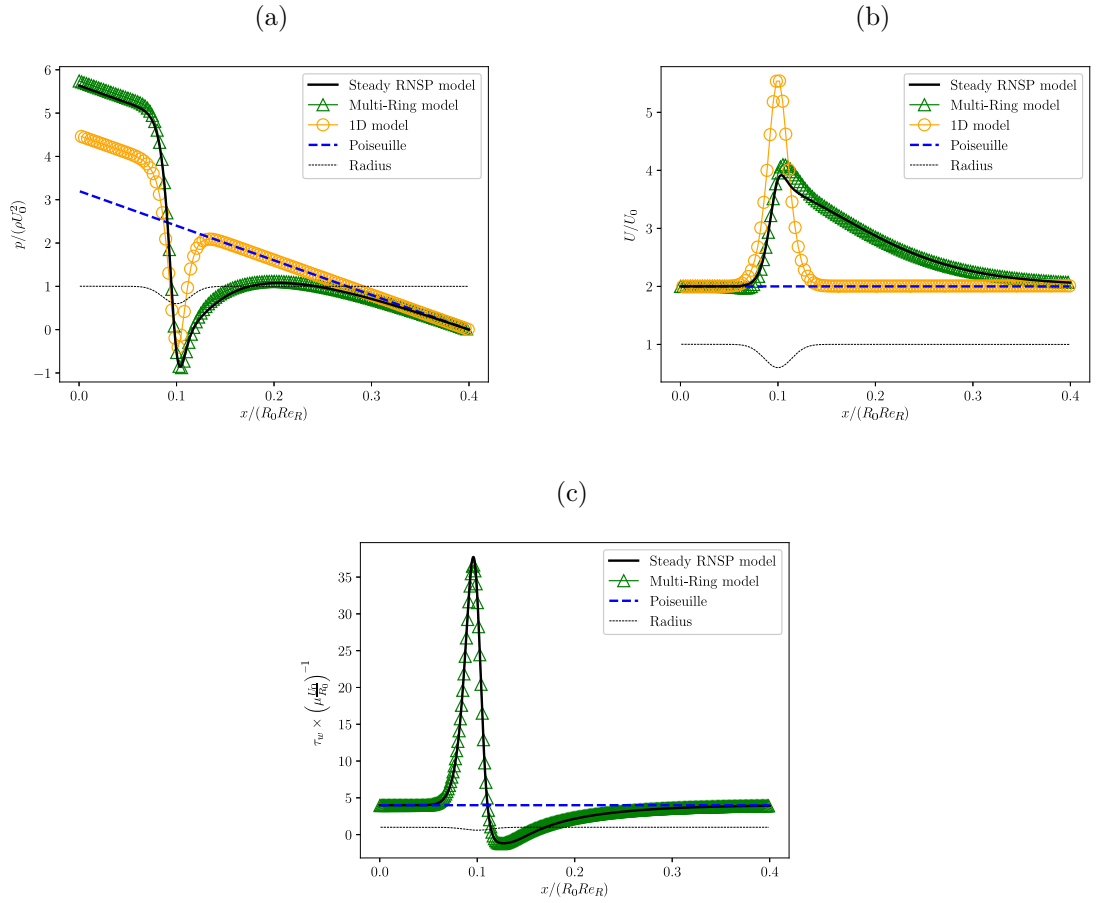

FIGURE 6.4 – Dimensionless (a) center pressure, (b) center velocity, and (c) WSS along the stenosis represented in Figure 6.3 with the properties of Table 6.3. (—) corresponds to the steady RNSP model, (△) to the Multi-Ring model, (◯) to the 1D model and (- - -) to the Poiseuille pressure along a straight tube. (- - -) represents the radius $R(x)$ of the artery.

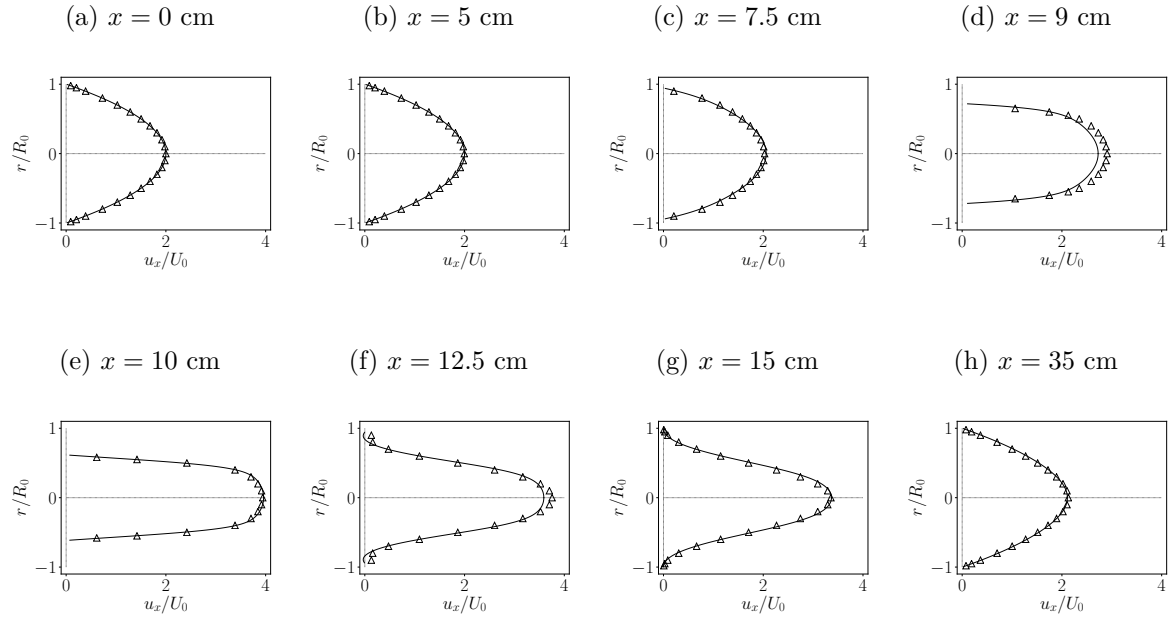

FIGURE 6.5 – Velocity profiles at different locations in the rigid stenosed artery, represented on Figure 6.3 with the properties of Table 6.3, computed with the Multi-Ring model (△) and the steady RNSP model (—).

The models used here allow computing the velocity and pressure fields in the entire domain. The relevant indicator for medical diagnosis is the pressure drop ΔP evaluated across the length of the stenosis [149]. In the following section, we compute the pressure drop in the same idealized stenosis with the algebraic model from [151], the 1D model, the Multi-Ring model, and the steady RNSP model.

6.4.3 Comparison of the pressure drop

We compare in Figure 6.6 the different algebraic formulation to compute the pressure drop across a stenosis: the original formula from Young and Tsai [151], the formula of Equation (6.4), the classical Bernouilli formula, and the empirical formula $\Delta P = 4U^2$, often used in clinical studies. We observe that there is not a strong difference between the original formula from [151] and Equation (6.4). The Bernouilli formula underestimates the pressure drop as it does not account for the Poiseuille pressure loss in a straight rigid tube. Finally, $\Delta P = 4U^2$ does not account for the degree of constriction, which is known to be a significant parameter in the pressure drop across a stenosis.

We compare the four reduced-order models to the invasive data introduced in Section 6.2. The characteristics are reported in Table 6.4: R_0, β, L_{st}, and U_0 come from 4D flow MRI, ΔP comes from catheterization. We also compare the models with *in vivo* pressure drop measurements in animals from [153].

In Figure 6.7, we show the dimensionless upstream to downstream pressure drop computed with our four models as a function of the degree of stenosis β. The comparison between the models and the invasive measurements shows that the steady RNSP and Multi-Ring model

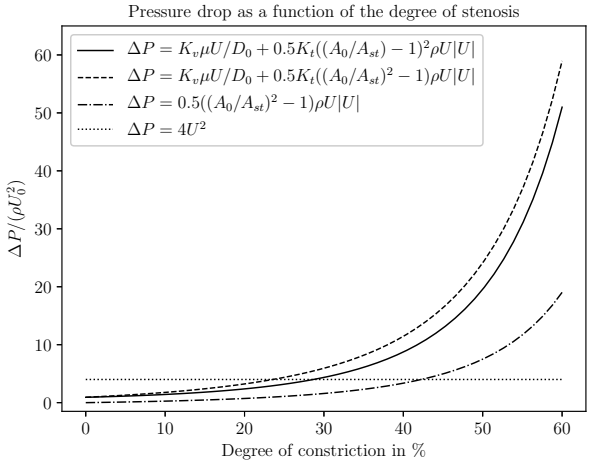

FIGURE 6.6 – Comparison of the different algebraic models for the pressure drop as a function of the degree of constriction expressed in % (*i.e.* -100β, $\beta < 0$). (——) corresponds to the original model from Young and Tsai [151], (- - -) corresponds to Equation (6.4), (-·-·-) corresponds to Bernouilli's formula, and (·····) corresponds to the empirical $4U^2$ formula often used in clinical studies.

TABLE 6.4 – Characteristics of the invasive pressure drop data measured with arterial catheter and 4D flow MRI. R_0: arterial radius in cm, β: degree of constriction of the stenosis, L_{st}: stenosis length in cm, U_0: velocity in cm/s, HR: heart rate in BPM, ΔP: pressure drop between upstream and downstream of the stenosis in mmHg.

n°	R_0	β	L_{st}	U_0	HR	ΔP
IM1	0.55	-0.28	3	115	61	20
IM2	0.55	-0.47	3.65	79	92	30

are the most accurate to predict the pressure drop. The 1D model gives a lower estimation whereas the Multi-Ring model gives an upper estimation. However, the 1D model remains a relevant first approximation for mild stenoses (less than 30%).

Similarly, in Figure 6.7, the comparison with *in vivo* measurements from [153] shows that the steady RNSP and Multi-Ring are the most accurate models to estimate the pressure drop across the stenosis. However, we can also observe that for mild stenosis, the 1D model gives a reasonable agreement with the *in vivo* measurements. Even if the 1D model might underestimate the pressure drop, it is a better starting point than the current algebraic formula with the empirical coefficients of the literature.

In Table 6.5, we compare the invasive pressure drop from catheterization to the numerical predictions of the algebraic, 1D, and Multi-Ring models. First, we can conclude once again that the algebraic formula (6.4) with the coefficients (6.5) does not allow predicting the pressure drop accurately. Second, we observe that the 1D model underestimates the value of the real pressure drop but is already much better than the algebraic model. Finally, the Multi-Ring model is very accurate for mild stenoses (IM1) and overestimates the pressure drop for more severe stenoses (IM2).

TABLE 6.5 – Comparison between the invasive measurement of the pressure drop and the numerical predictions of the algebraic, 1D, and Multi-Rind models. All the pressure drop are expressed in mmHg.

n°	Invasive	Algebraic model	1D model	Multi-Ring model
IM1	20	46	12.5	19.5
IM2	30	115	18.5	40

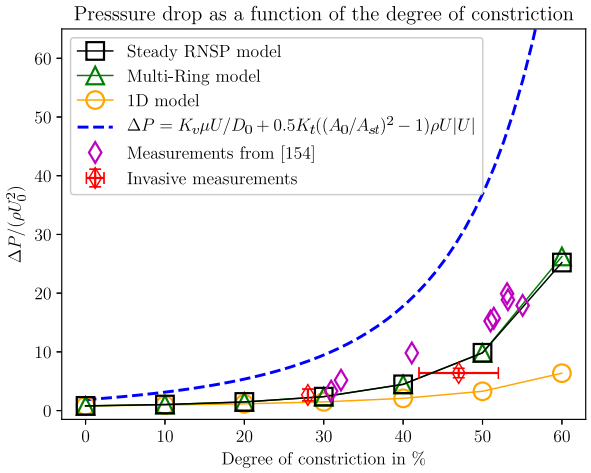

FIGURE 6.7 – Comparison of the dimensionless pressure drop across the stenosis as a function of the degree of constriction expressed in % (*i.e.* -100β, $\beta < 0$) for the algebraic model (6.4) with the coefficients (6.5) from [151] (---), the 1D model (◯), the Multi-Ring model (△), the steady RNSP model (□), *in vivo* measurements from [153] (◊), and arterial catheter invasive measurements (◊) presented in Section 6.2.

To give other order of magnitudes, we compute the trans-stenotic pressure drop in the idealized stenosis of Figure 6.3. We obtain $\Delta P = 16$ mmHg for the 1D model and $\Delta P = 33$ mmHg for the steady RNSP and Multi-Ring models, which seem to be reasonable values within the physiological range. We compared this pressure drop with the algebraic formula (6.4) using the values of the empirical coefficients (6.5) from [151] which gives $\Delta P = 89$ mmHg for the same configuration.

We showed in this section that the algebraic pressure drop computed with the coefficients (6.5) was clearly out of the physical range. Therefore, in the following section, we compare the 1D and Multi-Ring models to an algebraic formula to improve the estimation of the empirical coefficients with a parameter estimation process.

6.5 Comparison of the models: unsteady case

For the sake of simplicity, in Section 6.4, we compared the models using a steady input flow. In this section, we investigate the unsteady effects on the pressure drop across a stenosis using the 1D and the Multi-Ring models, as they are the only two approaches that account for unsteadiness.

We use the same geometry and properties of the stenosed artery as shown in Figure 6.3. We now impose at the inlet of the vessel $x = 0$ an oscillating velocity $U(t) = U_0 \sin(2\pi\omega t)$ with U_0 the amplitude of the input velocity and ω the frequency. At the outlet of the tube, we still impose a zero pressure, *i.e.* at $x = L$, $p = 0$.

6.5.1 Parameter estimation method

To compare the 1D and Multi-Ring models with the algebraic formula (6.4), we need to estimate the empirical coefficients K_v, K_u, and K_t. The objective is to study the dependence of these parameters on the stenosis properties. We therefore define a cost function $\mathcal{J}$ that measures the difference between the pressure drop of the model ΔP_{model}, either the 1D or Multi-Ring model, and the algebraic pressure drop ΔP_{alg} as

$$\mathcal{J}(\mathcal{P}) = \left(\int_0^T \left(\Delta P_{model} - \Delta P_{alg}(\mathcal{P}) \right)^2 \mathrm{d}t \right)^{1/2} \tag{6.8}$$

with $\mathcal{P} = \{K_v, K_u, K_t\}$ the set of parameters to estimate. We minimize the cost function $\mathcal{J}$ with respect to $\mathcal{P}$ using a Basin-Hopping algorithm running a L-BFGS-B descent at each step, described in Section 4.3.2.

6.5.2 Estimation of the coefficients using the 1D and Multi-Ring models

We choose to estimate the empirical coefficients K_v, K_u and K_t as a function of several parameters: the geometrical parameters that are the cross-section ratio A_0/A_{st} and the stenosis length L_{st}, the wall rheology parameter K, defined in Equation (2.15), and the Reynolds number Re_R, defined in Equation (5.4). We represent respectively in Figures 6.8, 6.9, 6.10 the estimated value of the empirical coefficient K_v, K_u, and K_t depending on these four parameters using the 1D and Multi-Ring models. Note that when we estimate one parameter, we fix the others.

In Figure 6.8a, we show the estimated value of the coefficient K_v as a function of the cross-section ratio A_0/A_{st}. We observe that for both the 1D and the Multi-Ring models the coefficient K_v depends on the cross-section ratio in the same amplitude for the low ratios. For higher cross-section ratios the coefficient K_v is higher with the 1D model. It explains why when compared to the invasive measurements (Table 6.5), the 1D and Multi-Ring models give similar results for a low ratio A_0/A_{st}, *i.e.* a small degree of constriction.

We compare our estimation of the coefficient K_v with two *in vivo* measurements from [154] for two configurations that are similar to ours (reported in Table 6.6) in Figure 6.8a. On one hand, the measurement with a low cross-section ratio gives a very good agreement, but on the other hand, the measurement with a higher ratio does not. We have several explanations for the differences. First, the geometry is different as the constriction in [154] is an abrupt reduction of the radius as opposed to ours that is smooth. Second, they are investigating steady flows, which may lead to differences if the unsteady effects are important. Finally, the aspect ratio of L_{st}/D_0 is smaller in their experiments than in our simulations.

In [154], the authors established an empirical expression for K_v (Equation (6.5a)) based on experimental data, which we show in Figure 6.8a. We observe that the expression (6.5a)

TABLE 6.6 – Estimation of the empirical coefficient K_v of Equation (6.4) from [154] for comparison with Figure 6.8a. β: degree of constriction, L_{st}: stenosis length, D_0: reference diameter, K_v: empirical coefficient of Equation (6.4).

	β	L_{st}/D_0	K_v	K_t
point 1	-0.375	2	421	1.65
point 2	-0.5	2	1160	1.72

does not match out estimation of the parameter K_v with none of the models.

In Figure 6.8b, we show that the dependence of K_v on the length of the stenosis L_{st} is linear for both models. The 1D and Multi-Ring estimation gives the same coefficient K_v for low to medium ratios. We also compare with the expression (6.5a) and add for reference the Poiseuille value of K_v in a straight tube that is $32L_{st}/D_0$. The Poiseuille expression underestimates the value of our coefficient, as the pressure drop in a straight tube is much smaller than in a stenosed tube (Figure 6.4a). Overall, the comparison with these two expressions stresses the linear dependence of K_v on the length of the stenosis.

Figure 6.8c shows that the wall elasticity does not influence the value of K_v as the coefficient does not vary significantly with K for both models. We however observe that the optimal values of K_v are very different from one model to the other. In fact, the cost function $\mathcal{J}$ (Equation (6.8)) is really small in both cases. A sensitivity analysis of the dependence of K_v on K would be necessary to show that the cost function does not vary a lot with respect to this parameter. When the elasticity of the wall becomes smaller, there is a slight increase in K_v, but it does not correspond to the value of the wall elasticity of large arteries [66].

Finally, we observe that there is no dependence of K_v on the Reynolds number Re_R as shown in Figure 6.8d for none of the models.

To summarize, we showed that K_v is only a function of the geometric parameters: the cross-section ratio A_0/Ast and the length of the stenosis L_{st}. This conclusion was obtained in [154] and more recently in [166].

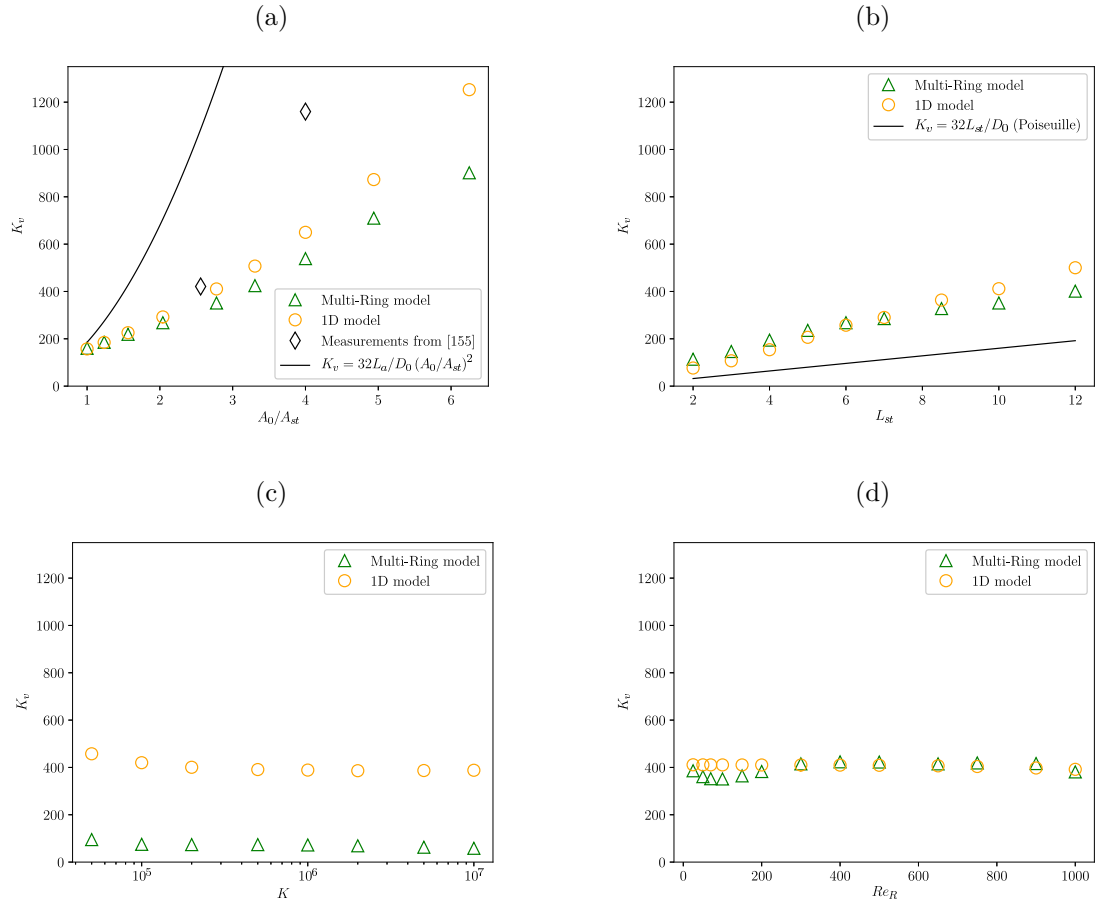

FIGURE 6.8 – Values of the coefficient K_v as a function of (a) the cross-section ratio A_0/A_{st}, (b) the length of the stenosis L_{st}, (c) the elasticity K, and (d) the Reynolds number based on the radius Re_R. The coefficient K_v is estimated from the 1D model (◯) and the Multi-Ring model (△) using the algebraic formula (6.4). We add on (a) *in vivo* measurements (◊) from [153], and the theory of Equation (6.5a) from [154] (—). We add on (b) the Poiseuille value of K_v in a straight tube. L_{st} and K are in CGS units, the other quantities are dimensionless.

Figure 6.9a shows that K_u depends on the cross-section ratio A_0/A_{st} for both the 1D and Multi-Ring models. The tendency is not the same, the estimation with the 1D model is linear, the one with the Multi-Ring model is not.

In Figure 6.9b, there is no obvious linear dependence of the coefficient K_u on the length of the stenosis estimated with the 1D model. We observe the opposite with the Multi-Ring model, K_u decreases with the increase in the length. When the length of the stenosis is really large, we recover the same values. Indeed, the 1D model becomes more accurate for longer stenoses.

Similarly to Figure 6.8c, Figure 6.9c shows that the value of K_u is not significantly affected by a variation in elasticity K. However, unlike Figure 6.8d, Figure 6.9d shows that K_u depends on the Reynolds number Re_R, and for low Reynolds numbers, both models give the same estimate of K_u. The variations in cross-section ratio and Reynolds number are however small compared to the variations in the length of the stenosis.

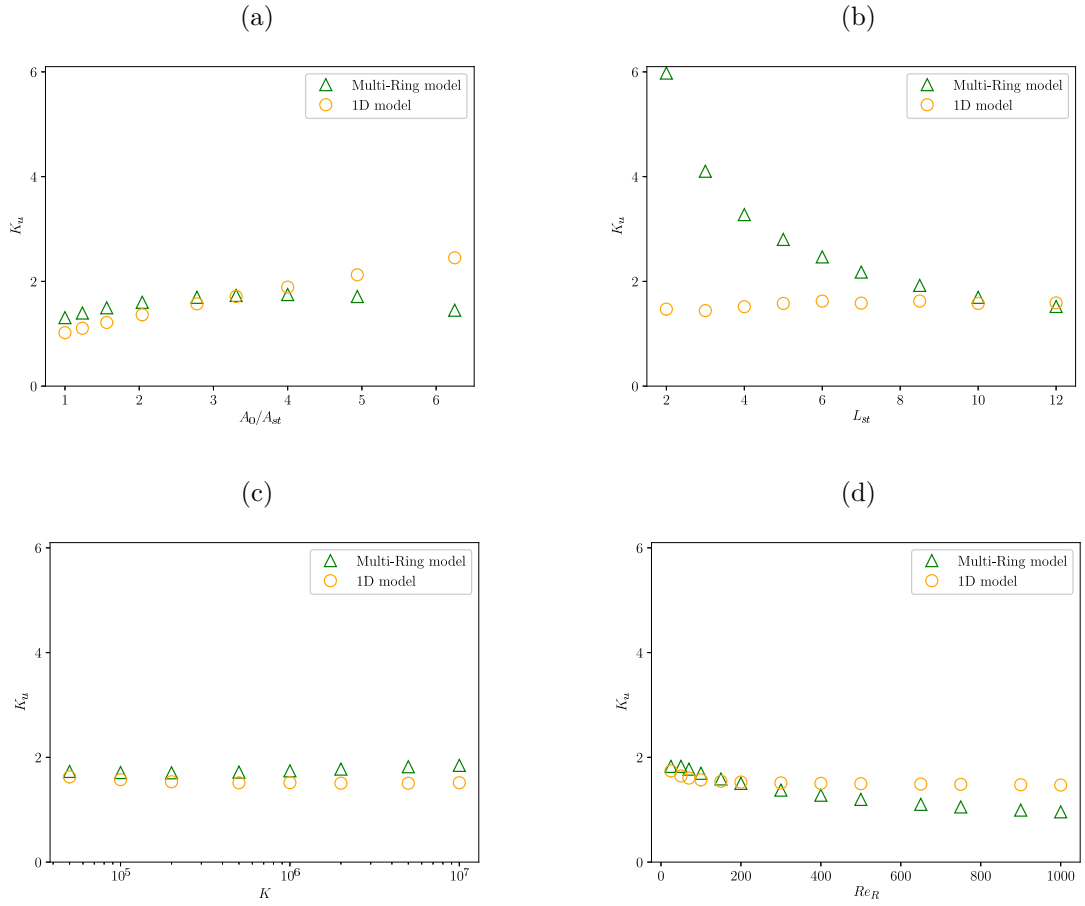

FIGURE 6.9 – Values of the coefficient K_u as a function of (a) the cross-section ratio A_0/A_{st}, (b) the length of the stenosis L_{st}, (c) the elasticity K, and (d) the Reynolds number based on the radius Re_R. The coefficient K_u is estimated from the 1D model (◯) and the Multi-Ring model (△) using the algebraic formula (6.4). L_{st} and K are in CGS units, the other quantities are dimensionless.

The first observation for the third coefficient K_t is that the estimated value of K_t is always close to zero when fitting the 1D model pressure drop but not zero when fitting the Multi-Ring model pressure drop. Indeed, the non-linear effects are accounted with more accuracy in the Multi-Ring model hence $K_t \neq 0$ in Equation (6.4). We show K_t as a function of the four stenosis parameters in Figures 6.10.

In Figure 6.10a, we show the estimated value of the coefficient K_t as a function of the cross-section ratio A_0/A_{st}. We observe that K_t highly depends on the cross-section ratio. We also show the two measurements from [154], reported in Table 6.6. Unlike for the coefficient K_v, these measurements do not match our estimation of K_t for similar reasons as mentioned previously. In Figure 6.10b, we observe that K_t does not vary with the length of the stenosis, in Figure 6.10c, that K_t is almost 0 when varying the elastic coefficient K, and finally in Figure 6.10d, K_t varies for small Reynolds number.

In this section, we estimated the three coefficient of the algebraic formula (6.4) that fit the trans-stenotic pressure drop computed with the 1D and Multi-Ring models. We showed their dependence on the stenosis parameters. In the following section, we present a comparison

between the models and the algebraic formula with the estimated coefficients.

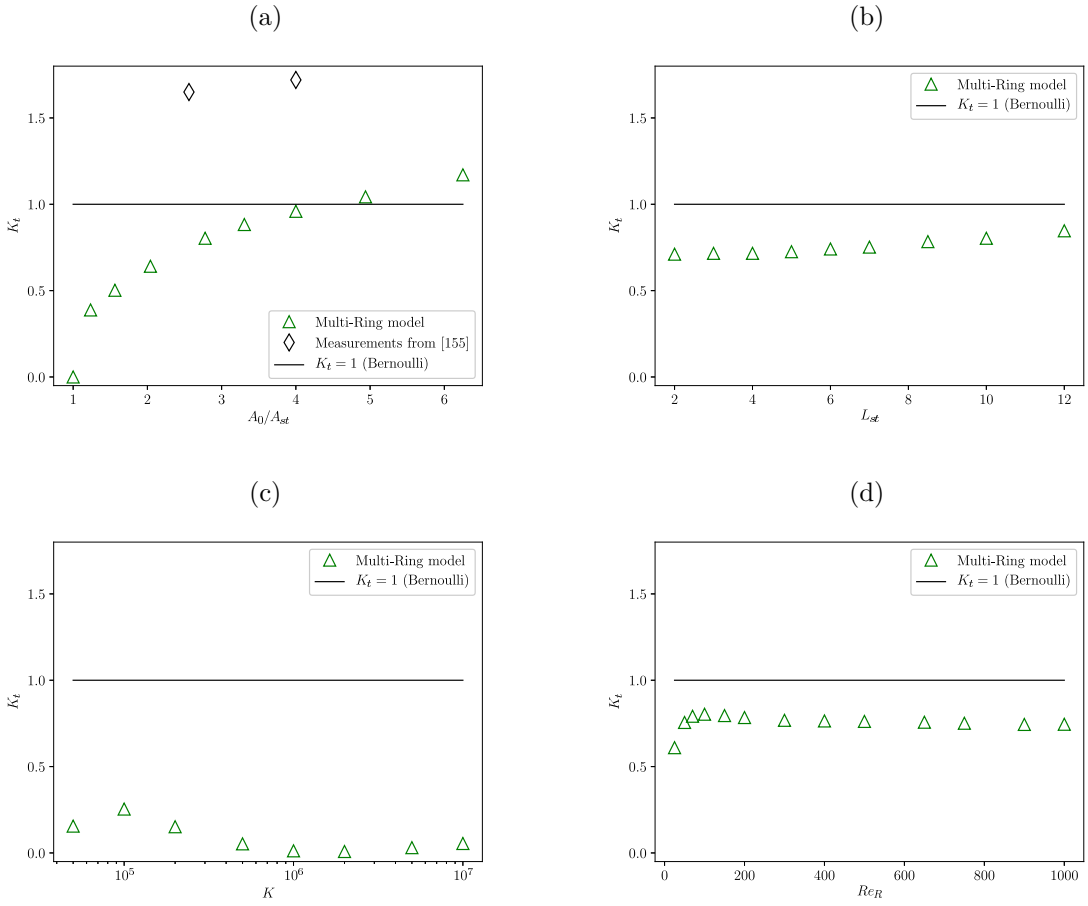

FIGURE 6.10 – Values of the coefficient K_t as a function of (a) the cross-section ratio A_0/A_{st}, (b) the length of the stenosis L_{st}, (c) the elasticity K and (d) the Reynolds number based on the radius Re_R. The coefficient K_t is estimated from the Multi-Ring model (△) using the algebraic formula (6.4). We add the value of K_t in the inviscid fluid hypothesis (Bernoulli). L_{st} and K are in CGS units, the other quantities are dimensionless.

6.5.3 Comparison between the 1D model and the Multi-Ring model

In Figures 6.11, we compare the pressure drop computed with the 1D model (Figure 6.11a) or the Multi-Ring model (Figure 6.11b) and the algebraic pressure drop from Equation (6.4) using the estimated optimal parameters K_v, K_u, and K_t reported in Table 6.7.

By comparing Figure 6.11a and 6.11b, we can see that the amplitude of the maximum pressure drop is higher for the Multi-Ring model than for the 1D, similarly to Figure 6.4a and 6.7. The Multi-Ring model is indeed more accurate as it accounts for the recirculation and the jet formation downstream of the stenosis.

With only two terms in Equation (6.4), we reproduce the shape of the 1D pressure drop between upstream and downstream of the stenosis under unsteady flow. By adding a non-linear term to Equation (6.4), we retrieve the shape of the unsteady pressure drop across the stenosis of the Multi-Ring model, with the same values for the other two coefficients.

TABLE 6.7 – Empirical dimensionless coefficients K_v, K_u, and K_t of the algebraic model 6.4, estimated with the parameter estimation of Section 6.5.1.

	K_v	K_u	K_t
1D model	400	1.5	0
Multi-Ring model	400	1.5	0.7

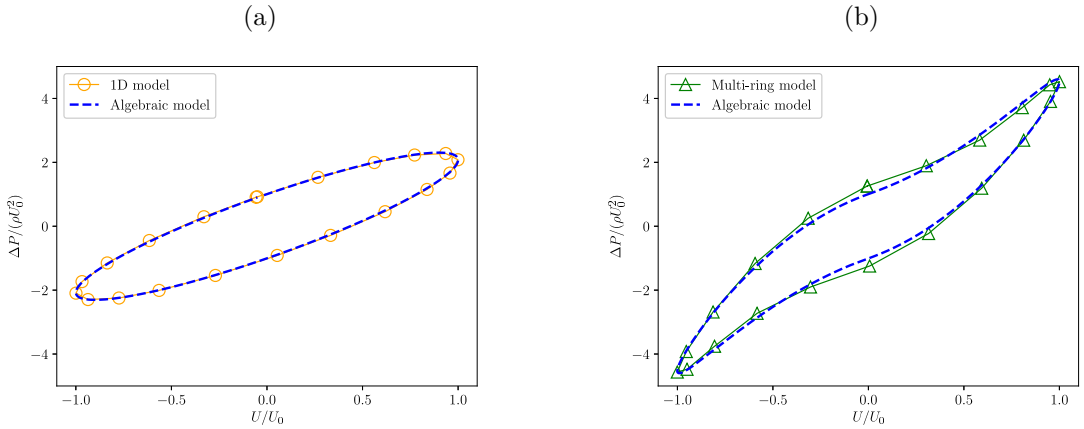

FIGURE 6.11 – Dimensionless pressure drop accross the stenosis as a function of the dimensionless instantaneous velocity. Comparison between the algebraic model (6.4) (---) and (a) the 1D model (◯), (b) the Multi-Ring model (△) for an unsteady input velocity with pulsation $\omega = 1$ s^{-1}. The properties of the stenosed artery are reported in Table 6.3 and the parameters K_v, K_u and K_t of the algebraic model are reported in Table 6.7.

The algebraic model with the three empirical coefficients can reproduce the unsteady pressure drop of our two models. This estimation of the three coefficients provides an immediate estimation of the pressure drop without computing the 1D or the Multi-Ring model for more accuracy.

6.6 Conclusion

In this study, we compared four reduced-order models (algebraic, 1D, Multi-Ring, steady RNSP) to compute the pressure drop across a stenosis. We analyzed the flow field in an idealized stenosis and highlighted that with a steady input flow, the steady RNSP, Multi-Ring, and 1D model behaved similarly in terms of the shape of center pressure between the beginning and the throat stenosis. We showed the limitation of the 1D model to estimate the trans-stenotic pressure drop as the flow is not modified downstream of the stenosis. However, the morphology of the center pressure between the beginning and the throat stenosis was similar in the steady RNSP, the Multi-Ring, and the 1D models.

Then, we used invasive measurements carried in patients at Necker Hospital and *in vivo* measurements from [154] to validate our approach. The data came from catheterization and

4D flow MRI, and allowed carrying a combined idealized/patient-specific method. We showed that the Multi-Ring model reproduced the measurements reasonably well, and the 1D model was accurate for mild stenoses. We concluded that both models provided better estimations of the pressure drop than the current algebraic model, with a reasonable computational cost.

Since the algebraic model (6.4) did not provide an accurate estimation of the trans-stenotic pressure drop with the coefficient 6.5, we estimated the three coefficients of these models based on the 1D and Multi-Ring models with a Basin-Hopping optimization method. We found that the coefficient K_v characterizing the viscous loss only depended on the cross-section ratio and the length of the stenosis. The coefficient K_u characterizing the inertial effects depended on the cross-section ratio, on the length of the stenosis, and also on the Reynolds number. For the last coefficient K_t, we observed that using the 1D model the non-linear term was negligible and that it depended mostly on the cross-section ratio. An important observation is that none of the three empirical coefficients strongly depend on the wall elasticity K. It means that either the wall elasticity does not play a significant role in the center pressure drop across the stenosis, or that the cost function is not sensitive to this parameter.

With the new values of the coefficients of the algebraic model, we obtain an instantaneous estimation of the trans-stenotic pressure drop only based on geometric (the cross-section ratio and length of the stenosis) and flow properties (the Reynolds number) that can be provided by 4D flow MRI.

The main drawback of this study was the number of invasive measurements. Based on a previous similar study, we estimated the number of necessary patients to obtain a good agreement between the invasive pressure drop and the model pressure drop. Three patients would be the minimum to validate the approach. Note that patients who undergo both catheterization and 4D flow MRI in the course of their medical care is quite rare. Therefore, the main perspective of the present study, to make a patient-specific estimation of the pressure drop, is to obtain more invasive pressure measurements with imaging from 4D flow MRI to compare our models to.

The second drawback of this study is that 4D flow MRI does not have a good temporal and spatial resolution. Therefore, the estimation of the geometric parameters is not really precise. Also, the resolution does not allow visualizing the profile of the velocity across the stenosis. This limitation prevents from improving the patient-specific management of the computation.

Finally, we carried a combined idealized/patient-specific approach in which we assumed axisymmetry and a shape for the constriction. To make patient-specific predictions of the pressure drop across a stenosis, we should compute the pressure in real geometries. This would require some high-quality imaging with a segmentation algorithm to determine the radius at each time and position of the artery. However, the reduced-order models that treat the arteries as straight axisymmetric elastic tubes have proven reliable in the literature and are a good starting point, if not better, compared to the current algebraic formulas.

7 Arteriovenous Fistula

The creation of a communication between an artery and a vein, called Arterio-Venous Fistula (AVF), to speed up the blood purification during hemodialysis of patients with renal insufficiency, induces significant rheological and mechanical modifications in the vascular network. In particular, an AVF can lead to the formation of stenosis that further perturbs the flow. Therefore, we investigate the impact of the creation of an AVF with a zero-dimensional (0D) network model and a one-dimensional (1D) model of the vascular system in the arm. We compare the simulated distribution of flow rate in this vascular system with Doppler ultrasound measurements in three configurations: before the creation of the AVF, after the creation of the AVF and after a focal reduction due to a hyper flow rate. We also explore the influence of a stenosis on the distribution of flow in the AVF with the 1D model. We highlight the importance of knowing the capillary resistance as it is a decisive parameter in the models.

Keywords: Arterio-Venous Fistula, 0D network model, resistance, hyper flow rate.

The text in this chapter is greatly inspired by the following submitted article

- J Ventre, S Abou Taam, J M Fullana, P-Y Lagrée. Distribution of flow in an Arteriovenous Fistula using reduced-order models. Submitted in *Journal of Biomechanical Engineering*.

Contents

7.1 Introduction

The kidney is a major organ of the human body whose function is to filter the blood and remove wastes and extra fluid from the human body. In case of insufficiency of this organ, various harmful substances accumulate and cause toxicity which can, in the end, be lethal. Thus it is fundamental to compensate for the malfunction of the kidneys.

Hemodialysis is a blood purification technique that relies on a filtration process. A machine collects the blood and restores it after achieving extra-renal purification (*i.e.* of waste products such as creatinine and urea).. It is a common practice in the treatment of renal failure but requires a fast and safe vascular access to ensure a sufficient flow rate during the filtration [176]. Hemodialysis relies on an essential technique, the Arterio-Venous Fistula (AVF) [177] that can be either native (use of an artery and vein of the patient) or prosthetic (unavailability of a vein leading to the use of a vascular prosthesis) [178]. An AVF is a junction between a main artery and a superficial vein in the arm.

The AVF creation is prone to develop in the near future as suggested by the last annual report of the Réseau Épidémiologique et Information en Néphrologie [179]. Indeed, since 2011, there was a significant increase in the number of elderlies ($>$ 85 y.o.), overweighted people, diabetics, or people with associated cardiovascular comorbidity. Moreover, there is a constant increase of about 8% of patients under hemodialysis [180]. This evolution is a major challenge for physicians in charge of the hemodialysis process because the comorbidities greatly affect the prognosis as well as the lifespan of the AVF. Finally, in Europe, we count more than 90,000 procedures per year for revision or re-operation as more than half the AVFs fail within 2 years [181]. This is why it is crucial to understand the hemodynamic and mechanical parameters involved in the creation of an AVF to optimize its lifespan [182].

Many complications can occur after the creation of an AVF, for instance, after creating the anastomosis, *i.e.* the suture of a vein on a donating artery, the vein can dilate under the effect of an increase in flow rate and pressure, as the venous wall is thin and compliant. On the contrary, the arterial wall is made of a lot of fibers and muscle cells which restrains the dilation of the vessel. These two elements lead to hemodynamic modifications fed by the progressive dilation of the vessels [183]. Although the complications are related to a physiological adaptation of the human body, the hemodynamics modified after the creation of the AVF plays a role in triggering these complications.

Among the complications, the most frequent is an arterial or venous stenosis that decreases the flow rate in the AVF, which in the continuity of Chapter 6 is the reason why we investigate this procedure. A steal syndrome can appear and thus lead to ischemia, a lack of tissue vascularization, ultimately resulting in necrosis. Another frequent complication is the excessive increase in flow rate due to an increase of the diameter of the superficial vein or the artery supplying the AVF. The patient can experience a hyper flow rate that often leads to cardiac, hemorrhagic, and ischemic problems [184]. From a mechanical point of view, during

the dilation of the artery or vein, the hemodynamic resistances decrease, which, in a system with constant pressure, increases the blood flow. We are thus facing a self-maintained phenomenon because the heart will adjust by increasing the blood flow. An increase in cardiac work is well tolerated over the medium term but can lead to heart failure when increasing too drastically, especially if the patient already has a weak heart [184]. Therefore the good functioning of an AVF requires an early diagnosis of complications.

Despite empirical guidelines on the creation of an AVF [185], many parameters such as the position, the length, the diameter, and the material of the prosthesis intervene and are patient-specific hence the difficulty of understanding the mechanisms involved. The hemodynamics in patient-specific fistula has thus been investigated in many 3D Fluid-Structure Interaction (FSI) or Computational Fluid Dynamics (CFD) simulations [183,186–194] in normal or abnormal conditions. These studies provide insights into the hemodynamics and flow distribution inside the AVF. They essentially highlight that the Wall Shear Stress (WSS) is directly correlated to the vessel damages and plays an important role in the growth and remodeling of the AVF [195,196].

Although such models are realists, they are rarely used in clinical practice as they require a high computational cost and above all only account for small portions of the blood circulation, usually centered around the anastomosis. A few studies thus investigate reduced-order models to study the global hemodynamics associated with AVFs. For instance, in [197,198], the models are zero-dimensional/one-dimensional (0D/1D) models with a 1D description of the main vessels and the AVF and 0D Windkessel models of the rest of the systemic circulation (heat, aorta...).

The complexity of the physiological phenomena of the creation of the AVF and body adjustment cannot always be represented by a simple model. Thus we make a series of assumptions on the hemodynamics and mechanical properties of the vascular system to build a 0D network model [74] that characterizes the AVF. We compare this model with patient data extracted from the usual clinical practice of monitoring patients undergoing hemodialysis with an AVF or modifying their AVF if it was already present. We then focus on the region of the anastomosis to explore the influence of a venous stenosis on the distribution of flow in the AVF with a 1D network model.

The goal of this chapter is to develop an AVF model able to reproduce the distribution of flow in this vascular system and find an optimal configuration that prevents the appearance of complications. In Section 7.2, we describe the steps of the creation of an AVF and the evolution of and AVF in pathological conditions. Then, in Section 7.3, we present the patient data carried during routine clinical practice. We follow in Section 7.4 with the numerical models and show the results in Section 7.5.

7.2 The life of an AVF

In this section, we detail the creation of an AVF and the possible evolution in case of complications.

7.2.1 Creation of an AVF

The creation of a native AVF is based on a direct anastomosis between a donating artery of the deep arterial network and a receiving vein that is part of the superficial venous network that drains remotely into the deep venous network (Figure 7.1). It is the length of the superficial vein that determines the area of puncture for the extraction and introduction of the blood that must be sufficiently spaced to prevent recirculation.

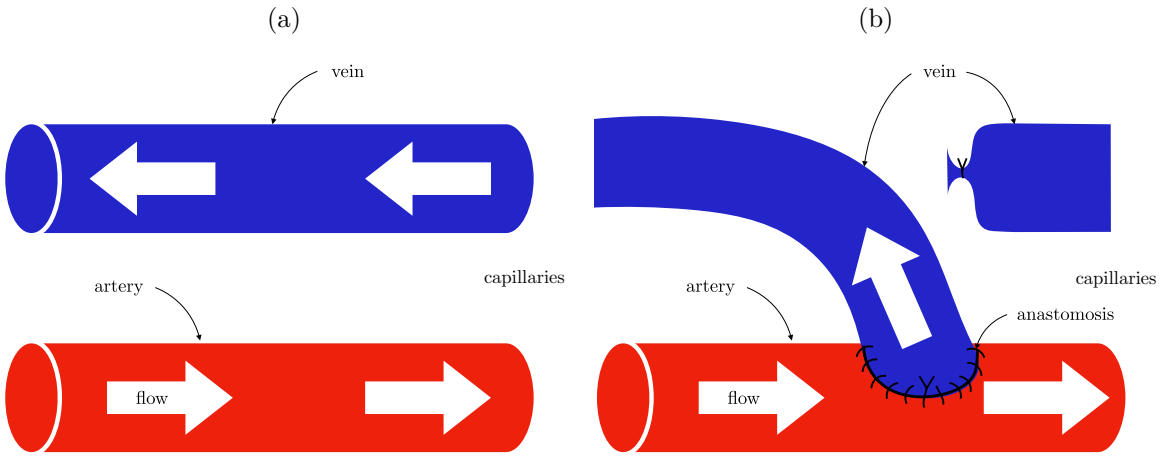

FIGURE 7.1 – Schematic representation of the creation of a native AVF. (a) The flow in the artery (in red) goes from left to right towards the capillaries that link the artery to the vein (in blue). (b) The artery (in red) is sutured to the superficial vein (in blue) with a laterolateral anastomosis between the lateral face of the donating artery and the cut end of the vein. The other end of the vein is sutured. The flow goes from upstream of the artery and divides into the artery and the superficial vein.

When there is no superficial venous segment that can be used to create a native AVF, a tubular prosthetic segment with a proximal anastomosis on the donating artery and a distal anastomosis on the deep or superficial venous network can be used.

One of the criteria of the extra-renal purification is to have a sufficient blood flow to filter the blood of the kidney failure patient in a sufficiently short time. The blood is extracted through the AVF and reintroduced at least 5 cm further into the AVF to avoid a flow recirculation. The flow in the AVF depends on various anatomical parameters of the arterial and venous networks but also on the hemodynamics, in particular, cardiac output. The vascular surgeon performing the AVF takes into account these different parameters to choose the site of creation of the arteriovenous anastomosis.

The criteria to the creation are that the AVF must remain permeable, have a sufficient flow rate, and at the same time not too high to avoid two pitfalls: heart failure and ischemia of the hand. The guidelines [185] suggest that the diameter of the donating artery must be greater than 0.2 cm and the diameter of the vein greater than 0.25 cm. The size of the anastomosis should be adapted to the arterial flow rate and the respective size of the vessels and should be neither too large nor too small, usually from 0.3 to 0.7 cm of diameter.

The hemodialysis machine adds a constraint as it cannot function at a flow rate lower than 500 mL/min. In a native fistula, the minimum accepted flow rate is 500 to 600 mL/min while in a prosthetic fistula, the minimum flow rate must be around 650 to 800 mL/min [178, 199]. The optimal flow rate for a native AVF therefore varies from 600 mL/min to 1200 mL/min [200]. A flow rate greater than 2000 mL/min is considered as a hyper-flow [201], potentially leading to heart failure [184].

7.2.2 Evolution of an AVF

The areas of hemodialysis are marked by the occurrence of stenoses in the arteries or veins, dilations of the superficial vein or the donating artery, a low arterial flow downstream of the anastomosis responsible for ischemia in the hand (digital flow rate < 30 mL/min), or a local hyper flow rate resulting in cardiac insufficiency. In the case of hyper flow rate, the surgeons use the banding technique [202], as shown in Figure 7.2 to reduce the flow rate and cardiac output thus limiting the risks of heart failure [203]. It consists of surgically narrowing the lumen of the superficial vein by creating a stenosis, which is also called diameter or focal reduction.

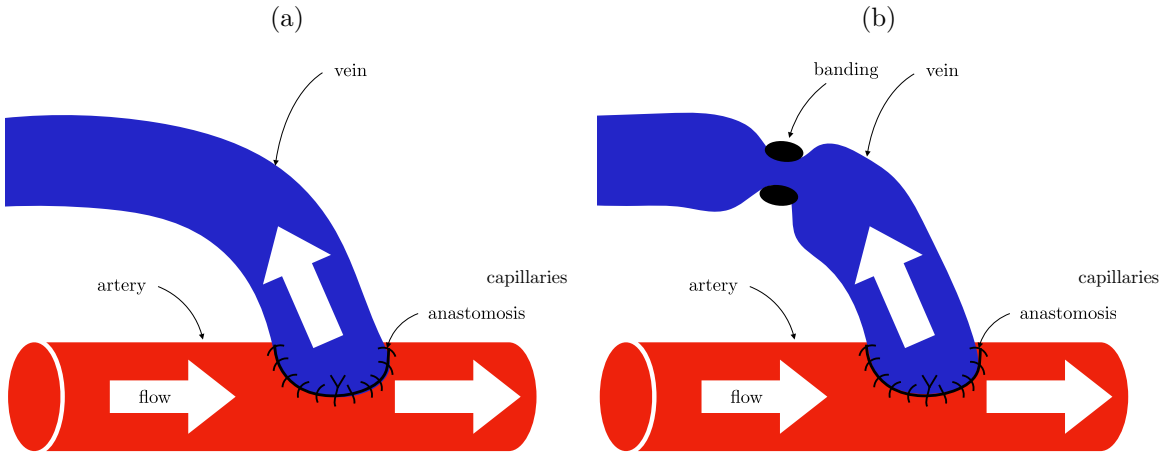

FIGURE 7.2 – Schematic drawing of diameter (or focal) reduction of the superficial vein, using the banding technique [202]. (a) The artery (in red) is sutured to the superficial vein (in blue) with a lateroterminal anastomosis between the lateral face of the donating artery and the cut end of the vein. The flow goes from upstream of the artery to downstream of the artery and the superficial vein. (b) The banding is placed on the superficial vein to reduce its cross-section thus reducing the flow rate in the vein.

To summarize, the realization of AVFs is based on the following guidelines [185, 204]: the diameter of the donating artery must be greater than 0.2 cm, the vein diameter must be greater than 0.25 cm, and the fistula diameter must be between 0.3 and 0.7 cm. We must also take into account the risk of ischemia in the hand as the flow rate can be greatly reduced because of the deviation of blood towards the AVF. Thus the flow in the hand should be the humeral flow before the creation of the AVF. Finally, we must take into account the threshold flow rate for the hemodialysis machine to function, which is 500 mL/min.

We are studying three different configurations.

- First, before the creation of the AVF, the non-pathological case: the blood flow comes from the humeral artery which divides into the radial and ulnar arteries to supply the capillary system of the hand. The return is through the venous system divided into a deep and superficial vein, as represented in Figure 7.1a.
- Second, just after the creation of the AVF by connecting the radial artery to the superficial venous system, as shown in Figure 7.1b. The flow goes either into the capillaries through the arterial system supplying the capillary system in the hand or into the fistula. A mechanism of diversion or steal can indeed appear if the fistula is not correctly dimensioned.
- Third, a hyper-flow rate configuration, there is a need to reduce the diameter of the vein to limit the flow in the fistula. This process is done by creating stenosis in the vein, a focal reduction, as represented in Figure 7.2b.

7.3 Data acquisition

In this section, we present the Doppler ultrasound measurements and the patient population we carry the study on.

7.3.1 Doppler ultrasound measurements

To determine the specific parameters of interest of the vessels for each patient, we choose to carry an anatomic and hemodynamic study of the vessels in each of the configurations. We use a morphological ultrasound with Doppler effect to obtain the hemodynamic data with a General Electric Logiq V2 Doppler. We obtain the flow measurements, lengths, and diameters of the arteries and veins.

As it is difficult to measure the flow using Doppler ultrasound in compliant veins, we consider that in the non-pathological case, the distribution of blood flow is 90% for the deep network and 10% for the superficial network.

7.3.2 Patient population

Two patients undergo Doppler ultrasound measurements as part of their medical care. We study the hemodynamics in the arterial and venous network in the three different configurations described in Section 7.2. For the first patient, we have Doppler data on the flows and diameters in the arterial and venous networks before the creation of the AVF and after the creation of the AVF. For the second patient, we have similar data but after the creation of the AVF and after a focal reduction of the AVF due to a hyper-flow rate.

The measured data are referred in Table 7.1 for the first patient before the creation of the AVF, Table 7.2 for the first patient after the creation of the AVF, Table 7.3 for the second patient after the creation of the AVF and Table 7.4 for the second patient after the focal reduction.

7.4 Numerical models of an AVF

In this section, we present how we build the numerical AVF models to reproduce the distribution of flow in the arterial and venous networks.

7.4.1 Zero-dimensional model

In Section 2.3.6, we presented the 0D models and in particular in Equation (2.68) we showed the simplest model that is often used as a boundary condition for 1D [22, 58, 72] or 3D models [29, 83]. This model states that in the case of a viscous fluid in a vessel of length L and diameter D, we can assume a Poiseuille flow that links the flow rate Q to the pressure jump between two points ΔP through

$$\Delta P = R(D, L)Q, \tag{7.1}$$

where $R(D, L)$ is the Poiseuille (or hydraulic) resistance defined in Equation (2.69) and depends on the diameter and the length of the vessel as $R(D, L) = 128\mu L/\pi D^4$.

This type of model is an electrical analogy as explained in Section 2.3.6. We assume that each vessel of the arterial and venous networks can be represented by a resistance of the type (2.69) that only requires geometric properties. With this basic tool, we can build a complex network by assembling the resistances in parallel and in series [74], which is what we show in the following section.

The 0D model gives only a first approximation of the problem considering the small amount of data that the Doppler provides, but in fact, provides relevant orders of magnitude of the blood flow in the veins and arteries. This data is part of the routine medical care that makes this model usable in everyday clinical practice.

7.4.2 Construction of the 0D AVF network model

We build two different networks of resistances that can represent all the configurations that we investigate in this study. The configuration before the AVF is shown in Figure 7.3 and the configuration after the creation of the AVF, including after the focal reduction, is represented in Figure 7.4. In the two figures we display: on the left a schematic representation of the main arteries and veins in the arm and hand and on the right the equivalent electric network model.

To build the networks, we start from the humeral artery that divides into the radial and ulnar arteries. The venous network decomposes into the superficial vein and the deep vein. We model each element of the vascular system (artery, vein, capillaries, fistula) by a resistor and can calculate the values of each resistance from the Doppler measurements of the lengths and diameters. We calculate the resistance of the fistula using the diameter of the anastomosis and assume that it has a length $L_f = 2$ cm. We model the capillary network by a high resistance at the end of the arterial segments. to take into account the multiple

existing bifurcations. We compute the flow in every branch of the circuit with Ohm's law, or in mechanical terms Equation (7.1), and Kirchhoff's law or conservation of flow.

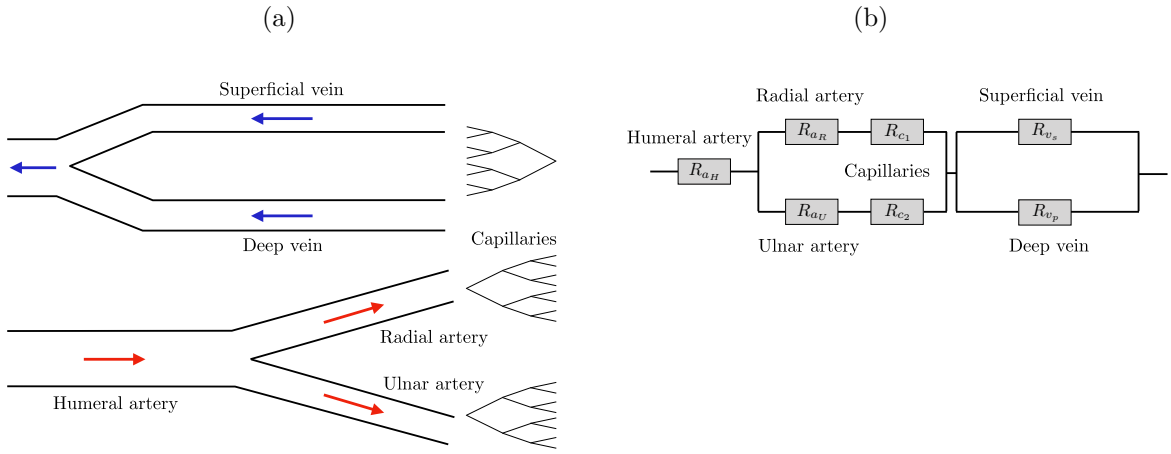

FIGURE 7.3 – Drawing of the 0D numerical network model of the arteriovenous system in the arm before the creation of the AVF. (a) Schematic representation of the main vessels in the arm and hand, (b) equivalent electrical network. We represent each vessel (arteries and veins) as well as the capillaries by a resistor.

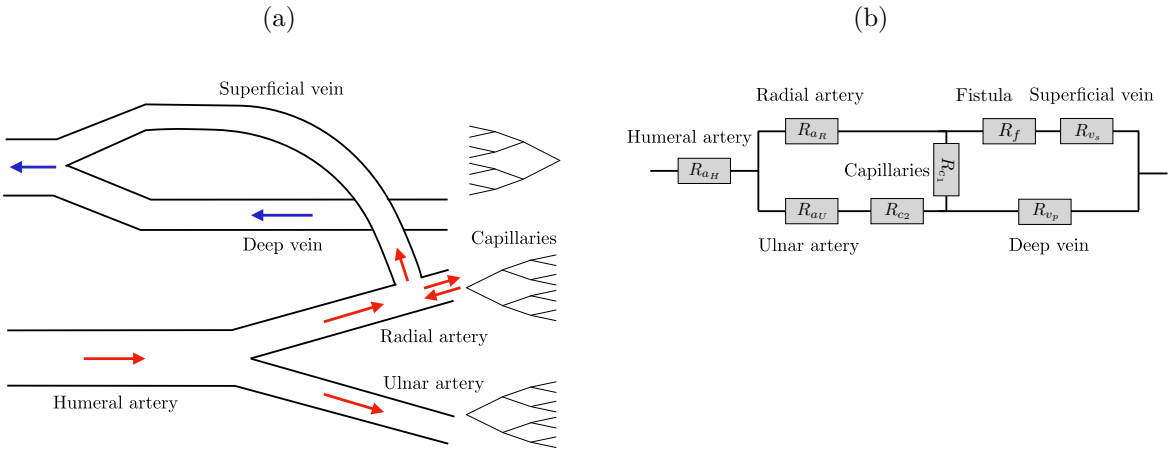

FIGURE 7.4 – Drawing of the numerical network model of the arteriovenous system in the arm after the creation of the radio-cephalic AVF. (a) Schematic representation of the main vessels in the arm and hand, (b) equivalent electrical network. We represent each vessel (arteries and veins) as well as the capillaries by a resistor. We also represent the fistula by a resistor R_f defined with the radius of the anastomosis and a length of $L_f = 2$ cm.

In the case before the creation of the AVF, we can calculate analytically the total resistance R_{tot} of the network using the composition of resistances in series and parallel

$$R_{tot} = R_{a_H} + \frac{(R_{a_R} + R_{c_1})(R_{a_U} + R_{c_2})}{R_{a_R} + R_{c_1} + R_{a_U} + R_{c_2}} + \frac{R_{v_s} R_{v_p}}{R_{v_s} + R_{v_p}}, \tag{7.2}$$

where $R_{a,c,v}$ represents respectively the arterial, capillary, or venous resistance with the initial of the vessel.

7.4.3 One-dimensional model

To study locally the hemodynamics we propose the 1D model of the simplified system to complete the 0D model. We solve the 1D equations (2.51) with the pressure law (2.16) in a 3-vessel network composed of two arteries, the humeral and the radial, and one vein, the superficial vein (Figure 7.5). It corresponds to the configuration after the creation of the AVF.

We use the same pressure law (2.16) for the artery and veins with a different Young's modulus E. We choose E based on the value of the Moens-Korteweg celerity (2.59) from Table III and VIII of [14]. We use the geometric parameters of the first patient measured with the Doppler (Table 7.2) reported in Table 7.5. The boundary conditions are the following: we impose the humeral flow rate at the inlet, apply a resistance boundary condition at the outlet of the radial artery and impose a zero pressure at the outlet of the superficial vein.

We define the venous stenosis as a reduction of the radius of the wall with the same shape as in Chapter 6

$$R(x) = R_0 \left(1 + \beta \exp\left(-\frac{(x - x_{st})^2}{x_l}\right)\right), \tag{7.3}$$

where β is the degree of constriction ($\beta < 0$), x_{st} is the axial position of the throat of the stenosis, and x_l is related to the length of the stenosis L_{st}.

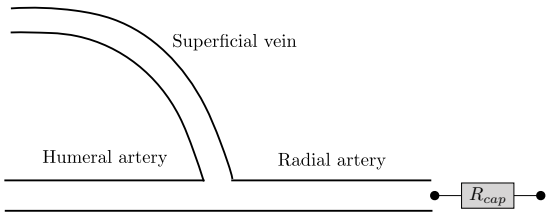

FIGURE 7.5 – Drawing of the 1D network model after the creation of the radio-cephalic AVF. Properties of the vessels are reported in Table 7.5.

7.5 Results

In this section, we present the results obtained from the numerical model of Section 7.4. We first investigate the influence of the capillary resistance in finding an optimal AVF, then compare the numerical model with the patient data of Section 7.3, and finally study the influence of a venous stenosis with the 1D model.

7.5.1 Results of the 0D model: capillary resistances

The capillary resistances play a crucial role in the numerical model. From a mechanical point of view, after the creation of the AVF, if the capillary resistances are too high, no flow will go into the deep vein. On the contrary, if the capillary resistances are too low, no flow will go

into the fistula. As we have no access to this parameter, we study two cases, one with a low capillary resistance and one with a high capillary resistance, to investigate which one gives the most physiological result.

The arterial resistances are of order 10^3 g·cm^{-4}·s^{-1}. We choose the low capillary resistance to be 10 times the order of magnitude of the arterial resistance ($R_{cap} = 10R_a$) and similarly, and the high capillary resistance to be 50 times the order of magnitude of the arterial resistance ($R_{cap} = 50R_a$).

Optimal fistula diameter

Figures 7.6 show the flow rate in the fistula (in red), *i.e.* in the superficial vein, and the flow rate in the hand (in blue) as a function of the fistula diameter. The solid, dashed, and dotted lines represent the flow constraints. The flow rate in the fistula must be between the dashed and the dotted line to respect the functioning limit of the hemodialysis machine. The flow rate in the hand must be above the solid line to avoid ischemia. The grey rectangle represents the range of the fistula diameter that respects these flow constraints. We studied the case of a low capillary resistance in Figure 7.6a and of a high capillary resistance in Figure 7.6b.

(a) $R_{cap} = 10R_a$ (b) $R_{cap} = 50R_a$

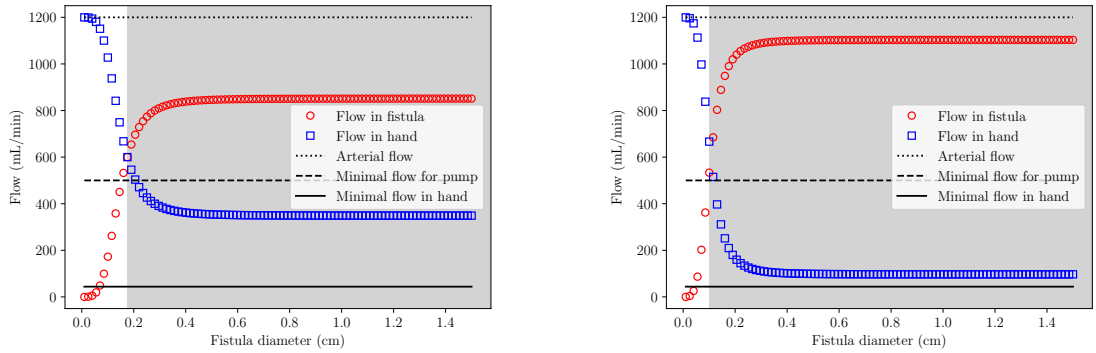

FIGURE 7.6 – Flow rate in the superficial vein and fistula (◯) and in the hand (□) after the creation of the AVF as a function of the fistula diameter. (····) corresponds to the humeral arterial flow, (---) represents the minimum flow for the hemodialysis machine to function and (——) corresponds to the minimum flow in the hand to avoid ischemia. The grey rectangle represents the range of the fistula diameter that respects these constraints. (a) The capillary resistances are 10 times the order of magnitude of the arterial resistances, (b) the capillary resistances are 50 times the order of magnitude of the arterial resistances.

The 0D model provides a lower bound for the fistula diameter under which the hemodialysis machine does not work. We obtain a minimal fistula diameter of 0.18 cm for the low capillary resistance and 0.12 cm for the high capillary resistance. The guidelines suggest that the anastomosis diameter should be between 0.3 and 0.7 cm. Our value is lower but remains reasonable considering the simplicity of the model.

We notice that the model does not give an upper boundary for the fistula diameter. Indeed,

because the length of the fistula is small ($L_f = 2$ cm), the resistance of the fistula R_f does not play the most important role in the model. We can, therefore, conclude that the model cannot provide a relevant and more precise range for the fistula diameter than the current guidelines.

As we showed that the diameter of the fistula does not play an important role, we investigate the influence of the superficial vein diameter on the distribution of flow.

Optimal diameter of the superficial vein

Figures 7.7 show the flow rate in the fistula (in red), *i.e.* in the superficial vein, and the flow rate in the hand (in blue) as a function of the diameter of the superficial vein. Similarly to Figure 7.6, the flow rate in the fistula must be between the dashed and the dotted line, and the flow rate in the hand must be above the solid line. The grey rectangle represents the range of the superficial vein diameter that respects the flow constraints. We studied the case of a low capillary resistance in Figure 7.7a and a high capillary resistance in Figure 7.7b.

Similarly to Figure 7.6, the 0D model provides a lower bound for the diameter of the superficial vein under which the hemodialysis machine does not work. We obtain a minimal diameter of the superficial vein of 0.27 cm for the low capillary resistance and 0.18 cm for the high capillary resistance. Both values seem in agreement with the guidelines.

However, varying the superficial vein diameter allows determining a maximal diameter of the superficial vein that respects the flow constraints for the high capillary resistance, which is 0.7 cm, which is completely in agreement with the guidelines. The model can thus predict the upper limit of the diameter of the superficial vein that prevents ischemia in the hand.

(a) $R_{cap} = 10R_a$ (b) $R_{cap} = 50R_a$

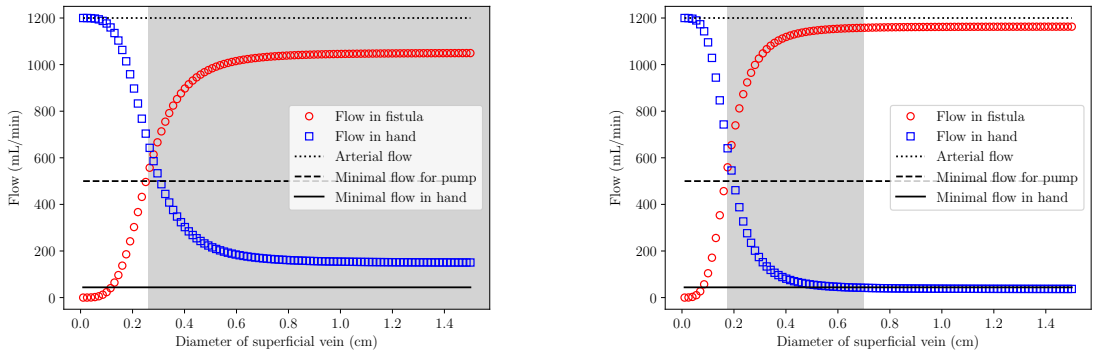

FIGURE 7.7 – Flow rate in the superficial vein and fistula (◯) and in the hand (□) after the creation of the AVF as a function of the diameter of the superficial vein. (·····) corresponds to the humeral arterial flow, (- - -) represents the minimum flow for the hemodialysis machine to function and (——) corresponds to the minimum flow in the hand to avoid ischemia. The grey rectangle represents the range of the diameter of the superficial vein that respects these constraints. (a) The capillary resistances are 10 times higher than the typical arterial resistance (b) the capillary resistances are 50 times higher than the typical arterial resistance.

Discussion

The first result of this study is that the model cannot determine the optimal diameter of the fistula which respects all the flow constraints, regardless of the capillary resistance. As mentioned, the length of the fistula is too small for the fistula resistance to play the major role in the distribution of flow. The parameter that influences the most on the distribution of flow is the superficial vein diameter. By varying this parameter and assuming a high capillary resistance, we can predict the bounds of the superficial vein diameter that respects the flow constraints. If the superficial vein dilates over 0.7 cm, the blood supply in the hand will no longer be sufficient. We also find that the vein diameter must be greater than 0.18 cm to respect the flow constraints, which agrees with the orders of magnitude suggested by the guidelines [185].

The estimation of the superficial vein diameter relies upon the approximation of a single diameter over the entire superficial vein segment which is not relevant in the case of AVF in which dilation and narrowing will occur. However, a simple calculation with the model allows determining a maximum average superficial vein diameter that respects the flow constraints.

Nonetheless we observe that the value of the capillary resistance creates, in the model, a decisive condition. The lack of measurement of this capillary resistance is a limitation in this study. From Figures 7.7, we notice that the high capillary resistance gives results close to the conditions found in clinical practice and can thus provide an acceptable approximation.

7.5.2 Comparison between Doppler and simulated flow rate using the 0D model

In this section, we compare the Doppler measurements with the numerical model in the three configurations detailed in Section 7.2. In the following, we use the large capillary resistance as it provides the conditions found in clinical practice.

Creation of the fistula

In Table 7.1, we compare the Doppler flow rate to the simulated flow rate before the creation of the fistula. The humeral flow rate is the input of our model. We recall that since we do not have precise measurements of the flow in the veins, we consider that the deep vein receives 90% of the arterial flow, and the superficial vein receives the remaining 10%. We recover the same distribution of blood in each vessel with the model compared to the Doppler measurements.

In Table 7.2, we show the results of the simulated flow rate after the creation of a fistula with an anastomosis of 0.3 cm. The humeral flow rate increases a lot, which is the objective of the creation of an AVF. We obtain a flow in the deep vein of 180 mL/min that comes from the hand, which is sufficient to avoid ischemia. We obtain a flow rate of 1020 mL/min in the fistula, which is within the constraints imposed by the hemodialysis machine.

The numerical findings show that the 0D model can reproduce the distribution of flow in a non-pathological scenario by imposing the measured humeral blood flow rate. The 0D model also confirms that the diameter of the fistula chosen by the surgeon is optimal as it respects all the flow constraints, which was not assessed by the Doppler measurements.

TABLE 7.1 – Parameters from Doppler and simulated results using the 0D network model before the creation of the AVF. The capillary resistances are 50 times the order of magnitude of the arterial resistances. D_0: measured reference diameter in cm, L: measured length of the vessel in cm. Flow rates are expressed in mL/min.

	D_0	L	Doppler flow rate	Simulated flow rate
Humeral artery	0.44	20	44	44
Radial artery	0.38	20	28	30.04
Ulnar artery	0.34	20	16	13.96
Deep vein	0.53	20	$\sim$ 90 % of humeral flow	39.9
Superficial vein	0.3	20	$\sim$ 10 % of humeral flow	4.1

TABLE 7.2 – Parameters from Doppler and simulated results using the 0D network model after the creation of the AVF. The capillary resistances are 50 times the order of magnitude of the arterial resistances. D_0: measured reference diameter in cm, L: measured length of the vessel in cm. Flow rates are expressed in mL/min.

	D_0	L	Doppler flow rate	Simulated flow rate
Humeral artery	0.44	20	1200	1200
Radial artery	0.38	20		1130
Ulnar artery	0.34	20		70
Deep vein	0.53	20		180
Superficial vein	0.3	18		1020
Fistula	0.3	2		1020

Focal reduction

We present the second patient that underwent focal reduction 3 years after the creation of the AVF. The superficial vein downstream of the fistula increased in diameter drastically, causing a hyper flow rate. This increase is not considered as an aneurysm, another pathological phenomenon, but is expected to appear after a period of maturation of the AVF. Indeed, the superficial vein undergoes a higher pressure regime and thus adapts by increasing its diameter.

In Table 7.3, we show the results of the model before the focal reduction. In this case, the flow rate in the humeral artery is not the sum of the flow rate in the radial and ulnar artery because of the imprecision of the Doppler measurement. Therefore we decide to take as an input of the model, the sum of the radial and ulnar flow rates. The humeral flow rate is 2700 mL/min which gives evidence of a hyper flow rate. The blood supply in the hand is sufficient however, we find a flow rate of 2200 mL/min in the fistula, which is out of the acceptable flow range. Therefore, there was a need for a focal reduction using the banding technique [202], described in Section 7.2, to reduce the diameter of the superficial vein.

Table 7.4 shows the comparison between the Doppler flow rate and the simulated flow rate after the focal reduction. By reducing the minimal diameter of the superficial vein from

Table 7.3 – Parameters from Doppler and simulated results using the 0D network model before focal reduction because of an hyper flow rate. The capillary resistances are 50 times the order of magnitude of the arterial resistances. D_0: measured reference diameter in cm, L: measured length of the vessel in cm. Flow rates are expressed in mL/min.

	D_0	L	Doppler flow rate	Simulated flow rate
Humeral artery	0.78	20	3500	2700
Radial artery	0.7	20	2200	2351
Ulnar artery	0.4	20	440	348
Deep vein	0.4	20		358
Superficial vein	0.5 to 1.3	18		2341
Fistula	0.4	2		2341

Table 7.4 – Parameters from Doppler and simulated results using the 0D network model after focal reduction because of an hyper flow rate. The capillary resistances are 50 times the order of magnitude of the arterial resistances. D_0: measured reference diameter in cm, L: measured length of the vessel in cm. Flow rates are expressed in mL/min.

	D_0	L	Doppler flow rate	Simulated flow rate
Humeral artery	0.72	20	930	930
Radial artery	0.59	20	800	700
Ulnar artery	0.35	20	116	230
Deep vein	0.4	20		243
Superficial vein	0.25 to 1.2	18		687
Fistula	0.4	2		687

0.5 cm to 0.25 cm, we recover a normal flow rate of 930 mL/min in the humeral artery. It thus leads to a flow reduction in the fistula of 687 mL/min. We also still obtain a non-ischemic flow in the hand of 243 mL/min.

The numerical results confirm that the reduction of the minimal diameter of the superficial vein respects the blood flow constraints. Indeed, as the humeral blood flow rate is the input of our model, we cannot predict the success of the focal reduction procedure that results from a physiological adjustment of the heart. We can only verify the success of the focal reduction procedure by recovering the distribution of flow in the hand and the fistula, which was not assessed with the Doppler measurements. It is interesting to remark that a simple calculation from the 0D model can determine how much focal reduction is necessary to recover a normal flow rate in the AVF.

The 0D model cannot anticipate the hyper flow ratebut can predict that a doubling in the diameter of the superficial vein results in a 40% decrease of the total resistance, *i.e.* an increase of the flow rate of 40%, in a system with constant pressure. However, a hyper flow rate is an increase of about 200%. A purely mechanical approach is thus not sufficient to explain such an increase, and the model cannot account for this physio-pathological behavior. This condition might be triggered by the increase in diameter and then self-maintained by

TABLE 7.5 – Geometric and material properties of the 1D model of an AVF. D_0: measured reference diameter in cm, L: measured length of the vessel in cm, E: Young's modulus in g·cm^{-1}·s^{-2}, R_{cap}: peripheral resistance in g·cm^{-4}·s^{-1}.

	D_0	L	E	R_{cap}
Humeral artery	0.44	20	$0.3{\cdot}10^7$	—
Radial artery	0.38	20	$0.3{\cdot}10^7$	1 or 5 $\cdot 10^4$
Superficial vein	0.3	20	$0.3{\cdot}10^6$	—

other chemical and biological phenomena.

7.5.3 One-dimensional results

We propose to study locally the influence of a stenosis on the distribution of blood flow in the system using the 1D model. The stenosis can be either surgical or pathological. We place a stenosis of length $L_{st} = 2$ cm in the superficial vein 3 cm from the anastomosis and vary the degree of constriction β (Equation (7.3)).

(a) $R_{cap} = 10R_a$ (b) $R_{cap} = 50R_a$

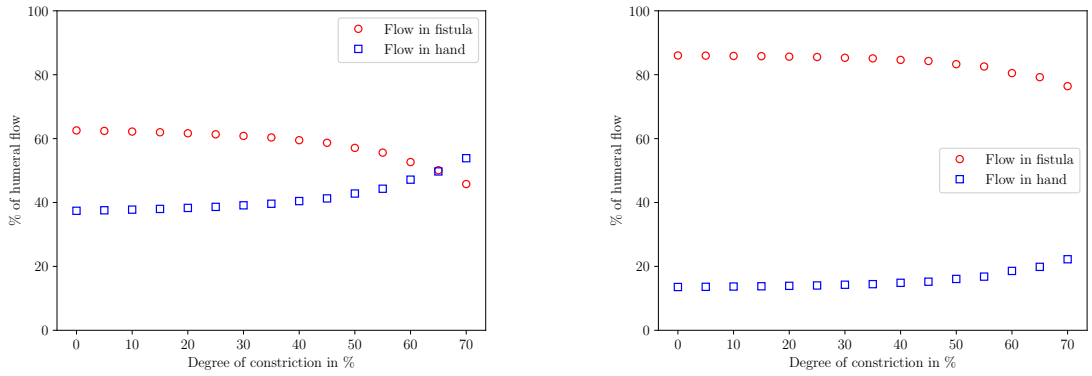

FIGURE 7.8 – Distribution of flow in % of humeral flow in the fistula (◯) and in the hand (□) using the 1D model depending on the degree of constriction of the stenosis expressed in % of radius reduction (see Section 6.4.1 and Figure 6.7 for definition of degree of constriction), the stenosis is placed 3 cm from the anastomosis and has a length $L_{st} = 2$ cm. The flow rate is measured at the middle of the artery.

Figures 7.8 show the distribution of flow in the hand, *i.e.* in the radial artery, and in the fistula, *i.e.* in the superficial vein, as a function of the degree of constriction of the stenosis. Similarly to the 0D model, we study two cases: one with a low capillary resistance $R_{cap} = 10R_a$ (Figure 7.8a), and one with a high capillary resistance $R_{cap} = 50R_a$ (Figure 7.8b). We first observe that this parameter is crucial and influences the distribution of flow in the AVF also in this model. Second, the reduction of flow in the fistula is not in the same amount depending on the capillary resistance. For a low capillary resistance, we obtain a 20% reduction of the flow in the fistula with a constriction of 70% compared to the non-pathological configuration. In the case of the high capillary resistance, this reduction is only of less than 10%. Depending on the humeral flow and the capillary resistance, the flow rate might be insufficient when the

stenosis is too severe. We can also conclude that, in the 1D model, the capillary resistance creates a decisive condition on the optimization of the AVF.

7.6 Conclusion

The number of clinical situations and the inter-individual variability in the surgical results after the creation or modification of an AVF could benefit from a decision-making tool to help the surgical strategy. We dedicated this study to develop simplified numerical models of the vascular network of the upper limb when it is modified by the creation of an AVF, for therapeutic purposes. We built the 0D network with resistances to model each vessel (arteries, veins, capillaries) to study the distribution of flow in this system. We studied three different configurations: the configuration prior to the creation of the AVF, the configuration after the creation of the AVF, and the configuration after the development of a hyper flow rate requiring a focal reduction.

First, we found that the simple 0D network model was unable to identify a value or a range for the anastomosis diameter. The range of acceptable fistula diameter is highly dependent on the capillary resistance which we do not measure and which is probably variable from one individual to another. Second, we found that the model provided a range of acceptable superficial vein diameter that respects the flow constraints, assuming a capillary resistance 50 times larger than the typical arterial resistance. The model allows determining a minimum and a maximum average superficial vein diameter that optimizes the AVF.

Then, we compared the 0D model to the Doppler ultrasound measurement carried on two patients during clinical routine practice. We showed that knowing the humeral flow rate and topology was enough to reproduce the distribution of flow in all three configurations: before the creation of the AVF (Table 7.1), after the creation of the AVF (Table 7.3), and after the focal reduction (Table 7.4). The model provides the quantitative values of the distribution of flow in the system when it was only assessed qualitatively during the clinical procedure. Nonetheless, we showed that the model was not sufficient to explain the hyper flow rate that occurs a few months to a few years after the creation of the AVF. A purely mechanical phenomenon could not explain the hyper flow but could be the trigger and then fed by other biological phenomena.

Finally, we used a 1D model to explore the distribution of flow when a venous stenosis develops or is created in the AVF. The 1D model is undoubtedly an improvement compared to the 0D model first because it accounts for the shape of the vessels and changes in radius. It is crucial in the study of venous stenoses as many of the complications induced by the creation of an AVF include changes in diameters in the fistula. It should however be noted that the 1D model contains fewer vessels than the 0D model and is thus less detailed in the distribution of flow, in particular in the hand.

In this study, we encountered a few limitations. The first was the lack of measurement or even order of magnitude of the capillary resistance which was a decisive parameter in both models. This parameter would greatly improve the models' predictions. It would allow making patient-specific decisions on the limits of the fistula diameter and of the diameter of the superficial vein and would thus improve the prognosis of the AVF. The second limitation was the model itself. It seems naturally essential to account for the remodeling of the arterial and venous walls when studying AVFs. Remodeling in this vascular system is an important

process that can explain many physio-pathological and mechanical developments that occur after the creation of the AVF [187,195], including the hyper flow [184,203]. Our 0D model can only reproduce phenomena that are purely mechanical, in particular narrowing or dilation of the vessels and the trigger of the hyper flow rate.

As any reduced-order model, the 1D model also several limitations. It is well-known that arteries and veins have different mechanical behaviors and thus using the same pressure law is only valid at order zero. The development of a vein model and incorporating it in a 1D closed-loop model as in [14] is a perspective to the present work and will be further discussed in the conclusion chapter 10. The choice of the capillary resistance remains the same problem as the 0D model and is still a decisive parameter in both models. The choice of the boundary conditions at the outlet of the superficial vein is also a limitation of the 1D model as it may influence the distribution of flow in the network. In Chapter 6, we showed that the Multi-Ring model was the most accurate model to study the influence of stenoses. Therefore, creating a network of vessels with the Multi-Ring model also represents an improvement to the present models.

However, despite all these limitations, the 0D network model can reproduce and predict the flow distribution in the AVF in different configurations given easily obtained non-invasive geometric data. The 1D model also provides relevant information on the distribution of flow and could be very useful in patient-specific modeling, provided a value of the capillary resistance.

8 Impact of aortic cross-clamping

When the severity of a stenosis becomes too important, repair surgery is the recommended intervention by clinical guidelines. Surgeries usually require cross-clamping, a common strategy to prevent blood from flowing in the operation zone. However, the immediate impact of aortic cross-clamping on the vascular properties during abdominal aortic aneurysm (AAA) repair or peripheral artery disease surgeries is unknown and thus we developed two numerical models to investigate it. To assess the validity of the models, we record continuous invasive pressure signals during surgeries, immediately before and after clamping. The first model is a 0D three-element Windkessel model which we couple to the Basin-Hopping parameter estimation algorithm to identify patient-specific parameters such as vascular resistance and compliance. The second model is a 9-artery network corresponding to an average human body in which we solve the 1D blood flow equations.

Keywords: aortic cross-clamping, zero-dimensional model, one-dimensional model, arterial waveform analysis, parameter estimation.

The text in this chapter is greatly inspired by the following published articles

- J Ventre, M T Politi, J M Fernandez, A R Ghigo, J Gaudric, S A Wray, J-B Lagaert, R Armentano, C Capurro, J-M Fullana, P-Y Lagrée. Parameter estimation to study the immediate impact of aortic cross-clamping using reduced order models. *International Journal for Numerical Methods in Biomedical Engineering*, p. e3261, 2019.
- M T Politi, J Ventre, J Fernandez, A Ghigo, J Gaudric, R Armentano, C Capurro, P-Y Lagrée. Effects of cross-clamping on vascular mechanics: comparing waveform analysis with a numerical model. *Journal of Surgical Research*, vol. 244, pp. 587–598, 2019.

Contents

8.1 Introduction

Open surgery is currently the gold standard for Abdominal Aortic Aneurysm (AAA) [205] or peripheral vascular diseases [206] such as stenosis repair surgery [72]. Most surgeries require aortic cross-clamping, an external compression of the artery that prevents the blood from flowing downstream thus providing a more stable operative field [207]. Yearly, it is performed in over a quarter of a million patients worldwide [208]. However, there is clinical evidence that suggests that the duration of aortic cross-clamping may be related to postoperative morbidity and mortality [209, 210]. This procedure naturally produces perturbations in cardiovascular hemodynamics [211, 212] but the exact mechanisms involved are not completely clear.

Many experimental studies in animals [213] and humans [214] have reported the hemodynamic changes caused by aortic clamping on gastrointestinal function [215], on cardiac output [216–218], and renal perfusion [219]. Nevertheless, only changes produced 5 to 60 minutes after aortic clamping have been described, whereas immediate changes remain unknown. Therefore, there is a gap in current knowledge as to which are the immediate changes after aortic clamping, and what is the effect of clamping on the hemodynamics and vascular properties. We believe it is crucial to understand the effects of clamping to minimize the risks of complications.

Clinicians usually have access to only minimal, if any, information on the vascular properties of their patients. Therefore, we record continuous invasive arterial pressure during peripheral vascular repair surgeries, before and after clamping of the abdominal aorta, measurements that are part of routine clinical procedure.

Though some mechanical modeling studies have investigated the local stress distribution [220] that causes arterial tissue damage produced by traumatic surgical instruments [221], to our knowledge, aortic cross-clamping has not been investigated using macroscopic blood flow models. Numerical models of the arterial network can provide information on important vascular features including compliance and resistance, given easily-obtained routine hemodynamic information such as continuous arterial pressure signals. As the final objective of this study is to predict the impact of the aortic clamping during surgery, we need to consider adequate models for real-time medical applications. We choose to compute two numerical models: a zero-dimensional (0D) Windkessel model, similar to the ones presented in Section

2.3.6 and the one-dimensional (1D) model detailed in Section 2.3.4.

To enhance the measured data, we introduce a parameter estimation strategy, based on the invasive measurements, to identify valuable information on vascular mechanics, otherwise difficult to obtain in a minimally invasive way. Arterial waveform analysis also allows calculating the diastolic time-constant of pressure waves [222–224]. We compare the numerical predictions of the blood flow models to those of arterial waveform analysis and to the invasive blood pressure measurements to investigate the immediate impact of aortic cross-clamping. We show that both the 0D and 1D models provide helpful information for medical diagnosis, at systemic and arterial scale respectively.

This chapter is organized as follows: in Section 8.2, we present the data acquisition method by indicating how we perform the invasive pressure measurements and the patients that we were enrolled. In section 8.3 we introduce the experimental method, the data analysis, and statistical tools used to evaluate the agreement. In Section 8.4 we briefly present the 0D model, the 1D model, and the parameter estimation method to compare the numerical models to the invasive measurements. In Section 8.5, we show the comparison between the experimental method and the 0D model on the cohort of patients. In Section 8.6, we focus on one patient to compare the two numerical models and the patient data. Finally, we summarize the results and give perspectives in Section 8.7.

8.2 Data acquisition

8.2.1 Invasive radial artery pressure measurements

We record arterial pressure signals of patients undergoing a repair intervention that required aortic cross-clamping. We obtain the continuous and invasive pressure data with a fluid-filled catheter from the right radial artery of the patients during the surgery. The use of invasive arterial pressure measurements during this type of surgery is part of the surgical protocol and, therefore, routine clinical practice. The recording of these pressure data does not modify the signal used for clinical monitoring nor presents additional risks for the patient during the surgery.

To carry these measurements, we use a disposable pressure transducer (TruWave, Edwards Lifescience®) and record the pressure signals with an analog-digital converter with internal hardware filters (low pass frequency set at 20 kHz, high pass frequency set at 0.05 Hz, MP150, BIOPAC Systems Inc.). We use the AcqKnowledge software to interpolate arterial pressure data at a frequency of 1000 Hz.

We record the pressure data in four different configurations: the pre-clamp configuration as prior to aortic clamping (Figure 8.1a), the post-clamp configuration during which the clamp is in place (Figure 8.1b), the pre-unclamp configuration which is right before removing the clamp, and the post-unclamp, right after removing the clamp.

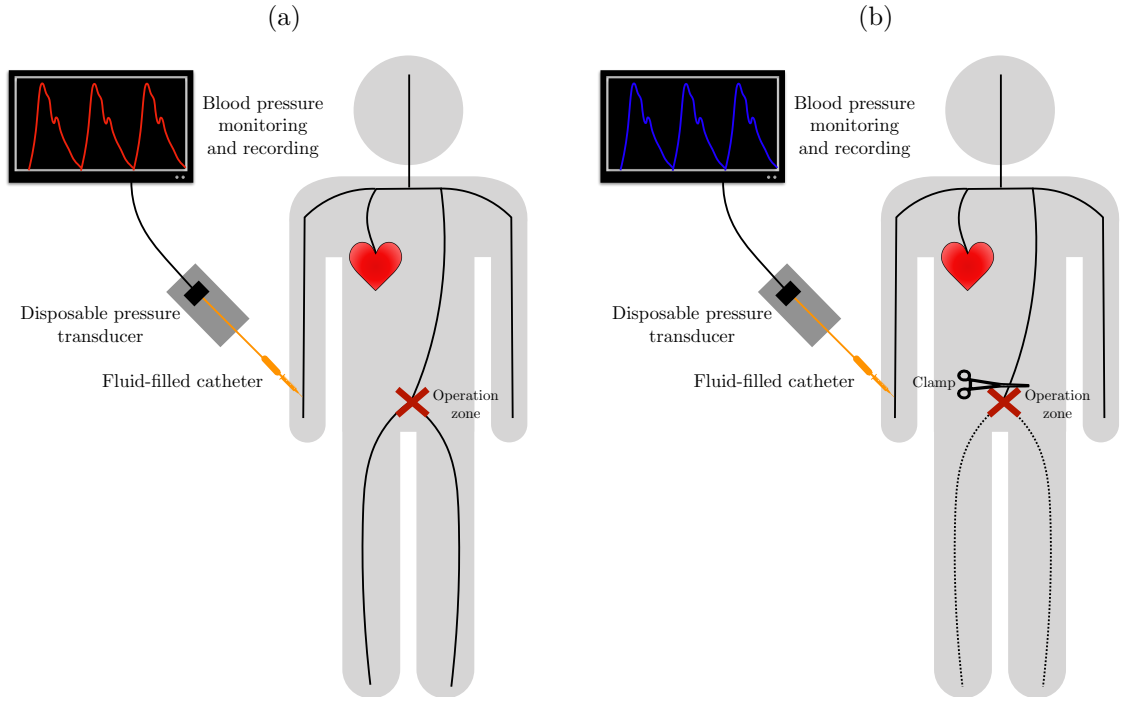

FIGURE 8.1 – Schematic representation of the clamping procedure and data collection. The fluid-filled catheter is positioned in the right radial artery, linked to a pressure transducer and monitor that records the blood pressure signal. We represent (a) the situation before clamping (pre-clamp) or after unclamping (post-unclamp) and (b) the abdominal clamping (post-clamp and pre-unclamp), all of them during peripheral vascular repair surgery.

8.2.2 Patient population

This study enrolls adult patients undergoing peripheral vascular surgery involving abdominal aortic clamping at the *Hôpital Universitaire Pitié-Salpêtrière* in Paris, France. We exclude patients with a) an irregular heart rhythm, b) waveform diastolic values that do not fit a single exponential decay, or c) a reduced left ventricular ejection fraction (<45%) measured by echocardiography or cardiac magnetic resonance during routine preoperative workup. The invasive arterial pressure measurements of 14 patients undergoing vascular surgery is measured; 3 patients are excluded (2 for having an irregular rhythm and 1 for having waveforms that do not fit a single exponential decay). We end up with 11 patients in the final study, of which 9 have an infra-renal AAA disease and underwent open repair surgery with either an aortoaortic tube graft (1 patient), an aorto-uni-iliac graft (2 patients) or an aorto-bi-iliac graft (6 patients). The remaining 2 patients have occlusive peripheral artery disease (a stenosis) and underwent aortobifemoral bypass surgeries. All selected aortic clamps are infrarenal. Table 8.1 shows patients' full clinical characteristics and Table 8.2 indicates patients' comorbidities and medication. Note that we have the information on the drugs injected to the patients but we consider a purely mechanical approach and discard any chemical or biological interaction.

8.2.3 Mean beat

For each configuration, we choose a stable set of beats manually through a 20 to 40-second interval immediately before and after each clamp/unclamp event. The beginning of each individual beat is automatically identified using local minimum pressure values. In order to

TABLE 8.1 – Patient clinical characteristics. Absolute values are presented as mean ± standard deviation (SD). DB: diabetes mellitus, SMK: smoking status, HT: arterial hypertension, DL: dyslipidemia, height in m, weight in kg.

Patient	Age	Sex	DB	SMK	HT	DL	Height	Weight
1	84	M	×	×	✓	✓	1.65	57
2	84	M	×	✓	✓	✓	1.62	65
3	80	M	×	✓	✓	×	1.70	74
4	46	M	×	✓	✓	✓	1.61	65
5	81	F	×	✓	✓	✓	1.56	48
6	64	M	×	✓	×	✓	1.90	110
7	49	F	×	✓	×	✓	1.67	71
8	58	F	×	✓	×	×	1.59	54
9	67	M	✓	✓	✓	✓	1.82	105
10	65	M	×	✓	✓	✓	1.75	85
11	78	F	×	✓	×	×	1.50	42
Total	69 ± 14	63.0%	9.1%	90.0%	63.6%	72.7%	1.67 ± 0.12	70.5 ± 21.9

obtain a mean beat, we average the signal by calculating the period of each beat, taking the median period, and normalizing every beat to this median period so that 50% of the beats are shortened and 50% lengthened by the normalization.

In the following, we describe the experimental model and statistical tools used to analyze the pressure measurements.

8.3 Experimental method

8.3.1 Arterial waveform analysis

We analyze the pressure signals with the arterial waveform analysis, which we refer to as the experimental method, using a custom algorithm developed in Matlab (R2018b, The MathWorks, Inc., Natick, Massachusetts). This method is based on a two-element Windkessel model [75] as it shows a single exponential decay during capacitor discharge defined by the diastolic time-constant τ. We use this feature to automatically detect the onset of the diastole for every cycle (Figure 8.2). Starting from the end of the beat (iteration number 0), we fit the data with the model using 100 ms intervals with 1 ms backward steps. We evaluate the exponential growth coefficient $1/\tau$ and define the maximum rate of change $\delta(1/\tau)$ of this coefficient as the onset of the diastole (▲ in Figure 8.2). Once the onset of diastole is found, we fit the pressure data from the entire diastolic period to a single exponential function to obtain the final diastolic time-constant (····· in Figure 8.2).

With the arterial waveform analysis, we calculate the diastolic time-constant for the 11 patients in the four configurations in two different manners: a) from each beat of the 20 to 40-second pressure signal which gives a median τ or b) from the mean beat which gives the mean τ.

Table 8.2 – Patient comorbidities and medication. CAD: coronary artery disease, HF: heart failure, IC: intermittent claudication, BB: Beta-blockers, ACEI: angiotensin-converting enzyme inhibitors, ARBs: angiotensin II receptor antagonists, CCB: calcium channel blockers.

Patient	CAD	HF	IC	Aspirin	Statins	BB	ACEI ARBs	CCB	Diuretics
1	×	×	×	✓	✓	×	×	✓	✓
2	✓	×	✓	✓	✓	✓	✓	×	×
3	✓	×	✓	✓	✓	✓	✓	×	✓
4	×	×	×	✓	✓	×	✓	×	×
5	✓	×	✓	✓	✓	✓	✓	×	✓
6	✓	×	×	✓	✓	✓	✓	×	×
7	×	×	✓	✓	✓	✓	✓	×	✓
8	×	×	✓	✓	✓	×	✓	×	×
9	✓	×	✓	✓	✓	✓	✓	×	✓
10	×	×	×	✓	✓	×	×	✓	×
11	×	×	×	✓	✓	×	✓	×	×
Total	45.5%	0%	54.5%	100%	100%	54.5%	81.8%	18.2%	45.5%

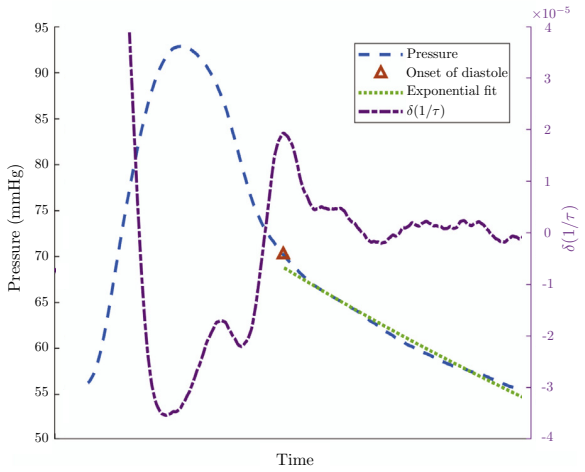

Figure 8.2 – Arterial waveform analysis to determine the onset of diastole and the diastolic time-constant. The x-axis corresponds to time. Starting from the end of the beat (right side of the figure), the exponential growth coefficient ($1/\tau$) of the arterial pressure curve (- - -) is estimated by fitting 100 ms intervals with 1 ms backwards steps. The onset of diastole (▲) is obtained from the local maximum of $\delta(1/\tau)$ (- - -). Pressure data from the diastolic time interval is fitted to a single exponential function (·····) to obtain the final time-constant (τ).

Arterial waveform analysis is commonly used to calculate the time-constant of the diastolic portion of pressure waves [222–224]. However, this method is unable to estimate by itself the relative contribution of compliance (C) or resistance (R) to the time-constant (τ), *i.e.* considering $\tau = RC$. Using a numerical model of the arterial network allows these important vascular features, compliance and resistance being estimated along with the time-constant. Such a numerical model therefore offers an appropriate means of comparison with classic waveform analysis, by comparing the estimated time-constants, while offering valuable information on vascular mechanical properties. We use, in addition to the waveform analysis, two numerical models that can highlight the changes in vascular mechanics after aortic cross-clamping and unclamping during vascular surgeries in adult patients. We present these two models in Section 8.4.

8.3.2 Statistical analysis

A one-way analysis is conducted to assess the distribution of each covariate. We calculate the mean and standard deviation (SD) for normally distributed variables and median and interquartile range (IQR) for non-normally distributed variables. Categorical variables are summarized with percentages in each category. Group comparisons involve two-tailed paired T-tests for normally distributed variables, Wilcoxon signed-rank test for non-normally distributed variables, and chi-square or Fischer's exact tests for categorical variables.

We assess correlation with Pearson's correlation coefficient (ρ) for variables with a multivariate normal distribution and with Spearman's correlation coefficient for variables with a non-normal multivariate distribution.

We use Bland-Altman plots [165] to assess the agreement qualitatively in which we represent the difference between two measurements on the y-axis plotted against the average of these measurements on the x-axis. The mean difference between the two measurements is called the center of agreement and is represented by a central horizontal line on the plot. The upper/lower Limits of Agreement (LoA) are ± 1.96 SD of the mean difference. The gap between the center of agreement and the x-axis (corresponding to zero differences) is called the bias. More detail about Bland-Altman plots can be found in Section 6.2.3 and Figure 6.2.

We verify normality in the distribution of the differences formally using Shapiro-Wilk tests. We consider that two-tailed tests were statistically significant at the standard 0.05 level and that a percentage bias (bias/mean waveform analysis time-constant) of 20% or less is acceptable.

We perform the statistical analysis using R software version 1.0.136 (packages ggplot2, BlandAltmanLeh, MVN). More detail about statistical tools and analysis can be found in textbooks such as [225].

8.4 Blood flow models

In this section, we briefly describe the 0D model, the 1D model, and the parameter estimation method to compare with the data presented in Section 8.2.

8.4.1 Windkessel model

0D equation

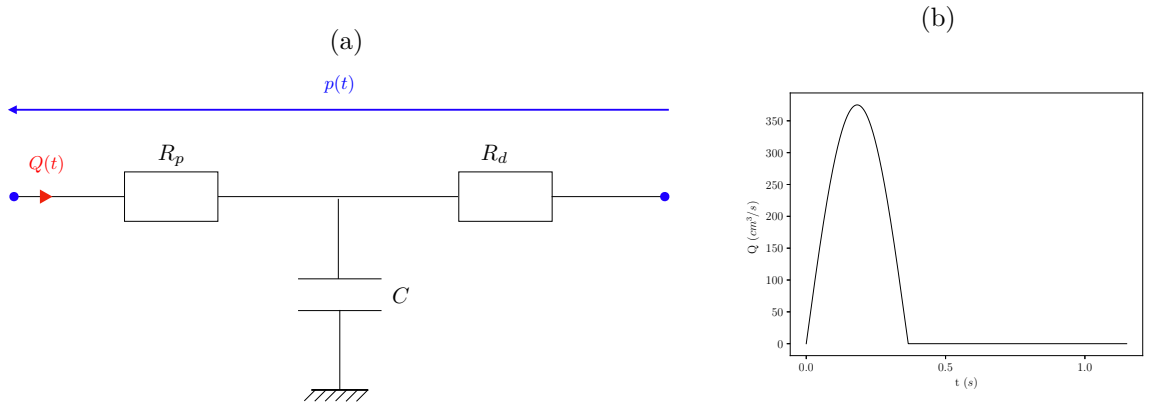

FIGURE 8.3 – (a) Electrical representation of the three-element Windkessel model describing the entire systemic circulation. The pressure $p(t)$ is linked to the flow rate $Q(t)$, that models the heart through Equation (8.1) where R_p is the proximal resistance, R_d is the distal resistance and C is the compliance. (b) Inlet boundary condition of the 0D and 1D models: flow rate $Q(t)$ modeling the heart. For instance, we choose the amplitude $Q_0 = 375$ cm^3/s, the ejection time $T_{ej} = 31.8\%$ of the heart period $T_c = 1.15$ s, which is the data of patient 3.

The three-element Windkessel model [75], introduced by Frank [76], is a modified version of the 0D blood flow Equations (2.66) obtained by averaging the blood flow equations (2.21) over all spatial dimensions (see Section 2.3). In this representation, the arterial network can then be interpreted as an electrical circuit constituted of resistors and capacitors. The three-element Windkessel model is composed of one capacitor C and two resistors R_p and R_d corresponding to the proximal and distal resistances respectively (Figure 8.3a). Resistors represent frictional forces due to viscosity while capacitors model the compliant effects of arteries. The Windkessel models are widely used in medical studies [67, 77, 226] because despite their simplicity they have a low computational cost and provide valuable information on the vascular system (vascular resistances and compliance) that are helpful for the medical diagnosis.

The analytical representation of the Windkessel model in Figure 8.3a is given by the following equation that links the pressure $p(t)$ to the flow rate $Q(t)$ ejected by the heart:

$$\left(1 + R_d C \frac{\mathrm{d}\cdot}{\mathrm{d}t}\right) p(t) = \left((R_p + R_d) + R_p R_d C \frac{\mathrm{d}\cdot}{\mathrm{d}t}\right) Q(t), \tag{8.1}$$

which can be solved in p or in Q depending on the unknown.

Boundary conditions

To minimize the number of model parameters, we choose to describe the flow rate $Q(t)$ ejected by the heart with a simple half-sine signal (Figure 8.3b). This heart model has proven reliable in previous works [64, 69], even though more complicated heart models can be found in the literature [14, 65, 82]. The input flow rate follows

$$Q(t) = \begin{cases} Q_0 \sin\left(\dfrac{\pi t}{T_{ej} T_c}\right) & \text{if } 0 < t < T_{ej} T_c, \\ 0 & \text{if } T_{ej} T_c \leq t < T_c, \end{cases} \tag{8.2}$$

characterized by three parameters: the amplitude Q_0 and the systolic ejection time T_{ej}, during which blood is injected in the system, and the heart period T_c. The first two parameters Q_0 and T_{ej} are unknown whereas the heart period is prescribed by the patient data.

Numerical resolution scheme

To solve the equation (8.1) numerically, we use an explicit Euler time-integration scheme

$$p^n + R_d C \frac{p^{n+1} - p^n}{\Delta t} = (R_p + R_d) Q^n + R_p R_d C \frac{Q^{n+1} - Q^n}{\Delta t}, \tag{8.3}$$

where p^{n+1} is the unknown pressure at time t^{n+1} and Q^n, Q^{n+1} the known flow rates at times t^n and t^{n+1} respectively, imposed through the inlet boundary condition (8.2). The time step $\Delta t = t^{n+1} - t^n$ is of order 10^{-4} s and $\Delta t \ll R_d C \simeq 1$ s, the characteristic time of diastolic exponential decrease.

8.4.2 One-dimensional model

1D equations

The 1D models have been used to describe blood flow in large arteries since, unlike 0D models, they can model the spatial propagation of pulse waves, one of the most important phenomena when studying large artery hemodynamics [9, 62, 63]. The 1D equations are obtained from the 3D Navier-Stokes equations (2.21) assuming a few weak hypotheses, described in Section 2.3.1. The details of the derivation can be found in Section 2.3.4.

We solve the 1D equations (2.51) coupled to the visco-elastic pressure law of Equation (2.18). We thus solve the system (2.54) with the friction coefficient C_f set to $22\pi\nu$ [227], *i.e.* $\xi = 9$, with $\nu = 5{\cdot}10^{-2}$ cm^2/s the kinematic viscosity of blood.

Boundary conditions

To model the systemic circulation in the pre-clamp configuration, we build a minimal network composed of nine main arteries [20] (Figure 8.4a) where we solve the 1D equations (2.54). At each bifurcation, we impose the conservation of mass and the continuity of pressure [228] without taking into account pressure losses at the junctions [61]. The boundary conditions are the following: at the inlet of the network (artery number 1) we impose the same periodic flow input signal $Q(t)$ as the 0D model (Equation (8.2)) and we apply resistance boundary conditions r_i at every terminal artery i to take into account the peripheral

circulation in the capillaries [22, 66] (Table 8.8). The post-clamp configuration consists of removing all distal arteries starting from the end of the abdominal aorta (artery 7). In practice, we apply a total reflection outlet boundary condition at the end of artery 7 ($R_t = 1$), corresponding to a complete occlusion of the vessel (see Figure 8.4b).

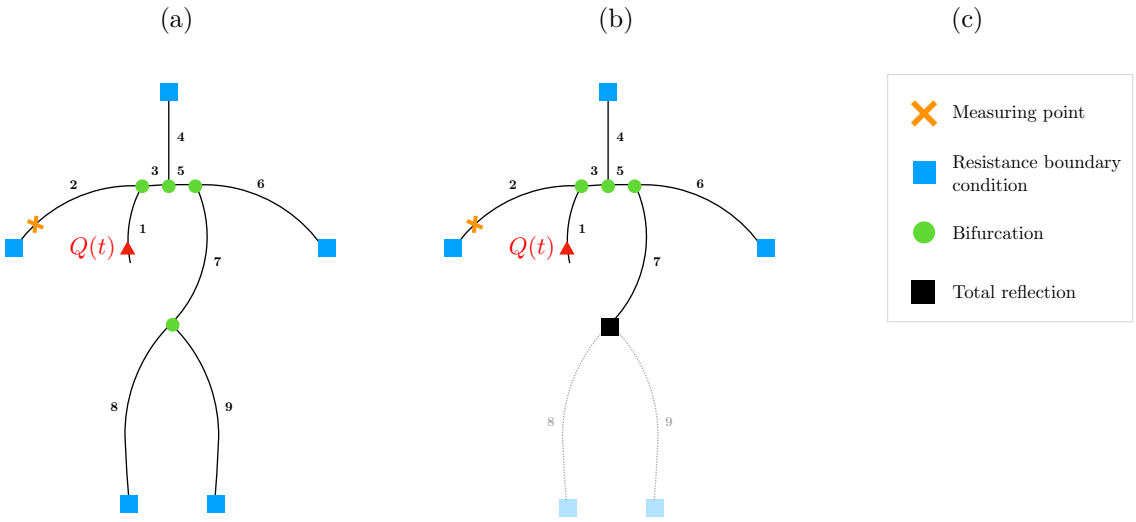

FIGURE 8.4 – Schematic representation of the 9-artery network. We represent (a) the configuration without the clamp (pre-clamp), (b) the configuration with the clamp (post-clamp), where we model the occlusion of artery 7 with a total reflection boundary condition. The green circles represent the bifurcations, the light blue squares represent the resistance boundary conditions, the black square is the point of clamping modeled by a total reflection ($R_t = 1$), and the orange cross is the pressure measurement point where we compare measured and simulated pressure waves.

Properties of the network

Table 8.3 presents the arterial geometric (length L, reference cross-section A_0, thickness h) and material (Young's modulus E) properties used in the numerical computations. We adjust these properties from similar models of the literature [74, 79] to the chosen 9-artery networks model to correspond to an average human body [20]. The resistance boundary conditions are estimated automatically with the process described in Section 8.4.3 and reported in the results section in Table 8.8.

Numerical resolution schemes

To solve the Equations (2.54), we use the finite volume method described in Section 4.2.4. We divide the time domain with a constant time step $\Delta t = 10^{-4}$ s and introduce a spacial mesh to discretize each artery with a constant step $\Delta x = 0.4$ cm, that are typical values for computation with enough precision.

TABLE 8.3 – Geometric and material properties of the 9-artery network model [20,66,72]. L: length in cm, A_0: reference cross-section in cm^2, h: arterial wall thickness in cm, E: Young's modulus in $g{\cdot}cm^{-1}{\cdot}s^{-2}$ (considered constant in each artery).

N°	Name	L	A_0	h	E
1	Aorta arch A	4.0	7.07	0.16	$0.7{\cdot}10^7$
2	Right subclavian radial artery	72.5	0.50	0.06	$0.4\ {\cdot}10^7$
3	Aorta arch B	2.0	5.31	0.12	$0.4{\cdot}10^7$
4	Left carotid artery	38.5	0.50	0.06	$0.6{\cdot}10^7$
5	Aorta arch C	3.9	4.52	0.1	$0.4\ {\cdot}10^7$
6	Left subclavian radial artery	69.1	0.50	0.06	$0.4{\cdot}10^7$
7	Aorta	34.5	2.01	0.1	$0.4{\cdot}10^7$
8	Right femoral artery	96.9	0.79	0.07	$1.2{\cdot}10^7$
9	Left femoral artery	96.9	0.79	0.07	$1.2{\cdot}10^7$

8.4.3 Parameter estimation

Typically, during the course of a clinical procedure, little is known about patient-specific vascular properties. Parameter estimation is a powerful tool to identify these physiological quantities. It can also allow following the evolution of a disease in a minimally invasive way. A review of the parameter estimation methods can be found in Section 4.3.

We propose an optimization strategy designed to automatically estimate both 0D and 1D model parameters using the patient data. Figure 8.6 presents the 3-step algorithm of the process in which:
(i) we estimate the 0D model parameters: the resistances (R_p and R_d), the compliance (C) and the ejection time (T_{ej}),
(ii) we estimate the resistance boundary conditions (r_i) of the 1D model to match the total resistance of the 1D model to the total resistance of the 0D model found in step *(i)*,
(iii) we estimate the amplitude of the input flow rate (Q_0) for both models using the 1D model.

(i) Estimation of the 0D model parameters
The objective of this first step is to estimate the 0D model parameters $\mathcal{P} = \{R_p, R_d, C, T_{ej}\}$ for each of the four configurations (pre-clamp, post-clamp, pre-unclamp, post-unclamp), solving an inverse problem based on the patient data. We define a cost-function $\mathcal{J}$ that characterizes the difference between the measured and simulated pressure waves, respectively $P_{measured}(t)$ and $P_{sim}(\mathcal{P}, t)$. We minimize this cost-function $\mathcal{J}$ with respect to $\mathcal{P}$, the set of parameters. The cost-function is

$$\mathcal{J}^{pre/post}(\mathcal{P}, t) = \left(\int_0^{T_c} \left(P_{measured}(t) - P_{sim}(\mathcal{P}, t) \right)^2 \mathrm{d}t \right)^{1/2}. \tag{8.4}$$

To calculate P_{num}, we solve Equation (8.1) and impose an arbitrary value of Q_0 such that the Systolic Volume (SV) V_s, *i.e.* ventricular ejection volume over a heartbeat, is within the typical range of 70 to 90 mL. We define the SV as the integral of the input flow rate $Q(t)$ over a heart period T_c. We impose the same SV V_s in all four configurations.

For each configuration we determine the optimal set of parameters $\mathcal{P}$ using the Basin-Hopping algorithm combined to the L-BFGS-B descent described in Section 4.3.1 and 4.3.2 from the Python SciPy library [229]. As it allows bound constraints, we require that all parameters have positive values and that the compliance remains in the interval $C \in [10^{-7}, 10^{-1}]$ $\mathrm{g}^{-1}\cdot\mathrm{cm}^4\cdot\mathrm{s}^2$.

This algorithm provides the optimal values of the 0D model parameters $\mathcal{P}$ in all four configurations, in the physiological parameter space, as the global optima of the cost-function $\mathcal{J}$.

(ii) Estimation of the resistance boundary conditions of the 1D model
The objective of this second step is to estimate the resistance boundary conditions r_i of the 1D network. We propose a new parameter estimation problem to identify the resistance boundary conditions r_i such that the total resistance of the 1D model $\tilde{R}_{tot,1D}$ matched that of the 0D model $R_{tot,0D} = R_p + R_d$ found in step *(i)*. Since the 0D total resistance is estimated from real invasive data, it seems reasonable to assume that it is the total resistance of the patient, which explains why we match the 1D resistance to the 0D resistance.

We can calculate analytically the total resistance of the 1D model for all configurations assuming a 0D analogy of the 1D network, as represented in Figure 8.5. This total resistance $\tilde{R}_{tot,1D}$ depends on the Poiseuille (or hydraulic) resistances R_i of each vessel [9] defined in Equation 2.69. The values of the Poiseuille resistances R_i for each vessel of the 9-artery network are fixed by the geometry (Table 8.3). The total resistance $\tilde{R}_{tot,1D}$ also depends on the resistance boundary conditions r_i of each terminal artery i.

We define a new cost function $\mathcal{J}$ in which we include both the pre- and post-clamp (respectively unclamp) values of the total resistance so that the optimal set of r_i preserves the ratio between the pre- and post-clamp (respectively unclamp) 0D total resistances. As $R_i \ll r_i$, we only minimize $\mathcal{J}$ with respect to the resistance boundary conditions r_i. We define a new cost function $\mathcal{J}$ as

$$\mathcal{J}(r_i) = (\tilde{R}^{pre}_{tot,1D}(R_i, r_i) - R^{pre}_{tot,0D})^2 + (\tilde{R}^{post}_{tot,1D}(R_i, r_i) - R^{post}_{tot,0D})^2, \tag{8.5}$$

where $\tilde{R}^{pre}_{tot,1D}$ (Figure 8.5a) and $\tilde{R}^{post}_{tot,1D}$ (Figure 8.5b) are the 1D total resistances where the superscript pre stands for pre-clamp or pre-unclamp and post for post-clamp or post-unclamp, $R^{pre}_{tot,0D}$ and $R^{post}_{tot,0D}$ are the 0D total resistances.

We use the Basin-Hopping algorithm combined to the L-BFGS-B gradient descent (Section 4.3) to minimize the cost function $\mathcal{J}$ from Equation (8.5) and obtain the boundary conditions r_i of the 1D network.

(iii) Estimation of the amplitude of the input flow rate for both models
The last parameter we estimate is the amplitude of the input flow rate Q_0. It is not possible to estimate this parameter in step *(i)* since in Equation (8.1), when neglecting the compliance, the pressure is linked to the flow rate through $p = R_{tot}Q$. As we only have pressure data, it is only possible to estimate either the resistance or the flow rate with the 0D model. Indeed, the algorithm can always find a balance between these two quantities that would minimize the cost function but that would not necessarily respectthe physiological values of either of the parameters. The lack of data on the flow rate is a limitation of the present study.

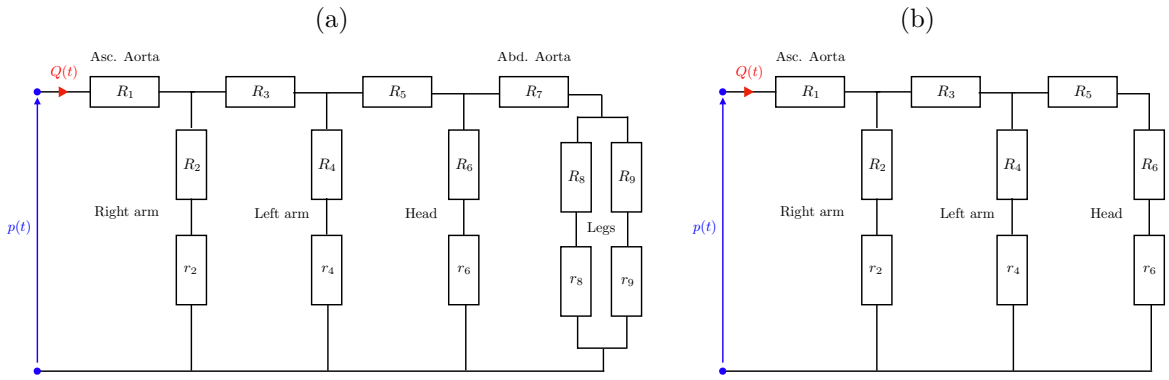

FIGURE 8.5 – Analogy of the 9-artery network with resistors. (a) The pre-clamp network shown in Figure 8.4 that has a total resistance $\tilde{R}^{pre}_{tot,1D}$, (b) the post-clamp network from Figure 8.4b that has a total resistance $\tilde{R}^{post}_{tot,1D}$. The labels of resistors are identical to the labels of arteries from the 1D network (Figure 8.4). The Poiseuille (or hydraulic) resistances R_i, and the resistance boundary conditions r_i are reported in Table 8.8.

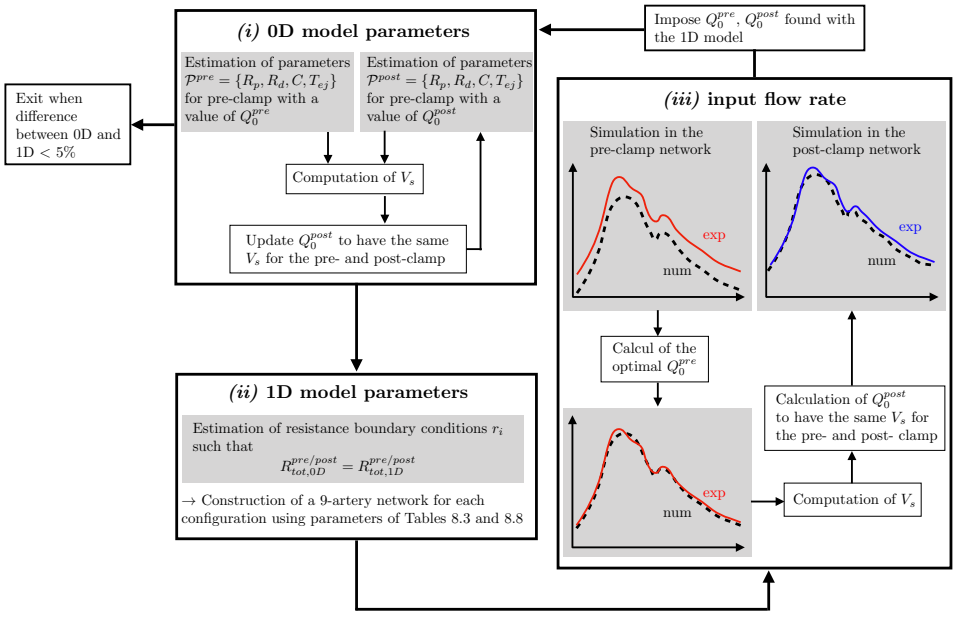

FIGURE 8.6 – Optimization algorithm described in Section 8.4.3 to estimate the patient-specific parameters of the 0D and 1D models. The parameters of the 0D model are $\mathcal{P}^{pre}$ for the pre-clamp configuration and $\mathcal{P}^{post}$ for the post-clamp configuration and are composed of the proximal resistance R_p, the distal resistance R_d, the compliance C and the ejection time T_{ej}. The flow rate Q_0^{pre} (respectively Q_0^{post}) corresponds to the amplitude of the input flow rate $Q(t)$ for the pre-clamp configuration (respectively post-clamp). The stroke volume V_s is the integral of the flow rate $Q(t)$ over one heart period T_c. The resistances r_i are the resistance boundary conditions of the 1D network (see Figure 8.5).

In step *(i)*, we impose an arbitrary value for the amplitude of the input flow rate Q_0.

In this step, we estimate this last parameter Q_0 for all four configurations, using the 1D model with the constraint of a constant stroke volume, within the range of 70 to 90 mL. We compute the 1D model in the "pre" configuration with the input flow rate characterized by the estimated value of the ejection time T_{ej} and the same arbitrary Q_0^{pre} as the 0D model. We use a gradient-based algorithm (see Section 4.3.1 for more detail) from the same SciPy library [229] to find the optimal value of the amplitude of the input flow rate Q_0^{pre} for this configuration. Convergence is reached when the correlation between measured and simulated pressure waves was superior to 0.95. Then we compute the stroke volume V_s, calculated the Q_0^{post} so that the stroke volume is identical between both configurations, and finally compute the 1D model for the "post" configuration. This last step provides values of Q_0 for the 0D and 1D models in all four configurations.

Since Q_0 changed from step *(i)* to step *(iii)*, the process is iterated to recalculate the new 0D total resistance with the optimal value of Q_0. We exit the loop when the 0D and 1D models have the same total resistance, the same amplitude of the input flow rate, and the same stroke volume between all configurations.

In the following, we present the result of the parameter estimation of the 0D model for the four configurations which corresponds to step *(i)* and compare the results to the waveform analysis described in Section 8.3.

8.5 Comparison between the waveform analysis and the 0D model on the cohort

In Figure 8.7, we show the comparison between the pressure measurements of one patient (patient 3) and the 0D model for all four configurations with the optimal set of parameters found using step *(i)* of the parameter estimation process of Section 8.4.3. We observe a strong correlation ($R^2 > 0.95$) between the patient data and the 0D model which shows that the 0D model can accurately reproduce the arterial pressure waveform in all configurations.

In the following, we quantify the agreement between the arterial waveform method and the 0D model based on the diastolic time-constant (Section 8.5.1). Then, in Section 8.5.2, we analyze the results of the 0D model in terms of resistance and compliance since the arterial waveform analysis cannot separate the resistive and compliant effects.

8.5.1 Diastolic time-constant τ

Changes in the diastolic time-constant measured by the waveform analysis

We start by quantifying the changes in the median τ calculated over the 20 to 40-second pressure signal with the experimental method.

In all individual patients the median time-constant decreases after clamping and increases after unclamping. All the details of the calculation can be found in Table C.1 of Appendix C. Aortic clamping induces a significant 10% reduction in the median diastolic time-constant of arterial pressure waves. Before clamping the median time-constant is 2.12 s [IQR:1.54-2.36], while after clamping it is 1.79 s [IQR:1.48-1.91], this difference is statistically significant (p=0.0033). Aortic unclamping induces a significant 17% increase in the median time-constant. Before unclamping the median time-constant is 1.77 s[IQR:1.52-1.99], while after

clamping it is 1.90 s [IQR:1.73-2.32], this difference is also statistically significant (p=0.0033).

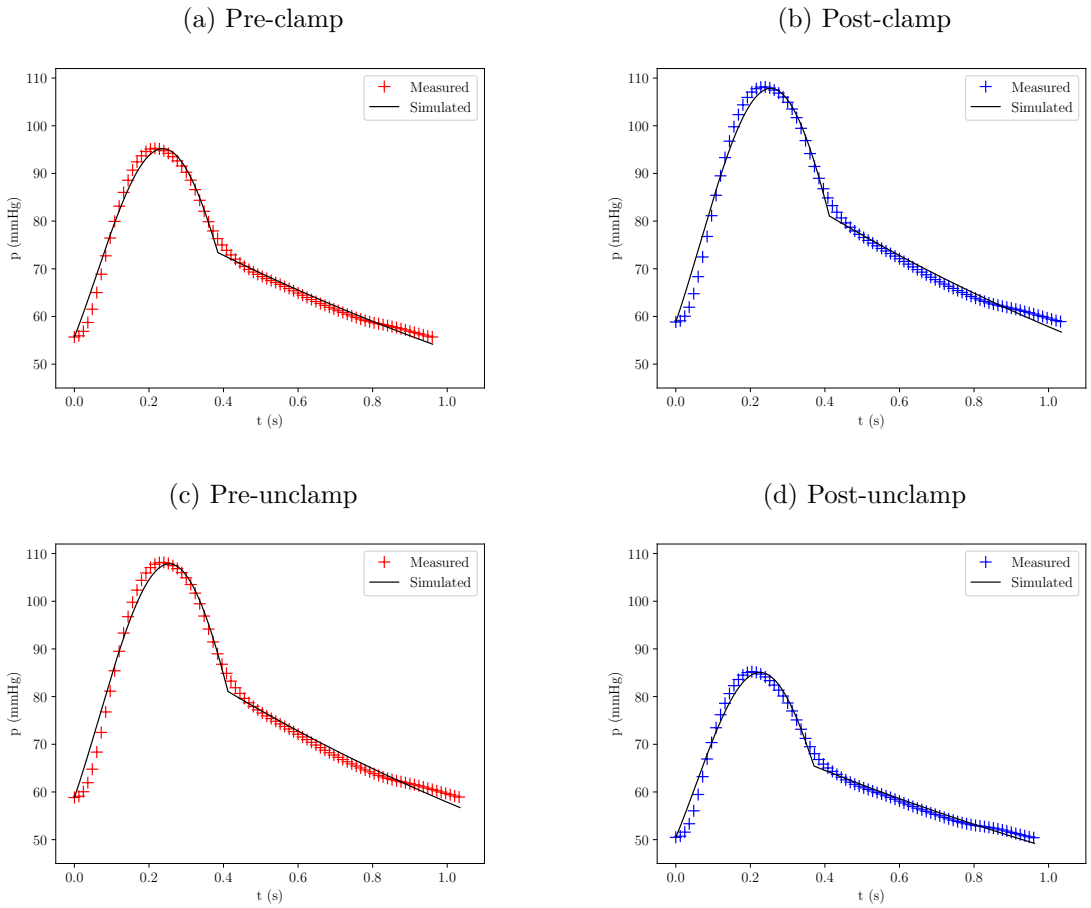

FIGURE 8.7 – Arterial pressure waveform and comparison with the Windkessel model for one representative patient (patient 3) undergoing aortic clamping and unclamping during vascular surgery. (+) and (+) corresponds to the measured pressure wave of the pre-clamp and pre-unclamp, respectively post-clamp and post-unclamp, configurations, (—) corresponds to the simulated pressure waves solving Equation (8.1).

Comparison between the absolute values of the diastolic time-constant

We now compare the diastolic time-constant calculated from the mean beat between the arterial waveform analysis (the mean τ) and the 0D model. We calculate the time-constant $\tau = R_d C$ of the mean beat of each patient before and after each intervention with the estimated parameters of the 0D model. We compare these values to the time-constant measured from the mean beat by arterial waveform analysis. Both methods suggest that the time-constant decreases after clamping and increases after unclamping as shown in Figure 8.8.

To assess quantitatively the agreement between the two methods, we use a correlation plot, shown in Figure 8.9a for clamping and Figure 8.9c for unclamping. We find a positive significant correlation between the values of the time-constant measured by both methods, which is moderate (ρ=0.51; p=0.01486) during clamping and strong (ρ=0.77; p=<0.0001) during unclamping.

To compare both methods, we use Bland-Altman plot [165], shown in Figure 8.9b for clamping and Figure 8.9d for unclamping. More detail about Bland-Altman plots can be found in Section 6.2.3 and Figure 6.2. The plots show appropriate agreement between the experimental and numerical values of the diastolic time-constant. In both settings, we find a small bias (13.7% for clamping, 14.7% for unclamping). For nearly all cases the differences between the two measurements are within the LoA, as reported in Table 8.4. However, there is a possible systematic bias observed for high values of the diastolic time-constant during aortic unclamping, where numerical values seem to overestimate waveform analysis values.

(a) Clamping

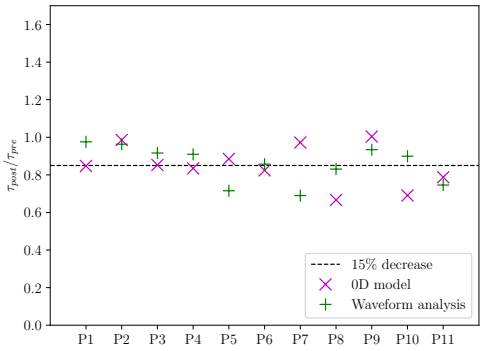

(b) Unclamping

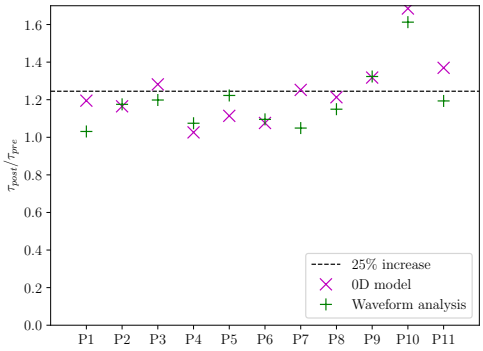

FIGURE 8.8 – Ratio of the diastolic time-constant τ between (a) post-clamp and pre-clamp and (b) post-unclamp and pre-unclamp. (×) represents the ratios estimated by the 0D model and (+) the ratios estimated by the arterial waveform analysis. (---) indicates the median percentage change for the diastolic time-constant estimated by the 0D model.

TABLE 8.4 – Agreement results from Bland-Altman plots. CI: confidence intervals, LoA: Limits of Agreement. Percentage changes are calculated regarding the mean time-constant measured by arterial waveform analysis.

Estimate	Clamping	Unclamping	Units
Bias	-0.260	-0.302	s
95%CI bias	-0.462 to -0.058	-0.514 to -0.09	s
Percentage bias	13.7	14.7	%
Upper LoA	0.632	0.635	s
95%CI Upper LoA	0.283 to 0.982	0.268 to 1.002	s
Lower LoA	-1.152	-1.238	s
95%CI Lower LoA	-1.502 to -0.803	-1.605 ro -0.871	s

(a) Clamping

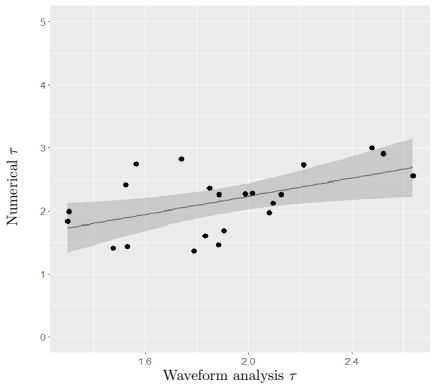

(b) Clamping

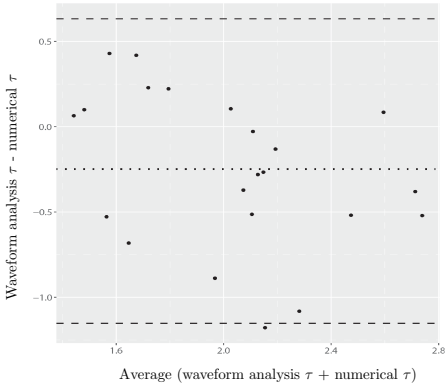

(c) Unclamping

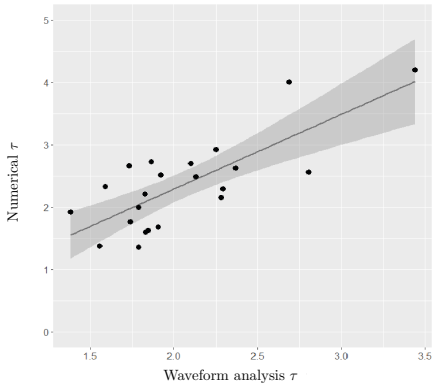

(d) Unclamping

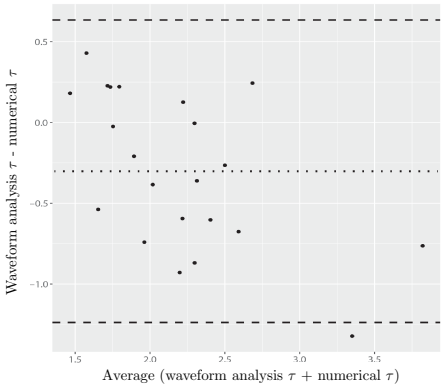

FIGURE 8.9 – Correlation plots between the absolute values of the diastolic time-constant τ estimated by the 0D model and the arterial waveform analysis after (a) clamping and (c) unclamping. Bland-Altman agreement plots between the two methods after (b) clamping and (d) unclamping. (·····) represents the mean difference between the two methods, (---) corresponds the upper and lower LoA (±1.96 SD of the mean difference).

Comparison between proportional changes in the diastolic time-constant

We calculate the overall proportional change in the diastolic time-constant after each intervention for each method. Clamping produces a median 10% [IQR:8-21%] decrease in the time-constant measured by arterial waveform analysis as compared to a median 16% [IQR:7-19%] decrease in the time-constant measured by the numerical model; there are no significant differences between these estimations (p=0.7646). Unclamping produces a median 18% [IQR:9-21%] increase in the time-constant measured by arterial waveform analysis as compared to a median 21% [IQR:14-30%] decrease in the time-constant measured by the numerical model; again there are no significant differences between these estimations (p=0.2061) (Figure 8.8).

Discussion

In this section, we indicated the immediate changes in the diastolic time-constant after abdominal aortic clamping and unclamping during vascular surgery.

The first important finding in this study is that the diastolic time-constant of radial arterial pressure waves before and after aortic cross-clamping and unclamping during vascular surgeries in adult patients can be calculated with two different methods: the arterial waveform analysis and the 0D model of the arterial network. We find that the absolute values of the diastolic time-constant differs in some patients when comparing both methods, thus limiting the 0D model to make patient-specific estimations. Furthermore, there may be a systematic overestimation when applying the numerical model to high values of the diastolic time-constant during unclamping. However, the overall correlation and agreement between measurements seem appropriate. The overall percentage changes in the diastolic time-constant estimated by each method show no significant differences. Additionally, the subset in which there is a possible systematic bias represents only 9% of all data. These results suggest that though the 0D model may have limitations for making patient-specific predictions, it can accurately identify the direction and magnitude of the proportional changes in the diastolic time-constant, similarly to the arterial waveform analysis. In our study, we systematically assess and quantify the correlation and agreement between the 0D model and pressure waveform analysis to measure the diastolic time-constant.

The second important finding in our study is that the diastolic time-constant decreases by 10-16% during clamping and increases by 18-21% during unclamping. These results comply with the only previous study, to our knowledge, that reports changes in the arterial diastolic time-constant during aortic clamping [230]. After abdominal aortic occlusion with a balloon catheter during 2 minutes in 7 male dogs, Van den Bos *et al.* reports a significant 16.6% decrease in the diastolic time constant of arterial pressure waves [230]. This result is comparable to ours in the location of the aortic clamping, the duration of the clamp, and in the magnitude of the reported change. In our study, we systematically find in all patients the decrease in the diastolic time-constant during clamping and its increase during unclamping. Also, as mentioned previously, we find a good agreement between both methods, experimental and numerical, regarding the direction and the magnitude of proportional change. We conclude that the 0D model of the arterial network can offer appropriate estimations of the immediate changes in vascular mechanics after aortic clamping and unclamping. Therefore, we use the 0D model and the parameter estimation process to asses the changes in total resistance and compliance after clamping and unclamping. In fact, the 0D model, unlike arterial waveform analysis can separate the resistive and compliant effects in the diastolic time-constant.

8.5.2 Total vascular resistance and compliance

Proportional changes in total vascular resistance and compliance

The 0D model allows estimating the total resistance ($R_{tot} = R_p + R_d$) and compliance (C) of the systemic arterial circuit. Therefore, we calculate the changes in these parameters after clamping and unclamping. All the calculations for each patient in all four configurations are reported in Table C.2 of Appendix C.

After abdominal aortic clamping, we find a significant 16% increase in the total Mean Vascular Resistance (R_{tot}) (from 1237.1 ± 250.2 g·cm^{-4}·s^{-1} to 1435.0 ± 317.7 g·cm^{-4}·s^{-1}; p=0.0019) and a significant 23% decrease in the mean Vascular Compliance (C) (from $2.25 \pm 0.83 \cdot 10^{-3}$ g^{-1}·cm^4·s^2 to $1.73 \pm 0.68 \cdot 10^{-3}$ g^{-1}·cm^4·s^2; p=0.0002), as shown in Figures 8.10a for R_{tot} and 8.10b for C.

After abdominal aortic unclamping, we find a significant 19% decrease in the total Mean Vascular Resistance (R_{tot}) (from 1241.9 ± 243.1 g·cm^{-4}·s^{-1} to 1003.8 ± 221.9 g·cm^{-4}·s^{-1}; p=0.0007) and a significant 56% increase in the mean Vascular Compliance (C) (from $2.03 \pm 0.75 \cdot 10^{-3}$ g^{-1}·cm^4·s^2 to $3.08 \pm 1.35 \cdot 10^{-3}$ g^{-1}·cm^4·s^2; p=0.001952), as shown in Figures 8.11a for R_{tot} and 8.11b for C.

(a) Resistance

(b) Compliance

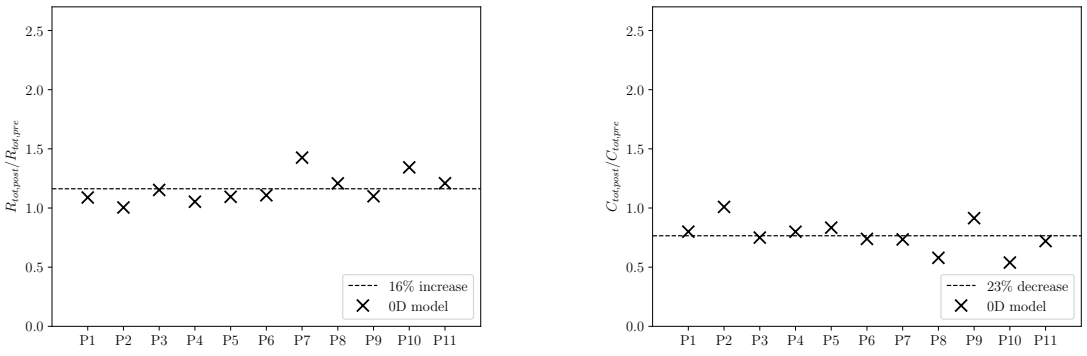

FIGURE 8.10 – Ratio of (a) the total resistance R_{tot} and (b) the total compliance C_{tot} between post-clamp and pre-clamp estimated with the 0D model (×). (---) indicates the median percentage change estimated by the 0D model.

(a) Resistance

(b) Compliance

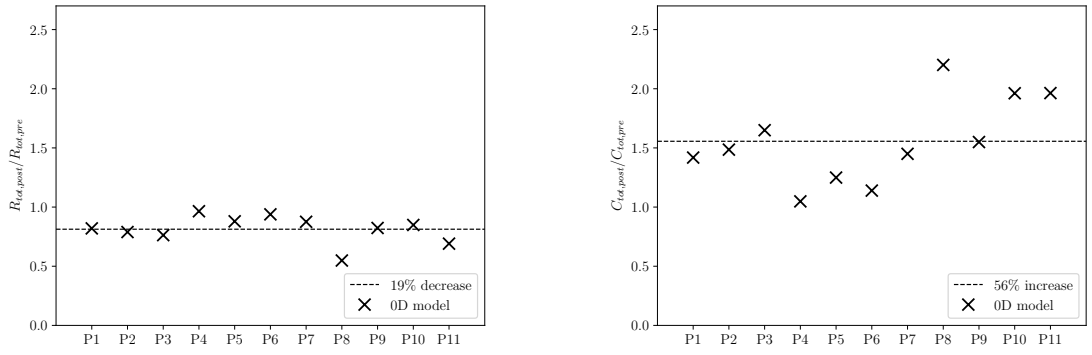

FIGURE 8.11 – Ratio of (a) the total resistance R_{tot} and (b) the total compliance C_{tot} between post-unclamp and pre-unclamp estimated with the 0D model (×). (---) indicates the median percentage change estimated by the 0D model.

Discussion

The important finding in this section is that during abdominal aortic clamping, the total vascular resistance (R_{tot}) increases and the compliance (C) decreases. During unclamping the opposite events occur, added to a local vasodilation of ischemic areas due to the accumulation of adenosine, lactate, and carbon dioxide during clamping [211]. This phenomenon possibly explains why in our study the percentage changes in vascular resistance, and especially in vascular compliance, are larger after unclamping than after clamping. Our results are in agreement with previous studies on the hemodynamic changes of abdominal aortic clamping, reported in Table 8.5. However, these previous studies have described hemodynamical changes 5 to 30 minutes after clamping using invasive methods such as transesophageal echocardiography or pulmonary artery catheters.

Although we cannot discard the influence of biological regulatory phenomena, a simple mechanical reasoning can explain our results. The changes in resistance and compliance after clamping can be interpreted by considering that the 0D model sees the arterial network as an assembly of resistive and compliant vessels connected in parallel. Since the total resistance of a network is the inverse of the sum of the inverse of each vessel resistance, when removing vessels from the circuit (*i.e.*, when clamping), the total resistance should increase. Similarly, as the total compliance is the sum of all vessel compliances, the total compliance should decrease with clamping, which was reported by very few authors in the literature (Table 8.6). Same reasoning goes for unclamping. Though these results may be qualitatively anticipated following this reasoning, the quantification of these changes is only possible through parameter estimation using the Windkessel model. In addition, the study of the hemodynamic impact of aortic clamping has usually focused on systemic arterial pressure and Mean Vascular Resistance, but Vascular Compliance has not been reported since clinical attention has been drawn on this parameter only recently [231].

In the following section, we show the comparison between the 0D, the 1D model, and the measured data of one representative patient (patient 1).

8.6 Comparison between the models and the measured data of one patient

8.6.1 Comparison between the 0D model and the measured data

In the section, we detail the results of one representative patients in terms of resistance, compliance but also heart function using the 0D model.

Using the 0D model and the patient measurements of blood pressure we estimated the patient-specific parameters $\mathcal{P} = \{R_p, R_d, C, T_{ej}\}$ for the pre-clamp and post-clamp configurations. These results, reported in Table 8.7, show a 10% increase in total resistance $R_{tot} = R_p + R_d$ and 20 % decrease in compliance C after clamping. Similar changes in the vascular resistance with clamping are found in [216, 217, 230, 232] and globally in all our patients (Table C.2). We also note that the proximal resistance R_p represents about 15% of the total resistance.

Table 8.7 also shows the changes in heart function, characterized by the three parameters Q_0, T_{ej}, and T_c. The estimated ejection time T_{ej}, which is a percentage of the heart period

Table 8.5 – Review of the literature on the changes in Mean Vascular Resistance (MVR) after clamping and unclamping.

	Clamp		Unclamp		Cohort		
	MVR	Time	MVR	Time	Size	Type	Surgery
Politi *et al.* [77]	**↗ 16%**	**30”**	**↘ 19%**	**30”**	**11**	**Human**	**elective open abdominal aortic aneurysm repair**
Montenij *et al.* [217]	↗ 16.8%	5’	↘ 36.3%	10’	22	Human	elective open abdominal aortic aneurysm repair
Klotz *et al.* [216]	↗ 20%	1-5’	↘ 26%	1-5’	6	Human	reconstructive surgery because of aneurysms
Attia *et al.* [232]	↗ 7.1%	1-3’			5	Human	
Biais *et al.* [213]	↗ 44.5%	10’			24	Pig	
Van Den Bos *et al.* [230]	↗ 22.7%	10’			24	Pig	
Martin-Cancho *et al.* [219]			↘ 55.6%	5’	18	Pig	Laparotomy
Martin-Cancho *et al.* [219]	↗ 38%	30’	↘ 42.4%	30’	18	Pig	Laparotomy
Martin-Cancho *et al.* [219]	↗ 39%	60’	↘ 33.2%	60’	18	Pig	Laparotomy

Table 8.6 – Review of the literature on the changes in Vascular Compliance (VC) after clamping.

	Clamp		Cohort	
	VC	Time	Size	Type
Politi *et al.* [77]	**↘ 25%**	**30”**	**11**	**Human**
Attia *et al.* [232]	↘ 23.2%	1-3’	5	Human
Van Den Bos *et al.* [230]	↘ 17.1%	2’	7	Dog

T_c, does not change significantly. However, the heart period T_c, which was prescribed by the patient data, increases with clamping. Since we assume and thus impose a constant SV, we estimate that the input flow rate Q_0 decreased by 10% with clamping. The morphology of diastole is well reproduced in patients that have a smooth curve as patient 1 (Figure 8.7). However, for patient 3, the dicrotic notch is really present and thus the shape of the diastolic portion of the pressure wave is not accurately reproduced by the 0D model.

We present in Figure 8.12 a comparison between the measured and the simulated pressure signal. The simulated pressure wave results from solving the 0D equation (8.1) with the optimal set of parameters $\mathcal{P}$ for the pre-clamp (Figure 8.12a) and post-clamp (Figure 8.12b), obtained with the step *(i)* of the parameter estimation process. The 0D model gives an accurate general description of the pressure curve in both configurations even though the systolic pressure peak is not well reproduced. The correlation coefficients between the simulated and the measured waves are $R^2 = 0.95$ for the pre-clamp and $R^2 = 0.97$ for the post-clamp.

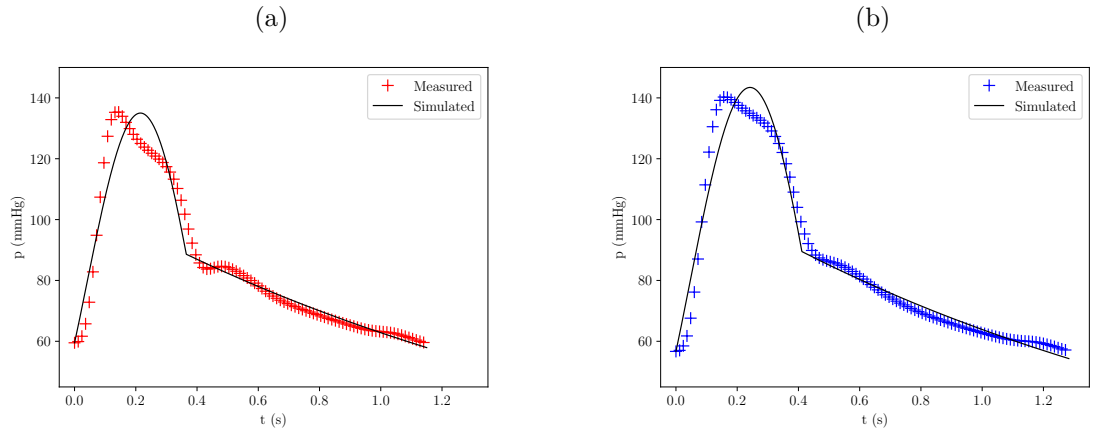

FIGURE 8.12 – Comparison between measured and simulated pressure signals using the 0D model for a patient (patient 1) undergoing aortic clamping during vascular surgery. (a) Pre-clamp configuration, (b) post-clamp configuration. (+) and (+) corresponds to the measured pressure wave of the pre-clamp (respectively the post-clamp) configuration, (——) corresponds to the simulated pressure waves solving Equation (8.1). For the pre-clamp situation, the correlation coefficient between the measured and simulated curve was $R^2 = 0.95$ and for the post-clamp situation $R^2 = 0.97$.

Even though we find a high correlation between the simulated and the measured pressure signal, we want to ensure that the values found with the algorithm minimized the cost function in the physiological parameter space. We therefore evaluate the sensitivity of the cost function $\mathcal{J}$ to the parameters of the 0D model. We represent in Figure 8.13 the cost function $\mathcal{J}^{pre}$ for the pre-clamp configuration as a function of the total resistance R_{tot} and the compliance C for a fixed ejection time $T_{ej} = 31.8\%$ and a fixed ratio between R_p and R_d set to 0.165. Figure 8.13 shows that the values reported in Table 8.7 minimize the cost function $\mathcal{J}$. The two black lines in Figure 8.13 represent the isovalues of the cost function $\mathcal{J}$ that correspond respectively to a +10% and +20% increase of $\mathcal{J}$ with respect to its minimum value. Within the 10% of $\mathcal{J}$, we find a variation of 18% in R_{tot} and a variation of 48% in C. This result shows that the cost function $\mathcal{J}$ is a lot more convex with respect to R_{tot} than C, meaning that the model is more sensitive to a change in total resistance than in compliance. Overall, this suggests that the value of C is less reliable.

TABLE 8.7 – Estimated parameters using the Windkessel model of Equation (8.1) for the pre-clamp and post-clamp configurations in one representative patient. R_p: estimated proximal resistance in g·cm^{-4}·s^{-1}, R_d: estimated distal resistance in g·cm^{-4}·s^{-1}, C: estimated compliance in g^{-1}·cm^4·s^2, T_{ej}: estimated ejection time in percentage of the heart period, T_c: heart period in s fixed by the data, Q_0: estimated amplitude of flow rate in cm^3/s, V_s: calculated Systolic Volume (SV) in cm^3.

	Model parameters			Heart function			
	R_p	R_d	C	T_{ej}	T_c	Q_0	V_s
Pre-clamp	205	1240	$1.29{\cdot}10^{-3}$	31.8	1.15	375	87.2
Post-clamp	260	1313	$1.04{\cdot}10^{-3}$	32.1	1.283	340	89
Changes between pre/post	+ 27 %	+ 6 %	- 20 %	+ 1 %	+ 12 %	- 10 %	—

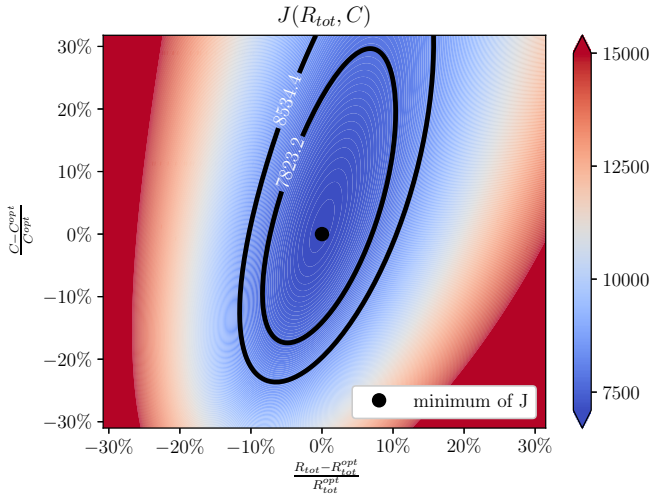

FIGURE 8.13 – Contour plot of the cost function $\mathcal{J}$ for Figure 8.12a as a function of the model parameters R_{tot} and C expressed as percentage of the optimal values R_{tot}^{opt} and C^{opt} respectively (values reported in Table 8.7), with a fixed ratio between R_d and R_p of 0.165 and a fixed ejection time $T_{ej} = 31.8\%$ for the pre-clamp situation. (•) represents the minimum of $\mathcal{J}$ estimated with the optimization process described in Section 8.4.3. (—) represent the isovalues of $\mathcal{J}$ at a +10 and +20 % increase of the minimum of the cost function $\mathcal{J}$.

For the unclamping procedure, we come to the same conclusion. We obtain a high correlation between the simulated and measured pressure waves, as represented in Figures 8.14: $R^2 = 0.95$ for the pre-unclamping configuration, and $R^2 = 0.97$ for the post-unclamping. The changes in total resistance, compliance and heart function are reported in details in Table C.2.

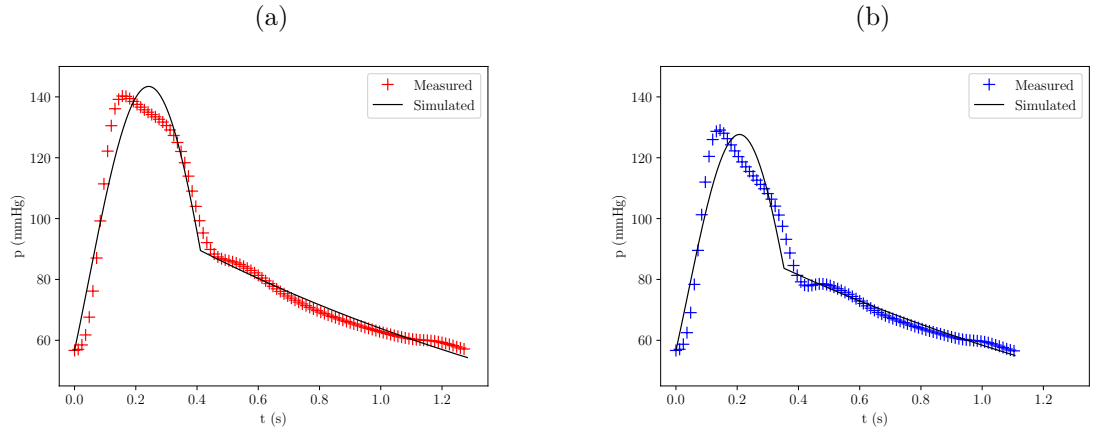

FIGURE 8.14 – Comparison between measured and simulated pressure signals using the 0D model for a patient (patient 1) undergoing aortic unclamping during vascular surgery. (a) Pre-unclamp configuration, (b) post-unclamp configuration. (+) and (+) corresponds to the measured pressure wave of the pre-unclamp (respectively the post-unclamp) configuration, (——) corresponds to the simulated pressure waves solving Equation (8.1). For the pre-clamp situation, the correlation coefficient between the measured and simulated curve was $R^2 = 0.95$ and for the post-clamp situation $R^2 = 0.97$.

8.6.2 Comparison between the 1D model and the patient data

The algorithm presented in Section 8.4.3 allows estimating the values of the resistance boundary conditions r_i, reported in Table 8.8. The values of r_i correspond to physiological values of the peripheral resistances and are similar to those reported in the literature [22]. As described in Section 8.4.3, the resistance boundary conditions r_i of the 1D networks are estimated such that the total resistance matched that of the 0D model. For this reason, there is the same 10% increase in total resistance as the 0D model between the pre-clamp and post-clamp configurations with the 1D model. We observe that both the pre-clamp and post-clamp configurations are fitted without any change in the resistance boundary conditions which means that there is no change in peripheral resistance with clamping. As we impose a constant stroke volume, the post-clamp configuration is fitted with a 10% decrease of the amplitude of the input flow rate compared to the pre-clamp configuration (see Table 8.7).

Similarly to the 0D model, we compare the measured and simulated pressure curves in Figure 8.15. The simulated pressure wave results from solving the 1D equations (2.54) in the 9-artery network with the optimal resistance boundary conditions r_i obtained with the step *(ii)* of the parameter estimation process, presented in Section 8.4.3. The correlation coefficients between the simulated and the measure pressure waves are $R^2 = 0.96$ for the pre-clamp and $R^2 = 0.97$ for the post-clamp configuration.

For similar reasons as the 0D model, the 1D model does not allow fitting properly the systolic portion of the pressure curve. However, we observe that the morphology of the diastolic portion is well reproduced as the 1D model recreates the presence and amplitude of the dicrotic notch [11]. We indeed notice that the amplitude of the notch is attenuated between the pre-clamp and post-clamp configurations, a phenomenon also seen in the simulated pressure wave.

TABLE 8.8 – Estimated resistance boundary conditions r_i of each segment modeling the peripheral circulation in the capillaries, imposed at the outlet of the 1D 9-artery network for the pre-clamp and post-clamp. The values of r_i were estimated automatically using the results from the 0D model with the 3-step process presented in Section 8.4.3. r_i: estimated resistance boundary condition in $g{\cdot}cm^{-4}{\cdot}s^{-1}$ for the pre-clamp and post-clamp configurations, R_t: reflection coefficient.

N°	Name	r_i (pre-clamp)	r_i (post clamp)
1	Aorta arch A	—	—
2	Right subclavian radial artery	$4.6{\cdot}10^3$	$4.6{\cdot}10^3$
3	Aorta arch B	—	—
4	Left carotid artery	$4.6{\cdot}10^3$	$4.6{\cdot}10^3$
5	Aorta arch C	—	—
6	Left subclavian radial artery	$4.6\ {\cdot}10^3$	$4.6\ {\cdot}10^3$
7	Aorta	—	$R_t = 1$
8	Right femoral artery	$30.3\ {\cdot}10^3$	—
9	Left femoral artery	$30.3{\cdot}10^3$	—

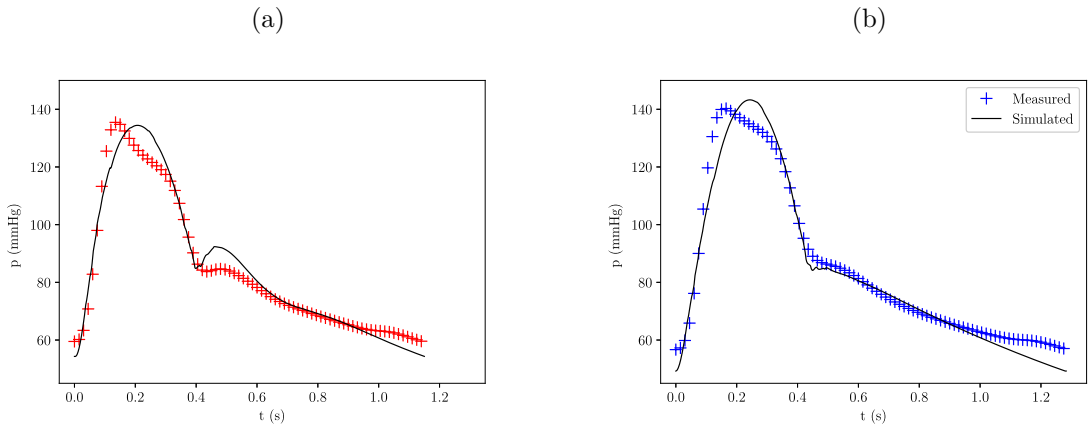

FIGURE 8.15 – Comparison between measured and simulated pressure waves using the 1D model for a patient undergoing aortic clamping during vascular surgery. (a) Pre-clamp configuration, (b) post-clamp configuration. (+) and (+) corresponds to the measured pressure wave of the pre-clamp (respectively the post-clamp) configuration, (—) corresponds to the simulated pressure waves solving Equation (2.54). For the pre-clamp situation, the correlation coefficient between the measured and simulated curve was $R^2 = 0.96$ and for the post-clamp situation $R^2 = 0.97$.

We draw the same conclusions when studying the pre to post-unclamp configuration with the 1D model. First, we observe a 20% decrease of the total resistance. Second, the 1D model is able to reproduce the impact of unclamping by simply adding the legs to the network (Figures 8.16) without changes in the peripheral resistances, reported in Table 8.9. And third, the 1D model cannot properly fit the systolic portion of the pressure curve because of the lack of data on the CO.

TABLE 8.9 – Estimated resistance boundary conditions r_i of each segment modeling the peripheral circulation in the capillaries, imposed at the outlet of the 1D 9-artery network for the pre-unclamp and post-unclamp. The values of r_i were estimated automatically using the results from the 0D model with the 3-step process presented in Section 8.4.3. r_i: estimated resistance boundary condition in g·cm^{-4}·s^{-1} for the pre-clamp and post-clamp configurations, R_t: reflection coefficient.

N°	Name	r_i (pre-unclamp)	r_i (post-unclamp)
1	Aorta arch A	—	—
2	Right subclavian radial artery	$4.6{\cdot}10^3$	$4.6{\cdot}10^3$
3	Aorta arch B	—	—
4	Left carotid artery	$4.4{\cdot}10^3$	$4.4{\cdot}10^3$
5	Aorta arch C	—	—
6	Left subclavian radial artery	$4.6\cdot10^3$	$4.6\cdot10^3$
7	Aorta	$R_t = 1$	—
8	Right femoral artery	—	$14.1\cdot10^3$
9	Left femoral artery	—	$14.1\cdot10^3$

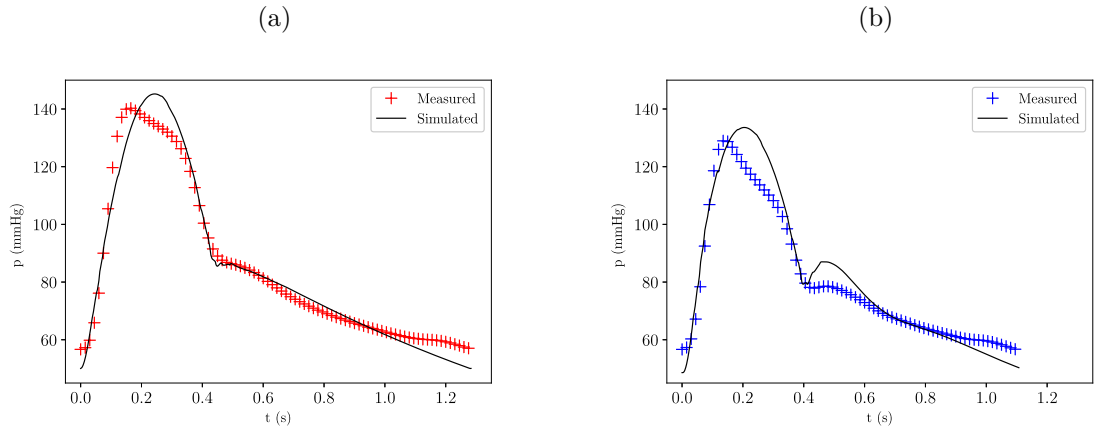

FIGURE 8.16 – Comparison between measured and simulated pressure waves using the 1D model for a patient undergoing aortic unclamping during vascular surgery. (a) Pre-unclamp configuration, (b) post-unclamp configuration. (+) and (+) corresponds to the measured pressure wave of the pre-clamp (respectively the post-clamp) configuration, (—) corresponds to the simulated pressure waves solving Equation (2.54). For the pre-unclamp situation, the correlation coefficient between the measured and simulated curve was $R^2 = 0.96$ and for the post-unclamp situation $R^2 = 0.93$.

8.6.3 Discussion

We showed that the 0D model gives an accurate description of the pressure waves in both the pre-clamp and post-clamp configurations (Figure 8.12), but overall for all four configura-

tions (Figure 8.14). The 0D model offers information on relevant global vascular parameters. Even though lumped analysis may initially be considered outdated, these results indicate that a simple and computationally efficient inverse method is enough to provide access to patient-specific vascular properties. Nevertheless, an important limitation of the 0D model is that it does not take into consideration wave propagation and reflection. These are currently considered major phenomena in vascular physiology and pathophysiology [15], since arterial stiffness studied through Pulse Wave Velocity (PWV) has shown to have a crucial role in the pathogenesis of arterial hypertension and atherosclerosis [231]. In particular, the 0D model has important limitations for describing the pressure wave during diastole (Figure 8.12) since it only fits the diastolic regime with an exponential function.

A sensitivity analysis of the 0D model shows that the model is much more sensitive to changes in total resistance than in compliance. This would suggest that the algorithm estimation of the total resistance of the patient has a higher level of precision, while there is more uncertainty surrounding the estimation of the compliance of the patient. Nonetheless, given that most methods in the literature that estimate arterial compliance are based on two- or three-element Windkessel models [233], it is reasonable to assume that this is currently the state of the art for a minimally invasive estimation of vascular compliance.

Similarly to the 0D model, the 1D model gives an accurate description of the pressure waves in both the pre-clamp and post-clamp configurations (Figure 8.15). However, as opposed to the 0D model, the 1D model accurately reproduces the diastolic part of the measured pressure waves in both the pre-clamp and post-clamp configurations. In particular, the 1D model captured the dicrotic notch [11], a small and brief increase in arterial pressure when the aortic valve closes, as the model accounts for the propagation and reflection of the pulse waves. The 1D model, as an assembly of tubes in which we solve the fluid equations with only a few weak hypotheses, allows recovering the physical properties of the arterial pressure wave that are not considered with the 0D model. We can thus consider that the 1D model is an improvement of the 0D model and allows its validation by giving similar results.

The fitting of the pressure waves with the 1D model is achieved for both configurations without changing the resistance boundary conditions. It suggests that numerical clamping, *i.e.* imposing a total reflection at the end of the abdominal aorta, by itself can reproduce and even predict the impact of surgical clamping on the pressure wave morphology. This result is observed under the assumption that the peripheral resistances would not be affected by clamping because of the short acquisition time. We believe the hypothesis of constant peripheral resistances after clamping would no longer be valid in the long-term due to neuro-hormonal reactions that occur during longer time scales. In conclusion, determining the patient-specific total resistance along with the distribution of peripheral resistances with the parameter estimation process is sufficient for the 1D model to accurately reproduce the impact of clamping on the pressure waveform.

One drawback of the 1D model study is that we use a very reduced arterial network, composed of only nine arteries. Though limited in size, we believe that the network contains the minimal number of arteries needed to describe an average human body. Larger networks (like in [126]) increase the costs, the complexity of the problem and require more sophisticated methods to estimate the resistance boundary conditions, as there are more terminal vessels. In our case, the values from the 0D model are a good starting point for the 9-artery model. Future work will focus on developing an efficient identification technique for a large number

of parameters of the 1D model which would constitute a major improvement of this line of research.

The main drawback of the two models and the overall method is that we do not have access to measured information on continuous heart flow rate. This variable can be calculated in critically ill patients with an invasive central vein catheter using the thermodilution method or during cardiovascular surgeries in high-risk patients with transesophageal echocardiography using continuous-wave Doppler assessment. In this study, neither method was available. Hence, the peak systolic pressure cannot be described in either model because the shape of the model input heart signal (Figure 8.3b) is simplified compared to the physiological heart signal. Moreover, the amplitude of the input flow rate Q_0 cannot be estimated automatically with the 0D model because its value is linked to pressure through the total resistance that we estimated. Nonetheless, we show that the models can assess the change in Q_0 with clamping when assuming that the SV is constant. This change in the amplitude of the input flow rate might be a consequence of our assumption of a constant SV. Due to the lack of measured comparative data, we cannot verify this assumption, which is a limitation of our study. Despite this limitation, we feel that a constant SV is a safe assumption to make for at least three reasons. First, there is no clear prior evidence in the literature that suggests otherwise. Measured data on changes in SV during clamping are available from several small-sized clinical observational studies in adult patients undergoing cardiovascular surgeries. However, some data suggest that SV decreases [213, 215, 218], while others suggest that it stays the same [211, 217, 219]. These inconsistent findings are possibly due to differences in loading conditions, surgery techniques, and patient comorbidities [211]. A second reason to support our assumption of a constant SV is that, since we are interested in studying only the immediate impact of clamping, changes in SV during this short time frame, if any, could be considered as non-significant. Finally, if there are any significant changes due to clamping during this short time frame, they would involve a decrease, not an increase, in SV. However, since our patients all have a preserved left ventricular ejection fraction (*i.e.* a healthy heart), the systolic function of the left ventricle, and therefore the SV, is not expected to decrease during clamping. For these three reasons, we believe that, in spite of the lack of measured data, a constant SV is a safe assumption to make.

8.7 Conclusion

The objective of this work was to investigate the immediate impact of clamping and unclamping during vascular surgery, as it has not previously been explored with macroscopic blood flow models. We compared invasive measurements of pressure in the right radial artery for a cohort of 11 patients undergoing AAA repair or peripheral vascular surgery with the arterial waveform analysis method and the 0D model. We then focused on one patient to study and compare two numerical models (0D and 1D) to the invasive pressure measurements. Both the 0D and 1D model gave a different level of knowledge on the changes that occur immediately after clamping. We developed an inverse method based on patient data to identify patient-specific parameters using a three-element Windkessel 0D model for the systemic circulation. We highlighted two main changes in the vascular properties of the systemic circulation after clamping: on one hand, the total resistance increased by 16% and the total compliance decreased by 23% after clamping, and on the other hand, the total resistance decreased by 19% and the total compliance increased by 56% after unclamping. We showed that the estimated values of the resistance and compliance minimized the difference between the measured

pressure wave and simulated pressure wave. This model allowed determining resistance and compliance, which are useful parameters for interpreting a patient's hemodynamic condition in a critical care scenario, and which cannot be measured non-invasively.

Then we used a 1D model and developed a second parameter estimation technique to identify the values of the resistance boundary conditions. We observed that the numerical clamping can predict and reproduce the morphology of the measured curve without changes in peripheral resistances. On the contrary, heart function adjusted slightly under the action of clamping. We assumed that the SV would not change before and after the clamping event because the data acquisition was carried out in a very short time range. This assumption led to a 10% decrease in the amplitude of the input flow rate during clamping due to an increase in the heart period. Any automatic parameter identification method for problems with a large number of parameters would represent an improvement to the present work.

Overall, this study offers evidence supporting the use of numerical models to assess physiological quantities that cannot be easily measured by physicians (VC) or that can only be measured invasively by a central vein catheter (MVR) under a steady-state. This information on immediate changes in the vascular parameters could be useful for intra-operative patient monitoring and for assessing vascular prosthesis safety, thereby adding valuable information for decision-making in critical care scenarios.

Despite the fact that the estimation of the diastolic time-constant does not bring essential information for peripheral vascular surgeries, the assessment of this parameter is commonly used to study pulmonary hypertension [222–224]. It is indeed useful to explore its value in subgroups of patients with different types of pulmonary hypertension, which is why we investigate it in the following Chapter.

9 Pulmonary Hypertension

Pulmonary hypertension is a complex pathology that involves multiple clinical conditions and can complicate many forms of heart failure. We carry invasive pressure measurements from the right heart and pulmonary vascular network in one patient with heart failure using a Swan-Ganz catheter. We first study the Windkessel model of the pulmonary vascular network to evaluate the patient-specific hemodynamics involved in heart failure and pulmonary hypertension, which are difficult to assess through routine clinical studies. We then develop a 0D valve model to couple to the 1D blood flow model representing the pulmonary vascular network and compare the invasive pressure measurements with the numerical predictions of the 1D model.

Keywords: pulmonary hypertension, Swan-Ganz catheter, one-dimensional model, valve model.

Contents

9.1 Introduction

Pulmonary hypertension is a complex pathology that involves multiple clinical conditions and can complicate many cardiovascular and respiratory diseases [234]. Pulmonary hypertension is a rare condition, with less than 50 cases per million people. However, the consequences of the disease for those affected are often really severe.

Pulmonary hypertension is defined as an increase in mean pulmonary arterial pressure over 25 mmHg at rest, assessed by right heart catheterization. Right catheterization is a requirement for the diagnostic confirmation of pulmonary arterial hypertension and chronic pulmonary hypertension due to pulmonary embolism. Some specific indicators assessed by catheterization such as the pressure in the heart cavities, the transpulmonary pressure gradient, or the Systolic Volume (SV) allow classifying patients with pulmonary hypertension into various subgroups that have clinical and therapeutic relevance [235, 236]. For instance, a subgroup of these patients presents pre-capillary pulmonary hypertension, defined by a Left Atrium (LA) pressure above 15 mmHg and a pulmonary vascular resistance of 3 Wood units ($\approx$ 240 g·cm^{-4}·s^{-2}). This condition has a distinct clinical prognosis and therapeutic management as a group [237] that differs from patients with thromboembolism for instance.

In order to assess these classifying parameters, we carry right heart catheterization using Swan-Ganz catheter to record the pressure in several locations of the heart and pulmonary network. Similarly to the previous chapter, numerical models of the pulmonary network can provide information on important vascular features including compliance and resistance, given hemodynamic data obtained during medical care such as pressure and flow measurements. One of the conclusions of Chapter 8 was to apply the zero-dimensional (0D) Windkessel model to the pulmonary vascular network and assess the resistance, compliance, and diastolic time-constant [77]. These parameters could have relevance in the classification of pathologies associated with pulmonary hypertension [222–224]. Therefore in this chapter, we use the Windkessel model to estimate the resistances, compliance, and diastolic time-constant of both the pulmonary vascular network and the entire vascular network based on the invasive pressure measurements.

Besides evaluating vascular features such as resistance or compliance, the long-term goal of this study is to evaluate the influence of different pathological conditions, for instance high Left Atrium (LA) pressure or pulmonary embolism, on the pulmonary artery pressure. We thus use a one-dimensional (1D) model of the pulmonary vascular system [71] which we couple to a 0D valve model to represent the pulmonary valve [59].

The objective of this study is then to compare the numerical predictions of the 0D and 1D models with the invasive data in the pulmonary vascular network. It brings insights on the mechanical characteristics of the pulmonary circulation that cannot be calculated directly with the usual invasive diagnostic methods. The models also provide an alternative method for calculating relevant indicators such as the compliance whose measurement precision is questioned.

The chapter is organized as follows: in Section 9.2, we detail the clinical protocol to carry the Swan-Ganz catheter measurements and obtain other data. In Section 9.3, we briefly describe the 0D Windkessel model (presented in detail in the previous chapter), the 1D model, and the pulmonary valve model. In Section 9.4, we present the results of the 0D and

1D models and compare them to the measured data. We summarize our results and give perspectives in Section 9.5.

9.2 Swan-Ganz catheter measurements

The experimental data come from right heart catheterization, which is an invasive diagnostic procedure to evaluate the hemodynamic state of patients with heart failure and the pulmonary vascular resistances of patients with pulmonary hypertension. This is a cross-sectional, observational, and analytical study, with prospective data collection, carried at the Cardiovascular Institute of Buenos Aires (ICBA) that seeks to characterize the vascular mechanics of patients undergoing right catheterization. This data acquisition is carried in parallel with routine medical monitoring, without causing any harm to it or changes in the data.

To carry these measurements we use a fluid-filled Swan Ganz catheter connected to a disposable pressure transducer (TruWave, Edwards LifeScience) with an analog-to-digital converter with internal filters (low-pass frequency set to 20 kHz; high-pass frequency set to 0.05 Hz, MP150 BIOPAC Systems Inc.). The AcqKnowledge program records 20 to 40 beats of the blood pressure signal at a frequency of 1000 Hz. From the pressure sequence, we choose a stable set of beats that we average to obtain a mean beat that we use for comparison with the numerical models described in Section 9.3.

Right heart catheterization consists of measuring the pressure from the right heart and pulmonary vascular network in five locations: Right Ventricle (RV), proximal and distal pulmonary arteries, Left Atrium (LA) and right radial artery, as shown in Figure 9.1. The proximal pulmonary artery pressure is recorded in the main pulmonary artery, the distal pulmonary artery pressure is in the third generation of the pulmonary tree. To measure the pressure in the LA (measurement 4 in Figure 9.1), we inflate a balloon at the location of the distal measurement and record the pressure after this balloon. As all these measurements are not taken simultaneously, we use the Electrocardiogram (EKG) to synchronize the pressure data. We also carry thermodilution to obtain the Cardiac Output (CO) which allows calculating the Systolic Volume (SV) [238]. Computed Tomography (CT) scans allow visualization of the pulmonary vascular tree to obtain the length, proximal and distal diameters of each vessel of the first three generations. We also collect velocity data from the right ventricle outflow tract using two-dimensional transthoracic Doppler echocardiography [239, 240].

This study enrolls patients undergoing right catheterization for medical indication of any cause. Patients with clinical instability, who are under treatment with inotropics, those with a blood pressure curve that makes the analysis of the diastolic time-constant impossible for technical reasons, and those with an irregular ventricular rhythm are excluded.

We represent in Figure 9.2 the measured pressure in the 4 locations of the pulmonary network of a 70-years old female patient with acute heart failure due to stress cardiomyopathy, presenting with type 2 pulmonary hypertension owing to left heart disease (following 2008 Dana Point pulmonary hypertension classification [237]). The measurements are taken in the intensive care unit (ICU) with the patient sedated, intubated, and under mechanical ventilation and receiving inotropic agents (low-medium dose of milrinone).

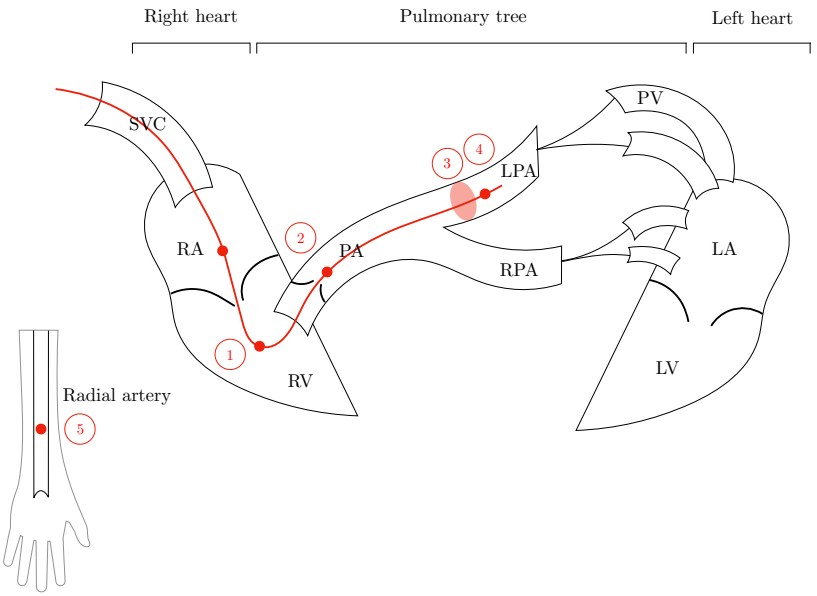

FIGURE 9.1 – Schematic representation of the heart cavities and the pulmonary vascular network indicating the locations of the Swan-Ganz pressure measurements. Measurement 1 is in the Right Ventricle (RV) called P_V, measurement 2 is in the proximal pulmonary artery (PA), measurement 3 is in the distal pulmonary artery which is in the third generation of the pulmonary tree, measurement 4 is at the same location as measurement 3 but with a balloon occluding the artery corresponding to the Left Atrium (LA) pressure also called the wedge pressure P_W, measurement 5 is in the right radial artery.

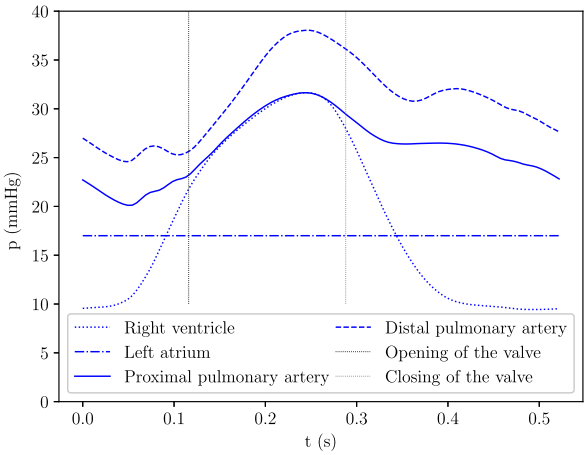

FIGURE 9.2 – Swan-Ganz pressure measurements in the pulmonary network. (·····) corresponds to the Right Ventricle (RV) pressure (measurement 1), (-·-·) corresponds to the Left Atrium (LA), or wedge, pressure (measurement 4), (——) corresponds to the proximal pulmonary artery pressure (measurement 2), and (- - -) corresponds to the distal pulmonary artery pressure (measurement 3). (·····) corresponds to the opening of the valve and (·····) corresponds to the closing of the valve.

From Figure 9.2, we identify the opening and closing of the valve when there is less than 1.5 mmHg of difference between the ventricle and proximal pulmonary artery pressure. We obtain that the valve opens at $t = 0.12$ s and closes at $t = 0.29$ s. From this data, we can identify pre-capillary pulmonary hypertension, as the wedge pressure is above 15 mmHg.

9.3 Model and methods

9.3.1 Zero-dimensional model

We use the same 0D Windkessel model as in Chapter 8 described in Equation (8.1) to model (a) the entire systemic circulation and (b) the pulmonary circulation. For the entire systemic circulation we set the pressure $p(t)$ of Equation (8.1) as the right radial artery pressure. For the pulmonary circulation, we consider that $p(t)$ is the difference between the pulmonary artery pressure P_{PA}, either the proximal or distal, and the wedge pressure P_W, as represented in Figure 9.3.

In both cases we use the Basin Hopping algorithm combined to the L-BFGS-B gradient descent described in Section 4.3 to estimate the vascular resistances and compliance based on (a) the radial artery pressure (measurement 5 in Figure 9.1) and (b) the pulmonary artery pressure (measurement 2 and 3 in Figure 9.1).

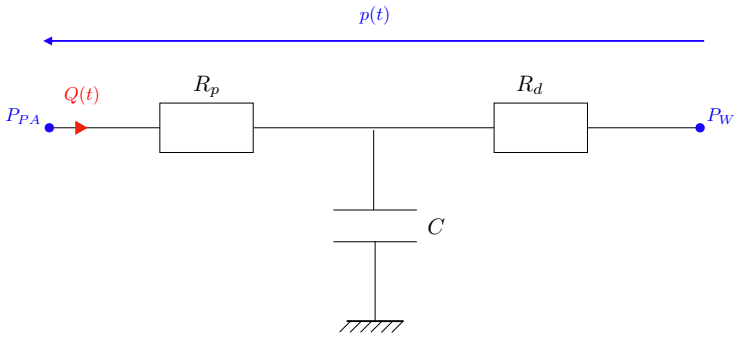

FIGURE 9.3 – Electrical representation of the 0D Windkessel model of the pulmonary vascular network. The pressure $p(t)$ is the difference between the pulmonary artery pressure P_{PA} and the wedge pressure P_W. The pressure $p(t)$ is linked to the flow rate $Q(t)$ that models the heart, through Equation (8.1) where R_p is the proximal resistance, R_d is the distal resistance, and C is the compliance.

9.3.2 One-dimensional model

We use the 1D model of Equation (2.54) to represent the pulmonary vascular network [71] described in Section 2.3.4. The network consists of three generations of 1D branches and resistances at the end of the terminal vessels to account for capillary circulation, as shown in Figure 9.4. We assume that all the peripheral resistances have the same value.

TABLE 9.1 – Geometric and material properties of the pulmonary artery network model taken from [71] and CT scans. L: length in cm, D_0: reference diameter in cm, h: arterial wall thickness cm, K: elastic coefficient of Equation (2.15) in g·cm^{-2}·s^{-2}, R: peripheral resistance in g·cm^{-4}·s^{-1}.

N°	Name	L	D_0	h	K	R
1	Pulmonary Artery	4.5	2.6	0.1	$6.94 \cdot 10^4$	—
2	Left Pulmonary Artery	3	2	0.1	$9.03 \cdot 10^4$	—
3	Right Pulmonary Artery	5.2	2.25	0.1	$8.02 \cdot 10^4$	—
4	Left Interlobular Artery	1.3	1.4	0.1	$1.29 \cdot 10^5$	$7.5 \cdot 10^2$
5	Left Trunk Artery	1.8	1.5	0.1	$1.20 \cdot 10^5$	$7.5 \cdot 10^2$
6	Right Trunk Artery	1.5	1.2	0.1	$1.50 \cdot 10^5$	$7.5 \cdot 10^2$
7	Right Interlobular Artery	1.5	1.1	0.1	$1.64 \cdot 10^5$	$7.5 \cdot 10^2$

The geometric properties, reported in Table 9.1, come from CT scan measurements. We impose the elastic coefficient K of each vessel by assuming that the compliance Eh/R_0 is constant based on [71], and we fix it at $12{\cdot}10^4$ g·cm^{-1}·s^{-2}.

For the boundary conditions, we develop a valve model (detailed in the following section) that we input as the inlet boundary condition. We impose the LA pressure, also called the wedge pressure P_W, as the outlet boundary condition.

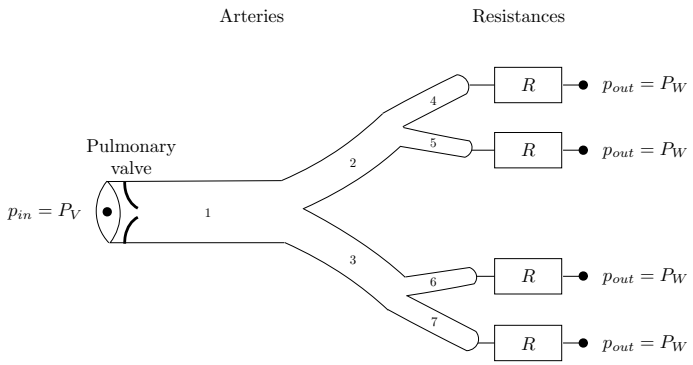

FIGURE 9.4 – Pulmonary vascular network model. The inlet boundary condition is the RV pressure P_V, the outlet boundary conditions are the LA pressure P_W. The properties of the network are reported in Table 9.1.

9.3.3 Pulmonary valve model

We couple the 1D Equations (2.54) to a pulmonary valve model. The functioning of the valve is the following: if the RV pressure is lower than the pressure in the first pulmonary artery, then the valve is closed, otherwise it is open. When the valve is open, there is a continuity

of pressure between the RV and the first pulmonary artery. This phenomenon translates into the following:

$$\begin{aligned} &\textbf{if} \quad p_{in} < p_0 \quad \textbf{then} \\ &\qquad\qquad \text{closed valve model} \\ &\textbf{else} \\ &\qquad\qquad p_{in} = P_V, \end{aligned} \tag{9.1}$$

where p_{in} is the RV pressure, *i.e.* the inlet boundary condition, and p_0 is the pressure in the first pulmonary artery.

We find different types of valve models in the literature. The valve is usually modeled as a pressure drop linked to the flow rate with one or more of the three following parameters that characterize the unsteadiness, the non-linearity, and the resistive behavior of the valve [241–245]. Some similar valve models can also be coupled to an equation on the dynamics of the valve opening as in [59].

Conceptually, the most straight forward model consists of imposing a zero flow when the inlet pressure p_{in} is lower than the pressure p_0 in the first pulmonary artery. More precise approaches consist of modeling the valve with a 0D model, similar to the one of Equation (2.66). The simplest one is by assuming a resistive behavior of the valve as in most models of the literature [59, 241–245], which gives the following model, similar to the one of Equation (2.68)

$$R_v Q = p_{in} - p_0 \tag{9.2}$$

with R_v a coefficient characterizing the resistance of the valve. Depending on the value of R, the valve is fully, partly, or completely closed, which we investigate in Section 9.4.2. Other model of the literature also include an inertance to the valve model which leads to the following

$$R_v Q + I\frac{\mathrm{d}Q}{\mathrm{d}t} = p_{in} - p_0 \tag{9.3}$$

with I the coefficient characterizing the inertance of the valve. The expression of this coefficient is $\rho l_{eff}/A_{eff}$ (Equation (2.67c)), where l_{eff} is the inertial length and A_{eff} the effective area of the valve.

9.4 Result

9.4.1 Result of the zero-dimensional model

In the following, we show the result of the parameter estimation of the Windkessel model on the right radial artery pressure and the pulmonary artery pressure.

Right radial artery pressure

We use the Windkessel model to estimate the two vascular resistances R_p and R_d as well as the compliance C from the right radial artery pressure. We impose Q_0 and T_{ej} using invasive measurements of the CO and SV from thermodilution.

TABLE 9.2 – Estimation of the total resistance and compliance from the radial artery pressure using the Windkessel model of Equation (8.1). R_p: proximal resistance in g·cm^{-4}·s^{-1}, R_d: distal resistance in g·cm^{-4}·s^{-1}, C: compliance in g^{-1}·cm^4·s^2, τ: diastolic time-constant in s T_{ej}: ejection time in percentage of heart period, T_c: heart period in s, Q_0: amplitude of the input flow rate in cm^3/s, V_s: Systolic Volume (SV) in cm^3.

Model parameters			Calculation	Heart function			
R_p	R_d	C	τ	T_{ej}	T_c	Q_0	V_s
165	1538	$2.48{\cdot}10^{-3}$	3.81	42	0.52	286	39

The results of the parameter estimation are reported in Table 9.2. We obtain similar orders of magnitude for the resistances and compliance as found in the case of patients undergoing aortic cross-clamping during vascular surgery (Tables 8.7 and C.2). We notice that the diastolic time-constant of this patient is higher than the values found in patients undergoing vascular surgeries.

We observe in Figure 9.5 that the Windkessel model fits the radial artery pressure with high accuracy (correlation coefficient $R^2 = 0.98$). The agreement between the measured and simulated pressure of a patient with pulmonary hypertension is satisfying, similarly to the same comparison in the case of a patient undergoing aortic cross-clamping during vascular surgery (Figures 8.7 and 8.12).

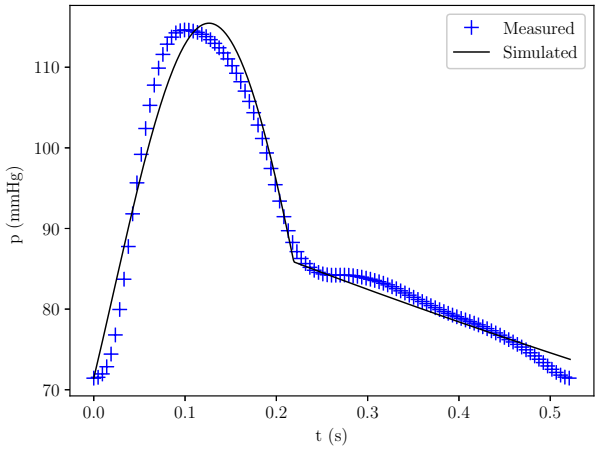

FIGURE 9.5 – Comparison between measured and simulated pressure waves in the right radial artery using the 0D model. (+) corresponds to the measured pressure wave, (—) corresponds to the simulated pressure waves solving Equation (8.1).

As mentioned previously, the interest of the Windkessel model is to obtain information on importation vascular features that cannot be obtained otherwise. The measurement of the radial artery pressure is minimally invasive and gives access to the total resistance and compliance, provided a measurement of the CO which is invasive. These parameters can be relevant indicators to follow up the evolution of the disease or can allow classifying the pathologies related to pulmonary hypertension.

For now, we only study one patient which prevents us from discriminating pathologies according to the values of resistance, compliance, or diastolic time-constant. We also cannot relate these values to medication or comorbidities. However, in the near future, we will enroll more patients in this study. It will allow using the model to estimate important vascular indicators and thus separate the effects of each disease on the resistance, compliance, and diastolic time-constant.

Pulmonary artery pressure

We do the same process as in the previous section but based on the proximal and distal pulmonary artery pressure. The parameter estimation process provides values of the pulmonary vascular resistances R_p and R_d and compliance C.

In Table 9.3, we report the optimal values of resistances and compliance found with the Windkessel model estimated from the proximal and distal pulmonary artery pressure. We compare them to the measured values of resistance and compliance. The measured pulmonary vascular resistance, corresponding to $R_p + R_d$ in the model, is calculated by dividing the transpulmonary pressure gradient by the CO [246]. The transpulmonary pressure gradient is the difference between the mean pulmonary artery pressure P_{PA_m} and the wedge pressure P_W [235]. The mean pulmonary artery pressure is

$$P_{PA_m} = \frac{1}{3}P_{PA_s} + \frac{2}{3}P_{PA_d}, \tag{9.4}$$

where $P_{PA_{m,s,d}}$ stand for the mean, the systolic, and the diastolic pressure in the pulmonary artery. The systolic pressure is the maximum and the diastolic is the minimum value of the pressure over a cardiac cycle. The pulmonary vascular compliance is calculated by dividing the SV by the difference between the systolic and diastolic pulmonary artery pressure.

We observe in Table 9.3 that the Windkessel model tends to overestimate the values of resistances and compliance compared to the measured values. The proximal parameters are overestimated by 30-40%, the distal parameters by 15-30%. The orders of magnitude remain however really close. The pulmonary vascular resistance is a classifying parameter suggested by the guidelines [238] and the 0D model can assess it.

We note that the diastolic time-constant of the pulmonary artery pressure is much smaller than the one based on the radial artery pressure. We remind that the diastolic time-constant cannot be directly deduced from the invasive data as $\tau = R_dC$ and the measurements only provide a value of the total resistance, *i.e.* $R_p + R_d$. The diastolic time-constant could be a decisive indicator of the type of pulmonary hypertension of the patient, however, as we only study one patient it is still difficult to relate this parameter to pathologies.

In Figure 9.6, we compare the Windkessel model to the proximal and distal pulmonary artery pressure waves. For the proximal pulmonary artery pressure, the agreement between the measured and simulated pressure waves is $R^2 = 0.94$, for the distal pulmonary artery pressure, it is $R^2 = 0.90$, which are high correlation coefficients. However, qualitatively, the fit is not satisfying. We observe that for both the proximal and distal pressure, the diastolic portion of the pressure curve does not have an exponential-like morphology and thus cannot be correctly fitted by the Windkessel model. Although it provides a satisfying estimation of

TABLE 9.3 – Estimation of total resistance and compliance from the pulmonary artery pressure using the Windkessel model of Equation (8.1). R_p: proximal resistance in g·cm^{-4}·s^{-1}, R_d: distal resistance in g·cm^{-4}·s^{-1}, C: compliance in g^{-1}·cm^4·s^2, τ: diastolic time-constant in s T_{ej}: ejection time in percentage of heart period, T_c: heart period in s, Q_0: amplitude of the input flow rate in cm^3/s, V_s: Systolic Volume (SV) in cm^3.

		Model parameters			Calculation	Heart function			
		R_p	R_d	C	τ	T_{ej}	T_c	Q_0	V_s
Proximal	Simulated	28	167	$4.04{\cdot}10^{-3}$	0.67	54	0.52	215	38.5
	Measured	148		$2.48{\cdot}10^{-3}$	—	—	0.52	—	38.2
Distal	Simulated	26	227	$3.09\ {\cdot}10^{-3}$	0.7	58	0.52	205	39.5
	Measured	219		$2.13{\cdot}10^{-3}$	—	—	0.52	—	38.2

the vascular resistance and compliance, the 0D model is not appropriate for analyzing the pressure curve in the pulmonary circulation. Therefore, we use a 1D model of the pulmonary circulation and present the results in the following section.

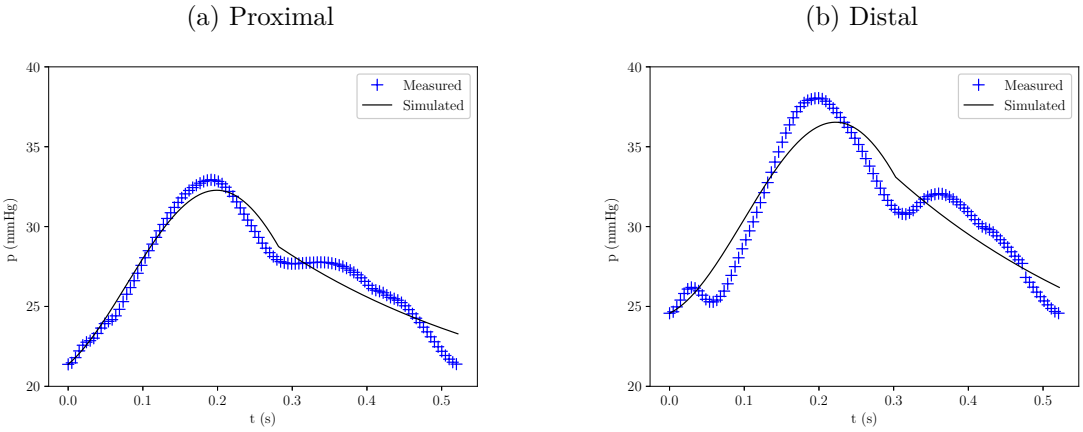

FIGURE 9.6 – Comparison between measured and simulated pressure waves in (a) the proximal pulmonary artery ($R^2 = 0.94$) and (b) the distal pulmonary artery ($R^2 = 0.90$) using the 0D model. (+) corresponds to the measured pressure wave, (——) corresponds to the simulated pressure wave solving Equation (8.1).

9.4.2 Results of the one-dimensional model

We present in the following the tests of the valve model, the comparison with the invasive data, and investigate the influence of different parameters on the pulmonary artery pressure signal.

Test of the valve model

We first verify that the valve model is valid. In Figure 9.7, we show the flow rate in the first pulmonary artery for two values of the resistance R_v of Equation (9.2): a small R_v in Figure 9.7a and a large R in Figure 9.7b. With a small resistance, we observe that there is a

backflow which means that the blood can go backward after crossing the valve, which is not what happens physiologically. When the resistance is large, we notice that the flow is blocked ($Q = 0$) and that the model actually prevents backflow, *i.e.* the flow rate is never negative.

We also show the pressure in the first pulmonary artery for the two values of the resistance. We observe that with a small resistance (Figure 9.7c), the valve is always open because the pulmonary artery pressure is actually the ventricle pressure P_V. On the contrary, when the resistance is large (Figure 9.7d), the pulmonary artery pressure is different from the ventricle pressure which indicates that the valve indeed closes and opens. We conclude that with a large resistance, our valve model behaves as expected.

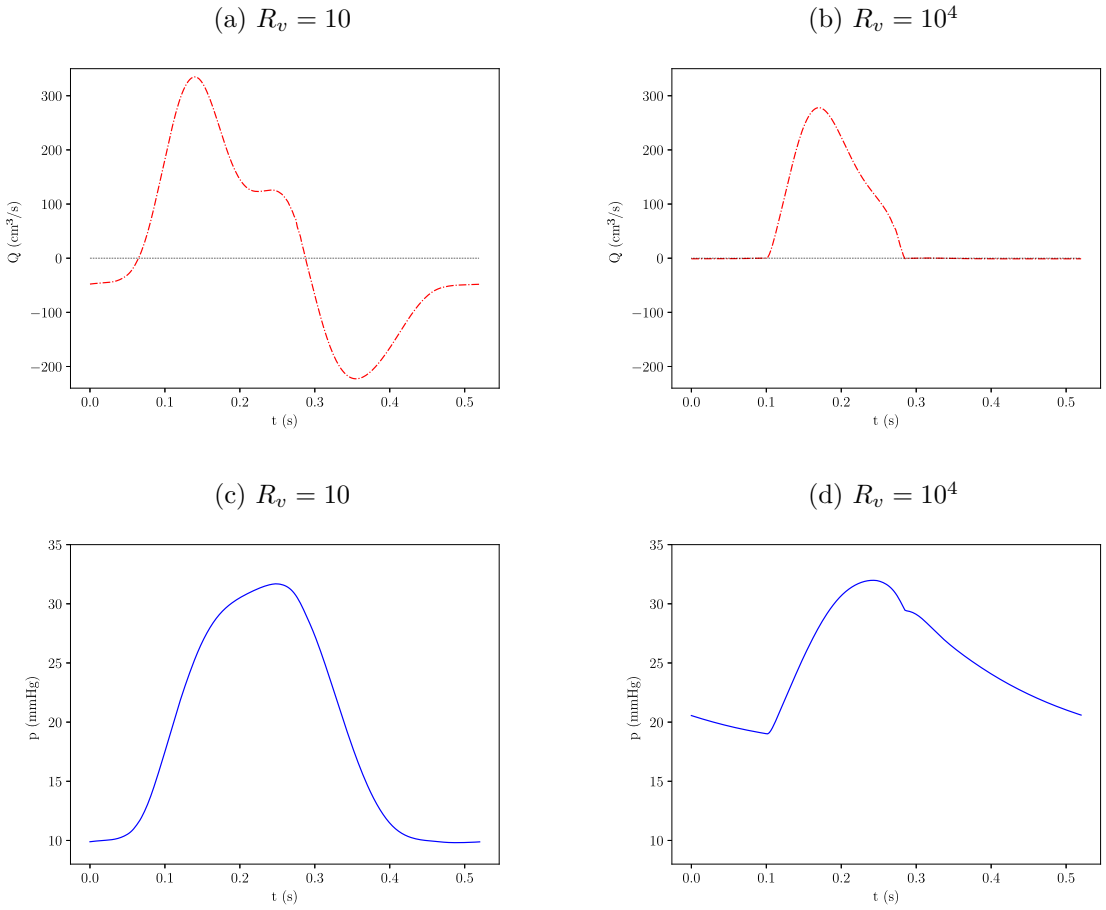

FIGURE 9.7 – Simulated (a) and (b) flow rate, (c) and (d) pressure in the first pulmonary artery to test the valve model of Equation (9.2). (a) and (c) $R_v = 10$ g·cm^{-4}·s^{-1}, and (b) and (d) $R_v = 10^4$ g·cm^{-4}·s^{-1}.

To confirm that the valve model works, we plot the imposed pressure (the ventricle pressure P_V) and the pulmonary artery pressure in Figure 9.8. When the valve is open, the pulmonary pressure is supposed to match the ventricle pressure, which is the case for any valve, in particular the aortic valve as represented in Figure 1.6. We indeed observe in Figure 9.8 that the pressure in the pulmonary artery is the pressure in the ventricle (see Figure 9.2) when the valve is open which is when the flow rate is positive. We also recognize the dicrotic notch right after the valve closes [11].

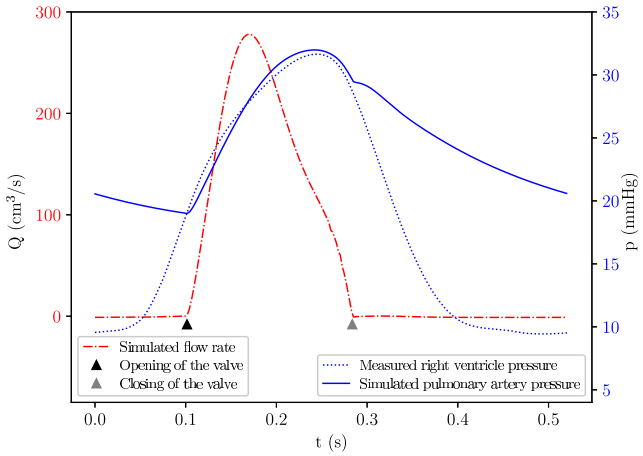

FIGURE 9.8 – Flow rate (in red) and pressure (in blue) in the pulmonary network. (·····) corresponds to the measured ventricle pressure P_V that is imposed as a boundary condition before the valve, (——) corresponds to the simulated pulmonary artery pressure in the first pulmonary artery, (-·-·-) corresponds to the simulated flow rate in the first pulmonary artery, (▲) corresponds to the opening of the valve, (▲) corresponds to the closing of the valve.

Comparison with the invasive data

As the valve model of Equation (9.2) is valid, we now compare the predictions of the 1D model to the invasive data presented in Section 9.2. In Figure 9.8, we can identify the time of opening and closing of the valve and compare it to the measured times. With the 1D model, the valve opens at $t = 0.10$ s and closes at $t = 0.28$ s. The model predicts a valve opening and closing 0.01 s too early compared to the experimental estimation. The duration of the ejection, which is the time when the valve is open, is however the same.

In Figure 9.9, we show the measured and the simulated flow rate in the first pulmonary artery. The amplitude, the width, and the morphology of the measured and simulated flow rate are truly similar. The peaks are not synchronized, and we recover that the model predicts an early opening and closing compared to the measured data.

Finally, in Figures 9.10 we compare the measured and simulated pressure waves in the proximal (Figure 9.10a) and the distal (Figure 9.10b) pulmonary arteries. We observe that the amplitude and mean pressure of the simulated curve matches those of the measured curve in the proximal pulmonary artery. However, the morphology of the two signals is very different: the numerical prediction of the 1D model is smoother than the data. The reflections are not accounted for accurately with the model.

In Figure 9.10b, we represent the distal pulmonary artery pressure and we notice that neither the mean pressure nor the morphology of the pressure are correct. The reflections are not reproduced accurately by the 1D model either, the simulated signal is smoother. For that reason, the simulated distal resistance does not correspond to the measured distal resistance, as reported in Table 9.4.

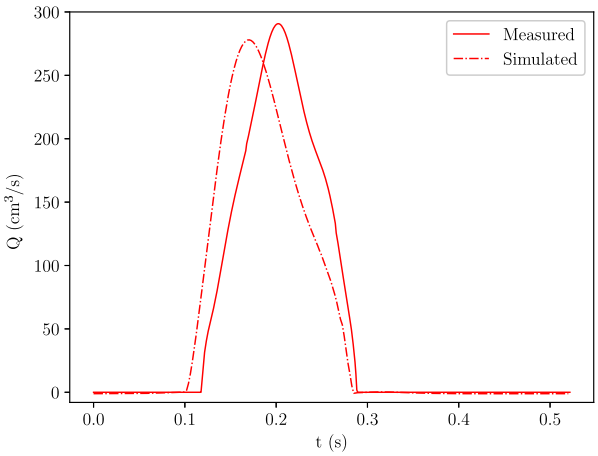

FIGURE 9.9 – Comparison between the measured and the simulated flow rate in the first pulmonary artery using the 1D model. (—) corresponds to the measured flow rate with Doppler echocardiography, (-·-·) corresponds to the simulated flow rate solving Equation (2.54) in the network with the properties reported in Table 9.1.

(a) Proximal

(b) Distal

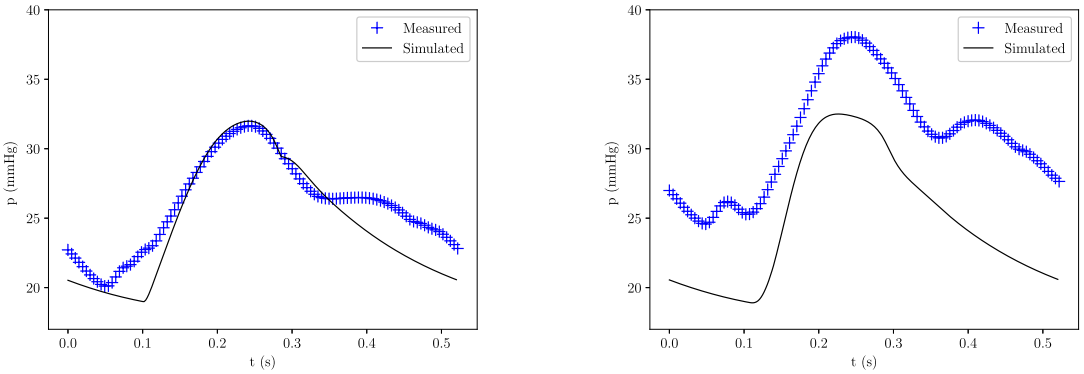

FIGURE 9.10 – Comparison between measured and simulated pressure waves in (a) the proximal pulmonary artery and (b) the distal pulmonary artery using the 1D model. (+) corresponds to the measured pressure wave, (—) corresponds to the simulated pressure waves solving Equation (2.54) in the network with the properties reported in Table 9.1.

We also notice that the mean pressure does not change drastically between the proximal (first pulmonary artery) and the distal pulmonary artery (third generation) compared to the measurements. Previous studies however show that the tappering of the vessels plays an important role in increasing the mean pressure of the distal pulmonary arteries [71, 247]. It would thus be relevant to take it into account to improve the fit of the data by the 1D model. Overall, the 1D model does not reproduce correctly the changes in pressure that occur in the pulmonary network.

In Table 9.4, we compare the measured and simulated properties of the network. We note that the proximal resistance fits perfectly the data, but the distal resistance, the CO, and

TABLE 9.4 – Comparison between the simulated and measure properties of the pulmonary network using the 1D model. R_p: proximal resistance in g·cm^{-4}·s^{-1}, R_d: distal resistance in g·cm^{-4}·s^{-1}, CO: Cardiac Output in mL/min, V_s: Systolic Volume (SV) in cm^3.

	R_p	R_d	CO	V_s
Simulated	152	156	3.31	28.8
Measured	148	219	4.4	38

the Systolic Volume are underestimated by the 1D model.

As we do not manage to fit the pulmonary artery pressure accurately, we try relaxing a few parameters of the model. For instance, we account for the veins in the pulmonary tree, however it does not improve the fit, neither in terms of morphology nor in terms of mean pressure. We try decreasing the elastic coefficient K of the third generation which slightly improves the fit of the data. We also relax the hypothesis that all the peripheral resistances have the same value which also improves the fit of the pulmonary artery pressure. Considering the large amount of geometric, mechanical, physiological, or model parameters, it is challenging to find the optimal combination to fit accurately the data.

Influence of different pathologies on the pulmonary artery pressure

Besides evaluating vascular features such as resistance, compliance, and diastolic time-constant for patient-specific predictions, the long-term goal of this study is to explore the influence of different pathological conditions on the pulmonary artery pressure. In Figure 9.11, we investigate the influence of LA pressure on the proximal (Figure 9.11a) and distal (Figure 9.11b) pulmonary artery pressure as in [71].

An increase in LA pressure mainly changes the duration of the valve opening thus decreasing the SV. As can be expected, an increase in the wedge pressure leads to an increase in the mean pressure in the proximal and distal pulmonary arteries. We note from Figure 9.11b that P_W also influences the reflections in the pulmonary vascular network as the morphology, in particular the peak, of the pressure changes slightly with P_W.

Some patients with pulmonary hypertension also present a high vascular resistance, which we study in Figure 9.12. The increase in peripheral resistance also tends to reduce the duration of the valve opening, the SV, and the mean pressure. It also changes the propagation and reflections of the wave in the distal pulmonary artery (Figure 9.12b). We also note that, unlike an increase in wedge pressure, an increase in peripheral resistance tends to change the morphology of diastole as the reflections are modified.

These preliminary results show great potential for the 1D model to reproduce and predict the hemodynamics of the pulmonary vascular network, qualitatively and quantitatively. Moreover, our results comply with previous studies [16, 71, 247].

(a) Proximal (b) Distal

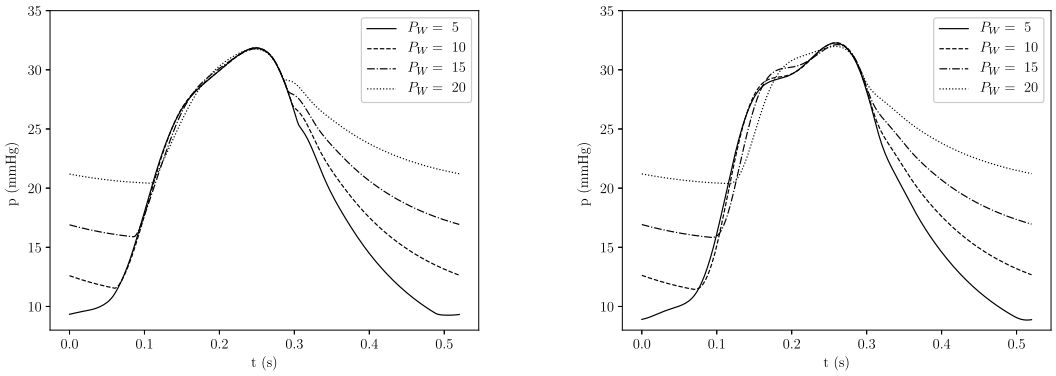

FIGURE 9.11 – Effect of LA pressure on the morphology of (a) the proximal and (b) the distal pulmonary artery pressure. (——) corresponds to $P_W = 5$mmHg, (- - -) to $P_W = 10$mmHg, (-·-·-) to $P_W = 15$mmHg, and (·····) to $P_W = 20$mmHg.

(a) Proximal (b) Distal

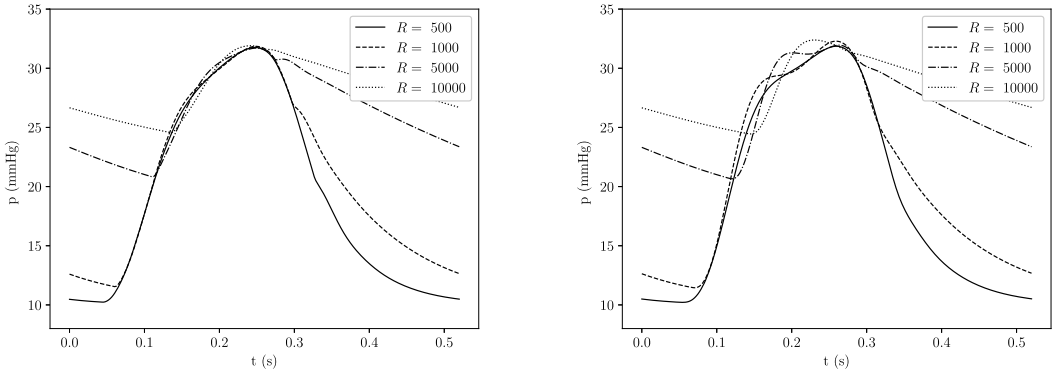

FIGURE 9.12 – Effect of peripheral resistance on the morphology of (a) the proximal and (b) the distal pulmonary artery pressure. . (——) corresponds to $R = 5{\cdot}10^2$ g·cm^{-4}·s^{-1}, (- - -) to $R = 1{\cdot}10^3$ g·cm^{-4}·s^{-1}, (-·-·-) to $R = 5{\cdot}10^3$ g·cm^{-4}·s^{-1}, and (·····) to $R = 1{\cdot}10^4$ g·cm^{-4}·s^{-1}.

9.5 Conclusion

In Section 9.4.1, we showed that similarly to Chapter 8, the 0D Windkessel model was appropriate to estimate the resistance, compliance, and diastolic time-constant based on the radial artery pressure. We are currently lacking other data sets to compare and classify the pathologies according to these parameters. We then used the proximal and distal pulmonary artery pressure to estimate the pulmonary resistance and compliance and obtained a good agreement with the measured values. However, the fit of the pulmonary artery pressure signals was qualitatively poor.

To summarize, the 0D Windkessel model provides values of the resistance, compliance, and diastolic time-constant that are relevant indicators in the case of pulmonary hypertension and that allow classifying patients. Nonetheless, this model does not predict and reproduce

the morphology of the pressure signals in the pulmonary tree.

In Section 9.4.2, we used the 1D model coupled to a simple resistive pulmonary valve model. We first tested this valve model and showed it behaved as expected when the resistance of the valve model was large. Once the valve model was validated, we compared the simulated and measured data in the pulmonary network. The 1D model predicted that the valve opened too early compared to the data but we obtained the same duration of ejection (valve open). Despite this delay, the morphology and amplitude of the simulated flow rate in the pulmonary network was really accurate. On the contrary, the prediction of the pressure in the pulmonary arteries did not give a good agreement with the measured data.

The final goal of this study is to evaluate the impact of different pathologies on the pressure signal in the pulmonary vascular network. Therefore, we studied the influence of high LA pressure and high peripheral resistance. Overall, our preliminary results of the 1D model show a great potential to reproduce and predict the mechanics involved in pulmonary hypertension.

As we do not have data or orders of magnitude of every single parameter of the model, we had to make some assumptions. In particular, we assumed that the quantity Eh/R_0 was constant, that the thickness h was the same in all vessels, that the peripheral resistances had the same values etc. We also assumed that the vessels were straight when other studies showed that the tappering was important in the pulmonary vascular network. All these hypotheses can be questioned and thus represent limitations to our study. However, we showed that some parameters were improving the fit of the pulmonary artery pressure such as the elastic coefficient K or the peripheral resistances.

This is an on-going study and we only presented preliminary results. We expect to enroll patients in the near future to attain the final goal. A large database would allow us to evaluate the resistance, compliance, and diastolic time-constant of the systemic and pulmonary vascular networks in subgroups of patients non-invasively thanks to the numerical models. We could also explore the impact of specific pathologies on the pressure waveforms using the 1D model.

In this chapter, we presented real invasive data from the heart cavities (RV and LA) that provided precise information on the flow and pressure in the heart. It could allow building a 0D heart model as in [14] that we could couple to the 1D model. The data could bring values of the parameters of the heart model with a parameter estimation method. The difficulty would be to obtain data from a patient that does not have heart failure or whose heart is not affected by pulmonary hypertension. Thus the estimated values of the 0D heart model could be applied in non-pathological scenarios or in cases where the pathology does not come from the heart.

10 Conclusion

10.1 General conclusions

This thesis deals with the mathematical modeling and numerical resolution of blood flow in the large arteries. Proposed as predictive tools, blood flow models need to be computed in real medical time therefore we used reduced-order models. Reduced-order models have the advantage of being good compromises between accuracy and computational cost.

The first part consists of the modeling and methodological aspects of the thesis. We derived step by step four reduced-order models in Chapter 2 based on a series of assumptions on the flow symmetries, the rheological properties of blood and the arterial wall, and the geometry of the arteries. We characterized the behavior of the arterial wall with two state laws using a linear approximation. We detailed the simplifications from the full incompressible Navier-Stokes equations to obtain a simplified two-dimensional (2D) model called the Reduced Navier-Stokes Prandtl (RNSP) model solved in steady condition with a rigid wall (steady RNSP model) or in unsteady condition with an elastic wall (Multi-Ring model). We then derived the one-dimensional (1D) model from the previous one and highlighted some properties of the system such as the wave propagation. Finally, we simplified the previous 1D model into the zero-dimensional (0D) model.

In Chapter 3, we improved the description of the arterial wall by rigorously deriving three polynomial hyperelastic models, as arterial wall mechanics is known to play a crucial in blood flow modeling. This approach allowed considering large deformations of the arterial wall that cannot be correctly captured by the linear model. We combined these hyperelastic laws to the 1D model and showed that the hyperelastic models smoothed the shock created by large deformations of the arterial tissue. This approach could be pertinent in the study of precise arterial pathologies or in veins however, experimental data was lacking to test *in vivo* the accuracy of the hyperelastic models.

The numerical models need to be solved with accurate resolution schemes to be used as predictive tools, which we presented in Chapter 4. The objective of this thesis was to study the previous reduced-order models in different medical scenarios and compare them against real invasive data from routine clinical procedures. The models can give access to vascular indicators and the pressure and flow mapping provided optimization methods that identify the model and physical parameters. We used this technique frequently in the application part (Part II) of the thesis and therefore reviewed and detailed a few optimization techniques used to estimate model parameters based on invasive data to make patient-specific predictions.

As stated above, all the models come from simplifications of the Navier-Stokes equations,

testing the hypotheses is crucial, which we did against analytic solutions from the literature for the steady RNSP and the Multi-ring model. Thanks to our collaboration with Pr. Mami Matsukawa and her students Hiroto Shimizu and Fumiaki Iwase from Doshisha University in Japan, we were able to compare the reduced-order models to experimental measurements in artificial arteries. The first configuration was a network of artificial arteries made from silicon tubes in which we studied clamping. Qualitatively, the numerical predictions of the 1D model were satisfying. The second experiment consisted of measuring the flow velocity with Particle Image Velocimetry (PIV) and comparing the center-line velocity with the Multi-Ring and 1D models. Again, we obtained a satisfying agreement between the models and the measurements. The validity of the model's hypotheses was assessed in multiple different configurations, analytic or experimental.

The second part deals with the biomedical applications and was carried thanks to many collaborations with physicians, each bringing us a problematic of their everyday clinical practice. In particular, we collaborated with Dr. Maria Teresa Politi (Facultad de Medicina, Buenos Aires, Argentina), Dr. Juan Fernandez (British Hospital, Buenos Aires, Argentina) as part of the ECOS-Sud project between France and Argentina. We also worked with Dr. Julien Gaudric (Hôpital la Pitié Salpétrière, Paris, France), Dr. Salam Abou Taam (Hôpital Privé Claude Galien, Quincy-sous-Sénart, France), and Dr. Francesca Raimondi (Hôpital Necker, Paris, France), which led us to study a variety of pathological conditions.

We addressed in Chapter 6 the clinical issue of the pressure drop in vascular stenoses. The pressure drop in this situation is a crucial indicator to determine the treatment strategy however the only way to measure it is by catheterization which is really invasive. The goal was therefore to assess the pressure drop across a stenosis using non-invasive patient data from 4D flow MRI with a hierarchy of models from 0D to 2D. We used all the models developed in Chapter 2 to study the influence of a stenosis on the flow, and compared them with invasive catheterization data. We found that the Multi-Ring model was the most accurate to reproduce the pressure drop, the 1D model gave a satisfying agreement for mild stenoses. Finally, as the current 0D model was inaccurate, we estimated the empirical coefficients of this model to provide an immediate computation of the pressure drop based on geometric and rheological parameters that can be easily obtained from 4D flow MRI.

Then, we investigated the impact of the Arterio-Venous Fistula (AVF) in Chapter 7, a connection between a vein and an artery to speed up the blood filtration process for kidney failure patients. We considered two reduced-order models, a 0D network model composed of resistors and a 1D model. We identified that the capillary resistance in both models was a decisive parameter that prevented from finding an optimal configuration for the fistula. We showed that the 0D model was able to reproduce and predict the flow distribution in the AVF in different pathological configurations given easily obtained non-invasive geometric data. Finally, we explored the distribution of flow when a venous stenosis develops in the AVF with the 1D model.

Then, we explored the immediate impact of aortic cross-clamping and unclamping during vascular surgery (Chapter 8), as it is a common procedure in stenoses repair surgeries for instance. We used a 0D model, a 1D model, and arterial waveform analysis to compare to invasive pressure data obtained during surgeries. With an optimization method and the 0D model, we showed that the total resistance was systematically increasing after clamping and decreasing after unclamping, the total compliance was decreasing after clamping and

increasing after unclamping, which we assessed quantitatively and in a very short time frame after clamping/unclamping. We calculated the diastolic-time constant with arterial waveform analysis and the 0D model and obtained a high agreement between both methods. We highlighted a decrease after clamping and an increase after unclamping, this result might not be relevant in the case of clamping but might be a decisive indicator in other pathologies. Finally, we showed that both the 0D and 1D model reproduced the measured pressure waves with high accuracy.

The method of the diastolic time-constant used in Chapter 8 led us to study pathologies related to pulmonary hypertension in Chapter 9. We modeled the pulmonary network with the same 0D model as the previous chapter, and a 1D model coupled to a valve. We showed that the 0D model predicted the values of resistance and compliance of the pulmonary network by comparing them with invasive measurements. However, unlike the previous chapter, the 0D model did not give a good agreement with the pressure wave measured in the pulmonary arteries in terms of morphology and reflections. We thus used a 1D model coupled to a valve model that reproduced accurately the behavior of the pulmonary valve. We compared the numerical prediction of the 1D model to the invasive data which did not give a good agreement. Finally, we studied the influence of different conditions associated with pulmonary hypertension such as the increase in Left Atrium (LA) pressure or pulmonary vascular resistance. The preliminary results showed great potential for the model to study the influence of pathological conditions on the pressure waveforms in the pulmonary vascular network.

All of these findings have their limitations, as any modeling approach by definition, detailed at the end of each chapter. However all of the comparisons with measured data in patients, in real clinical scenarios gave good hopes that reduced-order models could be predictive and decision-making tools to improve the medical diagnosis.

There are multiple perspectives for the work presented in this thesis as the study of CVDs is still a wide and open subject. We divided them into two categories: the short-term perspectives that can be achieved in relatively quickly, and the long-term perspectives that are either not pressing issues or time-consuming.

10.2 Short-term perspectives

The work presented in this thesis essentially deals with the application of blood flow models to different medical scenarios. Two fundamental tools are currently missing in our models to complete the description and understanding of the cardiovascular system. The first one is a heart model. Most heart models found in the literature that are coupled to circulation models are 0D as they require minimum computational power. This first perspective would be in our opinion, the easiest to implement. In Chapter 3, we presented real invasive data from the heart cavities (RV and LA) of patients with different degrees of diseases giving us access to precise information on the flow and pressure in the heart. This data could provide values of the parameters of the 0D model using a simple parameter estimation method. The difficulty is usually to obtain data from healthy-ish patients such that the values of the 0D heart model can be applied in non-pathological scenarios or in cases where the pathology does not come from the heart. For instance, patients who have a heart transplant, or who have a non-severe form of pulmonary hypertension can be considered as the reference. We expect to have a large database for the study of pulmonary hypertension including the latter

type of patients which would allow developing a 0D heart model.

The cardiovascular system is a closed-loop circuit and thus modeling only the arterial part is insufficient. It is essential to model the venous circulation which is the second fundamental tool to add to our models. As described in Chapter 1, the venous system differs in many aspects from the arterial one. In particular, the pressure and flow regime and the wall rheology are different. Although it is a good first approximation, the venous system cannot be modeled as simply as an arterial model with a different elastic coefficient. The presence of valves and the absence of pulsatility are important parameters to account in models of the venous circulation.

All the medical scenarios we studied in this thesis (arterial stenoses, Arterio-Venous Fistula, aortic cross-clamping, and pulmonary hypertension) could benefit from a complete description of the cardiovascular system. However, a very precise model requires a large number of parameters that cannot necessarily be measured. It brings us to the third short-term perspective which is the development of an efficient parameter algorithm. As described in Chapter 4, parameter estimation methods allow making patient-specific predictions which are in the end the goal of reduced-order blood flow modeling. It also provides relevant indicators helping in the medical follow-up of a disease. Kálmán Filter, whether it is the ensemble or unscented version, is currently the most used and relevant approach for parameter estimation of reduced-order models such as the 0D and 1D models. In Appendix A, we started developing the Ensemble Kálmán Filter approach but did not manage to test it on more complex models.

This thesis resulted from numerous interactions with physicians. We only studied an extremely small part of cardiovascular pathologies and surgeries. Of course, many other conditions could benefit from reduced-order modeling to deepen the understanding of the hemodynamics involved. The collaborations with physicians should, therefore, be pursued as they bring us their knowledge on physiology, and provide real data from patients. The interactions could thus extend other medical scenarios or even fields of medicine to provide the advantage of reduced-order models.

10.3 Long-term perspectives

Besides a closed-loop model, the 1D approach could benefit other types of improvements such as a non-newtonian rheological law for blood. Accounting for the transport of drugs in the vessels is also an active and interesting field of research in order to determine the optimal point of drug injection to reach a specific target. This could potentially reduce the necessary doses of antibiotics for instance and thus limit the resistance of bacteria. Growth and remodeling models are also meaningful as theses processes are involved in many scenarios such as the development of Arterio-Venous Fistulas for instance.

We believe that the future of blood flow modeling for medical diagnosis does not rely on a full-body 3D model as in [39] that is computationally expensive and gives rise to many numerical difficulties. Even though we can expect the 3D models to become more efficient in the near future, clinicians are usually interested in small regions of the arterial network which do not typically require a 3D detailed flow mapping. The relevant strategy would be a multi-scale adaptation technique of the reduced-order models that would increase the model refinement depending on the studied medical scenario. For instance, studying an Abdominal

Aortic Aneurysm would require a precise description of the flow and topology in and around the aneurysm with a 3D approach, the rest of the arterial circulation would be modeled with the 1D approach, and the less important parameters involved in AAA such as organs, veins, pulmonary circulation would be described by 0D models. This adaptation strategy would provide an efficient and accurate tool for physicians in a variety of clinical scenarios.

Other perspectives involve technical improvements such as implementing the Multi-Ring model into a network, parallelizing the code, making it open source and user-friendly in order to make it a real diagnosis and decision-helping tool for physicians.

In the very long term, a full-body model should be developed that would include all the previous tools but also a description of the different organs and other tissues, the interaction with the respiratory system, the chemical and biological exchanges between the tissues, etc. However, this global human model raises many technical and modeling difficulties, computational resources, and also raises the problem of parameter estimation that must be resolved before reaching this colossal objective.

A Kálmán Filter

A.1 Introduction

As mentioned in Chapter 4, filtering approaches such as Kálmán filters are often used for data assimilation to estimate parameters from incomplete or noisy data sets. It is a common strategy for data assimilation and parameter estimation to study blood flow models and in particular 0D models [140, 141], 1D models [126, 127, 142], 3D FSI models [143, 144, 248]. Most studies that use Kálmán filters try to retrieve the elastic properties of the arterial vessels [126,144] or the values of terminal boundary condition coefficients [56,125] from synthetic data to prove its interest in real medical scenarios.

Kálmán filter methods are usually classified as either Unscented Kálmán Filter (UKF), Reduced Order Unscented Kálmán filter (ROUKF) or Ensemble Kálmán Filter (EnKF). In this appendix, we are interested in the Ensemble Kálmán Filter method. We first derive the algorithm in Section A.2, apply it to the damped harmonic oscillator equation and briefly discuss the results and drawbacks of the method in Section A.3.

A.2 Algorithm

In this Section, we derive the Ensemble Kálmán filter algorithm. We assume that the system can be written in the form

$$\mathbf{x}_{k+1} = f(\mathbf{x}_k, \mathbf{u}_k) + \mathbf{w}_k \tag{A.1}$$

with $\mathbf{x}_k \in \mathbb{R}^n$ the model state vector at time t_k, $\mathbf{u}_k \in \mathbb{R}^m$ the set of model parameters, m the number of model parameters and $\mathbf{w}_k \in \mathbb{R}^n$ the model error. The observations are linked to the model state through

$$\mathbf{y}_k = h(\mathbf{x}_k) + \mathbf{v}_k \tag{A.2}$$

with $\mathbf{y}_k \in \mathbb{R}^{nobs}$ the observations at time t_k, $nobs$ the number of observations and $\mathbf{v}_k \in \mathbb{R}^{nobs}$ the observations error. The errors $\mathbf{w}_k$ and $\mathbf{v}_k$ are assumed to be uncorrelated Gaussian model errors with $\mathbf{Q}_k$ and $\mathbf{R}_k$ the model and observation error covariance matrices, respectively. We generate a set of realization of the model state of size q_{ens} as $\mathbf{X}_k^f = (\mathbf{x}_k^{f_1}, ..., \mathbf{x}_k^{f_{q_{ens}}}) \in \mathbb{R}^{n \times q_{ens}}$. We define the mean of the model state on the ensemble $\overline{\mathbf{x}}_k^f \in \mathbb{R}^n$ as

$$\overline{\mathbf{x}}_k^f = \frac{1}{q_{ens}} \sum_{i=0}^{q_{ens}} \mathbf{x}_k^{f_i}. \tag{A.3}$$

We define the Kálmán gain as

$$\mathbf{K}_k = \mathbf{P}^f_{xy_k} \left(\mathbf{P}^f_{yy_k}\right)^{-1} \tag{A.4}$$

with the covariance matrices

$$\mathbf{P}^f_{xy_k} = \frac{1}{q_{ens}-1} \sum_{i=0}^{q_{ens}} \left[\mathbf{x}^{f_i}_k - \overline{\mathbf{x}}^f_k\right] \left[h(\mathbf{x}^{f_i}_k) - \overline{h(\mathbf{x}^f_k)}\right]^T, \tag{A.5}$$

$$\mathbf{P}^f_{yy_k} = \frac{1}{q_{ens}-1} \sum_{i=0}^{q_{ens}} \left[h(\mathbf{x}^{f_i}_k) - \overline{h(\mathbf{x}^f_k)}\right] \left[h(\mathbf{x}^{f_i}_k) - \overline{h(\mathbf{x}^f_k)}\right]^T + \mathbf{R}_k, \tag{A.6}$$

where

$$\overline{h(\mathbf{x}^f_k)} = \frac{1}{q_{ens}} \sum_{i=0}^{q_{ens}} h(\mathbf{x}^{f_i}_k). \tag{A.7}$$

Finally, we update the model state as

$$\mathbf{x}^{a_i}_k = \mathbf{x}^{f_i}_k + \mathbf{K}_k \left(\mathbf{y}^i_k - h(\mathbf{x}^{f_i}_k)\right) \qquad \text{for } i = 1, ..., q_{ens}. \tag{A.8}$$

A.3 Application to parameter estimation

In this Section A.2, we choose to study the simple second-order differential equation of damped harmonic oscillator

$$\frac{\mathrm{d}^2 y}{\mathrm{d}t^2} + k\frac{\mathrm{d}y}{\mathrm{d}t} + \omega^2 y = 0 \tag{A.9}$$

with y the position, k the attenuation and ω the frequency. We use $x = \dfrac{\mathrm{d}y}{\mathrm{d}t}$ to obtain the following discretized system

$$x^{n+1} = (1 - k\Delta t)x^n - \omega^2 \Delta t y^n, \tag{A.10a}$$
$$y^{n+1} = y^n + \Delta t x^n. \tag{A.10b}$$

We write the system in the following form

$$\mathbf{x}^{k+1} = F\mathbf{x}^k, \tag{A.11}$$

with the vector $\mathbf{x}$ containing the model states and the parameters we seek to estimate

$$\mathbf{x} = \begin{pmatrix} x \\ y \\ k \\ \omega^2 \end{pmatrix} \tag{A.12}$$

and

$$F = \begin{pmatrix} 1 - k\Delta t & -\omega^2\Delta t & 0 & 0 \\ \Delta t & 1 & 0 & 0 \\ 0 & 0 & 1 & 0 \\ 0 & 0 & 0 & 1 \end{pmatrix}. \tag{A.13}$$

We choose $n_{obs} = 1$ and generate a synthetic observation using the model with know values of the model parameters to estimate, the goal is to retrieve these values. We create the observation data set with $k_0 = 0.05$ s^{-2} and $\omega_0^2 = 1.5$ s^{-2} and solve the system (A.11) with a time step $\Delta t = 5{\cdot}10^{-2}$ s.

In Figures A.1, we present the estimated values of k and ω^2 compared to the target values. We show the values of the two parameters starting from the targeted parameters $k_0 = 0.05$ s^{-2} and $\omega_0^2 = 1.5$ s^{-2} in black, and starting from $k = 0.04$ s^{-2} and $\omega^2 = 2$ s^{-2} in blue. On one hand, we observe that starting from the accurate estimation of parameters allows the algorithm to find the solution faster. On the other hand, we observe that the algorithm does not manage to find the target values of the parameters after 4000 time steps if the initial estimate is far from the target.

In Figure A.2a, we show the comparison between the velocity x estimated with the Kálmán filter algorithm and the velocity computed with the model with the initial set of parameters k_0 and ω_0^2 . In Figure A.2b, we plot the Root Mean Squared Error (RMSE) as a function of time. We observe in Figure A.2a that after 2000 time steps the estimated state fits the model. We also notice that the RMSE error decreases to 0 with time.

A.4 Conclusion

In this appendix we only tested the Ensemble Kálmán Filter in a really simple configuration, applying it to the damped harmonic oscillator equation. Nonetheless, the Kálmán Filter as a parameter estimation method gave satisfying results. The main drawback was that the algorithm necessitated an initial estimate close to the target values, a large ensemble and a long simulation to find the optima.

Combining this optimization method with the 1D model however constitutes an important perspective of the present work as mentioned in the conclusion chapter 10.

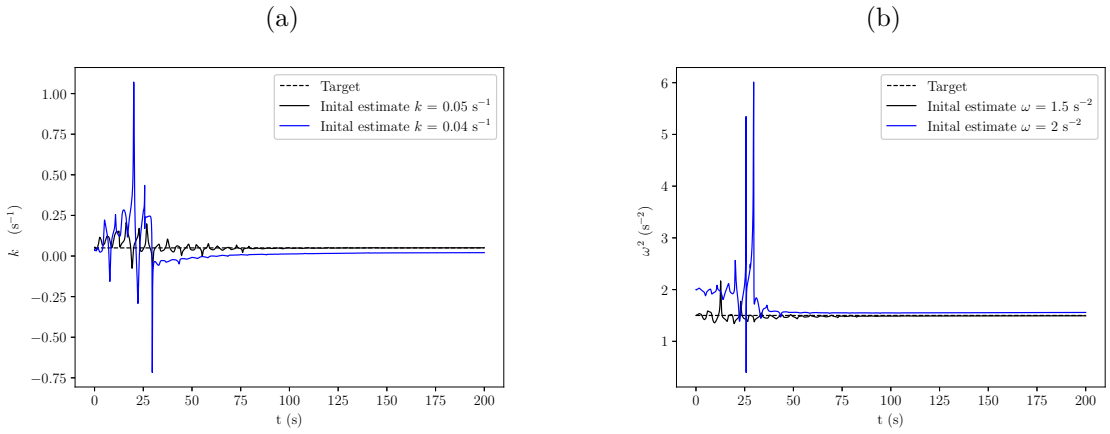

FIGURE A.1 – Mean estimation on the ensemble of the model parameters (a) k and (b) ω as a function of time using the Ensemble Kálmán Filter algorithm with $q_{ens} = 200$. (——) corresponds to the estimation of the parameters starting from the target values $k = 0.05$ s^{-1} and $\omega = 1.5$ s^{-2}. (——) corresponds to the estimation of the starting from $k = 0.04$ s^{-1} and $\omega = 2$ s^{-2}. (- - -) corresponds to the target values.

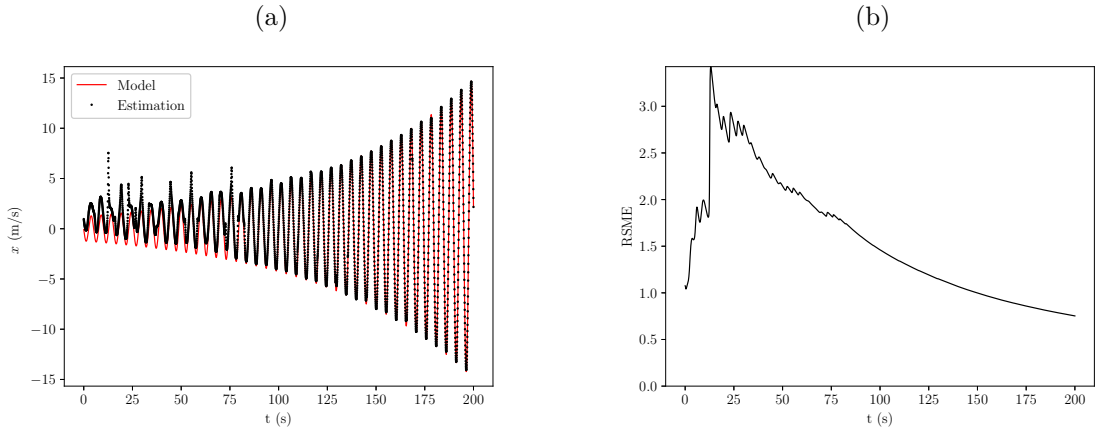

FIGURE A.2 – (a) Comparison between the mean estimation on the ensemble (•) and the target (—) as a function of time with $q_{ens} = 200$. (b) RMSE between the estimation and the target of the as a function of time using the Ensemble Kálmán Filter algorithm with $q_{ens} = 200$.

B PIV velocity profiles

The experimental work was carried as part of a collaboration between the Institut Jean le Rond d'Alembert of Sorbonne Université in Paris (France) and the Laboratory of Electronics and Ultrasounds of Doshisha University in Kyoto (Japan).

B.1 Introduction

In Chapter 5 we presented a comparison of the Multi-Ring and 1D models against Particle Image Velocimetry (PIV) measurements in an artificial artery in which we placed a stenosis, *i.e.* a constriction in the tube. We compared the center velocity data with the models which gave a good agreement. We show here the full velocity profiles at the entry, at the neck, and at the exit of the stenosis measured with PIV and computed with the Multi-Ring model.

B.2 Results

We plot the velocity profiles measured with the PIV set-up, as described in Section 5.3.4, at the entry (Figure B.1), at the neck (Figure B.2), and at the exit (Figure B.3) of the stenosis at different times.

In Figure B.1, we compare the velocity profile measured with PIV with the velocity profile computed with the Multi-Ring model. We first observe similar order of magnitudes, and similar patterns, in particular at t = 0.2 s. Overall, the agreement between the measured and the computed data is not satisfying at all. Similar conclusions can be drawn from Figure B.3, the only similarities is at t = 0.2 s. We believe that the agreement between the Multi-Ring model and the PIV measurements would be a lot higher if the time resolution was better. Indeed, the slope of the velocity (Figure B.1a for instance) is really high and thus a small delay between the Multi-Ring profile and the PIV profile could lead to large differences.

In Figure B.2, we only plot the measured velocity profile, as the agreement with is very poor and thus irrelevant. We notice several similarities between the velocity profiles measurement with PIV and computed with the steady RNSP and Multi-Ring models under steady flow in Chapter 6 (Section 6.4). We recover here the flattening of the profile at the neck of the stenosis as in Figures 6.5d and 6.5e and the presence of a jet at the exit of the stenosis as in Figures 6.5f and 6.5g.

Overall, we observe that the profiles are not symmetric with respect to the center-line $r = 0$, especially at the exit of the stenosis. If the particles are not sufficiently small or have

a higher density than the fluid they cannot be considered as tracers because they influence the fluid dynamics and thus the velocity measurement, which could be an explanation for the asymmetric velocity profiles.

B.3 Conclusion

We noticed that the velocity profiles measured with PIV were not symmetric, which would be expected considering the configuration. The comparison with the Multi-Ring model does not provide a good agreement as the model is by definition symmetric. A problem of synchronization of the model and data could lead to great differences in the velocity profiles at the slope of the velocity is high. We however recover some similarities with the profile in a stenosis in steady condition, found in Chapter 6.

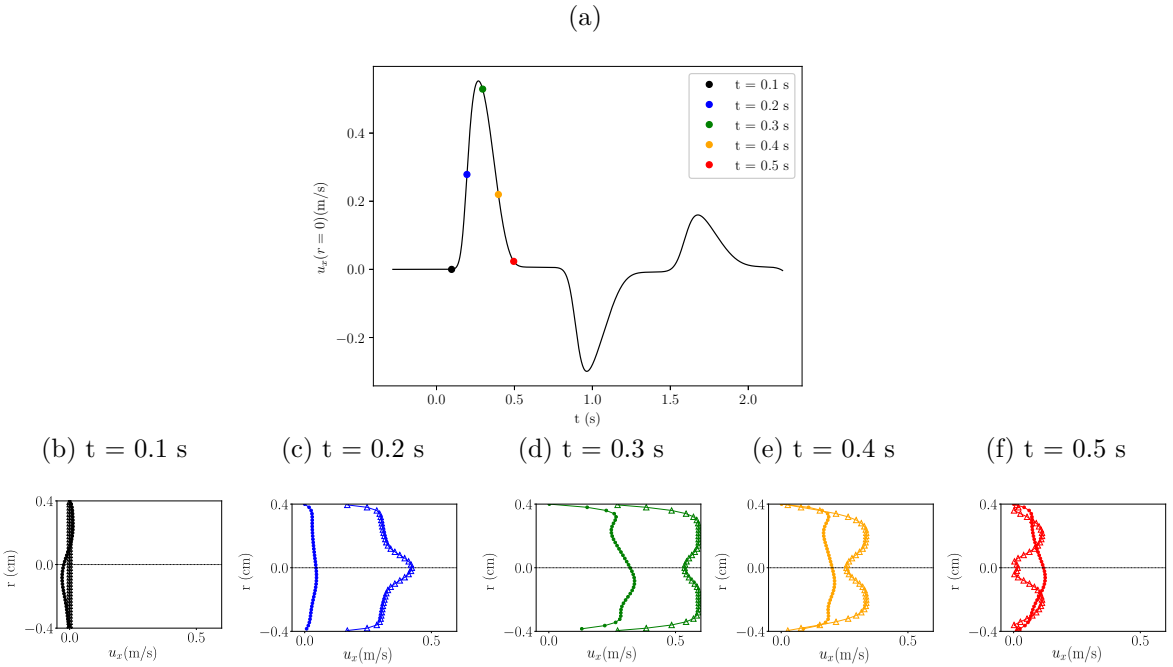

FIGURE B.1 – Velocity (a) at the center-line and (b)-(f) profiles for different times at the entry of the stenosis measured with PIV. (b) corresponds to $t = 0.1$ s (●), (c) corresponds to $t = 0.2$ s (●), (d) corresponds to $t = 0.3$ s (●), (e) corresponds to $t = 0.4$ s (●), (f) corresponds to $t = 0.5$ s (●). (△) correspond to the Multi-Ring model and (●) to the PIV measurements.

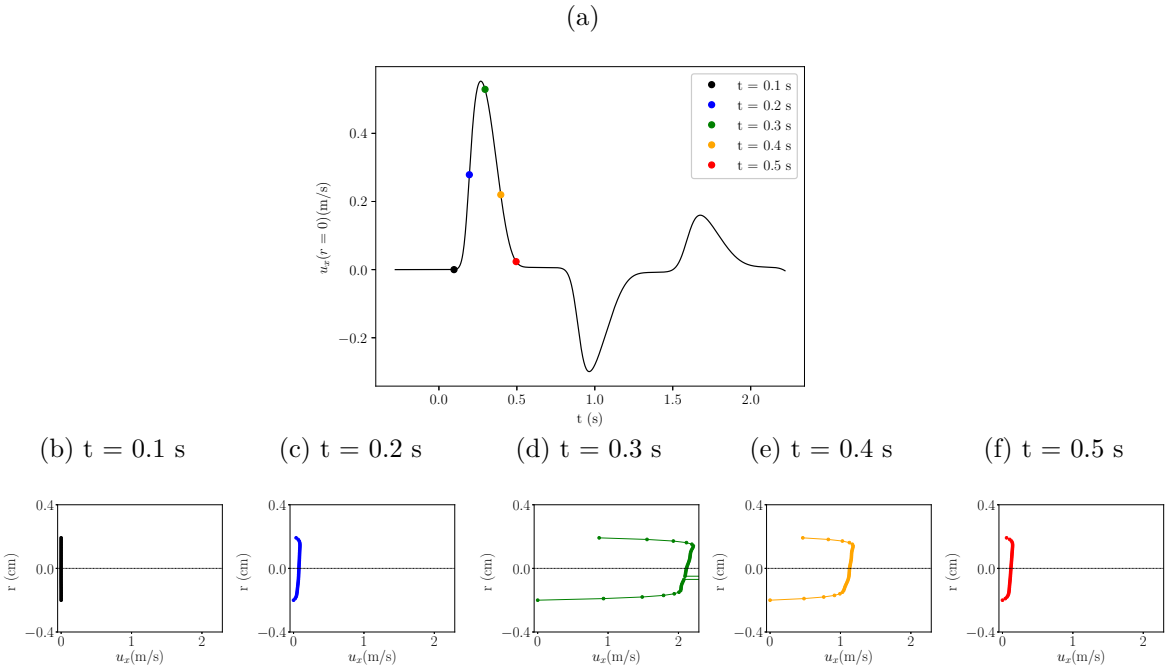

FIGURE B.2 – Velocity (a) at the center-line and (b)-(f) profiles for different times at the neck of the stenosis measured with PIV. (b) corresponds to $t = 0.1$ s (•), (c) corresponds to $t = 0.2$ s (•), (d) corresponds to $t = 0.3$ s (•), (e) corresponds to $t = 0.4$ s (•), (f) corresponds to $t = 0.5$ s (•).

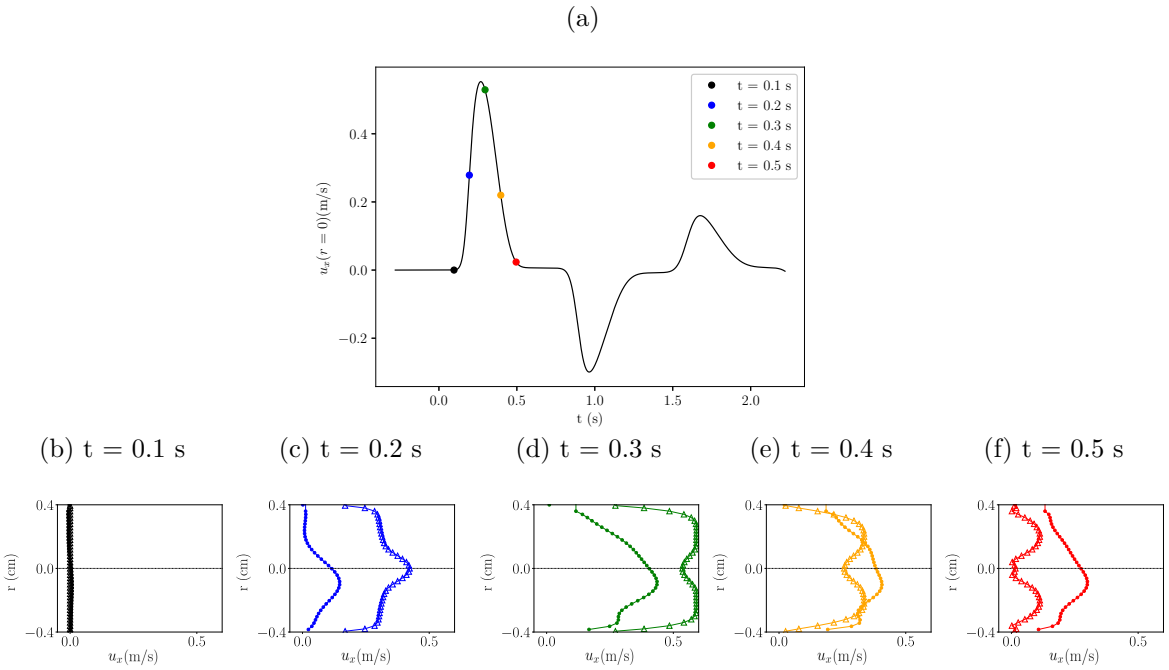

FIGURE B.3 – Velocity (a) at the center-line and (b)-(f) profiles for different times at the exit of the stenosis measured with PIV. (b) corresponds to $t = 0.1$ s (•), (c) corresponds to $t = 0.2$ s (•), (d) corresponds to $t = 0.3$ s (•), (e) corresponds to $t = 0.4$ s (•), (f) corresponds to $t = 0.5$ s (•). (△) correspond to the Multi-Ring model and (•) to the PIV measurements.

C Statistical analysis and results of aortic cross-clamping

We report in Table C.1 the statistical analysis of the pre- and post-clamp and unclamp pressure waves with the arterial waveform analysis method for each patient described in Section 8.3.

We report in Table C.2 the estimated 0D model parameters for the pre- and post-clamp and unclamp configurations for each patient described in Section 8.4.

Table C.1 – Detailed statistical analysis of the median time-constant (τ) of individual beats from an interval before (Pre τ) and after (Post τ) aortic clamping and unclamping in patients undergoing vascular surgery. IQR: interquartile range, % difference: perce ntage difference between time-constant values before and after clamping/ unclamping. Wilcoxon signed-rank test is used to compare the median values of the time-constant (τ) before and after clamping (or unclamping).

Clamp	Pre τ	IQR	Post τ	IQR	% difference	p
1	1.83	1.96 -1.74	1.75	1.83 -1.66	-4.37	0.0422
2	1.52	1.61-1.44	1.48	1.39 -1.55	-2.63	0.0002
3	2.08	2.22-1.97	1.88	2.09 -1.78	-9.62	0.0024
4	2.22	2.64-1.93	2.02	2.21-1.85	-9.01	<0.0003
5	2.36	4.29-1.68	1.79	2.42-1.47	-24.15	<0.0001
6	1.50	1.57-1.45	1.26	1.40-1.18	-16	<0.0001
7	2.50	2.74-2.31	1.70	1.82-1.63	-32	<0.0001
8	1.54	1.66-1.47	1.28	1.37-1.23	-16.88	<0.0001
9	2.15	2.33-1.85	1.99	2.12-1.83	-7.44	0.0448
10	2.12	2.28-2.06	1.91	2.02-1.83	-9.91	0.0327
11	2.4	2.78-2.17	1.82	1.74-1.95	-24.17	0.0001
Unclamp	Pre τ	IQR	Post τ	IQR	% difference	p
1	1.75	1.81-1.68	1.83	1.95-1.74	4.57	0.0396
2	1.44	1.76-1.38	1.78	1.99-1.68	23.61	<0.0001
3	1.88	1.96-1.81	2.26	2.40-2.14	20.21	0.0001
4	1.77	1.87-1.63	1.90	2.04-1.75	7.34	0.0042
5	1.86	2.03-1.70	2.06	2.24-1.96	10.75	0.0112
6	1.95	2.01-1.87	2.13	2.24-2.00	9.01	<0.0001
7	1.70	1.79-1.65	1.83	1.89-1.71	7.47	0.0184

8	1.37	1.47-1.30	1.66	1.89-1.35	21.19	<0.0001
9	1.99	2.20-1.88	2.32	2.50-2.04	16.62	0.0021
10	2.14	2.21-2.02	3.82	5.02-2.80	78.07	<0.0001
11	2.26	2.34-2.18	2.67	2.83-2.58	18.09	<0.0001

TABLE C.2 – Estimated parameters using the Windkessel model of Equation (8.1) for all patients in the four configurations. R_p: proximal resistance in g·cm^{-4}·s^{-1}, R_d: distal resistance in g·cm^{-4}·s^{-1}, C: compliance in 10^{-3} g^{-1}·cm^4·s^2, T_{ej}: ejection time in percentage of the heart period, T_c: heart period in s, Q_0: amplitude of flow rate in cm^3/s, V_s: Systolic Volume (SV) in cm^3.

		Model parameters			Calculation	Heart function			
		R_p	R_d	C	τ	T_{ej}	T	Q_0	V_s
Patient 1	Pre-clamp	204.7	1240.1	1.29	1.605	31.7	1.15	375	87.1
	Post-clamp	260.1	1313.2	1.04	1.36	32.1	1.283	340	89
	Pre-unclamp	260.2	1313.2	1.04	1.36	32.1	1.283	340	89
	Post-unclamp	183.6	1106.3	1.47	1.625	31.8	1.107	395	88.6
Patient 2	Pre-clamp	149.1	1158.2	1.236	1.431	33.9	1.038	410	92
	Post-clamp	182.2	1130.9	1.248	1.41	34.6	1.04	410	93.9
	Pre-unclamp	158.1	1070.7	1.285	1.376	31.8	1.066	430	92.9
	Post-unclamp	129.9	839.6	1.908	1.602	31.8	1.074	430	93.5
Patient 3	Pre-clamp	140.7	1204	1.64	1.974	40	0.961	265	64.9
	Post-clamp	181.5	1368.7	1.23	1.684	39.8	1.034	252	66
	Pre-unclamp	181.5	1368.7	1.23	1.684	39.8	1.034	252	66
	Post-unclamp	119.2	1063.4	2.029	2.157	38.5	0.962	280	66
Patient 4	Pre-clamp	112.4	1437.6	1.902	2.734	38.3	0.756	340	62.6
	Post-clamp	132.3	1500.5	1.521	2.281	38.6	0.774	345	65.7
	Pre-unclamp	129.3	1233.1	2.16	2.663	43.1	0.613	380	63.9
	Post-unclamp	107.5	1207	2.264	2.733	40.4	0.669	380	65.3
Patient 5	Pre-clamp	124.1	695.3	3.672	2.552	55.1	0.578	352	71.4
	Post-clamp	159.2	737.8	3.062	2.259	51	0.606	370	72.7
	Pre-unclamp	150.2	658.1	3.495	2.30	52	0.591	365	71.5
	Post-unclamp	124.2	586.9	4.367	2.562	52.5	0.594	360	71.4
Patient 6	Pre-clamp	170.9	1114.5	2.164	2.412	43.4	0.696	350	67.4
	Post-clamp	180.8	1242.8	1.60	1.988	42.4	0.705	350	66.6
	Pre-unclamp	157.6	1146.4	2.194	2.513	41.8	0.688	370	67.7
	Post-unclamp	141	1082.9	2.499	2.705	41.4	0.675	380	67.6
Patient 7	Pre-clamp	47.5	911.5	3.186	2.903	25	0.822	550	72
	Post-clamp	161.5	1206	1.804	2.822	41.9	0.704	380	71.3
	Pre-unclamp	50.2	978.6	1.804	1.765	24.5	0.702	640	70.2
	Post-unclamp	55.8	845.1	2.616	2.211	27.9	0.669	610	72.5
Patient 8	Pre-clamp	172.1	1116.3	2.458	2.743	46.6	0.65	380	73.2

	Post-clamp	272.4	1284.5		1.424	54	0.679	315	73.6
	Pre-unclamp	180.3	1147.5	1.676	1.923	53.2	0.67	325	73.8
	Post-unclamp	95.7	632.3	3.689	2.332	47.9	0.54	445	73.3
Patient 9	Pre-clamp	91.8	856.3	2.638	2.258	46.2	0.654	380	73.1
	Post-clamp	102	940.3	2.412	2.267	45	0.658	385	72.6
	Pre-unclamp	177.9	1098.4	1.819	1.998	42.9	0.695	380	72.1
	Post-unclamp	116.8	934.1	2.818	2.633	42.9	0.684	390	72.8
Patient 10	Pre-clamp	93.2	1472.8	1.442	2.123	37.9	0.916	390	86.3
	Post-clamp	217.8	1886.3	0.777	1.466	42.2	1.138	280	85.7
	Pre-unclamp	52.9	901.4	2.767	2.494	52.6	0.524	490	86
	Post-unclamp	35.7	774.2	5.43	4.203	50.5	0.469	570	85.9
Patient 11	Pre-clamp	24.4	1070.9	2.801	3	20.9	0.71	900	85
	Post-clamp	154.6	1170.3	2.019	2.362	46.5	0.73	400	86.5
	Pre-unclamp	106	1140.3	2.569	2.929	42.7	0.707	450	86.6
	Post-unclamp	65.5	795.5	5.044	4.012	39.7	0.698	490	86.5

Publications, conferences and collaborations

Publications

- J. Ventre, S. Abou Taam, J. M. Fullana, P.-Y. Lagrée. **Distribution of flow in an Arteriovenous Fistula using reduced-order models**. Submitted in *Journal of Biomechanical Engineering*.

- J. Ventre, F. Raimondi, N. Boddaert, J.-M. Fullana, P.-Y. Lagrée. **Reduced-order models of blood flow: application to arterial stenoses.** Book Chapter, publication in 2020.

- J. Ventre, F. Raimondi, N. Boddaert, J.-M. Fullana, P.-Y. Lagrée. **Reduced order models for blood pressure drop across arterial stenoses.** *In: Ateshian G., Myers K., Tavares J. (eds) Computer Methods, Imaging and Visualization in Biomechanics and Biomedical Engineering. CMBBE 2019. Lecture Notes in Computational Vision and Biomechanics*, vol 36. Springer, Cham
DOI Link

- J. Ventre, M. T. Politi, J. M. Fernandez, A. R. Ghigo, J. Gaudric, S. A. Wray, J.-B. Lagaert, R. Armentano, C. Capurro, J.-M. Fullana, P.-Y. Lagrée. **Parameter estimation to study the immediate impact of aortic cross-clamping using reduced order models.** *International Journal for Numerical Methods in Biomedical Engineering*, 2019.
DOI Link

- M. T. Politi, J. Ventre, J. Fernandez, A. Ghigo, J. Gaudric, R. Armentano, C. Capurro, P.-Y. Lagrée. **Effects of cross-clamping on vascular mechanics: comparing waveform analysis with a numerical model.** *Journal of Surgical Research*, vol. 244, pp. 587–598, 2019.
DOI Link

Conferences

- Congrès de la Société de Biomécanique, Metz, 2020.
Retinal micro-vascular network: data and model.
L. Julien, J. Ventre, P.-Y. Lagrée, A. Ramkhelawon, F. Rossant, M. Atlan, M. Pâques, J.-M. Fullana.

- Virtual Human Physiology, Paris, 2020.
One-dimensional model of the pulmonary vascular network to study pulmonary hypertension.

J. Ventre, M. T. Politi, J. M. Fernandez, P. Spaletra, M. Abud, M. L. Suarez, R. Ronderos, M. Diez, C. Capurro, J. M. Fullana, P.-Y. Lagrée.

- World Congress in Computational Mechanics - Eccomas, Paris, 2020.
  One-dimensional model of the pulmonary vascular network to study pulmonary hypertension.
  J. Ventre, M. T. Politi, J. M. Fernandez, P. Spaletra, M. Abud, M. L. Suarez, R. Ronderos, M. Diez, C. Capurro, J. M. Fullana, P.-Y. Lagrée.

- Congrès de la Société de Biomécanique, Poitiers, 2019.
  Reduced models for computing pressure drop across stenosis.
  J. Ventre, F. Raimondi, N. Boddaert, J.-M. Fullana, P.-Y. Lagrée.
  Abstract

- Computer Methods in Biomechanics and Biomedical Engineering, New-York, 2019.
  Reduced order models for blood pressure drop across arterial stenoses.
  J. Ventre, F. Raimondi, N. Boddaert, J.-M. Fullana, P.-Y. Lagrée.
  Abstract

- Journée Annuelles du GDR Mecabio, Montpellier, 2018.
  Aortic clamping analyzed by numerical models.
  J. Ventre, M. T. Politi, J. M. Fernández, A. Ghigo, S. Wray, J. Gaudric, I. Khelifa, R. Armentano, P.-Y. Lagrée, C. Capurro, J. M. Fullana.

- World Congress of Biomechanics, Dublin, 2018.
  Aortic cross-clamping during vascular surgery analyzed by the diastolic time-constant of arterial pressure waves.
  J. Ventre, M. T. Politi, J. M. Fernández, A. Ghigo, S. Wray, J. Gaudric, I. Khelifa, R. Armentano, P.-Y. Lagrée, C. Capurro, J. M. Fullana.
  Abstract

- Journée Annuelles du GDR Mecabio, Toulouse, 2018.

Collaborations

- Laboratory of Ultrasonic Electronics, Doshisha University, Kyotanabe, Japan.
  Collaborators: M. Matsukawa, F. Iwase, H. Shimizu.
  We fabricated models of visco-elastic artificial arteries made of silicon. We performed pressure and PIV measurements in these tubes and compared the data with the 1D and Multi-Ring models. This experimental work was carried during a 3-weeks exchange at the Laboratory of Ultrasonic Electronics and a 2-week exchange at Institut Jean le Rond d'Alembert. The work is presented in Chapter 5.

- Labotorio de Biomembranas, Faculta de Medicina de Buenos Aires, Buenos Aires, Argentina.
  Collaborators: M. T. Politi, J. M. Fernandez, C. Capurro.
  ECOS-Sud Project France-Argentine.
  We compared numerical predictions of the 0D and 1D models to experimental measurements of (a) the pressure during abdominal surgery to study the impact of aortic cross-clamping, and (b) the pressure in different location of the pulmonary circulation. This work was carried during 2 × 1 month exchange at the Laboratorio de Biomembranas and 3 × 1 month at Institut Jean le Rond d'Alembert. The work is presented in Chapters 8 and 9 and resulted in two publications.

- Centre de Référence Malformations Cardiaques Congénitales Complexes (M3C), Necker Hospital, Paris, France.
  Collaborators: F. Raimondi.
  We collaborated with a cardiologist from Necker Hospital to compute the trans-stenotic pressure drop from 4D flow MRI data using several reduced-order models. The work is presented in Chapter 6 and resulted in two publications.

- Claude Galien Private Hospital, Quincy-sous-Sénart, France.
  Collaborators: S. Abou Taam.
  We studied the development and evolution of an arteriovenous fistula in collaboration with a vascular surgeon from Claude Galien Private Hospital. This work is reported in Chapter 7.

Acronyms

AAA Abdominal Aortic Aneurysm. 141, 142, 144, 167, 188, 189

AVF Arterio-Venous Fistula. 28, 101, 123–139, 186, 188

BFGS Broyden-Fletcher-Goldfard-Shanno. 76–78, 115, 151, 152, 173

BPM Beat Per Minute. 18, 34, 113

CFD Computational Fluid Dynamics. 108, 125

CGS centimeter, gram, second. 33, 34, 117–119

CI Confidence Interval. 106, 156

CO Cardiac Output. 171, 175–177, 181, 182

CoA Aortic CoArctation. 104, 105

CT Computed Tomography. 22, 171, 174

CVDs Cardiovascular diseases. 16, 22, 187

EKG Electrocardiogram. 171

FSI Fluid-Structure Interaction. 23, 24, 27, 51, 77, 108, 125, 191

HR Heart Rate. 113

IQR Inter-Quartile Range. 147, 154, 155, 157, 199

LA Left Atrium. 18, 19, 170–172, 174, 182–184, 187

LoA Limits of Agreement. 106–108, 147, 156, 157

LV Left Ventricle. 18, 19, 25

MRA Magnetic Resonance Angiography. 68

MRI Magnetic Resonance Imaging. 22, 28, 68, 103–106, 113, 121, 186

MVR Mean Vascular Resistance. 159–161, 167

PIV Particle Image Velocimetry. 79, 80, 86, 96–98, 111, 186, 195–197, 204

PWV Pulse Wave Velocity. 164

RA Right Atrium. 18, 19

RBC Red Blood Cell. 39

RMSE Root Mean Squared Error. 193, 194

RNSP Reduced Navier-Stokes Prandtl. 25, 27, 28, 33, 39, 43, 44, 47, 53, 68–70, 76, 79–84, 98, 99, 109–114, 121, 185, 186, 195

RV Right Ventricle. 18, 19, 171, 172, 174, 175, 184, 187

SD Standard Deviation. 106, 107, 145, 147, 157

SV Systolic Volume. 151, 160, 163, 166, 167, 170, 171, 175–178, 182, 200

VC Vascular Compliance. 159–161, 167

WSS Wall Shear Stress. 25, 47–49, 81, 83–85, 108, 110–112, 125

List of Tables

List of Figures

Bibliography

[1] C. Singer, *On Anatomical Procedures: De Anatomicis Administrationibus*. No. 7, Wellcome historical medical museum, 1956. 17

[2] P. Le Floch-Prigent and D. Delaval, "The discovery of the pulmonary circulation by ibn al nafis during the 13th century: an anatomical approach (543.9)," *The FASEB Journal*, vol. 28, pp. 543–9, 2014. 17

[3] A. Vesalius, "De humani corporis fabrica libri septem (on the fabric of the human body in seven books)," *Padua: School of Medicine*, 1543. 17

[4] W. Harvey *et al.*, "Exercitatio anatomica de motu cordis et sanguinis in animalibus," *Frankfurt am Main*, 1628. 17

[5] K. H. Leitz and G. Ziemer, "The history of cardiac surgery," in *Cardiac Surgery*, pp. 3–31, Springer, 2017. 18

[6] J. Booth, "A short history of blood pressure measurement," 1977. 18, 19

[7] B. Newman, *Voice of the living light: Hildegard of Bingen and her world*. University of California Press, 1998. 19

[8] V. Sweet, "Hildegard of bingen and the greening of medieval medicine," *Bulletin of the History of Medicine*, vol. 73, no. 3, pp. 381–403, 1999. 19

[9] L. Formaggia, A. Quarteroni, and A. Veneziani, *Cardiovascular Mathematics: Modeling and simulation of the circulatory system*, vol. 1. Springer Science & Business Media, 2010. 21, 23, 24, 25, 55, 151, 154

[10] R. Comolet and R. Comolet, *Biomécanique circulatoire*. Masson, 1984. 23, 24, 42

[11] M. T. Politi, A. Ghigo, J. M. Fernández, I. Khelifa, J. Gaudric, J.-M. Fullana, and P.-Y. Lagrée, "The dicrotic notch analyzed by a numerical model," *Computers in biology and medicine*, vol. 72, pp. 54–64, 2016. 23, 28, 166, 169, 183

[12] C. Audebert, M. Bekheit, P. Bucur, E. Vibert, and I. E. Vignon-Clementel, "Partial hepatectomy hemodynamics changes: Experimental data explained by closed-loop lumped modeling," *Journal of Biomechanics*, vol. 50, pp. 202–208, 2017. 24, 29, 54

[13] J. P. Mynard and J. J. Smolich, "One-dimensional haemodynamic modeling and wave dynamics in the entire adult circulation," *Annals of biomedical engineering*, vol. 43, no. 6, pp. 1443–1460, 2015. 24, 40, 82

[14] L. O. Muller and E. F. Toro, "A global multiscale mathematical model for the human circulation with emphasis on the venous system," *International Journal for Numerical Methods in Biomedical Engineering*, vol. 30, pp. 681–725, 2014. 24, 27, 28, 29, 54, 133, 141, 151, 188

[15] W. W. Nichols, M. F. O'Rourke, and V. C, *McDonald's Blood Flow in Arteries: Theoretical, Experimental and Clinical principles*. Hodder Arnold, 2011. 24, 25, 27, 169

[16] Y.-C. Fung, *Biomechanics: mechanical properties of living tissues*. Springer Science & Business Media, 2013. 24, 40, 186

[17] M. Thiriet, *Biology and mechanics of blood flows: Part II: Mechanics and medical aspects*. Springer Science & Business Media, 2007. 24

[18] K. H. Parker, "A brief history of arterial wave mechanics," *Medical & biological engineering & computing*, vol. 47, no. 2, pp. 111–118, 2009. 25

[19] P. Segers, F. Dubois, D. De Wachter, and P. Verdonck, "Role and relevancy of a cardiovascular simulator," *Cardiovascular Engineering*, vol. 3, no. 1, pp. 48–56, 1998. 25

[20] M. Saito, Y. Ikenaga, M. Matsukawa, Y. Watanabe, T. Asada, and P.-Y. Lagrée, "One-dimensional model for propagation of a pressure wave in a model of the human arterial network: Comparison of theoretical and experimental results," *Journal of Biomechanical Engineering*, vol. 133, no. 12, pp. 121–005, 2011. 25, 70, 82, 89, 90, 151, 152, 153

[21] K. S. Matthys, J. Alastruey, J. Peiró, A. W. Khir, P. Segers, P. R. Verdonck, K. H. Parker, and S. J. Sherwin, "Pulse wave propagation in a model human arterial network: assessment of 1-D numerical simulations against in vitro measurements," *Journal of biomechanics*, vol. 40, no. 15, pp. 3476–3486, 2007. 25, 82

[22] J. Alastruey, A. W. Khir, K. S. Matthys, P. Segers, S. J. Sherwin, P. R. Verdonck, K. H. Parker, and J. Peiró, "Pulse wave propagation in a model human arterial network: Assessment of 1-D visco-elastic simulations against in vitro measurements," *Journal of biomechanics*, vol. 44, no. 12, pp. 2250–2258, 2011. 25, 28, 29, 40, 50, 54, 75, 82, 131, 152, 166

[23] D. W. Liepsch and R. Zimmer, "The dynamics of pulsatile flow in distensible model arteries," *Technology and Health Care*, vol. 3, no. 3, pp. 185–199, 1995. 25

[24] D. N. Ku and D. P. Giddens, "Laser doppler anemometer measurements of pulsatile flow in a model carotid bifurcation," *Journal of biomechanics*, vol. 20, no. 4, pp. 407–421, 1987. 25

[25] E. M. Pedersen, H.-W. Sung, A. C. Burlson, and A. P. Yoganathan, "Two-dimensional velocity measurements in a pulsatile flow model of the normal abdominal aorta simulating different hemodynamic conditions," *Journal of biomechanics*, vol. 26, no. 10, pp. 1237–1247, 1993. 25

[26] G. A. Holzapfel, *Nonlinear Solid Mechanics*. John Wiley & Sons, Inc., 2000. 25, 58, 59, 64

[27] C. A. Figueroa, I. E. Vignon-Clementel, K. E. Jansen, T. J. Hughes, and C. A. Taylor, "A coupled momentum method for modeling blood flow in three-dimensional deformable arteries," *Computer methods in applied mechanics and engineering*, vol. 195, no. 41-43, pp. 5685–5706, 2006. 25, 110

[28] M. A. Fernández, J.-F. Gerbeau, and C. Grandmont, "A projection semi-implicit scheme for the coupling of an elastic structure with an incompressible fluid," *International Journal for Numerical Methods in Engineering*, vol. 69, no. 4, pp. 794–821, 2007. 25

[29] M. E. Moghadam, I. E. Vignon-Clementel, R. Figliola, A. L. Marsden, M. O. C. H. A. M. Investigators, *et al.*, "A modular numerical method for implicit 0D/3D coupling in cardiovascular finite element simulations," *Journal of Computational Physics*, vol. 244, pp. 63–79, 2013. 25, 29, 54, 131

[30] C. A. Taylor, T. J. R. Hughes, and C. K. Zarins, "Finite element modeling of blood flow in arteries," *Computer methods in applied mechanics and engineering*, vol. 158, no. 1-2, pp. 155–196, 1998. 25

[31] L. Mannoni, *Etienne-Jules Marey: la mémoire de l'oeil:[... publié à l'occasion de l'exposition" Le mouvement en lumière: Etienne-Jules Marey", réalisée par la Fondation Electricité de France et la Cinémathèque française à l'Espace Electra, Paris, du 13 janvier au 19 mars 2000].* G. Mazzotta, 1999. 26

[32] C. Chnafa, S. Mendez, and F. Nicoud, "Image-based large-eddy simulation in a realistic left heart," *Computers & Fluids*, vol. 94, pp. 173–187, 2014. 26, 41

[33] J. Lantz, R. Gårdhagen, and M. Karlsson, "Quantifying turbulent wall shear stress in a subject specific human aorta using large eddy simulation," *Medical engineering & physics*, vol. 34, no. 8, pp. 1139–1148, 2012. 26

[34] P. D. Stein and H. N. Sabbah, "Turbulent blood flow in the ascending aorta of humans with normal and diseased aortic valves.," *Circulation research*, vol. 39, no. 1, pp. 58–65, 1976. 26

[35] S. S. Varghese and S. H. Frankel, "Numerical modeling of pulsatile turbulent flow in stenotic vessels," *J. Biomech. Eng.*, vol. 125, no. 4, pp. 445–460, 2003. 26, 110

[36] K. M. Khanafer, J. L. Bull, and R. Berguer, "Fluid–structure interaction of turbulent pulsatile flow within a flexible wall axisymmetric aortic aneurysm model," *European Journal of Mechanics-B/Fluids*, vol. 28, no. 1, pp. 88–102, 2009. 26

[37] H. J. Kim, I. E. Vignon-Clementel, J. S. Coogan, C. A. Figueroa, K. E. Jansen, and C. A. Taylor, "Patient-specific modeling of blood flow and pressure in human coronary arteries," *Annals of biomedical engineering*, vol. 38, no. 10, pp. 3195–3209, 2010. 26, 70

[38] I. E. Vignon-Clementel, A. L. Marsden, and J. A. Feinstein, "A primer on computational simulation in congenital heart disease for the clinician," *Progress in Pediatric Cardiology*, vol. 30, no. 1-2, pp. 3–13, 2010. 26

[39] N. Xiao, J. D. Humphrey, and C. A. Figueroa, "Multi-scale computational model of three-dimensional hemodynamics within a deformable full-body arterial network," *Journal of computational physics*, vol. 244, pp. 22–40, 2013. 26, 192

[40] F.-B. Tian, L. Zhu, P.-W. Fok, and X.-Y. Lu, "Simulation of a pulsatile non-newtonian flow past a stenosed 2D artery with atherosclerosis," *Computers in biology and medicine*, vol. 43, no. 9, pp. 1098–1113, 2013. 27

[41] P.-Y. Lagree and S. Lorthois, "The RNS/Prandtl equations and their link with other asymptotic descriptions: Application to the wall shear stress scaling in a constricted pipe," *International Journal of Engineering Science*, vol. 43, no. 3, pp. 352 – 378, 2005. 27, 45, 46, 70, 71, 82, 110

[42] J. R. Womersley, "XXIV. Oscillatory motion of a viscous liquid in a thin-walled elastic tube—I: The linear approximation for long waves," *The London, Edinburgh, and Dublin Philosophical Magazine and Journal of Science*, vol. 46, no. 373, pp. 199–221, 1955. 27, 82, 85

[43] P.-Y. Lagrée, "An inverse technique to deduce the elasticity of a large artery," *The European Physical Journal-Applied Physics*, vol. 9, no. 2, pp. 153–163, 2000. 27, 46, 50, 71, 79, 82

[44] F. Chouly and P.-Y. Lagrée, "Comparison of computations of asymptotic flow models in a constricted channel," *Applied Mathematical Modelling*, vol. 36, no. 12, pp. 6061–6071, 2012. 27, 82, 110

[45] E. Audusse, M.-O. Bristeau, B. Perthame, and J. Sainte-Marie, "A multilayer Saint-Venant system with mass exchanges for shallow water flows. derivation and numerical validation," *ESAIM: Mathematical Modelling and Numerical Analysis*, vol. 45, no. 1, pp. 169–200, 2011. 27, 46, 70, 72

[46] A. R. Ghigo, J.-M. Fullana, and P.-Y. Lagrée, "A 2D nonlinear multiring model for blood flow in large elastic arteries," *Journal of Computational Physics*, vol. 350, pp. 136–165, 2017. 27, 46, 70, 71, 72, 82

[47] M. Mirramezani, S. L. Diamond, H. I. Litt, and S. C. Shadden, "Reduced order models for transstenotic pressure drop in the coronary arteries," *Journal of Biomechanical Engineering*, vol. 141, no. 3, pp. 31005–31011, 2019. 27, 70, 71, 82, 110, 111

[48] J. Ventre, F. Raimondi, N. Boddaert, J. Fullana, and P.-Y. Lagrée, "Reduced-order models for blood pressure drop across arterial stenoses," *Computer Methods, Imaging and Visualization in Biomechanics and Biomedical Engineering. CMBBE 2019. Lecture Notes in Computational Vision and Biomechanics*, vol. 36, 2020. 27, 28, 50, 110

[49] L. Euler, "Principia pro motu sanguinis per arterias determinando. opera posthuma mathematica et physica anno 1844 detecta.," vol. 2, pp. 814–823, 1775. 27

[50] O. Delestre and P.-Y. Lagrée, "A 'well-balanced'finite volume scheme for blood flow simulation," *International Journal for Numerical Methods in Fluids*, vol. 72, no. 2, pp. 177–205, 2013. 27, 28, 70, 73, 74

[51] X. Wang, J.-M. Fullana, and P.-Y. Lagrée, "Verification and comparison of four numerical schemes for a 1D viscoelastic blood flow model," *Computer methods in biomechanics and biomedical engineering*, vol. 18, no. 15, pp. 1704–1725, 2015. 27, 40, 68, 74, 75, 80

[52] E. Boileau, P. Nithiarasu, P. J. Blanco, L. O. Müller, F. E. Fossan, L. R. Hellevik, W. P. Donders, W. Huberts, M. Willemet, and J. Alastruey, "A benchmark study of numerical schemes for one-dimensional arterial blood flow modelling," *International Journal for Numerical Methods in Biomedical Engineering*, vol. 31, no. 10, p. e02732, 2015. 27, 28, 80

[53] A. R. Ghigo, O. Delestre, J.-M. Fullana, and P.-Y. Lagrée, "Low-shapiro hydrostatic reconstruction technique for blood flow simulation in large arteries with varying geometrical and mechanical properties," *Journal of Computational Physics*, vol. 331, pp. 108–136, 2017. 27, 28, 70, 74

[54] J. P. Mynard and P. Nithiarasu, "A 1D arterial blood flow model incorporating ventricular pressure, aortic valve and regional coronary flow using the locally conservative Galerkin (LCG) method," *Communications in Numerical Methods in Engineering*, vol. 24, no. 5, pp. 367–417, 2008. 27, 28, 70

[55] P. Reymond, F. Merenda, F. Perren, D. Rufenacht, and N. Stergiopulos, "Validation of a one-dimensional model of the systemic arterial tree," *American Journal of Physiology-Heart and Circulatory Physiology*, vol. 297, no. 1, pp. H208–H222, 2009. 27, 28, 54, 70, 82

[56] J. Alastruey, K. H. Parker, J. Peiró, and S. J. Sherwin, "Lumped parameter outflow models for 1-D blood flow simulations: effect on pulse waves and parameter estimation," *Communications in Computational Physics*, vol. 4, no. 2, pp. 317–336, 2008. 27, 73, 79, 195

[57] M. S. Olufsen, C. S. Peskin, W. Y. Kim, E. M. Pedersen, A. Nadim, and J. Larsen, "Numerical simulation and experimental validation of blood flow in arteries with structured-tree outflow conditions," *Annals of biomedical engineering*, vol. 28, no. 11, pp. 1281–1299, 2000. 27, 82

[58] D. Guan, F. Liang, and P. A. Gremaud, "Comparison of the windkessel model and structured-tree model applied to prescribe outflow boundary conditions for a one-dimensional arterial tree model," *Journal of biomechanics*, vol. 49, no. 9, pp. 1583–1592, 2016. 27, 29, 54, 131

[59] J. P. Mynard, M. R. Davidson, D. J. Penny, and J. J. Smolich, "A simple, versatile valve model for use in lumped parameter and one-dimensional cardiovascular models," *International Journal for Numerical Methods in Biomedical Engineering*, vol. 28, no. 6-7, pp. 626–641, 2012. 27, 29, 54, 174, 179

[60] J.-M. Fullana and S. Zaleski, "A branched one-dimensional model of vessel networks," *Journal of Fluid Mechanics*, vol. 621, pp. 183–204, 2009. 27, 75

[61] J. P. Mynard and K. Valen-Sendstad, "A unified method for estimating pressure losses at vascular junctions," *International journal for numerical methods in biomedical engineering*, vol. 31, no. 7, p. e2717, 2015. 27, 75, 151

[62] F. N. Van de Vosse and N. Stergiopulos, "Pulse wave propagation in the arterial tree," *Annual Review of Fluid Mechanics*, vol. 43, pp. 467–499, 2011. 28, 151

[63] J. Alastruey, K. H. Parker, and S. J. Sherwin, "Arterial pulse wave hemodynamics," *11th International Conference on Pressure Surges*, vol. 30, pp. 401–443, 2012. 28, 40, 53, 54, 151

[64] S. J. Sherwin, L. Formaggia, J. Peiró, and V. Franke, "Computational modelling of 1D blood flow with variable mechanical properties and its application to the simulation of wave propagation in the human arterial system," *International Journal for Numerical Methods in Fluids*, vol. 43, pp. 673–700, Oct. 2003. 28, 151

[65] A. Quarteroni, A. Veneziani, and C. Vergara, "Geometric multiscale modeling of the cardiovascular system, between theory and practice," *Computer Methods in Applied Mechanics and Engineering*, vol. 302, pp. 193–252, 2016. 28, 29, 54, 151

[66] J. J. Wang and K. H. Parker, "Wave propagation in a model of the arterial circulation," *Journal of biomechanics*, vol. 37, no. 4, pp. 457–470, 2004. 28, 55, 89, 90, 119, 152, 153

[67] J. Ventre, M. T. Politi, J. M. Fernández, A. R. Ghigo, J. Gaudric, S. A. Wray, J.-B. Lagaert, R. Armentano, C. Capurro, J. M. Fullana, and P. Y. Lagrée, "Parameter

estimation to study the immediate impact of aortic cross-clamping using reduced order models," *International Journal for Numerical Methods in Biomedical Engineering*, p. e3261, 2019. 28, 29, 40, 55, 70, 76, 82, 150

[68] J. Alastruey, K. Parker, J. Peiró, S. Byrd, and S. Sherwin, "Modelling the circle of willis to assess the effects of anatomical variations and occlusions on cerebral flows," *Journal of biomechanics*, vol. 40, no. 8, pp. 1794–1805, 2007. 28

[69] J. Ryu, X. Hu, and S. C. Shadden, "A coupled lumped-parameter and distributed network model for cerebral pulse-wave hemodynamics," *Journal of biomechanical engineering*, vol. 137, no. 10, pp. 101–114, 2015. 28, 29, 54, 151

[70] F. Liang, K. Fukasaku, H. Liu, and S. Takagi, "A computational model study of the influence of the anatomy of the circle of Willis on cerebral hyperperfusion following carotid artery surgery," *Biomedical engineering online*, vol. 10, no. 84, 2011. 28

[71] M. U. Qureshi, G. D. Vaughan, C. Sainsbury, M. Johnson, C. S. Peskin, M. S. Olufsen, and N. Hill, "Numerical simulation of blood flow and pressure drop in the pulmonary arterial and venous circulation," *Biomechanics and modeling in mechanobiology*, vol. 13, no. 5, pp. 1137–1154, 2014. 28, 82, 174, 177, 178, 185, 186

[72] A. R. Ghigo, S. Abou Taam, X.-F. Wang, P.-Y. Lagrée, and J.-M. Fullana, "One-dimensional arterial network model for bypass grafts assessment," *Medical Engineering and Physics*, vol. 43, pp. 39–47, 2016. 28, 29, 50, 54, 82, 89, 90, 131, 144, 153

[73] A. R. Ghigo, X.-F. Wang, R. Armentano, J.-M. Fullana, and P.-Y. Lagrée, "Linear and Nonlinear Viscoelastic Arterial Wall Models: Application on Animals," *Journal of Biomechanical Engineering*, vol. 139, no. 1, pp. 11–19, 2017. 28, 39, 40, 82

[74] N. Westerhof, F. Bosman, C. J. De Vries, and A. Noordergraaf, "Analog studies of the human systemic arterial tree," *Journal of biomechanics*, vol. 2, no. 2, pp. 135–136, 1969. 28, 29, 54, 127, 131, 152

[75] N. Westerhof, J.-W. Lankhaar, and B. E. Westerhof, "The arterial windkessel," *Medical & Biological Engineering & Computing*, vol. 47, no. 2, pp. 131–141, 2009. 28, 147, 150

[76] O. Frank, "Die grundform des arteriellen puls," *Z Biof*, vol. 37, pp. 483–526, 1899. 28, 150

[77] M. T. Politi, J. Ventre, J. M. Fernández, A. Ghigo, J. Gaudric, R. Armentano, C. Capurro, and P.-Y. Lagrée, "Effects of cross-clamping on vascular mechanics: Comparing waveform analysis with a numerical model," *Journal of Surgical Research*, vol. 244, pp. 587–598, 2019. 29, 54, 70, 76, 150, 163, 174

[78] A. Noordergraaf, P. D. Verdouw, and H. B. K. Boom, "The use of an analog computer in a circulation model," *Progress in Cardiovascular Diseases*, vol. 5, no. 5, pp. 419–439, 1963. 29

[79] A. P. Avolio, "Multi-branched model of the human arterial system," *Medical and Biological Engineering and Computing*, vol. 18, no. 6, pp. 709–718, 1980. 29, 54, 152

[80] N. Stergiopulos, B. E. Westerhof, and N. Westerhof, "Total arterial inertance as the fourth element of the windkessel model," *American Journal of Physiology-Heart and Circulatory Physiology*, vol. 276, no. 1, pp. H81–H88, 1999. 29

[81] V. Milišić and A. Quarteroni, "Analysis of lumped parameter models for blood flow simulations and their relation with 1D models," *ESAIM: Mathematical Modelling and Numerical Analysis*, vol. 38, no. 4, pp. 613–632, 2004. 29

[82] L. Formaggia, D. Lamponi, M. Tuveri, and A. Veneziani, "Numerical modeling of 1D arterial networks coupled with a lumped parameters description of the heart," *Computer Methods in Biomechanics and Biomedical Engineering*, vol. 9, no. 5, pp. 273–288, 2006. 29, 54, 151

[83] I. E. Vignon-Clementel, C. A. Figueroa, K. E. Jansen, and C. A. Taylor, "Outflow boundary conditions for 3D simulations of non-periodic blood flow and pressure fields in deformable arteries," *Computer methods in biomechanics and biomedical engineering*, vol. 13, no. 5, pp. 625–640, 2010. 29, 54, 131

[84] N. Westerhof, "Analog studies of human systemic arterial hemodynamics (Ph. D. thesis)," *Philadelphia, University of Pennsylvania*, 1968. 36

[85] M. Taylor, "An experimental determination of the propagation of fluid oscillations in a tube with a visco-elastic wall; together with an analysis of the characteristics required in an electrical analogue," *Physics in Medicine & Biology*, vol. 4, no. 63, 1959. 40

[86] R. L. Armentano, J. G. Barra, J. Levenson, A. Simon, and R. H. Pichel, "Arterial wall mechanics in conscious dogs: assessment of viscous, inertial, and elastic moduli to characterize aortic wall behavior," *Circulation Research*, vol. 76, no. 3, pp. 468–478, 1995. 40

[87] W. Seed and N. Wood, "Velocity patterns in the aorta," *Cardiovascular research*, vol. 5, no. 3, pp. 319–330, 1971. 41

[88] F. Van de Vosse and M. Van Dongen, "Cardiovascular fluid mechanics-lecture notes," *Faculty of Applied Physics, Faculty of Mechanical Engineering, Eindhoven University of Technology, Eindhoven, Netherlands*, 1998. 41

[89] J.-F. Stoltz, M. Singh, and P. Riha, *Hemorheology in practice*, vol. 30. IOS press, 1999. 42

[90] D. Quemada, "Hydrodynamique sanguine: hémorhéologie et écoulement du sang dans les petits vaisseaux," *Le Journal de Physique Colloques*, vol. 37, pp. 9–22, 1976. 42

[91] A. Ghigo, P.-Y. Lagrée, and J.-M. Fullana, "A time-dependent non-newtonian extension of a 1D blood flow model," *Journal of Non-Newtonian Fluid Mechanics*, vol. 253, pp. 36–49, 2018. 42

[92] A. I. Moens, *Die Pulscurve*. Brill, 1878. 43, 52, 55, 62, 63, 66, 92

[93] D. Korteweg, "Ueber die fortpflanzungsgeschwindigkeit des schalles in elastischen röhren," *Annalen der Physik*, vol. 241, no. 12, pp. 525–542, 1878. 43, 52, 55, 62, 63, 66, 92

[94] M. Van Dyke, *Perturbation methods in fluid mechanics*. 1964. 44

[95] L. Prandtl, "Motion of fluids with very little viscosity," 1928. 45

[96] S. Ling and H. Atabek, "A nonlinear analysis of pulsatile flow in arteries," *Journal of Fluid Mechanics*, vol. 55, no. 3, pp. 493–511, 1972. 46

[97] F. De Vita, P.-Y. Lagrée, S. Chibbaro, and S. Popinet, "Beyond shallow water: appraisal of a numerical approach to hydraulic jumps based upon the boundary layer theory," *European Journal of Mechanics-B/Fluids*, vol. 79, pp. 233–246, 2020. 46

[98] S. J. Sherwin, V. Franke, J. Peiro, and K. Parker, "One-dimensional modelling of a vascular network in space-time variables," *Journal of Engineering Mathematics*, vol. 47, pp. 217–250, 2003. 49

[99] T. J. Hughes and J. Lubliner, "On the one-dimensional theory of blood flow in the larger vessels," *Mathematical Biosciences*, vol. 18, no. 1-2, pp. 161–170, 1973. 49, 50

[100] N. Smith, A. Pullan, and P. J. Hunter, "An anatomically based model of transient coronary blood flow in the heart," *SIAM Journal on Applied mathematics*, vol. 62, no. 3, pp. 990–1018, 2002. 50

[101] L. Formaggia, D. Lamponi, and A. Quarteroni, "One-dimensional models for blood flow in arteries," *Journal of engineering mathematics*, vol. 47, no. 3-4, pp. 251–276, 2003. 50

[102] Y. Fung, K. Fronek, and P. Patitucci, "Pseudoelasticity of arteries and the choice of its mathematical expression," *American Journal of Physiology-Heart and Circulatory Physiology*, vol. 237, no. 5, pp. H620–H631, 1979. 58

[103] M. Mooney, "A theory of large elastic deformation," *Journal of applied physics*, vol. 11, no. 9, pp. 582–592, 1940. 58, 62

[104] R. Rivlin, "Large elastic deformations of isotropic materials IV. further developments of the general theory," *Philosophical Transactions of the Royal Society of London. Series A, Mathematical and Physical Sciences*, vol. 241, no. 835, pp. 379–397, 1948. 58, 62

[105] R. Rivlin, "Large elastic deformations of isotropic materials. V. the problem of flexure," *Proceedings of the Royal Society of London. Series A. Mathematical and Physical Sciences*, vol. 195, no. 1043, pp. 463–473, 1949. 58, 62

[106] R. Rivlin, "Large elastic deformations of isotropic materials VI. further results in the theory of torsion, shear and flexure," *Philosophical Transactions of the Royal Society of London. Series A, Mathematical and Physical Sciences*, vol. 242, no. 845, pp. 173–195, 1949. 58, 62

[107] L. Treloar, "The elasticity of a network of long-chain molecules. I," *Transactions of the Faraday Society*, vol. 39, pp. 36–41, 1943. 58, 61

[108] L. Treloar, "The elasticity of a network of long-chain molecules—II," *Transactions of the Faraday Society*, vol. 39, pp. 241–246, 1943. 58, 61

[109] C. Wex, S. Arndt, A. Stoll, C. Bruns, and Y. Kupriyanova, "Isotropic incompressible hyperelastic models for modelling the mechanical behaviour of biological tissues: a review," *Biomedical Engineering/Biomedizinische Technik*, vol. 60, no. 6, pp. 577–592, 2015. 58, 68

[110] M. T. Duong and U. D.-I. R. M. Itskov, *Hyperelastic Modeling and Soft-Tissue Growth Integrated with the Smoothed Finite Element Method-SFEM*. PhD thesis, Universitätsbibliothek der RWTH Aachen, 2015. 59

[111] R. W. Ogden, "Large deformation isotropic elasticity–on the correlation of theory and experiment for incompressible rubberlike solids," *Proceedings of the Royal Society of London. A. Mathematical and Physical Sciences*, vol. 326, no. 1567, pp. 565–584, 1972. 60

[112] R. Ogden, "Elastic deformations of rubberlike solids," in *Mechanics of solids*, pp. 499–537, Elsevier, 1982. 60

[113] O. H. Varga, *Stress-strain behavior of elastic materials; selected problems of large deformations*. Interscience, 1966. 63

[114] G. R. Barrenechea and F. Chouly, "A finite element method for the resolution of the Reduced Navier-Stokes/Prandtl equations," *ZAMM-Journal of Applied Mathematics and Mechanics/Zeitschrift für Angewandte Mathematik und Mechanik: Applied Mathematics and Mechanics*, vol. 89, no. 1, pp. 54–68, 2009. 70

[115] I. E. Vignon Clementel and C. A. Taylor, "Outflow boundary conditions for one-dimensional finite element modeling of blood flow and pressure waves in arteries," *Wave Motion*, vol. 39, no. 4, pp. 361–374, 2004. 70

[116] J. Wan, B. Steele, S. A. Spicer, S. Strohband, G. R. Feijo´ o, T. J. Hughes, and C. A. Taylor, "A one-dimensional finite element method for simulation-based medical planning for cardiovascular disease," *Computer Methods in Biomechanics & Biomedical Engineering*, vol. 5, no. 3, pp. 195–206, 2002. 70

[117] J. Britton and Y. Xing, "Well-balanced discontinuous galerkin methods for the one-dimensional blood flow through arteries model with man-at-eternal-rest and living-man equilibria," *Computers & Fluids*, p. 104493, 2020. 70

[118] L. H. Thomas, "Elliptic problems in linear difference equations over a network," *Watson Sci. Comput. Lab. Rept., Columbia University, New York*, vol. 1, 1949. 71, 72

[119] M.-O. Bristeau and B. Coussin, "Boundary conditions for the shallow water equations solved by kinetic schemes," 2001. 72

[120] B. Perthame, *Kinetic formulation of conservation laws*, vol. 21. Oxford University Press, 2002. 74

[121] C. Audebert, P. Bucur, M. Bekheit, E. Vibert, I. E. Vignon-Clementel, and J.-F. Gerbeau, "Kinetic scheme for arterial and venous blood flow, and application to partial hepatectomy modeling," *Computer Methods in Applied Mechanics and Engineering*, vol. 314, pp. 102–125, 2017. 74

[122] R. J. LeVeque *et al.*, *Finite volume methods for hyperbolic problems*, vol. 31. Cambridge university press, 2002. 75

[123] S. Urquiza, P. Blanco, M. Vénere, and R. Feijóo, "Multidimensional modelling for the carotid artery blood flow," *Computer Methods in Applied Mechanics and Engineering*, vol. 195, no. 33-36, pp. 4002–4017, 2006. 75

[124] O. San and A. E. Staples, "An improved model for reduced-order physiological fluid flows," *Journal of Mechanics in Medicine and Biology*, vol. 12, no. 03, p. 1250052, 2012. 75

[125] L. Itu, P. Sharma, T. Passerini, A. Kamen, C. Suciu, and D. Comaniciu, "A parameter estimation framework for patient-specific hemodynamic computations," *Journal of Computational Physics*, vol. 281, pp. 316–333, 2015. 76, 79, 195

[126] D. Lombardi, "Inverse problems in 1D hemodynamics on systemic networks: A sequential approach," *International journal for numerical methods in biomedical engineering*, vol. 30, no. 2, pp. 160–179, 2014. 76, 79, 169, 195

[127] R. Lal, B. Mohammadi, and F. Nicoud, "Data assimilation for identification of cardiovascular network characteristics," *International journal for numerical methods in biomedical engineering*, vol. 33, no. 5, p. e2824, 2017. 76, 79, 195

[128] C. G. Broyden, "Quasi-newton methods and their application to function minimisation," *Mathematics of Computation*, vol. 21, no. 99, pp. 368–381, 1967. 78

[129] R. Fletcher and M. J. D. Powell, "A rapidly convergent descent method for minimization," *The computer journal*, vol. 6, no. 2, pp. 163–168, 1963. 78

[130] D. Goldfarb, "A family of variable-metric methods derived by variational means," *Mathematics of computation*, vol. 24, no. 109, pp. 23–26, 1970. 78

[131] D. F. Shanno, "Conditioning of Quasi-Newton Methods for Function Minimization," *Mathematics of Computation*, vol. 24, no. 111, pp. 647–656, 1970. 78

[132] P. J. Van Laarhoven and E. H. Aarts, "Simulated annealing," in *Simulated annealing: Theory and applications*, pp. 7–15, Springer, 1987. 79

[133] D. J. Wales and J. P. K. Doye, "Global optimization by basin-hopping and the lowest energy structures of lennard-jones clusters containing up to 110 atoms," *Journal of Physical Chemistry A*, vol. 101, no. 28, p. 5111–5116, 1997. 79

[134] D. J. Wales and H. A. Scheraga, "Global optimization of clusters, crystals, and biomolecules," *Science*, vol. 285, no. 5432, pp. 1368–1372, 1999. 79

[135] Z. Li and H. A. Scheraga, "Monte carlo-minimization approach to the multiple-minima problem in protein folding," *Proceedings of the National Academy of Sciences*, vol. 84, no. 19, pp. 6611–6615, 1987. 79

[136] M. Ismail, W. A. Wall, and M. W. Gee, "Adjoint-based inverse analysis of windkessel parameters for patient-specific vascular models," *Journal of Computational Physics*, vol. 244, pp. 113–130, 2013. 79

[137] V. Martin, F. Clément, A. Decoene, and J.-F. Gerbeau, "Parameter identification for a one-dimensional blood flow model," in *ESAIM: Proceedings*, vol. 14, pp. 174–200, EDP Sciences, 2005. 79

[138] R. L. Spilker and C. A. Taylor, "Tuning multidomain hemodynamic simulations to match physiological measurements," *Annals of biomedical engineering*, vol. 38, no. 8, pp. 2635–2648, 2010. 79

[139] R. Fletcher and C. M. Reeves, "Function minimization by conjugate gradients," *The computer journal*, vol. 7, no. 2, pp. 149–154, 1964. 79

[140] S. Pant, C. Corsini, C. Baker, T.-Y. Hsia, G. Pennati, I. E. Vignon-Clementel, M. of Congenital Hearts Alliance (MOCHA) Investigators, *et al.*, "Data assimilation and modelling of patient-specific single-ventricle physiology with and without valve regurgitation," *Journal of biomechanics*, vol. 49, no. 11, pp. 2162–2173, 2016. 79, 195

[141] D. Canuto, J. L. Pantoja, J. Han, E. P. Dutson, and J. D. Eldredge, "An ensemble kalman filter approach to parameter estimation for patient-specific cardiovascular flow modeling," *Theoretical and Computational Fluid Dynamics*, pp. 1–24, 2020. 79, 195

[142] A. Caiazzo, F. Caforio, G. Montecinos, L. O. Muller, P. J. Blanco, and E. F. Toro, "Assessment of reduced-order unscented kalman filter for parameter identification in 1-dimensional blood flow models using experimental data," *International journal for numerical methods in biomedical engineering*, vol. 33, no. 8, p. e2843, 2017. 79, 195

[143] P. Moireau, C. Bertoglio, N. Xiao, C. A. Figueroa, C. Taylor, D. Chapelle, and J.-F. Gerbeau, "Sequential identification of boundary support parameters in a fluid-structure vascular model using patient image data," *Biomechanics and modeling in mechanobiology*, vol. 12, no. 3, pp. 475–496, 2013. 79, 195

[144] C. Bertoglio, D. Barber, N. Gaddum, I. Valverde, M. Rutten, P. Beerbaum, P. Moireau, R. Hose, and J.-F. Gerbeau, "Identification of artery wall stiffness: In vitro validation and in vivo results of a data assimilation procedure applied to a 3D fluid–structure interaction model," *Journal of Biomechanics*, vol. 47, no. 5, pp. 1027–1034, 2014. 79, 195

[145] N. Xiao, J. Alastruey, and C. Alberto Figueroa, "A systematic comparison between 1-D and 3-D hemodynamics in compliant arterial models," *International journal for numerical methods in biomedical engineering*, vol. 30, no. 2, pp. 204–231, 2014. 82

[146] P. Reymond, Y. Bohraus, F. Perren, F. Lazeyras, and N. Stergiopulos, "Validation of a patient-specific one-dimensional model of the systemic arterial tree," *American Journal of Physiology-Heart and Circulatory Physiology*, vol. 301, no. 3, pp. H1173–H1182, 2011. 82

[147] P. J. Blanco, S. M. Watanabe, M. A. R. Passos, P. A. Lemos, and R. A. Feijóo, "An anatomically detailed arterial network model for one-dimensional computational hemodynamics," *IEEE Transactions on biomedical engineering*, vol. 62, no. 2, pp. 736–753, 2014. 82

[148] E. by the Association for European Paediatric Cardiology (AEPC), A. F. Members, H. Baumgartner, P. Bonhoeffer, N. M. De Groot, F. de Haan, J. E. Deanfield, N. Galie, M. A. Gatzoulis, C. Gohlke-Baerwolf, *et al.*, "ESC guidelines for the management of grown-up congenital heart disease (new version 2010) the task force on the management of grown-up congenital heart disease of the european society of cardiology (ESC)," *European heart journal*, vol. 31, no. 23, pp. 2915–2957, 2010. 106

[149] C. A. Warnes, R. G. Williams, T. M. Bashore, J. S. Child, H. M. Connolly, J. A. Dearani, P. del Nido, J. W. Fasules, T. P. Graham, Z. M. Hijazi, *et al.*, "ACC/AHA 2008 guidelines for the management of adults with congenital heart disease: a report of the american college of cardiology/american heart association task force on practice guidelines (writing committee to develop guidelines on the management of adults with congenital heart disease) developed in collaboration with the american society of echocardiography, heart rhythm society, international society for adult congenital

heart disease, society for cardiovascular angiography and interventions, and society of thoracic surgeons," *Journal of the American College of Cardiology*, vol. 52, no. 23, pp. e143–e263, 2008. 106, 107, 115

[150] L. Hatle, A. Brubakk, A. Tromsdal, and B. Angelsen, "Noninvasive assessment of pressure drop in mitral stenosis by Doppler ultrasound.," *Heart*, vol. 40, no. 2, pp. 131–140, 1978. 106

[151] D. F. Young and F. Y. Tsai, "Flow characteristics in models of arterial stenoses I. steady flow," *Journal of biomechanics*, vol. 6, no. 4, pp. 395–402, 1973. 106, 110, 111, 112, 115, 116, 117

[152] D. F. Young and F. Y. Tsai, "Flow characteristics in models of arterial stenoses II. unsteady flow," *Journal of biomechanics*, vol. 6, no. 5, pp. 547–559, 1973. 106, 111

[153] D. F. Young, N. R. Cholvin, and A. C. Roth, "Pressure drop across artificially induced stenoses in the femoral arteries of dogs.," *Circulation research*, vol. 36, no. 6, pp. 735–743, 1975. 106, 109, 110, 115, 116, 117, 120

[154] B. D. Seeley and D. F. Young, "Effect of geometry on pressure losses across models of arterial stenoses," *Journal of biomechanics*, vol. 9, no. 7, pp. 439–448, 1976. 106, 111, 112, 118, 119, 120, 121, 123, 213

[155] A. Giardini and T. A. Tacy, "Pressure recovery explains Doppler overestimation of invasive pressure gradient across segmental vascular stenosis," *Echocardiography*, vol. 27, no. 1, pp. 21–31, 2010. 106

[156] F. Donati, S. Myerson, M. M. Bissell, N. P. Smith, S. Neubauer, M. J. Monaghan, D. A. Nordsletten, and P. Lamata, "Beyond bernoulli: improving the accuracy and precision of noninvasive estimation of peak pressure drops," *Circulation: Cardiovascular Imaging*, vol. 10, no. 1, p. e005207, 2017. 106

[157] Z. Stankovic, B. D. Allen, J. Garcia, K. B. Jarvis, and M. Markl, "4D flow imaging with MRI," *Cardiovascular diagnosis and therapy*, vol. 4, no. 2, pp. 173–192, 2014. 106, 107

[158] M. Markl, S. Schnell, C. Wu, E. Bollache, K. Jarvis, A. J. Barker, J. D. Robinson, and C. K. Rigsby, "Advanced flow MRI: emerging techniques and applications," *Clinical radiology*, vol. 71, no. 8, pp. 779–795, 2016. 106

[159] J. Bock, A. Frydrychowicz, R. Lorenz, D. Hirtler, A. J. Barker, K. M. Johnson, R. Arnold, H. Burkhardt, J. Hennig, and M. Markl, "In vivo noninvasive 4D pressure difference mapping in the human aorta: phantom comparison and application in healthy volunteers and patients," *Magnetic resonance in medicine*, vol. 66, no. 4, pp. 1079–1088, 2011. 106

[160] T. Puiseux, A. Sewonu, O. Meyrignac, H. Rousseau, F. Nicoud, S. Mendez, and R. Moreno, "Reconciling PC-MRI and CFD: An in-vitro study," *NMR in Biomedicine*, vol. 32, no. 5, p. e4063, 2019. 106

[161] E. Riesenkampff, J. F. Fernandes, S. Meier, L. Goubergrits, S. Kropf, S. Schubert, F. Berger, A. Hennemuth, and T. Kuehne, "Pressure fields by flow-sensitive, 4D, velocity-encoded CMR in patients with aortic coarctation," *JACC: Cardiovascular Imaging*, vol. 7, no. 9, pp. 920–926, 2014. 106

[162] L. Goubergrits, F. Hellmeier, D. Neumann, V. Mihalef, M. A. Gulsun, M. Chinali, A. Secinaro, K. Runte, S. Schubert, F. Berger, *et al.*, "Patient-specific requirements and clinical validation of MRI-based pressure mapping: A two-center study in patients with aortic coarctation," *Journal of Magnetic Resonance Imaging*, vol. 49, no. 1, pp. 81–89, 2019. 106

[163] S. Saitta, S. Pirola, F. Piatti, E. Votta, F. Lucherini, F. Pluchinotta, M. Carminati, M. Lombardi, C. Geppert, F. Cuomo, *et al.*, "Evaluation of 4D flow MRI-based non-invasive pressure assessment in aortic coarctations," *Journal of biomechanics*, vol. 94, pp. 13–21, 2019. 106

[164] B. Casas, J. Lantz, P. Dyverfeldt, and T. Ebbers, "4D flow MRI-based pressure loss estimation in stenotic flows: Evaluation using numerical simulations," *Magnetic resonance in medicine*, vol. 75, no. 4, pp. 1808–1821, 2016. 106

[165] J. M. Bland and D. G. Altman, "Statistical methods for assessing agreement between two methods of clinical measurement," *The lancet*, vol. 327, no. 8476, pp. 307–310, 1986. 108, 149, 158

[166] S. Heinen, D. van den Heuvel, J. de Vries, F. van de Vosse, T. Delhaas, and W. Huberts, "A geometry-based model for non-invasive estimation of pressure gradients over iliac artery stenoses," *Journal of biomechanics*, vol. 92, pp. 67–75, 2019. 110, 119

[167] A. M. Shaaban and A. J. Duerinckx, "Wall shear stress and early atherosclerosis: a review," *American Journal of Roentgenology*, vol. 174, no. 6, pp. 1657–1665, 2000. 110, 113

[168] D. A. Steinman, "Image-based computational fluid dynamics modeling in realistic arterial geometries," *Annals of biomedical engineering*, vol. 30, no. 4, pp. 483–497, 2002. 110

[169] A. Caiazzo, G. Montecinos, L. O. Müller, E. M. Haacke, and E. F. Toro, "Computational haemodynamics in stenotic internal jugular veins," *Journal of mathematical biology*, vol. 70, no. 4, pp. 745–772, 2015. 110

[170] N. Stergiopulos, D. Young, and T. Rogge, "Computer simulation of arterial flow with applications to arterial and aortic stenoses," *Journal of biomechanics*, vol. 25, no. 12, pp. 1477–1488, 1992. 111

[171] F. Liang, S. Takagi, R. Himeno, and H. Liu, "Multi-scale modeling of the human cardiovascular system with applications to aortic valvular and arterial stenoses," *Medical & biological engineering & computing*, vol. 47, no. 7, pp. 743–755, 2009. 111

[172] L. Itu, P. Sharma, K. Ralovich, V. Mihalef, R. Ionasec, A. Everett, R. Ringel, A. Kamen, and D. Comaniciu, "Non-invasive hemodynamic assessment of aortic coarctation: validation with in vivo measurements," *Annals of biomedical engineering*, vol. 41, no. 4, pp. 669–681, 2013. 111

[173] T. Koeppl, G. Santin, B. Haasdonk, and R. Helmig, "Numerical modelling of a peripheral arterial stenosis using dimensionally reduced models and kernel methods," *International journal for numerical methods in biomedical engineering*, vol. 34, no. 8, p. e3095, 2018. 111

[174] H. Xiao, A. Avolio, and D. Huang, "A novel method of artery stenosis diagnosis using transfer function and support vector machine based on transmission line model: A numerical simulation and validation study," *Computer methods and programs in biomedicine*, vol. 129, pp. 71–81, 2016. 111

[175] M. Strocchi, C. Contarino, Q. Zhang, R. Bonmassari, and E. F. Toro, "A global mathematical model for the simulation of stenoses and bypass placement in the human arterial system," *Applied Mathematics and Computation*, vol. 300, pp. 21–39, 2017. 111

[176] X. Berard, S. Déglise, F. Alonso, F. Saucy, P. Meda, L. Bordenave, J.-M. Corpataux, and J.-A. Haefliger, "Role of hemodynamic forces in the ex vivo arterialization of human saphenous veins," *Journal of vascular surgery*, vol. 57, no. 5, pp. 1371–1382, 2013. 126

[177] M. J. Brescia, J. E. Cimino, K. Appel, and B. J. Hurwich, "Chronic hemodialysis using venipuncture and a surgically created arteriovenous fistula," *New England Journal of Medicine*, vol. 275, no. 20, pp. 1089–1092, 1966. 126

[178] I. Van Tricht, D. De Wachter, J. Tordoir, and P. Verdonck, "Hemodynamics and complications encountered with arteriovenous fistulas and grafts as vascular access for hemodialysis: a review," *Annals of biomedical engineering*, vol. 33, no. 9, pp. 1142–1157, 2005. 126, 129

[179] N. Sadaghianloo, S. Declemy, and R. Hassen-Khodja, "Les abords vasculaires pour hémodialyse en 2018," *JMV-Journal de Médecine Vasculaire*, vol. 43, no. 2, p. 79, 2018. 126

[180] A. Grassmann, S. Gioberge, S. Moeller, and G. Brown, "ESRD patients in 2004: global overview of patient numbers, treatment modalities and associated trends," *Nephrology Dialysis Transplantation*, vol. 20, no. 12, pp. 2587–2593, 2005. 126

[181] A. Biuckians, E. C. Scott, G. H. Meier, J. M. Panneton, and M. H. Glickman, "The natural history of autologous fistulas as first-time dialysis access in the KDOQI era," *Journal of vascular surgery*, vol. 47, no. 2, pp. 415–421, 2008. 126

[182] R. Ponikvar, "Surgical salvage of thrombosed native arteriovenous fistulas for hemodialysis by interventional nephrologists," *Therapeutic Apheresis and Dialysis*, vol. 13, no. 4, pp. 340–344, 2009. 126

[183] Z. Kharboutly, V. Deplano, E. Bertrand, and C. Legallais, "Numerical and experimental study of blood flow through a patient-specific arteriovenous fistula used for hemodialysis," *Medical engineering & physics*, vol. 32, no. 2, pp. 111–118, 2010. 126, 127

[184] M. A. Saleh, W. M. El Kilany, V. W. Keddis, and T. W. El Said, "Effect of high flow arteriovenous fistula on cardiac function in hemodialysis patients," *The Egyptian Heart Journal*, vol. 70, no. 4, pp. 337–341, 2018. 126, 127, 129, 141

[185] A. N. Sidawy, L. M. Spergel, A. Besarab, M. Allon, W. C. Jennings, F. T. Padberg Jr, M. H. Murad, V. M. Montori, A. M. O'Hare, K. D. Calligaro, *et al.*, "The society for vascular surgery: clinical practice guidelines for the surgical placement and maintenance of arteriovenous hemodialysis access," *Journal of vascular surgery*, vol. 48, no. 5, pp. S2–S25, 2008. 127, 129, 130, 136

[186] B. Ene-Iordache, L. Mosconi, G. Remuzzi, and A. Remuzzi, "Computational fluid dynamics of a vascular access case for hemodialysis," *J. Biomech. Eng.*, vol. 123, no. 3, pp. 284–292, 2001. 127

[187] Z. Kharboutly, M. Fenech, J. Treutenaere, I. Claude, and C. Legallais, "Investigations into the relationship between hemodynamics and vascular alterations in an established arteriovenous fistula," *Medical engineering & physics*, vol. 29, no. 9, pp. 999–1007, 2007. 127, 141

[188] I. Decorato, Z. Kharboutly, C. Legallais, and A.-V. Salsac, "Numerical study of the influence of wall compliance on the haemodynamics in a patient-specific arteriovenous fistula," *Computer Methods in Biomechanics and Biomedical Engineering*, vol. 14, pp. 121–123, 2011. 127

[189] A. K. Niemann, S. Thrysoe, J. V. Nygaard, J. M. Hasenkam, and S. E. Petersen, "Computational fluid dynamics simulation of av fistulas: from MRI and ultrasound scans to numeric evaluation of hemodynamics," *The journal of vascular access*, vol. 13, no. 1, pp. 36–44, 2012. 127

[190] I. Decorato, Z. Kharboutly, T. Vassallo, J. Penrose, C. Legallais, and A.-V. Salsac, "Numerical simulation of the fluid structure interactions in a compliant patient-specific arteriovenous fistula," *International journal for numerical methods in biomedical engineering*, vol. 30, no. 2, pp. 143–159, 2014. 127

[191] Z. Kharboutly, J.-M. Treutenaere, I. Claude, and C. Legallais, "Arterio-venous fistula: two cases realistic numerical blood flow simulations," in *2007 29th Annual International Conference of the IEEE Engineering in Medicine and Biology Society*, pp. 2980–2983, IEEE, 2007. 127

[192] B. Ene-Iordache and A. Remuzzi, "Blood flow in idealized vascular access for hemodialysis: a review of computational studies," *Cardiovascular engineering and technology*, vol. 8, no. 3, pp. 295–312, 2017. 127

[193] A. de Villiers, A. McBride, B. Reddy, T. Franz, and B. Spottiswoode, "A validated patient-specific FSI model for vascular access in haemodialysis," *Biomechanics and modeling in mechanobiology*, vol. 17, no. 2, pp. 479–497, 2018. 127

[194] I. Decorato, A.-V. Salsac, C. Legallais, M. Alimohammadi, V. Diaz-Zuccarini, and Z. Kharboutly, "Influence of an arterial stenosis on the hemodynamics within an arteriovenous fistula (AVF): Comparison before and after balloon-angioplasty," *Cardiovascular Engineering and Technology*, vol. 5, no. 3, pp. 233–243, 2014. 127

[195] L. D. Browne, K. Bashar, P. Griffin, E. G. Kavanagh, S. R. Walsh, and M. T. Walsh, "The role of shear stress in arteriovenous fistula maturation and failure: a systematic review," *PloS one*, vol. 10, no. 12, p. e0145795, 2015. 127, 141

[196] C. V. Cunnane, E. M. Cunnane, and M. T. Walsh, "A review of the hemodynamic factors believed to contribute to vascular access dysfunction," *Cardiovascular engineering and technology*, vol. 8, no. 3, pp. 280–294, 2017. 127

[197] S. Manini, K. Passera, W. Huberts, L. Botti, L. Antiga, and A. Remuzzi, "Computational model for simulation of vascular adaptation following vascular access surgery in haemodialysis patients," *Computer methods in biomechanics and biomedical engineering*, vol. 17, no. 12, pp. 1358–1367, 2014. 127

[198] W. Huberts, A. Bode, W. Kroon, R. Planken, J. Tordoir, F. Van de Vosse, and E. Bosboom, "A pulse wave propagation model to support decision-making in vascular access planning in the clinic," *Medical engineering & physics*, vol. 34, no. 2, pp. 233–248, 2012. 127

[199] J. T. Daugirdas, T. A. Depner, J. Inrig, R. Mehrotra, M. V. Rocco, R. S. Suri, D. E. Weiner, N. Greer, A. Ishani, R. MacDonald, *et al.*, "KDOQI clinical practice guideline for hemodialysis adequacy: 2015 update," *American Journal of Kidney Diseases*, vol. 66, no. 5, pp. 884–930, 2015. 129

[200] K. Konner, B. Nonnast-Daniel, and E. Ritz, "The arteriovenous fistula," *Journal of the American Society of Nephrology*, vol. 14, no. 6, pp. 1669–1680, 2003. 129

[201] P. Zamboli, S. Lucà, S. Borrelli, C. Garofalo, M. E. Liberti, M. Pacilio, S. Lucà, G. Palladino, and M. Punzi, "High-flow arteriovenous fistula and heart failure: could the indexation of blood flow rate and echocardiography have a role in the identification of patients at higher risk?," *Journal of nephrology*, vol. 31, no. 6, pp. 975–983, 2018. 129

[202] S. Isoda, H. Kajiwara, J. Kondo, and A. Matsumoto, "Banding a hemodialysis arteriovenous fistula to decrease blood flow and resolve high output cardiac failure: report of a case," *Surgery today*, vol. 24, no. 8, pp. 734–736, 1994. 129, 137

[203] J. M. MacRae, S. Pandeya, D. P. Humen, N. Krivitski, and R. M. Lindsay, "Arteriovenous fistula-associated high-output cardiac failure: a review of mechanisms," *American Journal of Kidney Diseases*, vol. 43, no. 5, pp. e21.1–e21.6, 2004. 129, 141

[204] R. Navuluri and S. Regalado, "The KDOQI 2006 vascular access update and fistula first program synopsis," in *Seminars in interventional radiology*, vol. 26, pp. 122–124, © Thieme Medical Publishers, 2009. 130

[205] W. G. MEMBERS, E. J. Benjamin, M. J. Blaha, S. E. Chiuve, M. Cushman, S. R. Das, R. Deo, S. D. de Ferranti, J. Floyd, M. Fornage, *et al.*, "Heart disease and stroke statistics—2017 update: a report from the American Heart Association," *Circulation*, vol. 135, no. 10, p. e146, 2017. 144

[206] V. Aboyans, J.-B. Ricco, M.-L. E. Bartelink, M. Björck, M. Brodmann, T. Cohnert, J.-P. Collet, M. Czerny, M. De Carlo, S. Debus, *et al.*, "2017 ESC guidelines on the diagnosis and treatment of peripheral arterial diseases, in collaboration with the european society for vascular surgery (ESVS) document covering atherosclerotic disease of extracranial carotid and vertebral, mesenteric, renal, upper and lower extremity arteries endorsed by: the european stroke organization (ESO) the task force for the diagnosis and treatment of peripheral arterial diseases of the european society of cardiology (ESC) and of the european society for vascular surgery (ESVS)," *European heart journal*, vol. 39, no. 9, pp. 763–816, 2018. 144

[207] R. Erbel, V. Aboyans, C. Boileau, E. Bossone, R. Di Bartolomeo, H. Eggebrecht, A. Evangelista, V. Falk, H. Frank, O. Gaemperli, *et al.*, "2014 ESC guidelines on the diagnosis and treatment of aortic diseases: Document covering acute and chronic aortic diseases of the thoracic and abdominal aorta of the adult the task force for the diagnosis and treatment of aortic diseases of the european society of cardiology (ESC)," *European Heart Journal*, vol. 35, no. 41, pp. 2873—-2926, 2014. 144

[208] R. S. D'Agostino, J. P. Jacobs, V. Badhwar, G. Paone, J. S. Rankin, J. M. Han, D. McDonald, F. H. Edwards, and D. M. Shahian, "The society of thoracic surgeons adult cardiac surgery database: 2017 update on outcomes and quality," *The Annals of thoracic surgery*, vol. 103, no. 1, pp. 18–24, 2017. 144

[209] A. Salsano, D. R. Giacobbe, E. Sportelli, G. M. Olivieri, R. Natali, M. Prevosto, V. Del Bono, C. Viscoli, and F. Santini, "Aortic cross-clamp time and cardiopulmonary bypass time: prognostic implications in patients operated on for infective endocarditis," *Interactive cardiovascular and thoracic surgery*, vol. 27, no. 3, pp. 328–335, 2018. 144

[210] V. G. Ruggieri, K. Bounader, J. P. Verhoye, F. Onorati, A. S. Rubino, G. Gatti, T. Tauriainen, M. De Feo, D. Reichart, M. Dalén, *et al.*, "Prognostic impact of prolonged cross-clamp time in coronary artery bypass grafting," *Heart, Lung and Circulation*, vol. 27, no. 12, pp. 1476–1482, 2018. 144

[211] M. Zammert and S. Gelman, "The pathophysiology of aortic cross-clamping," *Best Practice & Research Clinical Anaesthesiology*, vol. 30, no. 3, pp. 257–269, 2016. 144, 162, 170

[212] M. T. Politi, S. A. Wray, J. M. Fernández, J. Gaudric, A. R. Ghigo, P.-Y. Lagrée, C. Capurro, J.-M. Fullana, and R. Armentano, "Impact of arterial cross-clamping during vascular surgery on arterial stiffness measured by the augmentation index and fractal dimension of arterial pressure," *Health and technology*, vol. 6, no. 3, pp. 229–237, 2016. 144

[213] M. Biais, J. Calderon, M. Pernot, L. Barandon, T. Couffinhal, A. Ouattara, and F. Sztark, "Predicting fluid responsiveness during infrarenal aortic cross-clamping in pigs," *Journal of cardiothoracic and vascular anesthesia*, vol. 27, no. 6, pp. 1101–1107, 2013. 144, 163, 170

[214] C. Li, Y.-S. Li, M. Xu, S.-H. Wen, X. Yao, Y. Wu, C.-Y. Huang, W.-Q. Huang, and K.-X. Liu, "Limb remote ischemic preconditioning for intestinal and pulmonary protection during elective open infrarenal abdominal aortic aneurysm repaira randomized controlled trial," *The Journal of the American Society of Anesthesiologists*, vol. 118, no. 4, pp. 842–852, 2013. 144

[215] Y. Kotake, T. Yamada, H. Nagata, J. Takeda, and H. Shimizu, "Descending aortic blood flow during aortic cross-clamp indicates postoperative splanchnic perfusion and gastrointestinal function in patients undergoing aortic reconstruction," *British journal of anaesthesia*, vol. 108, no. 6, pp. 936–942, 2012. 144, 170

[216] K.-F. Klotz, S. Klingsiek, M. Singer, H. Wenk, S. Eleftheriadis, H. Kuppe, and P. Schmucker, "Continuous measurement of cardiac output during aortic cross-clamping by the oesophageal doppler monitor odm 1," *BJA: British Journal of Anaesthesia*, vol. 74, no. 6, pp. 655–660, 1995. 144, 162, 163

[217] L. J. Montenij, W. F. Buhre, S. A. De Jong, J. H. Harms, J. A. Van Herwaarden, C. L. Kruitwagen, and E. E. De Waal, "Arterial pressure waveform analysis versus thermodilution cardiac output measurement during open abdominal aortic aneurysm repair: A prospective observational study," *European Journal of Anaesthesiology (EJA)*, vol. 32, no. 1, pp. 13–19, 2015. 144, 162, 163, 170

[218] A. Lafanechère, P. Albaladejo, M. Raux, T. Geeraerts, R. Bocquet, A. Wernet, Y. Castier, and J. Marty, "Cardiac output measurement during infrarenal aortic surgery: echo-esophageal doppler versus thermodilution catheter," *Journal of cardiothoracic and vascular anesthesia*, vol. 20, no. 1, pp. 26–30, 2006. 144, 170

[219] M. F. Martín-Cancho, V. Crisóstomo, F. Soria, C. Calles, F. M. Sánchez-Margallo, I. Díaz-Güemes, and J. Usón-Gargallo, "Physiologic responses to infrarenal aortic cross-clamping during laparoscopic or conventional vascular surgery in experimental animal model: comparative study," *Anesthesiology research and practice*, vol. 2008, 2008. 144, 163, 170

[220] N. Famaey, G. Sommer, J. Vander Sloten, and G. A. Holzapfel, "Arterial clamping: finite element simulation and in vivo validation," *Journal of the mechanical behavior of biomedical materials*, vol. 12, pp. 107–118, 2012. 144

[221] B. Fereidoonnezhad, R. Naghdabadi, and G. A. Holzapfel, "Stress softening and permanent deformation in human aortas: continuum and computational modeling with application to arterial clamping," *Journal of the mechanical behavior of biomedical materials*, vol. 61, pp. 600–616, 2016. 144

[222] R. V. Mackenzie Ross, M. R. Toshner, E. Soon, R. Naeije, and J. Pepke-Zaba, "Decreased time constant of the pulmonary circulation in chronic thromboembolic pulmonary hypertension," *American Journal of Physiology-Heart and Circulatory Physiology*, vol. 305, no. 2, pp. H259–H264, 2013. 145, 149, 171, 174

[223] A. Pagnamenta, R. Vanderpool, S. Brimioulle, and R. Naeije, "Proximal pulmonary arterial obstruction decreases the time constant of the pulmonary circulation and increases right ventricular afterload," *Journal of applied physiology*, vol. 114, no. 11, pp. 1586–1592, 2013. 145, 149, 171, 174

[224] T. R. Assad, E. L. Brittain, Q. S. Wells, E. H. Farber-Eger, S. J. Halliday, L. N. Doss, M. Xu, L. Wang, F. E. Harrell, C. Yu, *et al.*, "Hemodynamic evidence of vascular remodeling in combined post-and precapillary pulmonary hypertension," *Pulmonary circulation*, vol. 6, no. 3, pp. 313–321, 2016. 145, 149, 171, 174

[225] S. A. Glantz, "Primer of biostatistics," 2002. 149

[226] P. Segers, S. Brimioulle, N. Stergiopulos, N. Westerhof, R. Naeije, M. Maggiorini, and P. Verdonck, "Pulmonary arterial compliance in dogs and pigs: the three-element windkessel model revisited," *American Journal of Physiology-Heart and Circulatory Physiology*, vol. 277, no. 2, pp. H725–H731, 1999. 150

[227] N. P. Smith, A. J. Pullan, and P. J. Hunter, "An anatomically based model of transient coronary blood flow in the heart," *SIAM Journal on Applied Mathematics*, vol. 62, no. 3, pp. 990–1018, 2001. 151

[228] J. C. Stettler, P. Niederer, and M. Anliker, "Theoretical analysis of arterial hemodynamics including the influence of bifurcations," *Annals of biomedical engineering*, vol. 9, no. 2, pp. 145–164, 1981. 151

[229] E. Jones, T. Oliphant, and P. Peterson, "{SciPy}: Open source scientific tools for {Python}," 2014. 154, 156

[230] G. C. V. D. Bos, N. Westerhof, G. Elzinga, and P. Sipkema, "Reflection in the systemic arterial system: effects of aortic and carotid occlusion," *Cardiovascular research*, vol. 10, no. 5, pp. 565–573, 1976. 160, 162, 163

[231] B. Williams, G. Mancia, W. Spiering, E. Agabiti Rosei, M. Azizi, M. Burnier, D. L. Clement, A. Coca, G. De Simone, A. Dominiczak, *et al.*, "2018 ESC/ESH guidelines for the management of arterial hypertension," *European heart journal*, vol. 39, no. 33, pp. 3021–3104, 2018. 162, 169

[232] R. R. Attia, J. D. Murphy, M. Snider, D. G. Lappas, R. C. Darling, and E. Lowenstein, "Myocardial ischemia due to infrarenal aortic cross-clamping during aortic surgery in patients with severe coronary artery disease.," *Circulation*, vol. 53, no. 6, pp. 961–965, 1976. 162, 163

[233] N. Stergiopulos, J. J. Meister, and N. Westerhof, "Evaluation of methods for estimation of total arterial compliance," *American Journal of Physiology-Heart and Circulatory Physiology*, vol. 268, no. 4, pp. H1540–H1548, 1995. 169

[234] N. Galiè, M. Humbert, J.-L. Vachiery, S. Gibbs, I. Lang, A. Torbicki, G. Simonneau, A. Peacock, A. Vonk Noordegraaf, M. Beghetti, *et al.*, "2015 ESC/ERS guidelines for the diagnosis and treatment of pulmonary hypertension: the joint task force for the diagnosis and treatment of pulmonary hypertension of the european society of cardiology (ESC) and the european respiratory society (ERS): endorsed by: Association for european paediatric and congenital cardiology (AEPC), international society for heart and lung transplantation (ISHLT)," *European heart journal*, vol. 37, no. 1, pp. 67–119, 2016. 174

[235] J.-L. Vachiéry, R. J. Tedford, S. Rosenkranz, M. Palazzini, I. Lang, M. Guazzi, G. Coghlan, I. Chazova, and T. De Marco, "Pulmonary hypertension due to left heart disease," *European Respiratory Journal*, vol. 53, no. 1, p. 1801897, 2019. 174, 181

[236] Z. Wang and N. C. Chesler, "Pulmonary vascular wall stiffness: an important contributor to the increased right ventricular afterload with pulmonary hypertension," *Pulmonary circulation*, vol. 1, no. 2, pp. 212–223, 2011. 174

[237] G. Simonneau, M. A. Gatzoulis, I. Adatia, D. Celermajer, C. Denton, A. Ghofrani, M. S. Gomez, R. K. Kumar, M. Landzberg, R. F. Machado, *et al.*, "Updated clinical classification of pulmonary hypertension," *Turk Kardiyoloji Dernegi Arsivi: Turk Kardiyoloji Derneginin yayin organidir*, vol. 42, no. 1, pp. 45–54, 2014. 174, 175

[238] M. M. Hoeper, R. Maier, J. Tongers, J. Niedermeyer, J. M. Hohlfeld, M. Hamm, and H. Fabel, "Determination of cardiac output by the Fick method, thermodilution, and acetylene rebreathing in pulmonary hypertension," *American journal of respiratory and critical care medicine*, vol. 160, no. 2, pp. 535–541, 1999. 175, 181

[239] L. G. Rudski, W. W. Lai, J. Afilalo, L. Hua, M. D. Handschumacher, K. Chandrasekaran, S. D. Solomon, E. K. Louie, and N. B. Schiller, "Guidelines for the echocardiographic assessment of the right heart in adults: a report from the american society of echocardiography: endorsed by the European Association of Echocardiography, a registered branch of the European Society of Cardiology, and the Canadian Society of Echocardiography," *Journal of the American Society of Echocardiography*, vol. 23, no. 7, pp. 685–713, 2010. 175

[240] R. M. Lang, L. P. Badano, V. Mor-Avi, J. Afilalo, A. Armstrong, L. Ernande, F. A. Flachskampf, E. Foster, S. A. Goldstein, T. Kuznetsova, *et al.*, "Recommendations for cardiac chamber quantification by echocardiography in adults: an update from the American Society of Echocardiography and the European Association of Cardiovascular Imaging," *European Heart Journal-Cardiovascular Imaging*, vol. 16, no. 3, pp. 233–271, 2015. 175

[241] C. S. Peskin, "The fluid dynamics of heart valves: experimental, theoretical, and computational methods," *Annual review of fluid mechanics*, vol. 14, no. 1, pp. 235–259, 1982. 179

[242] Y. Sun, B. Sjoberg, P. Ask, D. Loyd, and B. Wranne, "Mathematical model that characterizes transmitral and pulmonary venous flow velocity patterns," *American Journal of Physiology-Heart and Circulatory Physiology*, vol. 268, no. 1, pp. H476–H489, 1995. 179

[243] G. Szabó, D. Soans, A. Graf, C. J. Beller, L. Waite, and S. Hagl, "A new computer model of mitral valve hemodynamics during ventricular filling," *European journal of cardio-thoracic surgery*, vol. 26, no. 2, pp. 239–247, 2004. 179

[244] T. Korakianitis and Y. Shi, "Numerical simulation of cardiovascular dynamics with healthy and diseased heart valves," *Journal of biomechanics*, vol. 39, no. 11, pp. 1964–1982, 2006. 179

[245] P. J. Blanco and R. A. Feijóo, "A 3D-1D-0D computational model for the entire cardiovascular system," *Computational Mechanics, eds. E. Dvorking, M. Goldschmit, M. Storti*, vol. 29, pp. 5887–5911, 2010. 179

[246] S. Rosenkranz and I. R. Preston, "Right heart catheterisation: best practice and pitfalls in pulmonary hypertension," *European Respiratory Review*, vol. 24, no. 138, pp. 642–652, 2015. 181

[247] J. C. Greenfield JR and D. M. Griggs JR, "Relation between pressure and diameter in main pulmonary artery of man," *Journal of Applied Physiology*, vol. 18, no. 3, pp. 557–559, 1963. 185, 186

[248] S. Pant, B. Fabrèges, J.-F. Gerbeau, and I. Vignon-Clementel, "A methodological paradigm for patient-specific multi-scale CFD simulations: from clinical measurements to parameter estimates for individual analysis," *International journal for numerical methods in biomedical engineering*, vol. 30, no. 12, pp. 1614–1648, 2014. 195